

# Deterministic ultracold ion source targeting the Heisenberg limit



## Dissertation

zur Erlangung des Doktorgrades Dr. rer. nat.  
der Fakultät für Naturwissenschaften der Universität Ulm

vorgelegt von

**Wolfgang Schnitzler**

aus Mietingen

2010

Amtierender Dekan: Prof. Dr. Axel Groß

Erstgutachter: Prof. Dr. Ferdinand Schmidt-Kaler

Zweitgutachter: Prof. Dr. Johannes Hecker Denschlag

The work described in this thesis was carried out at the

Universität Ulm  
Institut für Quanteninformationsverarbeitung  
Albert-Einstein-Allee 11  
D-89069 Ulm

The experiment was funded by grants from the Landesstiftung Baden-Württemberg in the framework ‘atomics’ (Contract No. PN 63.14) and the excellence program.

# Abstract

The miniaturization of semiconductor devices has reached length scales of a few tens of nanometers where statistical Poissonian fluctuations of the number of doping atoms in a single transistor significantly affect the characteristic properties of the device. Further miniaturization will even cause statistical device failure. Thus, the ability to deterministically implant single doping atoms into solid state materials with high spatial resolution becomes more and more important. Although a variety of different approaches has been pursued in the last few years, most of these techniques are either restricted to certain ion species or require additional post-detection schemes to detect the implantation event.

Starting from our idea in 2005, this thesis reports on the experimental realization of a deterministic single-ion source, which is based on a specifically designed segmented linear Paul trap and could operate with a huge range of sympathetically cooled ion species, isotopes or ionic molecules.

Using numerical simulations, the properties of our novel ion source are simulated and the generated single-ion beam as well as its dependencies are studied in detail. Experimentally, we characterize our ion source by measuring the beam divergence as well as the velocity distribution of the extracted ions, and by studying the influence of various parameters on the beam quality. For single-ion extraction, we measure a mean velocity of 19.47 km/s with a  $1\sigma$ -spread of only 6.3 m/s and a beam divergence of 600  $\mu$ rad at a distance of 257 mm from the trap center. The total detection efficiency thereby amounts to nearly 90 %. Using a custom-built electrostatic einzel-lens, we demonstrate the focusing of an ion beam consisting of single  $^{40}\text{Ca}^+$  ions to a spot size of a few  $\mu\text{m}$ . Due to the small beam divergence and narrow velocity distribution of the generated single-ion beam, chromatic and spherical aberration at the einzel-lens is strongly reduced, presenting a promising starting point for focusing single ions on their way to the substrate.



# Zusammenfassung

Die Miniaturisierung von Halbleiterbauelementen hat mittlerweile Längenskalen erreicht, auf denen die Bauteile Strukturgrößen von nur noch wenigen Nanometern besitzen und statistische Fluktuationen in der Anzahl der Dotieratome eines einzelnen Transistors dessen charakteristische Eigenschaften maßgeblich beeinflussen. Eine weitere Verkleinerung würde sogar einen statistischen Ausfall der Bauelemente zur Folge haben. Es wird daher immer wichtiger Verfahren zu entwickeln, welche es ermöglichen, einzelne Atome deterministisch und mit hoher Genauigkeit in Festkörper zu implantieren. Obwohl in den letzten Jahren eine Vielzahl verschiedener Ansätze verfolgt wurde, sind die meisten dieser Verfahren entweder auf gewisse Ionensorten beschränkt oder auf eine nachträgliche Detektion des Implantations-Ereignisses angewiesen.

Ausgehend von unserer Idee im Jahr 2005 wird in der vorliegenden Arbeit über die experimentelle Realisierung einer deterministischen Einzelionenquelle auf der Basis einer eigens entwickelten segmentierten linearen Paulfalle berichtet, welche mit einer großen Anzahl von sympathetisch gekühlten Ionensorten, Isotopen und ionischen Molekülen betrieben werden kann.

Anhand von numerischen Simulationen werden die Eigenschaften unserer neuartigen Ionenquelle simuliert und die Abhängigkeiten des erzeugten Einzelionenstrahls im Detail untersucht. Die experimentelle Charakterisierung erfolgt dabei durch die Bestimmung der Strahldivergenz und der Geschwindigkeitsverteilung der extrahierten Ionen, sowie durch eine Untersuchung des Einflusses verschiedener Parameter auf die Strahlqualität. Für den Fall einzeln extrahierter  $^{40}\text{Ca}^+$ -Ionen messen wir in einem Abstand von 257 mm vom Fallenzentrum eine Geschwindigkeitsfluktuation von lediglich 6,3 m/s bei einer mittleren Geschwindigkeit von 19,47 km/s und einer Strahldivergenz von 600  $\mu\text{rad}$ . Die absolute Detektionseffizienz beläuft sich dabei auf nahezu 90 %. Mittels einer speziell angefertigten elektrostatischen Einzellinse wird der erzeugte Einzelionenstrahl dann auf eine Spotgröße von nur wenigen  $\mu\text{m}$  fokussiert. Aufgrund der geringen Strahldivergenz und der schmalen Geschwindigkeitsverteilung ist die chromatische und sphärische Aberration an der Einzellinse stark reduziert, was einen vielversprechenden Ausgangspunkt für die Fokussierung einzelner, in ein Substrat zu implantierender Ionen darstellt.



# List of scientific publications

In the course of this thesis, the achieved experimental results were published in six papers (see also appendix B):

## **New Journal of Physics**

---

### **Focusing a deterministic single-ion beam**

W. Schnitzler, G. Jacob, R. Fickler, F. Schmidt-Kaler and K. Singer

Published on 28th June 2010

(New Journal of Physics / Volume: 12 / Page: 065023 / Year: 2010)

## **Journal of Modern Optics**

---

### **Optimized focusing ion optics for an ultracold deterministic single ion source targeting nm resolution**

R. Fickler, W. Schnitzler, N. M. Linke, F. Schmidt-Kaler and K. Singer

Published on 18th August 2009

(Journal of Modern Optics / Volume: 56 / Page: 2061 / Year: 2009)

## **Physical Review Letters**

---

### **Deterministic Ultracold Ion Source Targeting the Heisenberg Limit**

W. Schnitzler, N. M. Linke, R. Fickler, J. Meijer, F. Schmidt-Kaler and K. Singer

Published on 19th February 2009

(Physical Review Letters / Volume: 102 / Page: 070501 / Year: 2009)

## **Applied Physics A**

---

### **Towards the implanting of ions and nanoparticles with nm spatial resolution**

J. Meijer, S. Pezzagna, T. Vogel, B. Burchard, H. H. Bukow, I. W. Rangelow, Y. Sarov, H. Wiggers, I. Plümel, F. Jelezko, J. Wrachtrup, F. Schmidt-Kaler, W. Schnitzler and K. Singer

Published on 1st May 2008

(Applied Physics A / Volume: 91 / Page: 567 / Year: 2008)

## **New Journal of Physics**

---

### **Transport of ions in a segmented linear Paul trap in printed-circuit-board technology**

G. Huber, T. Deuschle, W. Schnitzler, R. Reichle, K. Singer and F. Schmidt-Kaler

Published on 14th January 2008

(New Journal of Physics / Volume: 10 / Page: 013004 / Year: 2008)

## **Applied Physics A**

---

### **Concept of deterministic single ion doping with sub-nm spatial resolution**

J. Meijer, T. Vogel, B. Burchard, I. W. Rangelow, L. Bischoff, J. Wrachtrup, M. Domhan, F. Jelezko, W. Schnitzler, S. A. Schulz, K. Singer and F. Schmidt-Kaler

Published on 16th February 2006

(Applied Physics A / Volume: 83 / Page: 321 / Year: 2006)

# Contents

<b>1</b>	<b>Introduction</b>	<b>1</b>
<b>2</b>	<b>Single-ion implantation</b>	<b>5</b>
2.1	Applications . . . . .	5
2.1.1	Doping of semiconductor devices . . . . .	5
2.1.2	Solid state quantum computing . . . . .	7
2.2	Techniques for single-ion implantation . . . . .	13
2.2.1	Bottom-up approach . . . . .	14
2.2.2	Top-down approach . . . . .	15
2.2.3	Implantation by using atom or ion traps as ion sources . . . . .	19
<b>3</b>	<b>Theoretical foundations</b>	<b>25</b>
3.1	Confining charged particles in a linear Paul trap . . . . .	25
3.1.1	Dynamic radial confinement . . . . .	27
3.1.2	Static axial confinement . . . . .	30
3.1.3	Vibrational modes of linear ion crystals . . . . .	33
3.2	Light-ion interaction for trapped ions . . . . .	35
3.2.1	Hamiltonian of the trapped ion . . . . .	36
3.2.2	Interaction Hamiltonian . . . . .	37
3.2.3	Lamb-Dicke regime . . . . .	39

---

3.3	Laser cooling . . . . .	41
3.3.1	Energy levels of singly charged calcium . . . . .	42
3.3.2	Doppler cooling . . . . .	43
3.3.3	Sub-Doppler cooling methods . . . . .	45
<b>4</b>	<b>Experimental setup</b>	<b>49</b>
4.1	Ultra high vacuum setup . . . . .	49
4.2	Diode laser systems . . . . .	52
4.2.1	Grating stabilized diode laser DL 100 . . . . .	52
4.2.2	Frequency-doubled diode laser system DL-SHG 110 . . . . .	53
4.2.3	Pound-Drever-Hall frequency stabilization . . . . .	55
4.3	Optical setup . . . . .	56
4.4	Imaging system . . . . .	62
4.5	Trap voltage supplies . . . . .	64
4.6	Dynamic experimental control . . . . .	67
<b>5</b>	<b>Ion trap</b>	<b>69</b>
5.1	Segmented linear rail trap . . . . .	69
5.1.1	Trap design . . . . .	69
5.1.2	Fabrication of the printed circuit board ion trap . . . . .	74
5.2	Operation of the trap . . . . .	75
5.2.1	Photoionization schemes for ion generation . . . . .	76
5.2.2	Micromotion compensation methods . . . . .	79
<b>6</b>	<b>Ion trap as deterministic ion source</b>	<b>83</b>
6.1	Ion extraction . . . . .	83
6.1.1	Extraction mechanism . . . . .	83
6.1.2	Detection of extracted ions . . . . .	85

---

6.2	Dopant ions . . . . .	86
6.2.1	Generation and sympathetic cooling . . . . .	86
6.2.2	Mass determination . . . . .	88
<b>7</b>	<b>Characterization of the ion source</b>	<b>91</b>
7.1	Simulation of the ion source . . . . .	91
7.1.1	Numerical simulation of the ion beam . . . . .	93
7.1.2	Impact of the initial ion temperature . . . . .	95
7.1.3	Impact of the initial start position . . . . .	96
7.1.4	Impact of the phase of the rf voltage . . . . .	98
7.2	Experimental characterization . . . . .	99
7.2.1	Coarse aiming . . . . .	99
7.2.2	Deterministic extraction of ion crystals . . . . .	100
7.2.3	Phase dependence . . . . .	102
7.2.4	Pressure dependence . . . . .	103
7.2.5	Time-of-flight measurements . . . . .	104
7.2.6	Determination of the beam divergence . . . . .	106
7.3	Comparison between simulation and experiment . . . . .	109
<b>8</b>	<b>Focusing ion optics</b>	<b>113</b>
8.1	Theoretical foundations . . . . .	113
8.2	Ion ray tracing simulations . . . . .	116
8.2.1	Comparison of different lens designs . . . . .	117
8.2.2	Characterization of the einzel-lens . . . . .	119
8.2.3	Correction of the spherical aberration . . . . .	122
8.2.4	Ion reflection and post-acceleration . . . . .	125
8.3	Experimental results . . . . .	126

---

8.3.1	Experimental determination of the spot size . . . . .	126
8.3.2	Deterministic single-ion loading . . . . .	128
8.3.3	Modified einzel-lens and single-ion focusing . . . . .	129
<b>9</b>	<b>Detection of implanted ions</b>	<b>133</b>
9.1	Implantation through nano apertures . . . . .	133
9.2	Color centers . . . . .	134
9.3	Microscopy techniques . . . . .	137
9.3.1	STED microscopy . . . . .	137
9.3.2	Scanning tunneling microscopy . . . . .	140
<b>10</b>	<b>Summary and Outlook</b>	<b>143</b>
<b>A</b>	<b>Phase synchronization circuit</b>	<b>147</b>
<b>B</b>	<b>Scientific publications</b>	<b>149</b>
B.1	Physical Review Letters . . . . .	149
B.2	Journal of Modern Optics . . . . .	155
B.3	Applied Physics A - Materials Science & Processing . . . . .	171
B.4	New Journal of Physics . . . . .	185

# List of Figures

2.1	Doping profile of a pMOS nano-transistor . . . . .	6
2.2	Influence of the doping arrangement on semiconductor devices . . . . .	7
2.3	NIST X-trap . . . . .	8
2.4	Schematic drawing of a Si-P based solid state quantum computer . . . . .	9
2.5	Charge-based quantum computing using single donors in semiconductors . .	11
2.6	Nitrogen vacancy ( $NV^-$ ) color center in diamond . . . . .	12
2.7	Implantation of P in Si by using hydrogen passivated surfaces and a STM tip	14
2.8	Single-ion implantation by detection of secondary electrons . . . . .	16
2.9	Single-ion implantation by detection of electron-hole pairs . . . . .	18
2.10	Parallel single-atom deposition . . . . .	20
2.11	Single-ion source based on a magneto-optical trap . . . . .	22
2.12	Single ion source based on a segmented linear Paul trap . . . . .	23
3.1	Schematic drawing of a segmented linear Paul trap . . . . .	26
3.2	Stability diagram for a linear Paul trap . . . . .	28
3.3	Equilibrium positions and normal mode frequencies for linear ion crystals .	32
3.4	Stability of linear ion crystals . . . . .	35
3.5	Transition strengths . . . . .	40
3.6	Level scheme of singly charged calcium . . . . .	42
3.7	EMCCD images of Doppler cooled $^{40}\text{Ca}^+$ ions . . . . .	44

---

3.8	Sideband cooling scheme . . . . .	46
3.9	EIT cooling scheme . . . . .	47
4.1	Technical drawing of the main vacuum chamber . . . . .	50
4.2	Schematic drawing of the ultra high vacuum setup . . . . .	51
4.3	Schematic drawing of the diode laser DL 100 . . . . .	52
4.4	Schematic drawing of the frequency doubled diode laser system DL-SHG 110 . . . . .	54
4.5	Schematic drawing of the Pound-Drever-Hall frequency stabilization . . . . .	55
4.6	Schematic drawing of the experimental setup . . . . .	56
4.7	Picture of the experimental setup . . . . .	57
4.8	Schematic drawing of a double pass . . . . .	59
4.9	Assembly and mode spectrum of the low finesse cavity . . . . .	60
4.10	Characteristics of a photonic crystal fiber . . . . .	61
4.11	Schematic drawing of the custom-made lens system used for ion imaging . . . . .	63
4.12	Layout of a helical resonator . . . . .	65
4.13	GUI of the experimental control software MCP . . . . .	68
5.1	Technical drawing of one of the four trap blades . . . . .	70
5.2	Sketch of the segmented linear Paul trap . . . . .	71
5.3	Technical drawings of different blade designs . . . . .	72
5.4	Simulated radial pseudopotential . . . . .	73
5.5	Simulated axial potentials . . . . .	73
5.6	Simulated axial trapping potential . . . . .	74
5.7	Picture of the trap holder . . . . .	75
5.8	Level schemes for the ionisation of $^{40}\text{Ca}$ and $^{52}\text{Cr}$ . . . . .	76
5.9	Layouts of two different calcium ovens . . . . .	78
5.10	Micromotion compensation . . . . .	79

---

5.11	Bias-T circuit for micromotion compensation . . . . .	80
6.1	Schematic drawing of the axial trapping potential . . . . .	84
6.2	Schematic drawing of the utilized extraction mechanism . . . . .	85
6.3	Schematic drawing of the extraction setup . . . . .	86
6.4	Pictures of the electron multiplier tube used for ion detection . . . . .	87
6.5	Mixed ion crystal consisting of 10 $^{40}\text{Ca}^+$ ions and one dark ion . . . . .	88
6.6	Mass determination of prospective dopant atoms . . . . .	89
6.7	Fluorescence signal of a pure $^{40}\text{Ca}^+$ two-ion crystal as a function of the excitation frequency . . . . .	90
7.1	AutoCAD drawing of the segmented linear rail trap . . . . .	92
7.2	Simulated motion of the ions inside of the trap . . . . .	93
7.3	Numerical simulation of ion trajectories during extraction . . . . .	94
7.4	Dependence of the ion beam on the initial ion temperature . . . . .	96
7.5	Dependence of the ion beam on the initial start position . . . . .	97
7.6	Dependence of the ion beam on the phase of the rf voltage . . . . .	98
7.7	Typical detector signal in case of ion cloud extraction . . . . .	100
7.8	Deterministic extraction of ion crystals with varying size . . . . .	101
7.9	Hit rate for single ions as a function of the rf trigger phase . . . . .	102
7.10	Hit rate for single ions as a function of the vacuum base pressure . . . . .	103
7.11	Time-of-flight measurements for single ions and two-ion crystals . . . . .	105
7.12	Movable aperture plate used for the determination of the beam divergence .	106
7.13	Hit rate as a function of the deflection voltages for the 5 mm aperture . . .	107
7.14	Hit rate as a function of the deflection voltages for the 1 mm aperture . . .	108
7.15	Compensation of the drift of the ion beam . . . . .	109
7.16	Comparison of the simulation with the experiment . . . . .	110

7.17	Schematic drawing of the detector translation stage . . . . .	111
8.1	Aberration errors . . . . .	116
8.2	Operating modes of an electrostatic einzel-lens . . . . .	117
8.3	Comparison of different lens designs . . . . .	118
8.4	Pictures of the electrostatic einzel-lens (1 mm aperture) . . . . .	120
8.5	Potential distribution of the electrostatic einzel-lens . . . . .	121
8.6	Ion trajectories passing through the electrostatic einzel-lens . . . . .	122
8.7	$1\sigma$ -spot radius as a function of the lens voltage and the initial displacement of the ion beam . . . . .	123
8.8	Spherical aberration correction . . . . .	124
8.9	Ion reflection . . . . .	126
8.10	Experimental determination of the spot size . . . . .	128
8.11	Deterministic single-ion loading . . . . .	129
8.12	Modified electrostatic einzel-lens . . . . .	130
8.13	Hit rate for single ions as a function of the blade position . . . . .	131
8.14	Simulated $1\sigma_r$ -spot radii as a function of the spatial displacement of the ion beam . . . . .	132
9.1	Pierced AFM-tip consisting of SiN . . . . .	134
9.2	Fluorescence image of an NV color center pattern . . . . .	134
9.3	Second order auto-correlation function measurement . . . . .	135
9.4	Yield for NV color center creation as a function of the implantation energy	136
9.5	Straggling and vacancy generation as a function of the implantation energy	137
9.6	Principle of STED microscopy . . . . .	138
9.7	STED microscopy of $NV^-$ color centers . . . . .	139
9.8	Principle of nanoscale electron focusing . . . . .	141
9.9	Localization of single Co dopants by utilizing nanoscale electron focusing .	142

# Chapter 1

## Introduction

In an age of electronic data processing, the demand for more powerful and faster computers is unprecedented. As already stated by Gordon E. Moore in 1965, the number of transistors that can be placed inexpensively on an integrated circuit has increased exponentially, doubling approximately every two years [Moo65]. By now, the miniaturization of semiconductor devices has reached length scales of a few tens of nanometers where statistical Poissonian fluctuations of the number of doping atoms in a single transistor significantly affect the characteristic properties of the device, e.g. gate voltage or current amplification [Shi05]. Further miniaturization will even cause statistical device failure. Especially when thinking about future solid state quantum processors, statistical fluctuations of the dopant concentration are fatal for systems, which are based on single implanted qubit carriers like color centers in diamond or phosphorus dopants in silicon [Gur07, Neu08, Kan98, Gre08a].

Until recently, the only known methods to control the number of dopants resorted to statistical thermal sources followed by a post-detection of the implantation event which is either achieved by the observation of Auger electrons, photoluminescence, phonons, the generation of electron-hole pairs or changes in the conductance of field-effect transistors [Shi02, Per04b, Mit05, Bat07, Shi08]. However, to make the detection of such an event successful, the methods require either highly charged ions or high implantation energies which, as a down side, generate unintentional defects in the host material. In these systems, resolutions of less than 10 nm are achieved by means of masks and apertures, shielding the substrate from incident ions and leading to compulsory losses of doping atoms. Another fabrication method, which is specific for Si-surfaces, uses hydrogen terminated surfaces which are structured with the tip of a tunneling microscope followed by a chemical reactive surface binding of dopants such as phosphorus [O'B01, Sch03, Rue04, Pok07, Rue07].

With this technique, sub-nm resolution can be achieved but the applicability is mainly limited to specific substrates and impurities in the background gas can cause severe impairment. In order to circumvent the necessity of any post-detection schemes and to expand the applicability to a wider range of elements, deterministic single-ion sources on the basis of optical lattices [Gre07] and magneto-optical traps [Hil03b, Han06b, Han08] have been developed. Starting from a Bose-Einstein condensate (BEC) consisting of ultracold chromium atoms, the former method utilizes a Mott-Insulator transition in a three-dimensional optical lattice to generate a single-atom array which can then be deposited onto the substrate. The latter technique relies on a specifically designed magneto-optical trap (MOT), where trapped particles are selectively ionized and extracted out of the trap. Although both methods exhibit a predicted implantation resolution on the nanometer scale, the major drawback is given by the restriction on atom species, which feature a level scheme suitable for laser cooling and allow for Bose condensation. Thus, technologically important elements such as phosphorus and nitrogen are still inaccessible due to the lack of appropriate laser systems.

The main goal of this thesis was to develop a novel ultracold ion source which can be used for the deterministic implantation of a predetermined number of single ions into solid state materials [Mei06, Sch09a]. The presented technique is based on a segmented linear Paul trap with laser-cooled  $^{40}\text{Ca}^+$  ions, which is similar to setups that are used for scalable quantum information processing with ions [Row02]. Additionally loaded doping ions such as nitrogen cannot be directly laser-cooled, but it is still possible to sympathetically cool them by  $^{40}\text{Ca}^+$  ions due to the Coulomb interaction between the charged particles. Hence, this allows for operating the system with a huge range of ion species, isotopes or ionic molecules. Using an electrostatic einzel-lens, the focusing of an ion beam consisting of single  $^{40}\text{Ca}^+$  ions is demonstrated as well [Fic09b, Sch10].

The thesis is structured as follows: In chapter 2, different approaches for the realization of a deterministic single ion source will be presented, highlighting the advantages and limitations. Chapter 3 is dedicated to the basic theoretical foundations, which are necessary to understand the trapping and cooling of charged particles. A description of the experimental setup is given in chapter 4. Chapter 5 is concerned with the segmented linear Paul trap, which is used as deterministic point source for laser-cooled ions. The main emphasis is thereby placed on the design and fabrication process, with the last section being devoted to photoionisation schemes and micromotion compensation methods. A detailed description of the extraction mechanism is given in chapter 6. The generation, cooling and identification of prospective dopant ions is also discussed. The main experimental results

of the thesis are presented in chapters 7 and 8. In chapter 7, the main focus lies on the characterization of the deterministic single-ion source. Time-of-flight measurements are performed in order to determine the velocity distribution of the extracted ions, with the beam divergence being measured by using different sized apertures in combination with a nano positioning stage. Numerical simulations are used to study the dependencies of the generated single-ion beam in detail, allowing for a better understanding of the extraction process. Chapter 8 is concerned with the developed electrostatic einzel-lens, which is used to focus the extracted ions down to a spot size of a few  $\mu\text{m}$ . Here, a razor blade is employed as a well-defined tearing edge to determine the focal spot size. The properties of the developed ion optics are also discussed by means of numerical ray tracing simulations, including a brief description of the different operating modes and a comparison of different lens designs. Chapter 9 deals with the issue of how to prove that the implantation was indeed successful and that the placement and the spacing of the dopant ions match the expected values. In the final chapter, possible improvements of the experimental setup are discussed and future prospects of the experiment are indicated.



## Chapter 2

# Single-ion implantation

Ion implantation describes the action of artificially inserting charged impurity atoms in solid state materials. Standard techniques normally utilize an ion beam with doses of  $10^{12}$  to  $10^{18}$  ions per  $\text{cm}^2$  with mean implantation energies ranging from a few keV up to many MeV. Such ion beams are normally utilized for materials research purposes or for the doping of semiconductor devices. However, although already today several applications for the implantation of single ions are present, the development of deterministic single-ion sources was not possible until recently. After a description of possible applications (2.1), the different approaches for the realization of a deterministic single ion source will be presented and the assets and drawbacks of each system will be discussed (2.2).

## 2.1 Applications

### 2.1.1 Doping of semiconductor devices

Due to the ongoing miniaturization, state-of-the-art semiconductor devices [Nat08] have meanwhile reached length scales of a few tens of nanometers (see Fig. 2.1), containing only some hundreds of dopant atoms. Although single atom devices are still far from being industrially manufactured, it is predicted that within the next 5 years, the mean number of dopants in a single transistor will drop below 100 [Sem07], which will not only be a problem due to the statistical nature of current implantation techniques but also because of the cluster formation of the dopants, strongly limiting the size of future devices by forming electronically separated dopant-induced dots and introducing drastic changes in the current-voltage characteristics [Ebe04]. Due to the small number of dopants,

statistical Poissonian fluctuations of the dopant concentration are already in the region of about 10 %, becoming even more crucial upon further downsizing.

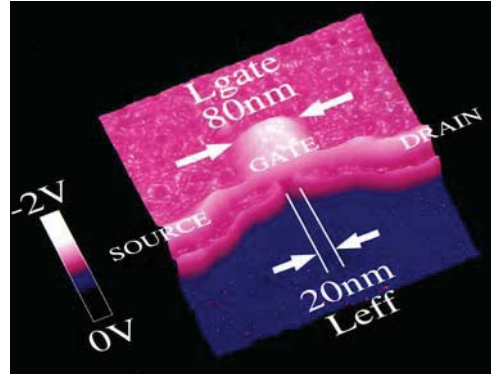


**Figure 2.1:** Scanning capacitance micrograph of the two-dimensional doping profile observed in an 80 nm gate length pMOSFET. Red or pink coloring indicates the p-type doping while the n-type doping is indicated by blue coloring, respectively. [Luc00]

Furthermore, the smaller the device, the more important becomes the positioning of its building blocks, i.e. the localization of the dopant atoms significantly affects the characteristic properties of the device. Hence, it is no more possible to assume a uniform homogeneous doping, but it is necessary to describe the density of the doping atoms at the corresponding implantation positions as a  $\delta$ -function, with the electrostatic potential being given by the Coulomb potential with a singularity at the point of each localized dopant [San01].

The influence of an ordered dopant distribution in contrast to a conventional random doping on the characteristic properties of a semiconductor device was for example studied in the group of T. Shinada in Japan by implanting  $P^{2+}$  ions one-by-one into the channel region of a field-effect transistor<sup>1</sup> at a center-to-center distance of 100 nm [Shi05], see also Fig. 2.2(b). Electrical measurements of the resulting transistors revealed that device-to-device fluctuations in the threshold voltage  $V_{th}$ <sup>2</sup> were by a factor of 3 less for those structures with ordered dopant arrays than for those with conventional random doping, with fluctuations in the range of  $\pm 0.1$  V and  $\pm 0.3$  V, respectively. It was also found that the devices with ordered dopant arrays exhibited a reduction in  $V_{th}$  relative to the undoped semiconductor which was twice that for a random dopant distribution. In case

<sup>1</sup> FET, **F**ield-**E**ffect **T**ransistor

<sup>2</sup> The threshold voltage  $V_{th}$  is usually defined as the voltage, which needs to be applied to the gate of a field-effect transistor in order to induce a current flow from the drain to the source contact of the transistor.

of an ordered distribution, the threshold voltage difference equaled  $\Delta V_{\text{th}} = 0.4 \text{ V}$  with a corresponding value of  $0.2 \text{ V}$  in case of a random distribution, see also Fig. 2.2. According to Shinada, this can be attributed to the uniformity of the electrostatic potential in the conducting channel region due to the ordered distribution of dopant atoms.

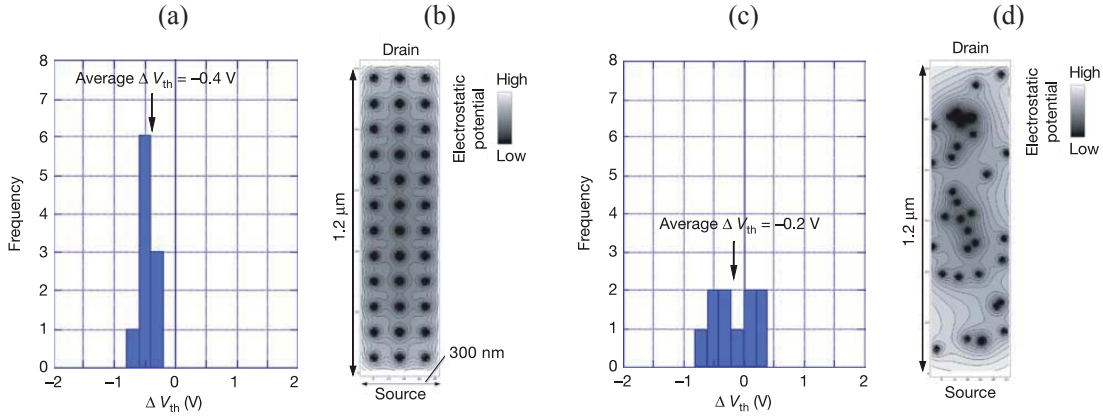


**Figure 2.2:** Histograms of the threshold voltage differences  $\Delta V_{\text{th}}$  before and after single ion implantation for 10 resistors. (a) Histogram for an ordered dopant distribution and (b) the associated contour plot of the Coulomb potentials. (c),(d): Corresponding plots for the conventional random dopant distribution. Gaussian fitting shows a standard deviation of only  $0.1 \text{ V}$  for the ordered distribution and  $0.3 \text{ V}$  for the random distribution, respectively. [Shi05]

Hence, by deterministically implanting single dopant atoms, it is not only possible to manufacture semiconductor devices with reproducible characteristics due to smaller fluctuations, but the reduction of the threshold voltage difference  $\Delta V_{\text{th}}$  also allows for a reduction of the operating voltages, effectively reducing the power consumption and therefore the heat dissipation of the devices.

### 2.1.2 Solid state quantum computing

In case of quantum information processing with ion traps, the trapping and shuttling of trapped ions in complex multi-zone trap structures is one of the key points in order to realize a future quantum computer. So far, a maximum number of eight ions has been entangled using a conventional linear ion trap [Häf05, Lei05]. However, in order to realize more complex quantum algorithms and to efficiently implement quantum registers, memories or even quantum error correction, a further upscaling of these systems to larger networks is inevitable. In current ion traps, the formation of 2D trap arrays is realized by utilizing different kinds of junctions, e.g. T-junctions [Moe05] or X-junctions [Bla09], which

not only allow for storing ions in different trap regions but also for swapping individual ions which are part of larger ion crystals. Figure 2.3 shows pictures of the NIST<sup>3</sup> X-trap featuring a total of 18 different trapping zones which are connected via an X-junction. Although the presented trap architecture allows for shuttling individual ions between different trapping zones with high efficiency and low heating rates, the technological effort to control and manufacture such traps is immense. Further upscaling to more complex structures will only be feasible using surface electrode traps, where one can rely on lithography and etching techniques which are also used for the production of semiconductor devices [Moe05].

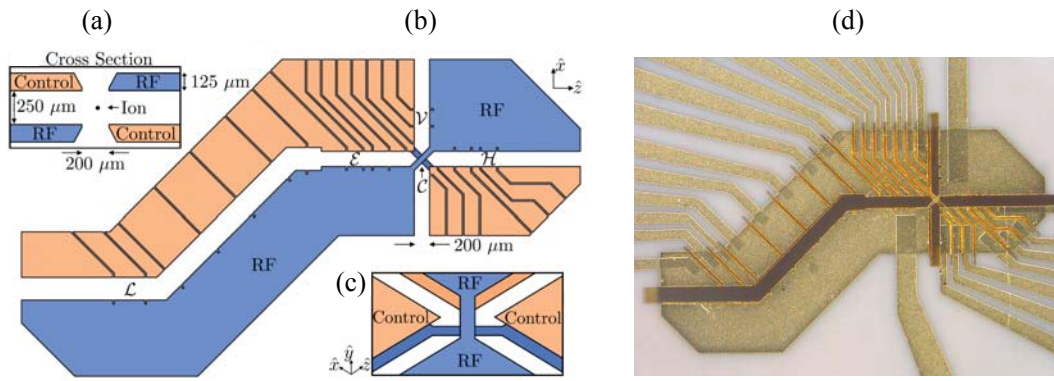


**Figure 2.3:** NIST X-trap featuring a total of 18 different trapping zones which are connected via an X-junction. (a) Cross-sectional view of the two layers of electrodes. (b) Top view of the electrode layout, with the rf electrodes indicated, and all other (control) electrodes held at rf ground. A nearly identical set of electrodes sits below these electrodes, with rf and control electrodes interchanged. 46 control electrodes support 18 different trapping zones. The loading zone ( $\mathcal{L}$ ), the main experimental zone ( $\mathcal{E}$ ), the vertical zone ( $\mathcal{V}$ ), the horizontal zone ( $\mathcal{H}$ ) and the center of the junction ( $\mathcal{C}$ ) are labeled. (c) Schematic of the rf bridges from an oblique angle (not to scale). (d) Close-up view of the assembled trap. [Bla09]

One of the main advantages of solid state based quantum computers is the prospect of a potential scalability of the utilized systems. However, in order to realize a future solid state quantum computer, the ability to deterministically implant single dopant atoms with high spatial resolution is even more crucial than in the case of semiconductor devices, as most of these systems rely on single implanted qubit carriers like phosphorus dopants in silicon or color centers in diamond. In the following subsections, a selection of these systems will be presented, highlighting the advantages and limitations.

<sup>3</sup> National Institute of Standards and Technology

### Nuclear spin based Si-P quantum computer

One of the most popular schemes for the realization of a solid state quantum computer is based on a proposal by B. E. Kane from the year 1998 [Kan98], where the nuclear spins of single phosphorus dopants are used as qubits, see Fig. 2.4 for a schematic drawing. Being buried at a depth of 10 nm below the surface of the silicon host material, the individual P-donors are placed at a distance of 20 nm with respect to each other. So-called A-gates above the P-donors, which are electrically isolated by a  $\text{SiO}_2$  layer, are used to control the strength of the hyperfine interactions of the nuclear spins beneath them. By applying an electric field to the electron-donor system, the electron wave function envelope is shifted away from the nucleus (see the two P-donors located on the left side of Fig. 2.4), effectively reducing the hyperfine interaction and thus leading to a change of the resonance frequency. A globally applied ac magnetic field  $B_{ac}$  with an amplitude of  $\sim 10^{-3}$  T then allows for flipping individual nuclear spins at resonance which are otherwise aligned due to a static magnetic field  $B_0 \geq 2$  T.

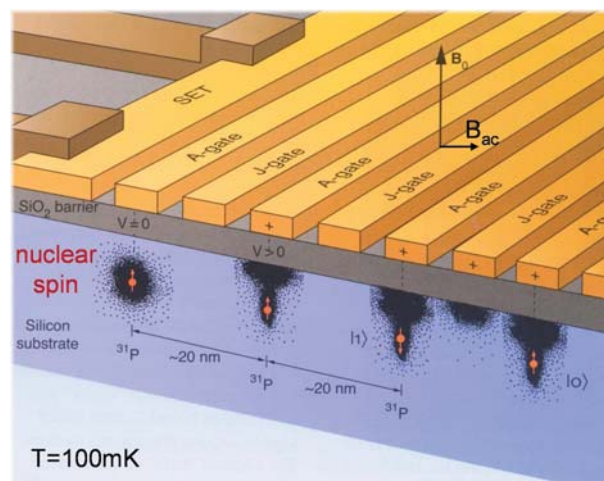


**Figure 2.4:** Schematic drawing of a Si-P based solid state quantum computer as proposed by B. E. Kane. J-gates are used to control the interaction between adjacent P-donors whereas A-gates are used to manipulate the interaction between the nuclear spins of the implanted phosphorus atoms and the external magnetic field  $B_{ac}$ . [Kan98]

Two-qubit operations are performed by utilizing so-called J-gates between the donors, which allow for turning on and off the electron-mediated coupling between adjacent nuclear spins. By applying a voltage to one of the J-gates, one can vary the electrostatic potential between two P-donors, effectively creating an overlap of the corresponding electron wave functions with the exchange coupling being directly proportional to the generated overlap

(see the two P-donors located on the right side of Fig. 2.4). Hence, a custom adjustment of the coupling of each spin to its neighbors and to  $B_{ac}$  enables different operations to be performed on each of the spins simultaneously. The readout of the nuclear spins is also done using the aforementioned J-gates. By adiabatically raising the voltage over a critical threshold  $U_J = \mu_B B/2$ , the distinct nuclear spin states are converted into states with different electron polarization. If one now applies different voltages to the A-gates, it is possible to determine the different electron spin states by performing a voltage measurement using sensitive single-electron capacitance techniques [Ash96]. The described spin measurement process can also be used to prepare individual nuclear spins in a prescribed state by first determining the state of a spin and flipping it if necessary.

One of the main advantages of the Kane proposal is based on the fact that the readout process of the nuclear spins is done purely electronically, not only allowing for an amplification of the measured signal using conventional electronics but also for an immediate subsequent processing. Using low-temperature electronics to bias the gates (e.g. by using on-chip capacitors), it will also be possible to operate the system at temperatures of a few hundred mK. According to Kane, this would result in decoherence times of up to  $10^6$  s, which theoretically would allow one to perform up to  $10^{10}$  logical operations without losing coherence<sup>4</sup>.

### Charge-based quantum computing using single donors in semiconductors

Another scheme for a scalable solid state quantum computer, which was first proposed by D. Loss and D. P. DiVincenzo in 1998 [Los98], utilizes two phosphorus dopants, which are both buried in a semiconductor crystal consisting of Si [Hol03]. Effectively forming a P-P<sup>+</sup> system with a single electron, the encoding of the two quantum logic states  $|0\rangle$  and  $|1\rangle$  is realized via the localization of the electron in the double well potential formed by the two donor P<sup>+</sup> ions, see also Fig. 2.5(a).

Similar to the Kane proposal, so-called barrier (B) and symmetry (S) gates are placed on top of an isolating layer consisting of SiO<sub>2</sub> and allow one to externally control the barrier height as well as the potential offset and symmetry between the two phosphorus dopants. The initialization and readout of this so-called charge qubit is done using a single electron transistor<sup>5</sup> with a calculated readout time of about 50 ps, which is considerably faster than the expected decoherence time in the range of a few  $\mu$ s. Furthermore, using a controlled

<sup>4</sup> Typical gate times in quantum information experiments range in the order of 100  $\mu$ s.

<sup>5</sup> SET, Single Electron Transistor

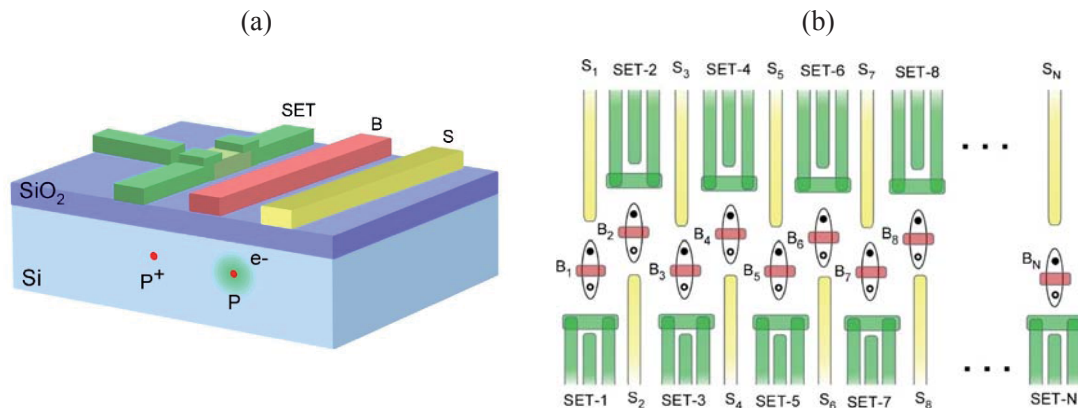


**Figure 2.5:** Buried charge qubit as proposed by L. C. L. Hollenberg. (a) The solid-state charge qubit is based on two buried P dopants in a Si semiconductor crystal, effectively forming a P-P<sup>+</sup> system with one electron. Barrier (B) and symmetry (S) gates allow one to control the barrier height as well as the potential offset and symmetry between the two P dopants. A single electron transistor (SET) is used for a charge-based readout of the qubit state. (b) Schematic of a scaled-up architecture based on the staggered CPHASE configuration. [Hol03]

phase arrangement (CPHASE), the system can be easily extended to a linear array of coupled qubits, see Fig. 2.5(b). Since two qubits act symmetrically on each other, it is possible to transmit quantum information either to the left or the right qubit in the array. Due to the long-range nature of the Coulomb coupling and the ability to tune the intraqubit tunneling rate using the B-gate, the constraints on the spacings of the buried phosphorus dopants are significantly relaxed in comparison with previous spin-based donor schemes. Nevertheless, the realization of the devices depicted in Fig. 2.5 requires to deterministically dope a semiconductor at the single-donor level with interdonor spacings in the range of 20 to 100 nm.

### Nitrogen vacancy (NV) color centers in diamond

One of the most promising candidates for the realization of a future solid state quantum computer are color centers in diamond [Gre08a, Pra08]. Color centers are optically active centers, which are either formed by an impurity or defect in the diamond host crystal, e.g. being responsible for the colors of emeralds and rubies. The color center mostly used in diamond is the negatively charged nitrogen vacancy (NV) center consisting of a substitutional nitrogen atom next to a missing carbon atom, see Fig. 2.6(b). Such NV centers can be created by single-ion implantation of nitrogen [Mei05, Rab06]. As this technique

does not require the presence of nitrogen in the host material, ultrapure (type IIa) diamond can be used as a substrate, effectively reducing the number of randomly distributed nitrogen atoms to a minimum. Depending on the implantation energy, numerous vacancies are created when the nitrogen atoms are implanted. However, in order to create a color center, these vacancies need to be located in close proximity to the implanted nitrogen atoms, which can be achieved by annealing the diamond at temperatures of 800 °C, leading to a random walk of the created vacancies inside of the diamond host crystal. During the annealing process, one of the mobile vacancies can now become trapped by an implanted nitrogen atom, either generating a neutral ( $NV^0$ ) or negatively charged ( $NV^-$ ) color center.

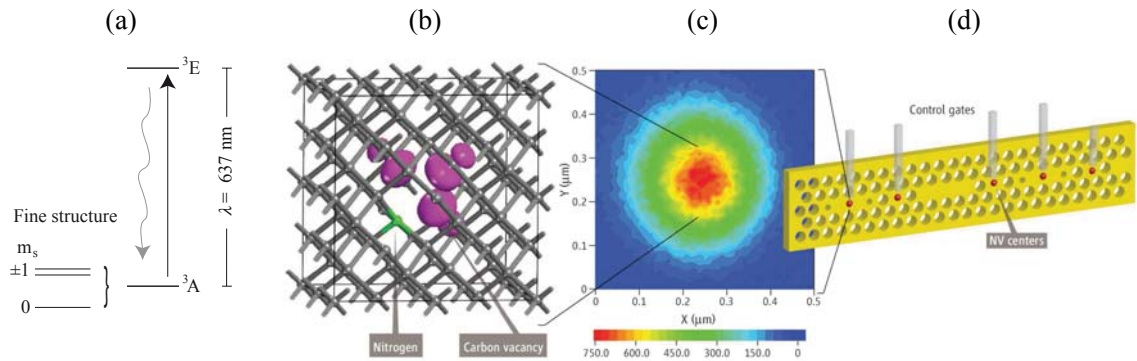


**Figure 2.6:** Nitrogen vacancy ( $NV^-$ ) color center in diamond. (a) Energy-level diagram of the NV center showing fluorescence at 637 nm, including the electron spin triplet of the ground state. (b) Schematic drawing of the electronic structure of the NV center with the nitrogen atom being depicted in green, showing the distribution of electron clouds (purple). (c) High-resolution confocal microscope image of a single NV center. The signal-to-background ratio is in excess of 50:1. (d) Schematic of a photon module (yellow) consisting of NV centers (red) in an array of photonic band-gap cavities. Tuning of each NV center to the cavity resonance is achieved via control gates (gray). [Gae06, Pra08]

For the negatively charged NV color center, the ground state is a spin triplet state  $^3A$ , originating from six unpaired electron spins. Due to the  $C_{3v}$  symmetry of the NV center, the ground state spin sublevels  $m_s = \pm 1$  are degenerate and the zero-field splitting from  $m_s = 0$  equals 2.87 GHz [Neu09]. The excited state  $^3E$  is also a spin triplet and is associated with a broadband photoluminescence emission with a zero phonon line at 637 nm, see also Fig. 2.6(a). However, photoluminescence can only be detected when the electron spin is in the  $m_s = 0$  spin sublevel. Although the structure of the excited-state spin depends on the local crystal environment, photon scattering on the  $^3A \leftrightarrow ^3E$  transition preserves

the spin of the  $m_s = 0$  state, whereas the  $m_s = \pm 1$  states can non-radiatively decay into the  $m_s = 0$  state. Hence, this leads to a strong spin polarization of the NV center by optical pumping, and also to a spin-dependent photon-scattering efficiency, allowing for the readout of the electronic spin state by monitoring the photoluminescence intensity. Figure 2.6(c) shows a high-resolution confocal microscope image of a single NV center with the signal-to-background ratio being in excess of 50:1. By using the  $m_s = 0$  and  $m_s = \pm 1$  ground state spin sublevels for the encoding of the quantum logic states, coherence times of up to 0.35 ms can be achieved at room temperature [Gae06].

Using these properties as a starting point, the group around J. Wrachtrup not only succeeded in driving Rabi oscillations between the  $m_s = 0$  and the  $m_s = \pm 1$  sublevels [Jel04a], but also demonstrated a conditional two-qubit operation in the form of a so-called CROT-gate, where the target qubit is not completely flipped, but undergoes a controlled rotation [Jel04b]. Recently, it was also possible to prove entanglement between the electron spin associated with the NV color center and the nuclear spins of proximal  $^{13}\text{C}$  nuclei [Chi06, Neu08]. By utilizing these electron-nuclear coupled systems, the group of M. Lukin already realized a few-qubit quantum register [Gur07], but one can also couple a pure proximal nitrogen atom to an  $\text{NV}^-$  center and readout its spin due to the mutual interaction [Gae06, Han06a].

Because of the easy state readout and the long coherence times, the spin states of the  $\text{NV}^-$  color center in diamond are a promising starting point for the realization of a solid state quantum computer. Hence, it is not astonishing that a variety of different approaches exists to upscale single color centers to larger networks. Possible ideas range from connecting several  $\text{NV}^-$  centers through chains of N defects [Han06a] to the implementation of  $\text{NV}^-$  centers in an array of photonic band-gap cavities [Dev07], see Fig. 2.6(d). In addition, new applications have been developed such as using NV color centers in diamond as single photon sources [Su08] or as highly sensitive magnetometers [Maz08, Tay08].

## 2.2 Techniques for single-ion implantation

Due to the variety of the aforementioned applications and the increasing necessity for single ion implantation, various groups worldwide are pursuing different approaches in order to develop a deterministic single-ion source, which will allow one to implant single dopant atoms with high spatial resolution. In the following chapters, the current status of the different projects will be presented and the assets and drawbacks of each system will be discussed.

### 2.2.1 Bottom-up approach

Exploiting the accuracy of a scanning tunneling microscope<sup>6</sup>, a technique developed in the group of M. Simmons revolves around the nanometer precise placement of single phosphorus atoms on a Si surface, which has been passivated with a monolayer of hydrogen [O'B01, Sch03]. Because the dopant atoms are only adsorbed on the surface of the substrate with a subsequent encapsulation by an overgrowth with silicon, this technique is often referred to as bottom-up approach.

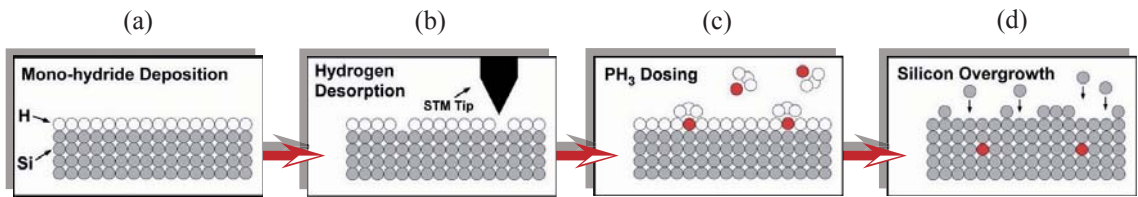


**Figure 2.7:** Schematic drawing of the process to fabricate an array of phosphorus qubits in silicon as used in the group of M. Simmons. (a) A low defect density Si(001)-surface is passivated with a monolayer of hydrogen. (b) Using a STM tip, individual hydrogen atoms are selectively desorbed from the surface. (c) The adsorption of the phosphorus atoms is achieved by exposing the surface to high purity phosphine (PH<sub>3</sub>) gas. (d) Low-temperature silicon overgrowth encapsulates the phosphorus atoms in the Si substrate. [O'B01]

Starting from a clean, low defect density Si(001)-surface by heating the sample to 1200 °C in a variable-temperature ultra high vacuum STM system and performing a controlled cool-down, a monolayer of atomic hydrogen is adsorbed to the surface, effectively forming a monohydride phase where one hydrogen atom bonds to each silicon atom, see Fig. 2.7(a). A STM tip is then used to desorb individual hydrogen atoms from the surface by the application of a controlled voltage pulse between the tip and the sample, see Fig. 2.7(b). As a reaction with the environment can only occur at locations, where the hydrogen atoms have been removed, exposing the surface to high purity phosphine (PH<sub>3</sub>) gas thus allows for adsorbing phosphine molecules to the corresponding positions on the surface, see Fig. 2.7(c). In order to allow for the adsorption of one phosphine molecule, and therefore only one phosphorus atom, it is necessary to desorb an area that exposes less than or equal to two silicon dimers as the phosphine bonds to the surface with a certain periodicity. By annealing the PH<sub>3</sub> dosed surface at low temperatures, the phosphine molecules then dissociate into P and H, allowing the P atoms to be incorporated into the surface. A surface diffusion of the P atoms and a desorption of the surrounding hydrogen-resist layer

<sup>6</sup> STM, Scanning Tunneling Microscope

can thereby be prevented by carefully adjusting the annealing temperature, leading to a overall lateral positioning accuracy of 1 nm for single P atoms [Sch03]. Using molecular beam epitaxy<sup>7</sup> at low temperatures, it is also possible to encapsule the incorporated P atoms by overgrowing them with a few monolayers of Si after the adsorption process, effectively minimizing the possibility of dopant diffusion and segregation out of the STM-patterned regions [Rue04], see also Fig. 2.7(d). Hence, a multi-level STM patterning combined with MBE growth allows for achieving atomic-scale resolution in all three spatial dimensions.

By utilizing this technique, it was not only possible to fabricate ordered Si:P dopant arrays with spacings of a few nanometers [Pok07], but also nanowires [Rue04] or even complete nanodevices such as a single electron transistor [Rue07]. However, although this method allows for placing single dopants with sub-nm resolution, one of the major drawbacks relies on the fact, that the applicability is restricted to Si substrates due to the required surface passivation with hydrogen. Hence, it cannot be utilized as a universal implantation technique for single ions.

### 2.2.2 Top-down approach

In contrast to the bottom-up approach mentioned above, where single dopant atoms are deposited on the surface of the substrate followed by an additional overgrowth with several atom layers of the host material, the main advantage of top-down implantation techniques relies on the fact, that they can be used irrespective of the utilized target substrate. Here, the dopant atoms are accelerated by means of electrostatic fields and impinge on the target, effectively penetrating the surface. The energy of the ions, as well as the ion species and the composition of the target thereby determine the depth of penetration of the ions in the solid. However, as conventional ion sources utilize an inductively coupled plasma<sup>8</sup> to generate the ions, the radiance of the resulting ion beam is way too high in order to be used for the implantation of single ions. Hence, in order to reduce the radiance and to simultaneously focus the generated ion beam, a large amount of additional apertures and ion-optical elements is necessary. Yet, as the thinned out ion beam still is probabilistic due to statistical fluctuations, a deterministic single-ion implantation can only be guaranteed by a post-detection of the implantation event followed by an accordant cut off of the ion beam. In the following chapters, several different top-down approaches will be presented, highlighting the advantages and limitations of each system.

---

<sup>7</sup> MBE, Molecular Beam Epitaxy

<sup>8</sup> ICP, Inductively Coupled Plasma

### Detection of the implantation event by the observation of secondary electrons

One possible method to control the number of dopants and to post-detect the implantation event relies on the generation of secondary electrons (SEs), which are emitted from the target upon ion impact. However, due to the finite detection efficiency, one has to ensure that a sufficient number of SEs is generated per implantation event. Using  $\text{SiO}_2$  - which is commonly used as a passivation film of Si surfaces for ultralarge scale integrated (ULSI) fabrication - and CR-39 (allyl diglycol carbonate) - which is often utilized as fission track detector - as target material, the group around T. Shinada implanted doubly charged Si and P ions with an implantation energy of 60 keV [Shi98, Shi99].

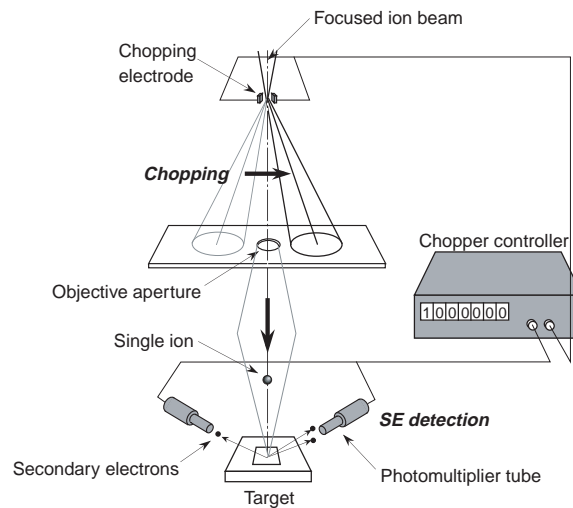


**Figure 2.8:** Principle of single-ion implantation as invented by T. Shinada. By utilizing a chopping electrode, the focused ion beam gets thinned out and can be switched off after the successful detection of an implantation event. [Shi99]

Starting from a focused ion beam with a current of 2 pA, a chopping electrode is used to thin out the beam, leading to an estimated number of 0.01 ions/chop for a chopping speed of 30  $\mu\text{m}/\text{s}$  and an ion beam opening time of 10 ns/chop, see also Fig. 2.8. The SEs, which are generated upon ion impact, are then detected using photomultiplier tubes<sup>9</sup>, with the SE detection efficiency depending on the target material and the PMT supply voltage. Using this technique, the group around T. Shinada was able to implant single  $\text{P}^{2+}$  ions in  $\text{SiO}_2$  with a resolution of 60 nm and an efficiency of over 90 % [Shi02]. However, due to the high implantation energies, the implantation event is accompanied by a damage of the surface of the utilized host crystal with straggling inside of the host material leading to variations in the implantation depth and the resolution in lateral direction.

<sup>9</sup> PMT, **P**hotomultiplier **T**ube

Hence, in order to reduce the amount of ion straggling, lower implantation energies must be employed. However, as a downside, an efficient detection of the implantation event via SEs can then only be guaranteed when highly charged ions are utilized. Using implantation energies of below 10 keV, the group around T. Schenkel already succeeded in detecting the implantation events of  $P^{13+}$ ,  $Te^{33+}$  and  $Xe^{40+}$  ions with an efficiency of 85 %, 95 % and 100 %, respectively [Per04b]. The experimental setup thereby resembles the one which is used in the group of T. Shinada, but with an additional scanning force microscope in the optical path allowing for imaging the device region to be implanted by using piezoresistive sensors [Per04a]. The probe tip features a small hole with a diameter of a few nm, which is used as an additional aperture and allows for transmitting single ions at a rate of a few hertz, see also chapter 9.1. Thus, the diameter of the hole in the scanning probe tip limits the minimum achievable placement accuracy, theoretically leading to implantation depths of about 20 nm with a resolution of 5 to 10 nm [Per04b]. However, as implanted ions mostly come to rest on interstitial positions in the lattice, an additional annealing step is necessary in order to incorporate the dopants into the lattice structure, effectively leading to a diffusion of the implanted ions inside of the host material and additionally limiting the achievable resolution.

Although it is possible to realize a deterministic single-ion source on the basis of SE detection, this technique is not universally applicable as the utilized host crystal is either damaged due to the high implantation energies or it is not possible to generate highly charged ions for certain elements. In addition, a further improvement of the resolution by means of additional masks cannot be accomplished as these would also lead to the production of unintentional SEs upon ion impact.

### **Detection of the implantation event by generating electron-hole pairs**

In order to circumvent the necessity to generate and detect SEs, the group around D. N. Jamieson developed a scheme, where on-chip ion detectors - integrated in the Si substrate itself - are utilized to signal the arrival of single phosphorus ions by the detection of electron-hole pairs [Jam05]. Hence, this approach enables the use of a nanoscale mask in order to localize the dopant atoms, so that only ions entering the substrate lead to registered events. Using a 250  $\mu\text{m}$  collimated beam of 14 keV phosphorus ions, a beam current of a few pA allows for ion-impact rates of just a few per minute through the apertures. Upon entering the substrate, these dopants then generate electron-hole pairs

which are detected using integrated PiN detectors<sup>10</sup>, see also Fig. 2.9.

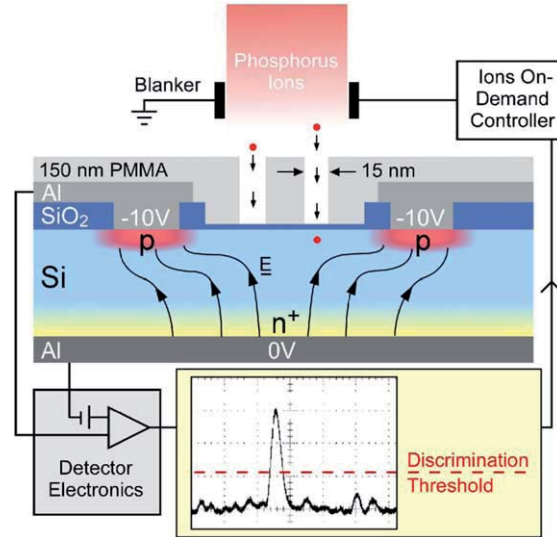


**Figure 2.9:** Schematic drawing of the detection of electron-hole pairs generated by single-ion implantation. Each single-ion impact produces an electron-hole plasma which leads to a current pulse. Accurate lateral positioning is achieved by a nanopatterned resist mask consisting of PMMA which was predefined using electron-beam lithography. [Mit05]

The used nanolithographic resist mask, which was predefined using electron-beam lithography<sup>11</sup>, consists of PMMA<sup>12</sup> and features apertures with a width of about 15 nm, allowing one to implant single phosphorus donors with a lateral positioning accuracy and mean depth of 20 nm [Mit05, Hop08]. In particular, this technique has been used to implant devices with only two phosphorus donors separated about 50 nm apart which are intended for use as solid state charge-based Si-P quantum bits [Hol03], see also chapter 2.1.2. However, the resolution is limited due to the minimal achievable structure sizes of the utilized nanolithographic resist masks, with straggling inside of the substrate still leading to an additional deterioration of the resolution.

<sup>10</sup>In contrast to a standard PN diode, a PiN diode features a wide, lightly doped ‘near’ intrinsic semiconductor region between a p-type semiconductor and an n-type semiconductor region, with the p-type and n-type regions being typically heavily doped due to their usage as ohmic contacts. Although the wide intrinsic region makes the PiN diode an inferior rectifier, it allows for using it as attenuator, RF switch or photodetector.

<sup>11</sup>EBL, **E**lectron-**B**eam **L**ithography

<sup>12</sup>**P**oly(**m**ethyl **m**ethacrylate), typically abbreviated as PMMA, is a transparent thermoplastic which is commonly called acrylic glass or plexiglas.

### 2.2.3 Implantation by using atom or ion traps as ion sources

In contrast to implantation techniques relying on conventional thermal ion sources, the following methods utilize a well-defined amount of trapped particles, which can be individually controlled and manipulated. Starting from the same initial point, namely the trapping and cooling of neutral atoms or ions, all presented techniques revolve around the generation of an ultracold ion beam by extracting the trapped particles - either by using magnetic or electric fields. The latter method, which is based on a segmented linear Paul trap, has been established in our group, with the development and characterization being the subject of this PhD thesis. Due to the auspicious characteristics of an ultracold ion beam, such ion sources are promising candidates for the realization of a deterministic single-ion source, allowing for the targeted implantation of single atoms with high spatial resolution.

#### Magneto-optical trap for parallel single-atom deposition

Using a magneto-optical trap (MOT) in conjunction with an optical dipole trap, the group around T. Pfau initially generates a Bose-Einstein condensate (BEC) consisting of ultracold chromium atoms. By subsequently inducing a Mott-Insulator transition in a three-dimensional optical lattice, ordered arrays of single atoms are formed which then can be accurately deposited onto a substrate [Gre08b], see Fig. 2.10(a).

In principal, a MOT is formed by three pairs of counterpropagating orthogonal laser beams, which intersect in the center of a magnetic quadrupole field. By tuning the laser beams slightly below an electronic transition, i.e. by red-detuning the laser beams, the atoms will absorb more photons if they move towards the light source due to the Doppler effect. Thus, if one applies light from two opposite directions, the atoms will always absorb more photons from the laser beam pointing opposite to their direction of motion. In each scattering event, the atom loses a momentum equal to the momentum of the photon, effectively leading to a cooling of the atoms, see also chapter 3.3.2. Spatial confinement is achieved by adding a spatially varying magnetic quadrupole field to the red-detuned optical field needed for laser cooling. This causes a Zeeman shift in the magnetic sensitive  $m_f$  levels, which increases with the radial distance from the center of the trap. Hence, if an atom moves away from the trap center, the atomic resonance is shifted closer to the frequency of the laser light, increasing the probability that the atom gets a photon kick towards the center of the trap<sup>13</sup>.

<sup>13</sup>For a more detailed description of the operating mode of a MOT, please see [Ste92].

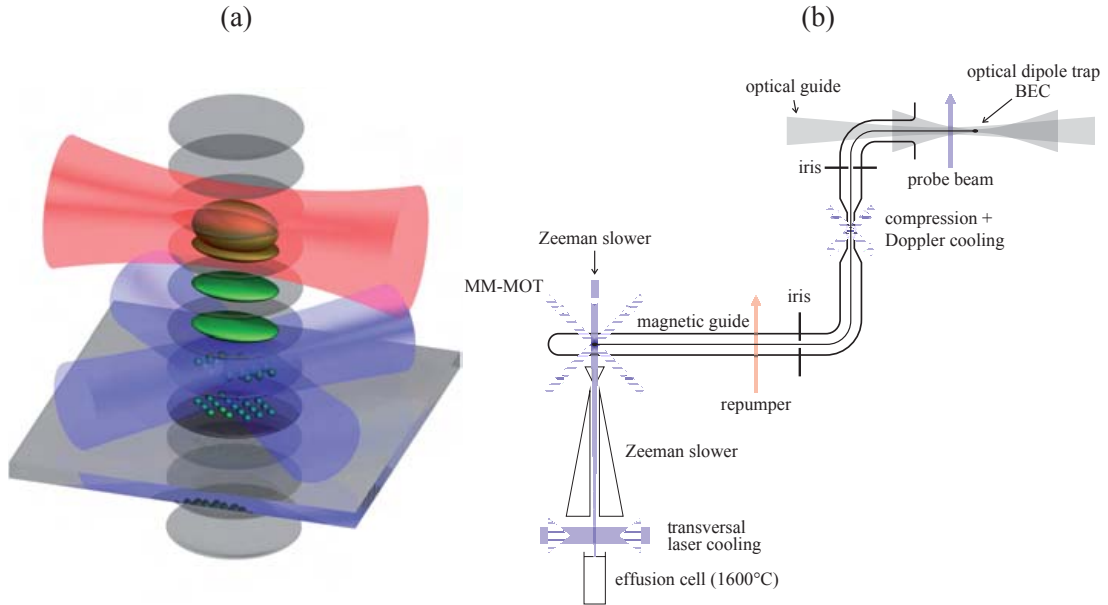


**Figure 2.10:** Parallel single-atom deposition as envisioned in the group of T. Pfau. (a) Schematic drawing of the procedure used for single-atom deposition. A transport wave (gray) allows for bringing atoms from a Bose-Einstein condensate (BEC) into close proximity to a transparent substrate. Using two additional orthogonal beams (blue), a three-dimensional optical lattice is formed above the substrate, with a superfluid to Mott-insulator transition being induced in the lattice. The generated single-atom arrays can then be deposited onto the substrate using the transport wave. (b) Schematic drawing of the experimental setup. [Gre08b]

Figure 2.10(b) shows a schematic drawing of the experimental setup used in the group of T. Pfau. At first, an MM-MOT<sup>14</sup> [Cre02] is loaded with chromium atoms from an effusion cell, which are slowed down by a Zeeman slower. The magnetic field gradient for the MOT is thereby formed by four bars which are also utilized as magnetic guide. The MOT itself consists of five beams, with four of them being diagonal to the axis of the magnetic guide. By detuning the diagonal MOT beams with respect to each other, the atoms are cooled in a moving frame and can be accelerated in the guide, effectively generating an atomic beam. The fifth beam is orthogonal to the axis of the magnetic guide and retroreflected. Traveling along the magnetic guide, the atoms pass through a compression zone, which, in combination with an additional Doppler cooling stage, increases the phase-space density before the atoms are transferred into an optical dipole trap via an optical guide. Here, a BEC is generated by means of evaporative cooling which is then superimposed with a three-dimensional optical lattice. In case of a repulsive interaction between the atoms

<sup>14</sup>Moving Molasses MOT

and by preparing an atom cloud with the proper initial density, one can now achieve that each lattice site is occupied by only one atom. Hence, by adjusting the potential depth of the optical lattice, it is possible to suppress the tunneling between adjacent lattice sites, effectively realizing a superfluid to Mott-insulator transition. A transport wave then allows for depositing the generated single-atom arrays onto a transparent substrate, see also Fig. 2.10(a).

So far, the group around T. Pfau was capable of continuously loading ultracold chromium atoms directly from the Zeeman slower into the horizontal magnetic guide by magneto-optical trapping, and to transport atoms along the guide [Gre07]. It was thereby possible to vary the mean velocity of the guided atoms between 0 m/s and 3 m/s with an observed atomic flux of  $2 \times 10^7$  atoms/s. Hence, the generation of the chromium BEC and the subsequent realization of the superfluid to Mott-insulator transition still need to be done<sup>15</sup>. The main advantage of the presented method relies on the high throughput of atoms, which can be arranged in well-defined arrays with accurately known lattice spacing and accuracy on the nanometer scale. However, a major drawback is given by the restriction of each MOT on certain atom species, as one can only trap atoms with a level scheme suitable for laser cooling. Although magneto-optical traps have already been realized for a variety of different elements (e.g. Na, Rb, Cs, Mg, Li, Ca, He, Cr, Yb), laser systems for technologically important elements such as phosphorus and nitrogen are currently still unavailable, with the necessity to generate a Bose-Einstein condensate leading to an added restriction in usable elements. In addition, it is necessary to utilize a substrate which is transparent for the employed transport wave, thus further limiting the applicability of the described method.

### Magneto-optical trap as single-ion source

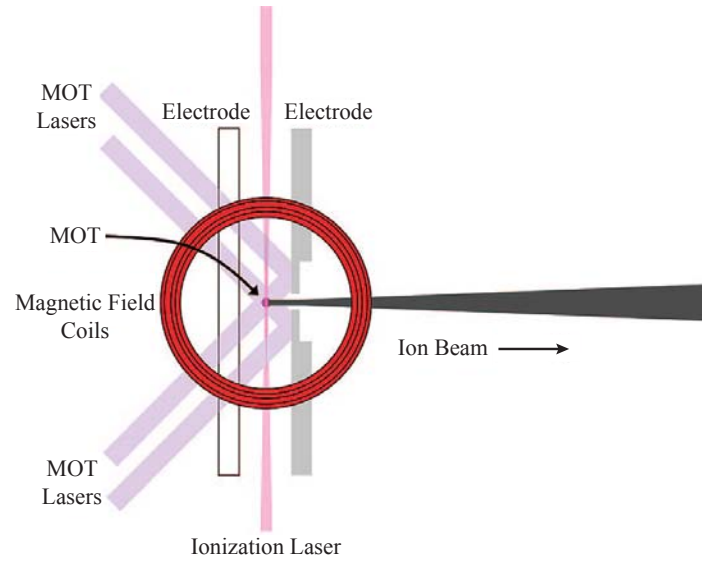
Another technique, which is also based on a magneto-optical trap, has been developed in the group of J. J. McClelland. In contrast to the aforementioned method, here, single Cr atoms are produced on demand by suppressing the stochastic nature and loss processes of the MOT. In a second step, the trapped particles are then ionized via a laser and extracted out of the MOT, thus realizing a deterministic source for single ions [Hil03a].

Figure 2.11 shows a schematic drawing of the specifically designed MOTIS<sup>16</sup> which is formed between two electrodes, one of which has a mirrored surface and the other con-

<sup>15</sup> Although up to now a chromium BEC has not been realized in this particular experiment, the group around T. Pfau was the first to produce a Bose-Einstein condensate of chromium in 2005 [Gri05].

<sup>16</sup> Magneto-Optical Trap Ion Source

sisting of a fused silica optical flat with a transparent conductive coating. Four of the six laser beams necessary to form the MOT pass through the window and reflect from the mirrored electrode, with the magnetic field being generated by a pair of coils. An ionization laser intersects the MOT and creates ions which are then extracted through a hole in the mirrored electrode.



**Figure 2.11:** Schematic drawing of a single-ion source based on a magneto-optical trap (MOT) which is formed between two electrodes, one of which has a mirrored surface (gray) and the other consisting of a fused silica optical flat with a transparent conductive coating (white). Four of the six laser beams necessary to form the MOT pass through the window and reflect from the mirrored electrode as shown (purple). Another pair of MOT beams (not shown) is oriented perpendicular to the page. The magnetic field of the MOT is generated by a pair of coils (red). An ionization laser (pink) intersects the MOT and creates ions which are then extracted through a hole in the mirrored electrode. [Han08]

By actively suppressing nearly all of the stochasticity inherent in the loading and loss processes of the MOT, the group around McClelland already demonstrated single-atom trap occupation probabilities as high as 98.7%, with an extraction efficiency of more than 90% at rates up to 10 Hz [Hil03a]. According to simulations, it will even be possible to increase the extraction rates up to a few kHz. Although no single ions have been generated and extracted up to now, it was already possible to deterministically extract ion clouds which were generated by using the aforementioned ionization laser, resulting in an ion beam with an energy fluctuation of about 0.3 eV and a beam divergence in the  $\mu\text{rad}$  regime. Ray tracing simulations predict that for a temperature of 100  $\mu\text{K}$ , a focused spot

size of about 7 nm will be feasible by using an electrostatic einzel-lens, with temperatures lower than 10  $\mu\text{K}$  even leading to sub-nm resolution [Han06b, Han08]. However, although being independent of the host substrate, the presented technique is also based on a MOT, thus featuring the same restrictions on certain ion species as already mentioned above.

### Segmented linear Paul trap as deterministic single-ion source

In order to realize a universal implantation technique for single ions, we have invented a deterministic ultracold single-ion source applicable to a wide range of ion species, isotopes and ionic molecules, which is based on a specifically designed segmented linear Paul trap, see Fig. 2.12 for a schematic drawing.

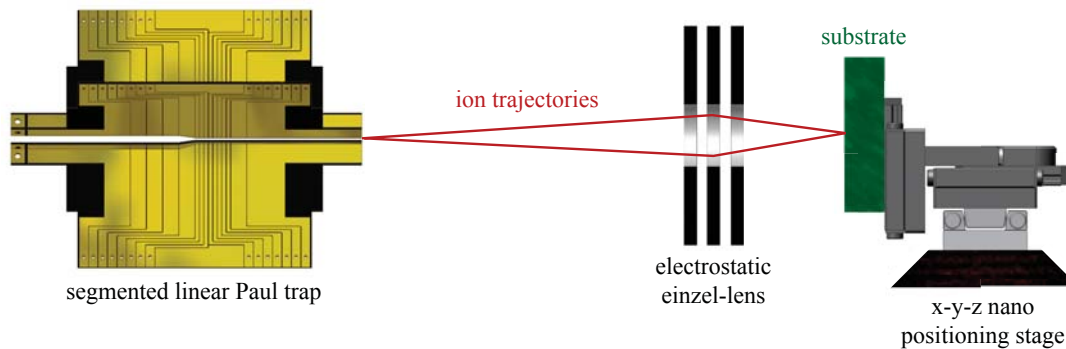


**Figure 2.12:** Implantation technique for single ions based on a segmented linear Paul trap. By using an electrostatic einzel-lens, deterministically extracted ions are focused onto a substrate, which is located on an x-y-z nano positioning stage. [Mei06, Sch09a]

Using a Paul trap allows for trapping and laser-cooling a huge variety of chemical elements and molecules, with the main limitation being the mass of the trapped particles. Although the problem still remains that certain elements cannot be directly laser-cooled (either caused by a non-existent closed cooling cycle or the non-availability of the necessary laser systems), it is still possible to trap them due to the Coulomb interaction between the charged particles. Relying on another laser-cooled ion species for cooling purposes, these elements can be sympathetically cooled [Lar86], allowing for loading and extracting them from the trap. By using more sophisticated cooling techniques like electromagnetically induced transparency<sup>17</sup> (see also chapter 3.3.3), it is even possible to cool mixed ion crystals to the motional ground-state as it allows for cooling of all degrees of freedom at different oscillation frequencies. Under these initial conditions, the Paul trap will operate

<sup>17</sup>EIT, Electromagnetically Induced Transparency

at the fundamental limit given by the Heisenberg uncertainty relation with a minimal position and momentum uncertainty of the trapped particles, effectively realizing the ‘perfect’ single-ion single-mode matter-wave source at the Heisenberg limit. Starting from these well-defined initial conditions, single ions are then deterministically extracted out of the trap and are focused onto a substrate by using an electrostatic einzel-lens, with spot sizes in the range of a few nm being feasible according to numerical simulations. The substrate itself is located on an x-y-z nano positioning stage, allowing for implanting single dopant atoms at specific locations with high spatial resolution. Alternatively, one could think of mounting the einzel-lens on the tip of an AFM<sup>18</sup>, thus allowing for determining the implantation position with respect to potential surface structures [Mei08b]. Due to the small beam divergence and narrow velocity distribution of the generated single-ion beam, chromatic and spherical aberration at the einzel-lens is strongly reduced presenting a promising starting point for focusing single ions on their way to the substrate. In addition, as the time of extraction as well as the velocity and the trajectories of the extracted ions are well-defined, it is possible to correct aberration effects using time-dependent electrostatic fields by simply switching the lens to another voltage at a specific time. Furthermore, our technique allows for implantation energies in the range of a few tens of eV, reducing the aforementioned straggling inside of the host material to a minimum.

Another important aspect is the deterministic nature of our novel single-ion source, as trapped particles can be imaged prior to extraction by utilizing proper optics in combination with an EMCCD<sup>19</sup> camera. By using a segmented linear Paul trap, it is even possible to either separate and transport trapped ion crystals [Hub08] or to determine the mass and therefore the species of sympathetically cooled ions by exciting collective vibrational modes of mixed ion crystals [Nae98, Dre04]. Hence, an additional post-detection of the implantation event is no more necessary.

---

<sup>18</sup> Atomic Force Microscope

<sup>19</sup> Electron-Multiplying Charge-Coupled Device

## Chapter 3

# Theoretical foundations

In order to better understand the physical concepts, which are involved in the trapping and cooling of charged particles, this chapter will mainly focus on the necessary theoretical foundations. After an explanation of how to confine charged particles in a linear Paul trap (3.1), the light-ion interaction for trapped ions will be discussed in detail (3.2) and different laser cooling techniques will be presented (3.3).

### 3.1 Confining charged particles in a linear Paul trap

Two different types of traps can be used to spatially trap charged particles for longer time periods without contact: Penning traps and Paul traps. The Penning trap, which was developed by Hans Georg Dehmelt at the University of Washington in Seattle [Deh67], uses static electric fields and a strong magnetic field in order to generate a harmonic trapping potential for charged particles. In 1973, scientists succeeded for the first time in trapping a single electron by using such a trap [Win73]. However, as the magnetic field causes a fast cyclotron motion of the charged particles, Penning traps cannot be used in experiments where the movement of the particles should be minimal. Paul traps avoid this cyclotron motion by using fast oscillating electric fields in order to trap charged particles. Originally developed by Wolfgang Paul at the University of Bonn in 1953, the generated fields from such traps were mainly utilized as quadrupole mass spectrometer for ions [Pau53]. It was not until 1958, when a further development allowed one to spatially trap charged particles [Pau58]<sup>1</sup>.

---

<sup>1</sup> W. Paul and H. G. Dehmelt shared the Nobel Prize in Physics in 1989 for the development of the Paul and Penning trap.

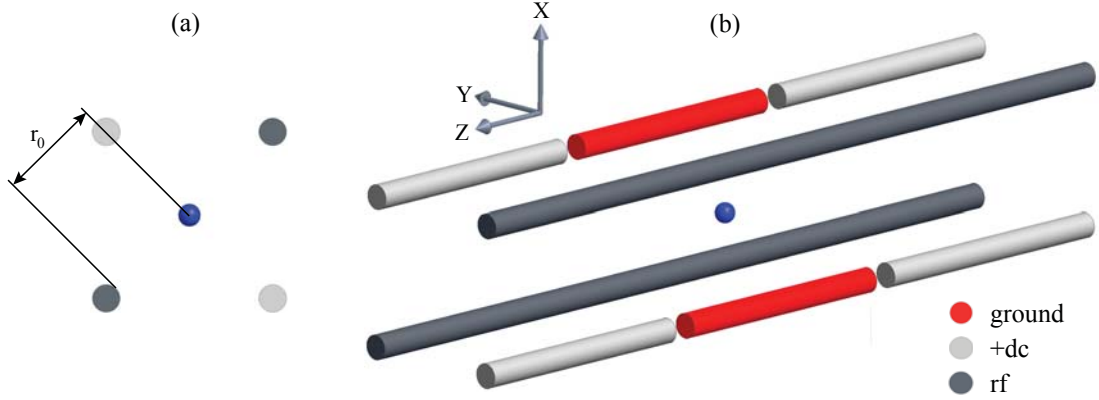


**Figure 3.1:** Schematic drawing of a segmented linear Paul trap with a confined ion (blue) inside. Dc electrodes are depicted in light gray, rf electrodes in dark gray, respectively. Grounded electrodes are colored red.  $r_0$  marks the distance between the trap center and the surface of the electrodes. (a) Front view. (b) Perspective view.

Figure 3.1 shows a schematic drawing of a segmented linear Paul trap. Here, an ac voltage<sup>2</sup> is supplied to two opposing rods (dark gray), resulting in an oscillating quadrupole potential, which alternately attracts and repels the charged particles. Due to the high frequency and the inertia of the charged particles, a so-called pseudopotential is generated, leading to a radial confinement of the ions. The axial confinement is achieved by applying dc voltages to the outer segments of the other two rods (light gray). Following the notation and approach of [Lei03], we assume that the generated potential can be decomposed into a time-independent static part  $\Phi_{\text{static}}$  and a time-dependent part  $\Phi_{\text{rf}}$ , that varies sinusoidally at the rf trap drive frequency  $\Omega_{\text{rf}}$ :

$$\begin{aligned} \Phi(x, y, z, t) &= \Phi_{\text{static}}(x, y, z) + \Phi_{\text{rf}}(x, y, z, t) \\ &= \frac{U}{2r_0^2} (\alpha x^2 + \beta y^2 + \gamma z^2) + \frac{\tilde{U}}{2r_0^2} \cos(\Omega_{\text{rf}} t) (\alpha' x^2 + \beta' y^2 + \gamma' z^2) \end{aligned} \quad (3.1)$$

Here,  $r_0$  denotes the distance between the trap center and the surface of the electrodes, see also Fig. 3.1(a). The parameters  $\alpha$ ,  $\beta$ ,  $\gamma$  as well as  $\alpha'$ ,  $\beta'$  and  $\gamma'$  are geometric factors, which describe the penetration of the electric fields with respect to the trap center<sup>3</sup>, with  $U$  being the amplitude of the dc voltage and  $\tilde{U}$  the amplitude of the rf voltage, respectively. For a given geometry, these geometric factors can either be calculated by numerical simulations or by experimentally determining the corresponding trap frequencies.

<sup>2</sup> In case of ions, the necessary ac voltage lies in the radio frequency regime, thus normally being referred to as rf voltage.

<sup>3</sup> Note, that for a perfect linear Paul trap, one can assume that the potential  $\Phi_{\text{rf}}$  is constant along the trap axis and therefore independent of  $z$ .

As the potential has to fulfill the Laplace equation  $\Delta\Phi = 0$  at every instant in time, the geometric factors have to obey certain restrictions:

$$\alpha + \beta + \gamma = 0, \quad (3.2)$$

$$\alpha' + \beta' + \gamma' = 0. \quad (3.3)$$

As one can see, it is not possible to generate a local three-dimensional minimum in free space with static electric fields, thus the potential can only trap charges in a dynamical way. In case of a linear Paul trap, one can now choose the electrode voltages in such a way, that a dynamic radial confinement in the  $x$ - $y$  plane and a static axial confinement in  $z$ -direction is generated for positively charged particles:

$$-(\alpha + \beta) = \gamma > 0, \quad (3.4)$$

$$\alpha' = -\beta' \quad (3.5)$$

In the following subsections, the radial and axial confinement of the linear Paul trap will be described in detail and possible vibrational modes of the trapped particles in the harmonic potential are discussed.

### 3.1.1 Dynamic radial confinement

The classical equations of motion for a particle with mass  $m$  and charge  $Z|e|$  in a potential of the form given by equation (3.1) were first studied by W. Paul, O. Osberghaus and E. Fischer in 1958 [Pau58]. As these are decoupled in the spatial coordinates, only the motion in the  $x$ -direction will be discussed in the following, with an analogous treatment being possible for the other directions. The equation of motion is then given by

$$\ddot{x} = -\frac{Z|e|}{m} \frac{\partial\Phi}{\partial x} = -\frac{Z|e|}{mr_0^2} \left[ U\alpha + \tilde{U} \cos(\Omega_{\text{rf}}t)\alpha' \right] x. \quad (3.6)$$

Using the substitutions

$$\xi = \frac{\Omega_{\text{rf}}t}{2}, \quad a_x = \frac{4Z|e|U\alpha}{m\Omega_{\text{rf}}^2 r_0^2}, \quad q_x = \frac{2Z|e|\tilde{U}\alpha'}{m\Omega_{\text{rf}}^2 r_0^2}, \quad (3.7)$$

equation (3.6) can now be transformed to the standard form of the so-called Mathieu differential equation:

$$\frac{d^2x}{d\xi^2} + [a_x - 2q_x \cos(2\xi)]x = 0. \quad (3.8)$$

The stable solutions of this differential equation can then be calculated using the Floquet theorem [Abr72]:

$$x(\xi) = A e^{i\beta_x \xi} \sum_{n=-\infty}^{\infty} C_{2n} e^{i2n\xi} + B e^{-i\beta_x \xi} \sum_{n=-\infty}^{\infty} C_{2n} e^{-i2n\xi}, \quad (3.9)$$

where the real-valued characteristic exponent  $\beta_x$  and the coefficients  $C_{2n}$  are functions of  $a_x$  and  $q_x$  only and do not depend on initial conditions.  $A$  and  $B$  are arbitrary constants that are used to either satisfy boundary conditions or to normalize a particular solution. By inserting equation (3.9) into (3.8), we obtain a recursion relation,

$$C_{2n+2} - D_{2n}C_{2n} + C_{2n-2} = 0, \quad D_{2n} = \frac{[a_x - (2n + \beta_x)^2]}{q_x}, \quad (3.10)$$

which connects the coefficients and  $\beta_x$  to  $a_x$  and  $q_x$ . In case of stable solutions, the particle oscillates in the  $x$ - $y$  plane with a finite amplitude, whereas for unstable solutions, the amplitude of the motion increases exponentially, leading to a loss of the particle as it leaves the trapping region.

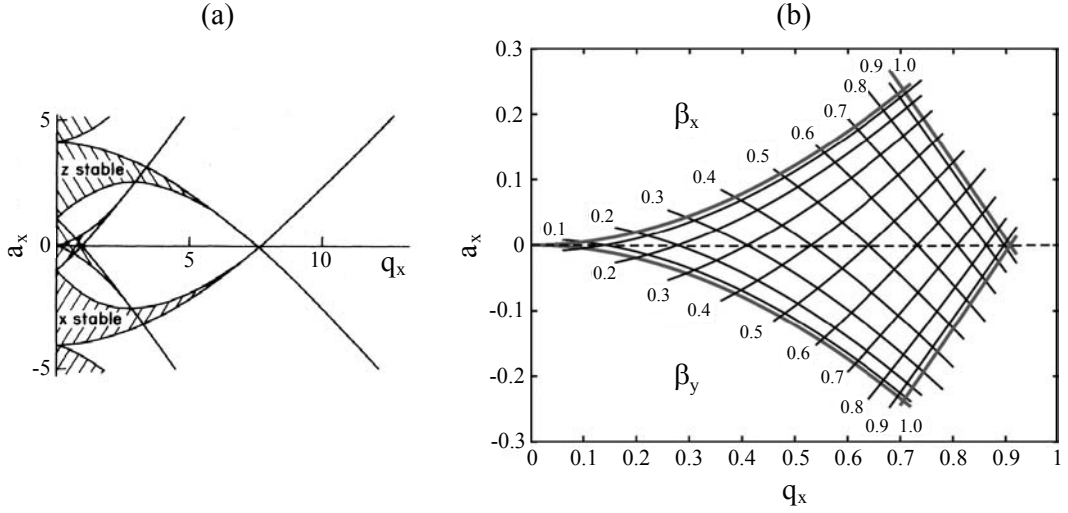


**Figure 3.2:** (a) Stability diagram for a linear Paul trap ( $\alpha + \beta = -\gamma$ ,  $\alpha' = -\beta'$ ,  $\gamma' = 0$ ). (b) First stability region. Depicted are the frequencies  $\omega_i$  ( $i \in \{x, y\}$ ) of the secular motion in units of  $\frac{\Omega_{\text{rf}}}{2}$ . In order to achieve a stable confinement, the frequencies  $\omega_i$  have to fulfill the condition:  $0 \leq \omega_i \leq \frac{\Omega_{\text{rf}}}{2}$ . [Gho95]

According to [Pau58, Gho95], the region of stability in the  $a_i$ - $q_i$  plane ( $i \in \{x, y, z\}$ ) is bounded by pairs of  $a_i$  and  $q_i$  that yield either  $\beta_i = 0$  or  $\beta_i = 1$ . The stable region that contains the points  $(a_i, q_i) = (0, 0)$  for all  $i \in \{x, y, z\}$  is often called the lowest stability region, with the exact shape of the stability regions depending on the parameters  $a_i$  and  $q_i$  for a given trap geometry. As one can see from equation (3.7), the parameters  $a_i$  and  $q_i$  also depend on the operating parameters, namely the trap drive frequency  $\Omega_{\text{rf}}$ , the amplitude of the rf voltage  $\tilde{U}$  as well as the dc voltage amplitude  $U$ . A trapped particle will be stable in all three dimensions, if

$$0 \leq \beta_i \leq 1 \quad \forall \quad i \in \{x, y, z\}. \quad (3.11)$$

Figure 3.2(a) shows the stability diagram for a linear Paul trap. Here, the parameters are related by

$$q_y = -q_x, \quad q_z = 0, \quad (3.12)$$

with the first stability region ( $|a_x| \geq 0$ ,  $q_x < 1$ ) being symmetric around the  $q_x$  axis, see also Fig. 3.2(b). In the case of ( $|a_x|, q_x^2$ )  $\ll 1$ , the lowest-order approximation of the ion trajectory yields

$$x(t) \approx 2AC_0 \cos\left(\beta_x \frac{\Omega_{\text{rf}}}{2} t\right) \left[1 - \frac{q_x}{2} \cos(\Omega_{\text{rf}} t)\right] \quad \text{with} \quad \beta_x \approx \sqrt{a_x + \frac{q_x^2}{2}}, \quad (3.13)$$

with the constant  $A$  being defined by the initial conditions. The motion of the particle in the  $x$ - $y$  plane can therefore be decomposed into two different oscillations: On the one hand in the so-called *secular motion*, a harmonic oscillation at the frequency

$$\omega_i = \beta_i \frac{\Omega_{\text{rf}}}{2} \ll \Omega_{\text{rf}} \quad \text{with} \quad i \in (x, y), \quad (3.14)$$

and on the other hand in a much faster, driven oscillation at the trap drive frequency  $\Omega_{\text{rf}}$ . This so-called *micromotion* is  $180^\circ$  out of phase with the driving field and a factor  $q_x/2$  smaller than the amplitude of the secular motion. If micromotion is neglected, the secular motion can be interpreted as the motion of a particle in a harmonic potential:

$$\Psi(x, y) = \frac{m}{2Z|e|} (\omega_x^2 x^2 + \omega_y^2 y^2) \quad (3.15)$$

In order to distinguish this potential from the potential  $\Phi$ , it is normally referred to as *pseudopotential*, with the depth in  $x$ - and  $y$ -direction being given by

$$\Psi_x = \frac{Z^2 e^2 \tilde{U}^2 \alpha'^2}{4m\Omega_{\text{rf}}^2 r_0^2} + \frac{Z|e|U\alpha}{2}, \quad (3.16)$$

$$\Psi_y = \frac{Z^2 e^2 \tilde{U}^2 \beta'^2}{4m\Omega_{\text{rf}}^2 r_0^2} - \frac{Z|e|U\beta}{2}. \quad (3.17)$$

If the secular motion in  $x$ - and  $y$ -direction is identical, equation (3.15) reduces to

$$\Psi(x, y) = \frac{m}{2Z|e|} \omega_r^2 (x^2 + y^2), \quad (3.18)$$

where

$$\omega_r = \frac{Z|e|\tilde{U}}{\sqrt{2}m\Omega_{\text{rf}}r_0^2} \quad (3.19)$$

is the angular frequency of oscillations in the radial direction. In case of a linear Paul trap, micromotion is not present along the  $z$ -direction as  $q_z = 0$ . However, in the radial  $x$ - $y$  plane, the amplitude of the micromotion only vanishes, if the ion is located in the center of the generated quadrupole potential. In the real experiment, this is normally

never the case, which is mainly due to asymmetries of the ion trap itself and patch electric charges on the insulated surfaces between the electrodes. In order to account for these stray electric fields, one has to add an additional term to equation (3.8):

$$\frac{d^2x}{d\xi^2} + [a_x - 2q_x \cos(2\xi)]x = \frac{Z|e|E_x}{m}. \quad (3.20)$$

An approximate solution of equation (3.20) is given by [Ber98]:

$$x(t) \approx \left( A_x + 2AC_0 \cos\left(\beta_x \frac{\Omega_{\text{rf}}}{2} t\right) \right) \left[ 1 - \frac{q_x}{2} \cos(\Omega_{\text{rf}} t) \right] \quad \text{with} \quad A_x = \frac{Z|e|E_x}{m\omega_x^2}. \quad (3.21)$$

As one can see, the additional electric field  $E_x$  causes a shift of the ion by the amount  $A_x$  out of the center of the trap, resulting in a micromotion with amplitude  $A_x \frac{q_x}{2}$ . Hence, in order to reduce the induced micromotion in the experiment to a minimum, static electric fields are utilized, see also chapter 5.2.2.

### 3.1.2 Static axial confinement

In order to achieve a three-dimensional confinement of charged particles in a linear Paul trap, the aforementioned quadrupole potential in the  $x$ - $y$  plane has to be superimposed with an additional static potential in  $z$ -direction. In case of our model (see Fig. 3.1), this is done by applying a positive voltage  $U$  to the outer segments of the dc electrodes. The static potential in  $z$ -direction close to the trap center can thereby be approximated by the harmonic potential [Rai92]

$$\begin{aligned} \Phi_{\text{static}}(x, y, z) &= \frac{\kappa U}{z_0^2} \left[ z^2 - \frac{1}{2} (x^2 + y^2) \right] \\ &= \frac{m}{2Z|e|} \omega_z^2 \left[ z^2 - \frac{1}{2} (x^2 + y^2) \right], \end{aligned} \quad (3.22)$$

with

$$\omega_z = \sqrt{\frac{2\kappa Z|e|U}{mz_0^2}} \quad (3.23)$$

being the angular frequency of axial oscillations in the trap. Here,  $z_0$  denotes the distance between the trap center and the outer segments, with  $\kappa$  again being a geometric factor, which describes the penetration of the electric field with respect to the trap center. As already mentioned above, this geometric factor in general cannot be calculated analytically, but it must be determined either by numerical simulations or by measuring the corresponding trap frequencies.

The pseudopotential well in the radial direction is weakened by the additional static potential and is given by [Rai92]:

$$\begin{aligned}\Psi(x, y) &= \frac{m}{2Z|e|} \left( \omega_r^2 - \frac{1}{2}\omega_z^2 \right) (x^2 + y^2) \\ &= \frac{m}{2Z|e|} (\omega_r')^2 (x^2 + y^2),\end{aligned}\quad (3.24)$$

where

$$\omega_r' = \sqrt{\omega_r^2 - \frac{1}{2}\omega_z^2} \quad (3.25)$$

denotes the angular frequency of radial oscillations in the presence of the static potential. As we are only considering cases where  $\omega_r \gg \omega_z$ , the radial pseudopotential changes only slightly, with  $\omega_r' \simeq \omega_r$ . However, in case of our experiment, the radial and axial trapping frequencies are quite similar, with  $\omega_r \approx 1.6\omega_z$ , see also chapter 5.1.1.

### Equilibrium positions

In the following, we consider an ion crystal consisting of  $N$  ions in a linear Paul trap. The ions are assumed to be strongly bound in the  $x$ - and  $y$ -direction but weakly bound in a harmonic potential in the  $z$ -direction, with the position of the  $m$ th ion being denoted as  $z_m(t)$ . The motion of each ion will be influenced by an overall harmonic potential due to the trap electrodes and by the Coulomb force exerted by all of the other ions. If we assume, that the binding potential in the  $x$ - $y$  plane is sufficiently strong, the motion along these axis can be neglected, with the potential energy  $E_{\text{pot}}$  thus being given by [Jam98]:

$$E_{\text{pot}} = \sum_{m=1}^N \frac{1}{2} m \omega_z^2 z_m(t)^2 + \sum_{\substack{n,m=1 \\ m \neq n}}^N \frac{Z^2 e^2}{8\pi\epsilon_0} \frac{1}{|z_n(t) - z_m(t)|}. \quad (3.26)$$

If the ions are sufficiently cold, the position of the  $m$ th ion can be approximated by the formula

$$z_m(t) \approx z_m^{(0)} + \zeta_m(t), \quad (3.27)$$

where  $z_m^{(0)}$  denotes the equilibrium position, with  $\zeta_m(t)$  being a small displacement in  $z$ -direction. The equilibrium positions will then be determined by the following equation:

$$\left[ \frac{\partial E_{\text{pot}}}{\partial z_m} \right]_{z_m=z_m^{(0)}} = 0. \quad (3.28)$$

By defining the length scale

$$l = \left( \frac{Z^2 e^2}{4\pi\epsilon_0 m \omega_z^2} \right)^{1/3} \quad (3.29)$$

and the dimensionless equilibrium position

$$u_m = \frac{z_m^{(0)}}{l}, \quad (3.30)$$

equation (3.28) can be rewritten as the following set of  $N$  coupled algebraic equations:

$$u_m - \sum_{n=1}^{m-1} \frac{1}{(u_m - u_n)^2} + \sum_{n=m+1}^N \frac{1}{(u_m - u_n)^2} = 0 \quad \text{with } m = 1, 2, \dots, N. \quad (3.31)$$

For  $N = 2$  and  $N = 3$ , these equations can be solved analytically:

$$N = 2 : \quad u_1 = -\left(\frac{1}{2}\right)^{2/3}, \quad u_2 = \left(\frac{1}{2}\right)^{2/3} \quad (3.32)$$

$$N = 3 : \quad u_1 = -\left(\frac{5}{4}\right)^{1/3}, \quad u_2 = 0, \quad u_3 = \left(\frac{5}{4}\right)^{1/3}. \quad (3.33)$$

For larger values of  $N$ , it is necessary to solve for the values of  $u_m$  numerically. Figure 3.3(a) shows the equilibrium positions for a linear ion crystal as a function of the number of ions.

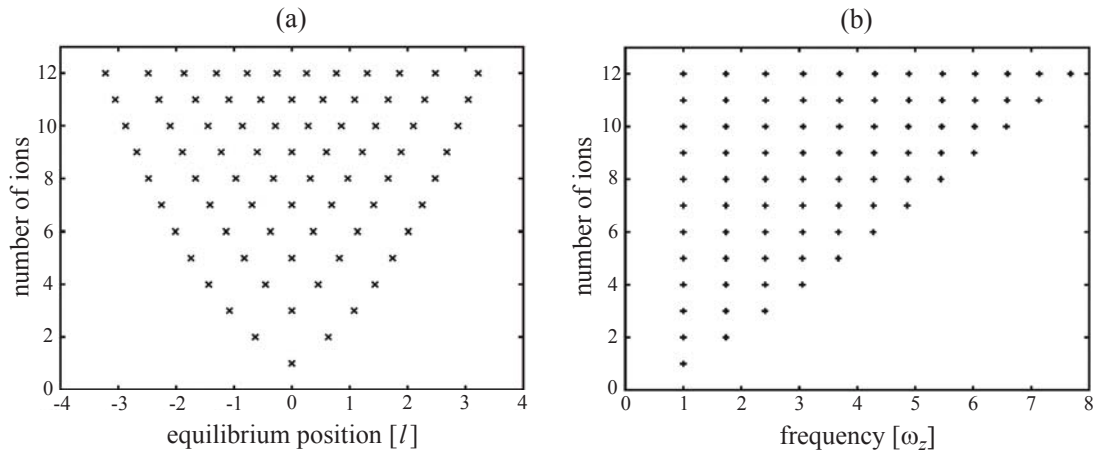


**Figure 3.3:** (a) Equilibrium positions for a linear ion crystal as a function of the number of ions  $N$ . The positions are in units of  $l$  as defined by equation (3.29). (b) Normal mode frequencies for a linear ion crystal as a function of the number of ions  $N$ . The frequencies are in units of  $\omega_z$ . [Ste97]

As one can see, the minimum value of the spacing between two adjacent ions occurs at the center of the ion crystal, with the spacings getting larger to the outside. The minimum inter-ion spacing for different numbers of ions is thereby given by:

$$z_{\min}(N) = \left( \frac{Z^2 e^2}{4\pi\epsilon_0 m \omega_z^2} \right)^{1/3} \frac{2.018}{N^{0.559}}. \quad (3.34)$$

### 3.1.3 Vibrational modes of linear ion crystals

To determine the vibrational modes of a linear ion crystal consisting of identical ions with mass  $m$ , one has to consider small oscillations of the ions about their equilibrium positions  $(x_m^{(0)} = 0, y_m^{(0)} = 0, z_m^{(0)})$ , which are described by the Lagrangian [Enz00]

$$\begin{aligned}
L = & \frac{m}{2} \left[ \sum_{n=1}^N \dot{\zeta}_n^2 - \omega_z^2 \sum_{n,m=1}^N A_{n,m} \zeta_n \zeta_m \right] \\
& + \frac{m}{2} \left[ \sum_{n=1}^N \dot{\xi}_n^2 - \omega_x^2 \sum_{n,m=1}^N B_{n,m} \xi_n \xi_m \right] \\
& + \frac{m}{2} \left[ \sum_{n=1}^N \dot{\eta}_n^2 - \omega_y^2 \sum_{n,m=1}^N B_{n,m} \eta_n \eta_m \right], \tag{3.35}
\end{aligned}$$

where  $(\xi_n, \eta_n, \zeta_n)$  are the displacements of the  $n$ th ion from its equilibrium position in the  $(x, y, z)$  directions, respectively. The coupling matrices  $A_{n,m}$  and  $B_{n,m}$  are given by the formulas

$$A_{n,m} = \begin{cases} 1 + 2 \sum_{\substack{p=1 \\ p \neq m}}^N \frac{l^3}{|\bar{z}_m - \bar{z}_p|^3} & \text{if } n = m, \\ \frac{-2l^3}{|\bar{z}_m - \bar{z}_n|^3} & \text{if } n \neq m. \end{cases} \tag{3.36}$$

$$B_{n,m} = \left( \frac{1}{\alpha} + \frac{1}{2} \right) \delta_{n,m} - \frac{1}{2} A_{n,m}, \tag{3.37}$$

where  $l$  is defined according to equation (3.29) and  $\delta_{n,m}$  is the Kronecker delta. The parameter  $\alpha$  characterizes the anisotropy of the trapping potential and is defined as

$$\alpha = \left( \frac{\omega_z}{\omega_r} \right)^2 \tag{3.38}$$

As one can see from equation (3.37), the motions in  $x$ -,  $y$ - and  $z$ -direction are coupled due to the Coulomb interaction. A calculation of the eigenvalues of the matrices  $A_{n,m}$  and  $B_{n,m}$  yields  $N$  vibrational modes for the axial and  $2N$  vibrational modes for the radial direction<sup>4</sup>, with the so-called *center-of-mass*<sup>5</sup> mode and the *breathing* mode being the eigenmodes with the lowest energies. Table 3.1 shows an overview of the axial and radial vibrational modes of linear ion crystals consisting of up to three identical ions, with Fig. 3.3(b) showing the normal mode frequencies in axial direction as a function of the number of ions  $N$ . For a detailed description of the vibrational modes of mixed ion crystals, please see [Mor00b, Rot03].

<sup>4</sup> Note, that if the radial trapping frequencies are degenerate ( $\omega_x = \omega_y = \omega_r$ ), the number of radial vibrational modes is reduced to  $N$ .

<sup>5</sup> COM, Center-Of-Mass

Number of ions	Vibrational modes					
	COM	axial Breathing	Wobble	COM	radial Rocking	Zigzag
1	$\omega_z$ 			$\omega_r$ 		
2	$\omega_z$ 	$\sqrt{3}\omega_z$ 		$\omega_r$ 	$\sqrt{\omega_r^2 - \omega_z^2}$ 	
3	$\omega_z$ 	$\sqrt{3}\omega_z$ 	$\sqrt{29/5}\omega_z$ 	$\omega_r$ 	$\sqrt{\omega_r^2 - \omega_z^2}$ 	

**Table 3.1:** Overview of the axial and radial vibrational modes of linear ion crystals consisting of up to three identical ions. [Deu07]

### Stability of linear ion crystals

In order to calculate the equilibrium positions and vibrational modes of the trapped ions, we hitherto assumed that the ions arrange in a linear crystal along the  $z$ -direction. Hence, in the following, we will estimate for which values of  $\omega_z$ ,  $\omega_r$  and  $N$  this assumption holds true. According to [Enz00], the eigenvalues of the coupling matrix  $A_{n,m}$  are defined by the formula

$$\sum_{m=1}^N A_{n,m} b_m^{(p)} = \mu_p b_n^{(p)}, \quad (3.39)$$

where  $\mu_p > 0$  is the eigenvalue,  $b_n^{(p)}$  the normalized eigenvector, and  $p$  ( $= 1, \dots, N$ ) the mode index, with the modes being enumerated in order of increasing eigenvalue. As one can see from equation (3.37), the coupling matrix  $B_{n,m}$  for the radial oscillations has identical eigenvectors to  $A_{n,m}$ , but has different eigenvalues:

$$\sum_{m=1}^N B_{n,m} b_m^{(p)} = \left( \frac{1}{\alpha} + \frac{1}{2} - \frac{\mu_p}{2} \right) b_n^{(p)}. \quad (3.40)$$

For these oscillations, the eigenvalues are no longer always positive. If  $\alpha$  is increased, a critical value occurs for which one of the eigenvalues of the radial oscillations becomes zero. Beyond this point, the radial oscillation is unstable and so is the linear configuration,

marking the onset of the so-called *zigzag* mode, see also Fig. 3.4. The critical value of  $\alpha$  is thereby given by

$$\alpha_{\text{crit}}(N) = \frac{2}{\mu_n - 1}, \quad (3.41)$$

where  $\mu_n$  is the largest eigenvalue of the matrix  $A_{n,m}$  for a given number of ions  $N$ .

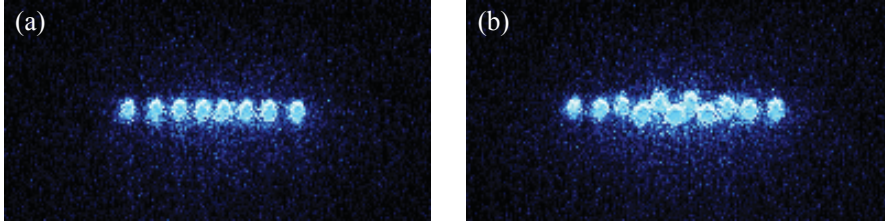


**Figure 3.4:** Stability of linear ion crystals. (a) EMCCD image of a linear ion crystal consisting of eight  $^{40}\text{Ca}^+$  ions. (b) EMCCD image of an ion crystal in zigzag-configuration consisting of eleven  $^{40}\text{Ca}^+$  ions.

As was already experimentally verified by [Enz00] for ion numbers up to  $N = 10$ , this critical anisotropy value can be approximated by a power-law of the form  $\alpha_{\text{crit}} = cN^\gamma$ , yielding<sup>6</sup>

$$\left(\frac{\omega_z}{\omega_r}\right)_{\text{crit}}^2 = 3.23N^{-1.83}. \quad (3.42)$$

## 3.2 Light-ion interaction for trapped ions

The light-ion interaction plays a significant role in our experiments, with light fields not only being used for ionizing the neutral calcium atoms, but also for cooling and imaging purposes as well as for manipulating the quantum states of the ions. With the help of suitable electromagnetic fields, the internal electronic levels of trapped ions can be coherently coupled to each other and the motional degrees of freedom of the ions.

The total Hamiltonian  $\hat{H}$  of the system thereby consists of two parts: the Hamiltonian  $\hat{H}_{\text{ion}}$  of the trapped ion and the Hamiltonian  $\hat{H}^{(i)}$  describing the interactions mediated by the applied light fields:

$$\begin{aligned} \hat{H} &= \hat{H}_{\text{ion}} + \hat{H}^{(i)} \\ &= \hat{H}^{(m)} + \hat{H}^{(e)} + \hat{H}^{(i)} \end{aligned} \quad (3.43)$$

Here,  $\hat{H}^{(m)}$  denotes the motional Hamiltonian of the ion, with  $\hat{H}^{(e)}$  describing the internal electronic level structure, respectively.

<sup>6</sup> Note, that the values for  $c$  and  $\gamma$  slightly differ from those determined by [Sch93] for ion crystals with ion numbers ranging from  $N = 2 - 500$  using molecular dynamics simulations ( $c = 2.53$ ,  $\gamma = -1.73$ ).

### 3.2.1 Hamiltonian of the trapped ion

For the quantum-mechanical treatment of the motion, we assume that the time-dependent potential is quadratic in each of the three Cartesian coordinates of the center of mass of the trapped particle. As in classical mechanics, the problem is thus separable into three one-dimensional problems, with the following discussion being restricted to the  $x$ -direction. By replacing the coordinate  $x$  by the respective operator  $\hat{x}$ , the time-dependent potential  $V(t)$  can be written as

$$V(t) = \frac{m}{2} W(t) \hat{x}^2, \quad (3.44)$$

where

$$W(t) = \frac{\Omega_{\text{rf}}^2}{4} [a_x + 2q_x \cos(\Omega_{\text{rf}} t)] \quad (3.45)$$

can be thought of as a time-varying spring constant, playing a role similar to  $\omega^2$  in the static potential harmonic oscillator. With these definitions, the Hamiltonian  $\hat{H}^{(m)}$  takes the form

$$\hat{H}^{(m)} = \frac{\hat{p}^2}{2m} + \frac{m}{2} W(t) \hat{x}^2 = \frac{\hat{p}^2}{2m} + \frac{m}{2} \omega^2 \hat{x}^2, \quad (3.46)$$

where  $\hat{x}$  and  $\hat{p}$  are the position and momentum operators. Using the operators

$$\begin{aligned} \hat{a} &= \sqrt{\frac{m\omega}{2\hbar}} \left( \hat{x} + \frac{i\hat{p}}{m\omega} \right) \\ \hat{a}^\dagger &= \sqrt{\frac{m\omega}{2\hbar}} \left( \hat{x} - \frac{i\hat{p}}{m\omega} \right), \end{aligned} \quad (3.47)$$

which are known as the *annihilation operator* ( $\hat{a}$ ) and the *creation operator* ( $\hat{a}^\dagger$ ) and fulfill the commutation relation  $[\hat{a}, \hat{a}^\dagger] = 1$ , the motional Hamiltonian can be rewritten as

$$\hat{H}^{(m)} = \hbar\omega \left( \hat{a}^\dagger \hat{a} + \frac{1}{2} \right). \quad (3.48)$$

The energy eigenstates of  $\hat{H}^{(m)}$  are so-called Fock states and fulfill the eigenvalue equation

$$\hat{H}^{(m)} |n\rangle = \hbar\omega \left( n + \frac{1}{2} \right) |n\rangle, \quad n = 0, 1, 2, \dots, \quad (3.49)$$

with the energy eigenvalues  $E_n$  being given by

$$E_n = \hbar\omega \left( n + \frac{1}{2} \right). \quad (3.50)$$

Here,  $n$  denotes the number of existing energy quanta  $\hbar\omega$ , with a single quantum unit of energy being referred to as *phonon* in the present case. Applying the annihilation and creation operators to the Fock states  $|n\rangle$  yields the relations

$$\begin{aligned} \hat{a}^\dagger |n\rangle &= \sqrt{n+1} |n+1\rangle \\ \hat{a} |n\rangle &= \sqrt{n} |n-1\rangle \\ \hat{a} |0\rangle &= 0, \end{aligned} \quad (3.51)$$

with  $|0\rangle$  being the motional ground state. The increase (decrease) of  $n$  by one therefore amounts to the creation (annihilation) of one phonon.

The internal electronic structure of the ion will be approximated by a two-level system with levels  $|g\rangle$  and  $|e\rangle$  of energy difference  $\hbar\omega_0 = \hbar(\omega_e - \omega_g)$ . For real ions, this approximation is justified if the frequencies of the electromagnetic fields that induce the coupling are only close to resonance for two internal levels. The corresponding two-level Hamiltonian is then given by [Lei03]

$$\begin{aligned}\hat{H}^{(e)} &= \hbar(\omega_g |g\rangle\langle g| + \omega_e |e\rangle\langle e|) \\ &= \hbar\frac{\omega_e + \omega_g}{2} (|g\rangle\langle g| + |e\rangle\langle e|) + \hbar\frac{\omega_0}{2} (|e\rangle\langle e| - |g\rangle\langle g|)\end{aligned}\quad (3.52)$$

By using the unity matrix  $\hat{I}$  and the three Pauli matrices according to the mapping

$$\begin{aligned}|g\rangle\langle g| + |e\rangle\langle e| &\mapsto \hat{I} \\ |g\rangle\langle e| + |e\rangle\langle g| &\mapsto \hat{\sigma}_x \\ i(|g\rangle\langle e| - |e\rangle\langle g|) &\mapsto \hat{\sigma}_y \\ |e\rangle\langle e| - |g\rangle\langle g| &\mapsto \hat{\sigma}_z,\end{aligned}\quad (3.53)$$

the Hamiltonian  $\hat{H}^{(e)}$  can be rewritten as

$$\hat{H}^{(e)} = \hbar\frac{\omega_0}{2}\hat{\sigma}_z, \quad (3.54)$$

where the energy is shifted by  $-\hbar\frac{\omega_e + \omega_g}{2}$  to suppress the state-independent energy contribution in equation (3.52). The Hamiltonian  $\hat{H}_{\text{ion}}$  of the trapped ion is thus given by

$$\hat{H}_{\text{ion}} = \hat{H}^{(m)} + \hat{H}^{(e)} = \hbar\omega \left( \hat{a}^\dagger \hat{a} + \frac{1}{2} \right) + \hbar\frac{\omega_0}{2}\hat{\sigma}_z \quad (3.55)$$

### 3.2.2 Interaction Hamiltonian

In the following, we assume that the applied light field is only irradiated along the  $x$ -direction. The corresponding wave vector  $\vec{k}$  thus only features one component  $k_x$ , with its norm being given by  $k = k_x$ . The light field can then be written as

$$\vec{E}(x, t) = \vec{E}_0 \left[ e^{i(kx - \omega_L t + \Phi)} + e^{-i(kx - \omega_L t + \Phi)} \right] \quad (3.56)$$

where  $E_0$  denotes the amplitude and  $\omega_L$  the angular frequency of the irradiated light field. According to [Lei03], the interaction Hamiltonian  $\hat{H}^{(i)}$  is given by

$$\hat{H}^{(i)} = \frac{\hbar}{2}\Omega (|g\rangle\langle e| + |e\rangle\langle g|) \times \left[ e^{i(k\hat{x} - \omega_L t + \Phi)} + e^{-i(k\hat{x} - \omega_L t + \Phi)} \right], \quad (3.57)$$

where the so-called Rabi frequency  $\Omega$  is a measure for the coupling strength between the trapped ion and the applied light field, with the explicit form of  $\Omega$  depending on the kind of interaction. By introducing the operators

$$\begin{aligned}\hat{\sigma}_+ &= \frac{\hat{\sigma}_x + i\hat{\sigma}_y}{2} \\ \hat{\sigma}_- &= \frac{\hat{\sigma}_x - i\hat{\sigma}_y}{2}\end{aligned}\quad (3.58)$$

and using the mapping

$$\begin{aligned}|e\rangle \langle g| &\mapsto \hat{\sigma}_+ \\ |g\rangle \langle e| &\mapsto \hat{\sigma}_-, \end{aligned}\quad (3.59)$$

equation (3.57) can be rewritten as

$$\hat{H}^{(i)} = \frac{\hbar}{2}\Omega(\hat{\sigma}_+ + \hat{\sigma}_-) \times \left[ e^{i(k\hat{x} - \omega_L t + \Phi)} + e^{-i(k\hat{x} - \omega_L t + \Phi)} \right]. \quad (3.60)$$

Using the annihilation and creation operators as defined in equation (3.47), the position operator  $\hat{x}$  can be rewritten as

$$\hat{x} = \sqrt{\frac{\hbar}{2m\omega}} (\hat{a} + \hat{a}^\dagger). \quad (3.61)$$

One can now define the so-called Lamb-Dicke parameter

$$\eta = k \cos(\Theta) x_0 = k \cos(\Theta) \sqrt{\frac{\hbar}{2m\omega}}. \quad (3.62)$$

Here,  $\Theta$  denotes the incident angle of the applied light field with respect to the  $x$ -axis, with  $x_0 = \sqrt{\hbar/(2m\omega)}$  being the extension of the ground-state wave function of the reference oscillator. Inserting equation (3.62) in (3.61) under the condition  $\Theta = 0^\circ$  thus yields:

$$\hat{x} = \frac{\eta}{k} (\hat{a} + \hat{a}^\dagger) \quad (3.63)$$

Using equation (3.63), the interaction Hamiltonian takes the form

$$\hat{H}^{(i)} = \frac{\hbar}{2}\Omega(\hat{\sigma}_+ + \hat{\sigma}_-) \times \left[ e^{i(\eta(\hat{a} + \hat{a}^\dagger) - \omega_L t + \Phi)} + e^{-i(\eta(\hat{a} + \hat{a}^\dagger) - \omega_L t + \Phi)} \right]. \quad (3.64)$$

### Transformation into the interaction picture

The simplest picture of the dynamics induced by the light field arises after transformation into the so-called *interaction picture*. Using the unitary operator

$$\hat{U} = e^{-\frac{i}{\hbar}\hat{H}_{\text{ion}}t}, \quad (3.65)$$

the transformed interaction Hamiltonian  $\hat{H}_{\text{int}}$  is then given by [Lei03]

$$\begin{aligned}\hat{H}_{\text{int}} &= \hat{U}^\dagger \hat{H}^{(i)} \hat{U} \\ &= \frac{\hbar}{2} \Omega \left( \hat{\sigma}_+ e^{i\omega_0 t} + \hat{\sigma}_- e^{-i\omega_0 t} \right) e^{\frac{i}{\hbar} \hat{H}^{(m)} t} \\ &\quad \times \left[ e^{i(\eta(\hat{a} + \hat{a}^\dagger) - \omega_L t + \Phi)} + e^{-i(\eta(\hat{a} + \hat{a}^\dagger) - \omega_L t + \Phi)} \right] e^{-\frac{i}{\hbar} \hat{H}^{(m)} t}.\end{aligned}\quad (3.66)$$

Multiplying the time-dependent factors in the above expressions leads to terms of the form  $e^{\pm i(\omega_L \pm \omega_0)t}$ . In the following, the rapidly oscillating terms with frequency  $\omega_L + \omega_0$  are neglected, since their contribution hardly affects the time evolution of the system due to the near resonant light-ion interaction ( $\omega_L \approx \omega_0$ ). For historical reasons, this approximation is normally referred to as the *rotating-wave approximation*<sup>7</sup>. By defining the parameter

$$\delta = \omega_L - \omega_0, \quad (3.67)$$

which denotes the detuning of the frequency of the applied light field with respect to the atomic resonance, the transformed interaction Hamiltonian can be written as

$$\hat{H}_{\text{int}}(t) = \frac{\hbar}{2} \Omega \left( \hat{\sigma}_+ \exp \left\{ i\eta \left( \hat{a} e^{-i\omega t} + \hat{a}^\dagger e^{i\omega t} \right) \right\} e^{i(\Phi - \delta t)} + H.c. \right) \quad (3.68)$$

The applied light field thus couples the states  $|g, n\rangle$  and  $|e, n'\rangle$ , effectively allowing for coupling the motional states with the internal electronic states of the ion. Depending on the detuning  $\delta$ , the interaction Hamiltonian will only couple certain internal and motional states. If  $\delta = m\omega$  with  $m \in \mathbb{Z}$ , the manifold of states  $|g, n\rangle$  will be resonantly coupled with  $|e, n+m\rangle$  for each  $n$ . The corresponding Rabi frequencies are then given by

$$\Omega_{n, n+m} = \Omega_{n+m, n} = \Omega \left\| \langle n+m | e^{i\eta(\hat{a} + \hat{a}^\dagger)} | n \rangle \right\| \quad (3.69)$$

### 3.2.3 Lamb-Dicke regime

The interaction Hamiltonian and the Rabi frequencies are further simplified if the ion is confined to the so-called Lamb-Dicke regime, where the extension of the ion's wave function is much smaller than the wavelength of the irradiated light field. The Lamb-Dicke regime is thereby defined by the condition

$$\eta^2(2n+1) \ll 1, \quad (3.70)$$

where  $n$  denotes the number of phonons. In this regime, the exponent in equation (3.68) can be expanded to the lowest order in  $\eta$ :

$$e^{i\eta(\hat{a} + \hat{a}^\dagger)} = 1 + i\eta \left( \hat{a} + \hat{a}^\dagger \right) + \mathcal{O}(\eta^2). \quad (3.71)$$

<sup>7</sup> RWA, **R**otating-**W**ave **A**pproximation

Thus, the interaction Hamiltonian takes the form

$$\hat{H}_{\text{LD}}(t) = \frac{\hbar}{2}\Omega \left( \hat{\sigma}_+ \left\{ 1 + i\eta \left( \hat{a}e^{-i\omega t} + \hat{a}^\dagger e^{i\omega t} \right) \right\} e^{i(\Phi - \delta t)} + H.c. \right). \quad (3.72)$$

As one can see,  $\hat{H}_{\text{LD}}(t)$  only contains three resonances: The first resonance for  $\delta = 0$  ( $m = 0$ ) is called the *carrier resonance* and has the form

$$\hat{H}_{\text{carrier}} = \frac{\hbar}{2}\Omega \left( \hat{\sigma}_+ e^{i\Phi} + \hat{\sigma}_- e^{-i\Phi} \right). \quad (3.73)$$

This Hamiltonian will give rise to transitions of the type  $|g, n\rangle \leftrightarrow |e, n\rangle$  with Rabi frequency

$$\Omega_{n,n} = (1 - \eta^2 n) \Omega, \quad (3.74)$$

not affecting the motional state of the ion.

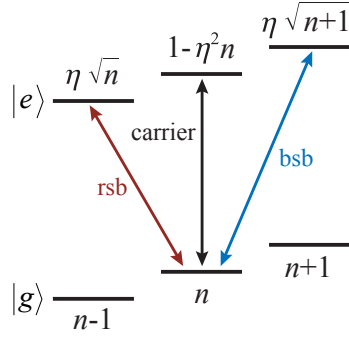


**Figure 3.5:** Transition strengths for the carrier (black), the red sideband (red) and the blue sideband (blue). Here,  $n$  denotes the number of phonons, with  $\eta$  being the Lamb-Dicke parameter.

The resonant part for  $\delta = -\omega$  ( $m = -1$ ) is called the *first red sideband* and is given by

$$\hat{H}_{\text{rsb}} = \frac{\hbar}{2}\Omega\eta \left( \hat{a}\hat{\sigma}_+ e^{i\Phi} + \hat{a}^\dagger\hat{\sigma}_- e^{-i\Phi} \right). \quad (3.75)$$

This Hamiltonian will give rise to transitions of the type  $|g, n\rangle \leftrightarrow |e, n-1\rangle$  with Rabi frequency

$$\Omega_{n,n-1} = \eta\sqrt{n}\Omega, \quad (3.76)$$

entangling the motional state with the internal electronic state of the ion. The Hamiltonian from equation (3.75) is thereby formally equivalent to the Jaynes-Cummings Hamiltonian known from cavity QED. Similarly to the absorption of a light quantum in cavity QED, this interaction removes one phonon of the secular motion while the ion goes from the ground to the excited state.

The counterpart of this interaction is the so-called *first blue sideband*, which is resonant for  $\delta = +\omega$  ( $m = +1$ ):

$$\hat{H}_{\text{bsb}} = \frac{\hbar}{2}\Omega\eta \left( \hat{a}^\dagger\hat{\sigma}_+ e^{i\Phi} + \hat{a}\hat{\sigma}_- e^{-i\Phi} \right). \quad (3.77)$$

This Hamiltonian gives rise to transitions of the type  $|g, n\rangle \leftrightarrow |e, n+1\rangle$ , with the Rabi frequency being given by

$$\Omega_{n,n+1} = \eta\sqrt{n+1}\Omega. \quad (3.78)$$

It has no direct counterpart in the atom-photon realm because such a process would violate energy conservation and is sometimes referred to as anti-Jaynes-Cummings coupling. Figure 3.5 shows the different transitions with the corresponding transition strengths for the carrier, the red sideband (rsb) and the blue sideband (bsb).

### 3.3 Laser cooling

Laser cooling of single particles has been applied routinely for almost two decades. Proposed by T. Hänsch and A. Schawlow [Hän75] and by D. J. Wineland and H. G. Dehmelt [Win75] in 1975, laser cooling was first observed by Neuhauser *et al.* [Neu78] with  $\text{Ba}^+$  ions and by Wineland *et al.* [Win78] with  $\text{Mg}^+$  ions in 1978. In contrast to early techniques, where the motion of the ion was damped due to collisions with background gas (*buffer gas cooling*) or by coupling the trap electrodes to an external electric circuit, laser cooling works by near-resonant excitation of an atomic transition. In the rest frame of the oscillating ion, the laser frequency thereby appears frequency-modulated with the trapping frequency, with the strength of the sidebands depending on the amplitude of the ionic motion. Two limiting cases are thereby of interest:

- $\omega \ll \Gamma$ : If the trapping frequency  $\omega$  is much lower than the decay rate  $\Gamma$  of the transition used for cooling, then the spacing of the sidebands is much smaller than the absorption width of the transition. The velocity of the ion, which is induced by the confining potential, thus changes on a longer timescale than the time it takes the ion to absorb or emit a photon. Hence, these processes can be assumed to change the momentum of the ion instantaneously. The ion thereby behaves like a free particle seeing a time-dependent Doppler-shifted laser frequency. In case of this so-called *Doppler cooling*, the cooling is provided by a velocity-dependent radiation pressure, with typical achievable temperatures being in the range of a few mK.
- $\omega \gg \Gamma$ : In the opposite case, the sidebands are resolved, so that the laser can be tuned to a specific sideband. If the energy of the absorbed photons is smaller than the mean energy of spontaneously emitted photons, the kinetic energy of the ion shrinks, allowing for cooling the ions to the motional ground state. This technique is normally referred to as *sideband cooling*.

After a brief description of the energy levels of singly charged calcium, the above mentioned cooling techniques will be explained by means of simple models in case of a two-level system, with an additional sub-Doppler cooling method being presented in chapter 3.3.3.

### 3.3.1 Energy levels of singly charged calcium

Figure 3.6 shows the energy levels of a singly charged  $^{40}\text{Ca}^+$  ion, with the transitions and lifetimes being depicted for the different states.

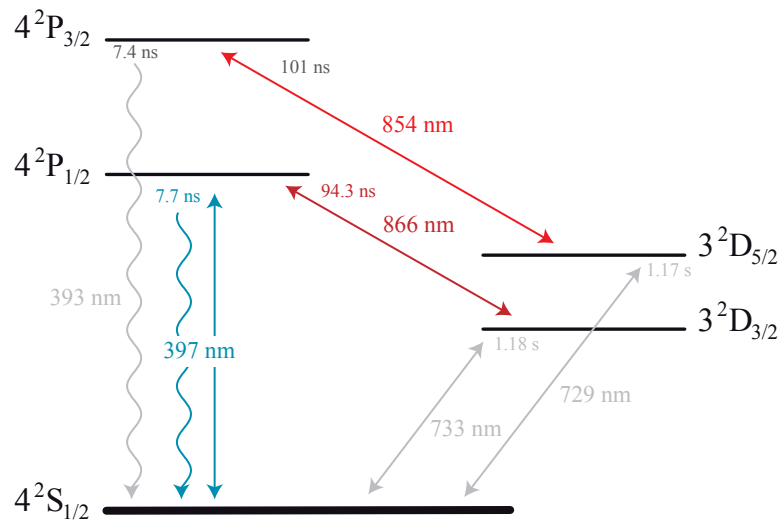


**Figure 3.6:** Transitions in  $^{40}\text{Ca}^+$  and lifetimes of the different states. The colored transitions are utilized for Doppler cooling and optical imaging. [Lin07]

In case of our experiment, the  $4^2\text{S}_{1/2} \leftrightarrow 4^2\text{P}_{1/2}$  dipole transition at a wavelength of 397 nm is of special interest, as it has a lifetime of only 7.7 ns and therefore can be used for Doppler cooling and optical imaging of the trapped  $^{40}\text{Ca}^+$  ions (see also chapters 3.3.2 and 4.4). The transition features a natural linewidth of  $2\pi \times 22.3$  MHz, allowing for scattering rates of about  $10^8$  photons per second [Nat06]. The natural linewidth  $\Gamma_{\text{nat}}$  is thereby given by

$$\Gamma_{\text{nat}} = \frac{1}{\tau}, \quad (3.79)$$

where  $\tau$  denotes the lifetime of the corresponding state. Taking another look at the level scheme depicted in Fig. 3.6, one can see that an ion, which has been excited to the  $4^2\text{P}_{1/2}$  state, cannot only decay back in the  $4^2\text{S}_{1/2}$  ground state, but it can also decay with a certain probability in the metastable  $3^2\text{D}_{3/2}$  state, which features a very long lifetime of 1.18 s. However, as the ion does not perform a fluorescence transition during this time span, it can neither be cooled nor detected. Hence, using an additional repumping laser

at a wavelength of 866 nm, the population of the  $3^2D_{3/2}$  state can be transferred back to the  $4^2P_{1/2}$  state, effectively closing the cooling cycle. Another so-called *dark state* is the  $3^2D_{5/2}$  state with a similar long lifetime of 1.17 s. Due to collisions with the residual background gas, the ion sometimes also ends up in this level, from where the population can be transferred back to the  $4^2S_{1/2}$  ground state by using another repumping laser at 854 nm.

### 3.3.2 Doppler cooling

In the following, we consider a two-level atom moving with velocity  $v$ , which interacts with a traveling wave laser field. The laser is characterized by its frequency  $\omega_L$  and the Rabi frequency  $\Omega$ , with  $\omega_0$  denoting the atomic resonance and  $\Delta = \omega_L - \omega_0$  the detuning of the laser. The laser exerts a radiation pressure force on the atom, which is given by [Roo00a]

$$F = \hbar k \Gamma \rho_{ee}, \quad (3.80)$$

where the occupation probability  $\rho_{ee}$  of the excited state is

$$\rho_{ee} = \frac{\Omega^2}{\Gamma^2 + 4(\Delta - kv)^2} \quad (3.81)$$

in the limit of low saturation. For small velocities, the radiation pressure force can be linearized around  $v = 0$ :

$$F = F_0 + \left. \frac{dF}{dv} \right|_{v=0} v, \quad (3.82)$$

with

$$F_0 = \hbar k \Gamma \frac{\Omega^2}{\Gamma^2 + 4\Delta^2} \quad (3.83)$$

and

$$\left. \frac{dF}{dv} \right|_{v=0} = F_0 \frac{8k\Delta}{\Gamma^2 + 4\Delta^2}. \quad (3.84)$$

$F_0$  is the time-averaged radiation pressure which displaces the ion slightly from the center of the trap. The velocity-dependent part of equation (3.82) provides a viscous drag, if the detuning  $\Delta$  is negative. The random nature of the absorption and emission processes now counteracts this cooling force, with the cooling rate being given by

$$\dot{E}_{\text{cool}} = \langle Fv \rangle = \left\langle \left( F_0 + \left. \frac{dF}{dv} \right|_{v=0} v \right) v \right\rangle = \left. \frac{dF}{dv} \right|_{v=0} \langle v^2 \rangle. \quad (3.85)$$

Spontaneously emitted photons lead to a diffusive spreading of the mean squared momentum. In case of uncorrelated spontaneous emission events, this results in a heating rate  $\dot{E}_{\text{heat}}^{\text{em}}$ , which is given by

$$\dot{E}_{\text{heat}}^{\text{em}} = \frac{1}{2m} \frac{d}{dt} \langle p^2 \rangle = \frac{1}{2m} (\hbar k)^2 \Gamma \langle \rho_{ee}(v) \rangle \approx \frac{1}{2m} (\hbar k)^2 \Gamma \rho_{ee}(v=0), \quad (3.86)$$

provided that the atomic velocity is small. A second contribution to the heating rate, similar in size to  $\dot{E}_{\text{heat}}^{\text{em}}$ , results from the fluctuations of the cooling force due to the discreteness of the absorption process. In the steady state, the cooling rate  $\dot{E}_{\text{cool}}$  equals the total heating rate  $\dot{E}_{\text{heat}} = \dot{E}_{\text{heat}}^{\text{em}} + \dot{E}_{\text{heat}}^{\text{abs}}$ , thus yielding

$$\dot{E}_{\text{cool}} + \dot{E}_{\text{heat}} = 0 \iff \left. \frac{dF}{dv} \right|_{v=0} \langle v^2 \rangle = \frac{1}{m} (\hbar k)^2 \Gamma \rho_{\text{ee}}(v=0). \quad (3.87)$$

Using the relation  $m \langle v^2 \rangle = k_{\text{B}} T$ , the cooling limit can be written as

$$T = \frac{\hbar \Gamma}{4k_{\text{B}}} \left( \frac{\Gamma}{-2\Delta} + \frac{-2\Delta}{\Gamma} \right). \quad (3.88)$$

The lowest temperatures are obtained if  $\Delta = -\frac{\Gamma}{2}$ :

$$T_{\text{min}} = \frac{\hbar \Gamma}{2k_{\text{B}}} =: \frac{\hbar \Gamma}{4k_{\text{B}}} (1 + \xi) \quad \text{with} \quad \xi = 1. \quad (3.89)$$

In the derivation, it was assumed, that the wave vector of spontaneously emitted photons points in or against the direction of the laser beam. If the photons are isotropically emitted into space, they cause heating in the transverse directions while the diffusive momentum spread in the cooled direction is proportionally smaller. The lower temperature can be accounted for by setting  $\xi = \frac{1}{3}$ .<sup>8</sup>

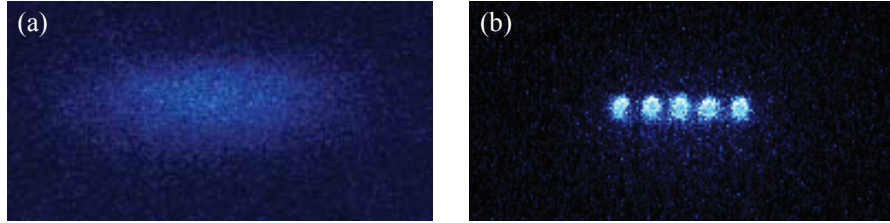


**Figure 3.7:** EMCCD images of Doppler cooled  $^{40}\text{Ca}^+$  ions. (a) Hot ion cloud. (b) Cold linear ion crystal consisting of five  $^{40}\text{Ca}^+$  ions.

In order to accomplish a cooling of the harmonic motion in all three oscillator directions  $\vec{e}_i$ , the laser beam is irradiated in such a way, that the wave vector  $\vec{k}$  has a non-vanishing overlap with every direction  $\vec{e}_i$ . If  $\Theta$  denotes the angle between the trap axis and the direction of the laser beam, the minimal temperature is given by

$$T_{\text{min}} = \cos^2(\Theta) \frac{\hbar \Gamma}{4k_{\text{B}}} (1 + \xi), \quad (3.90)$$

with the minimal mean phonon number in axial direction ( $z$ -direction) being

$$\langle n_z \rangle_{\text{min}} = \frac{k_{\text{B}} T_{\text{min}}}{\hbar \omega_z}. \quad (3.91)$$

<sup>8</sup> More detailed calculations also consider the nature of the atomic transition. In case of a dipole radiation pattern, one obtains  $\xi = \frac{2}{5}$  [Ste86].

As the number of scattered photons per time interval has to be large in order to achieve high cooling rates, Doppler cooling is suitable for transitions which feature a short lifetime of the excited state. In case of our experiment, Doppler cooling is performed on the  $4^2S_{1/2} \leftrightarrow 4^2P_{1/2}$  transition, yielding a mean ion temperature of about 2 mK, see also Fig. 3.7. The minimal achievable temperature is thereby limited due to the multi-level dynamics (e.g. the  $3^2D_{3/2}$  state), the micromotion (see also chapter 5.2.2) as well as the saturation of the utilized dipole transition.

### 3.3.3 Sub-Doppler cooling methods

As stated in the previous chapter, standard cooling techniques like Doppler cooling only allow for cooling the trapped particles to temperatures of a few mK. However, in order to cool the ions to the motional ground state, which e.g. is needed in case of quantum information processing, more sophisticated cooling techniques are necessary. In the following chapter, two of these techniques, namely sideband cooling and EIT<sup>9</sup> cooling will be explained in more detail.

#### Sideband cooling

As mentioned above, sideband cooling is a technique which allows one to cool ions to the motional ground state [Die89]. However, as this cooling technique only works in the Lamb-Dicke regime, one prerequisite is a successful Doppler cooling of the trapped particles. If the linewidth  $\Gamma$  of the cooling transition is much smaller than the trapping frequency  $\omega_z$ , the motional sidebands can be spectroscopically resolved. By driving transitions on the red sideband, i.e. by detuning the cooling laser to the frequency  $\omega_0 - \omega_z$ , one can then excite the ion from the  $|g, n\rangle$  to the  $|e, n - 1\rangle$  state, see also Fig. 3.8. From there, the ion spontaneously decays into the  $|g, n - 1\rangle$  state, effectively annihilating one phonon within each cooling cycle. However, such transitions imply long lifetimes of the excited states (typically of the order of 1 s), leading to a vastly reduced cooling rate due to the long time span needed for one cooling cycle. Hence, the population of the excited state is normally transferred to another state with a short lifetime (typically of the order of 10 ns), from where the ion rapidly decays into the ground state, increasing the number of cooling cycles per time interval.

<sup>9</sup> Electromagnetically Induced Transparency

The minimal achievable mean phonon number  $\langle n \rangle_{\text{SC}}$  is thereby given by [Pei99]

$$\langle n \rangle_{\text{SC}} = \left( \xi + \frac{1}{4} \right) \frac{\Gamma^2}{4\omega_z^2}. \quad (3.92)$$

Here, the constant  $\xi$  again denotes a geometric factor which depends on the geometry of excitation and photon reemission of the chosen transition. In case of  $^{40}\text{Ca}^+$  ions, sideband cooling can e.g. be implemented on the  $4^2\text{S}_{1/2} \leftrightarrow 3^2\text{D}_{5/2}$  quadrupole transition at a wavelength of 729 nm, with the  $4^2\text{P}_{3/2}$  state being used as a fast decay channel back into the ground state, see also Fig. 3.6.

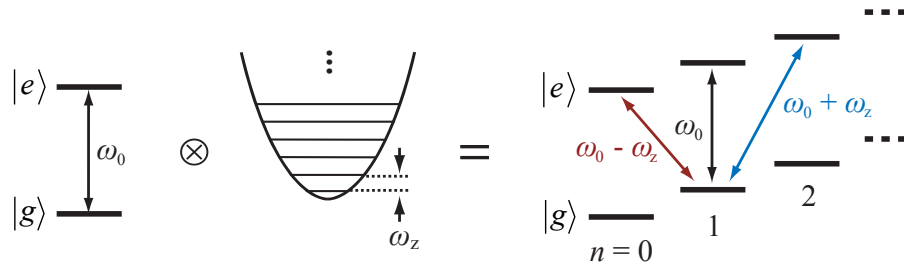


**Figure 3.8:** Sideband cooling scheme. The internal atomic energy levels  $|g\rangle$  and  $|e\rangle$  couple to the external energy levels of the harmonic trapping potential, resulting in a ladder-like structure. By exciting the red sideband at the frequency  $\omega_0 - \omega_z$  (depicted in red), one can annihilate one phonon (cooling) whereas an excitation on the blue sideband at the frequency  $\omega_0 + \omega_z$  (depicted in blue) results in the creation of one phonon (heating). The carrier transition at the frequency  $\omega_0$  (colored black) causes the excitation from the ground state  $|g\rangle$  to the excited state  $|e\rangle$  without changing the number of phonons. [Zie08]

In the absence of a suitably narrow electronic transition, it is also possible to design an effective two-level transition by using a  $\Lambda$ -configuration of atomic levels, where two stable or metastable states  $|g_1\rangle$  and  $|g_2\rangle$  are coupled by Raman transitions through the common excited state  $|e\rangle$  [Mar94]. Here, selective sideband excitation is accomplished by coherent Raman processes that transfer atoms from  $|g_1\rangle$  to  $|g_2\rangle$ , tuned to the red sideband of the two-photon transition. Repumping from  $|g_2\rangle$  to  $|g_1\rangle$  is accomplished with a third laser that induces spontaneous Raman scattering. The linewidth of the process is thereby mainly determined by the linewidth of the spontaneous Raman scattering and can easily be set to yield resolved sidebands. This cooling scheme is normally referred to as *Raman sideband cooling* [Hei90].

However, the major drawback of sideband cooling is the fact, that the cooling of larger ion crystals proves to be difficult due to the complicated emerging sideband structure and the necessity to repeatedly cool a large number of different oscillation modes<sup>10</sup>.

<sup>10</sup>For a more detailed description of the sideband cooling scheme, see [Esc03].

### EIT cooling

Electromagnetically induced transparency (EIT), which is also called *coherent population trapping* or *dark resonance*, arises in three-level (or multi-level) systems and consists of the cancellation of the absorption on one transition induced by simultaneous coherent driving of another transition. Here, the absorption on the  $|g, n\rangle \rightarrow |e, n\rangle$  carrier transition is suppressed, while enhancing the absorption on the  $|g, n\rangle \rightarrow |e, n-1\rangle$  sideband transition, thus decreasing the heating and increasing the cooling rate.

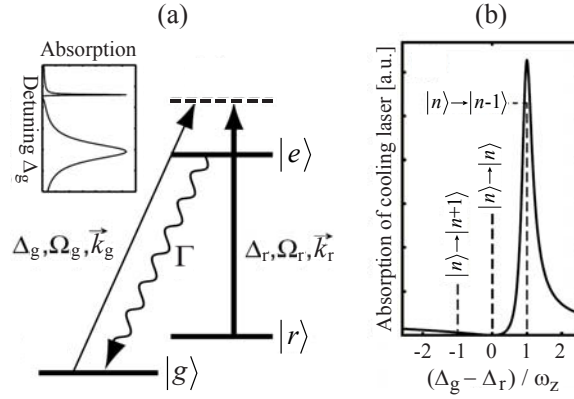


**Figure 3.9:** EIT cooling scheme. (a) Three-level system in  $\Lambda$ -configuration. By utilizing a Raman level (dashed line), the population of the excited state  $|e\rangle$  can be circumvented. The detuning  $\Delta$ , Rabi frequency  $\Omega$  and wave vector  $\vec{k}$  denote the relevant laser parameters for the cooling laser (index  $g$ ) and the coupling laser (index  $r$ ), with  $\Gamma$  being the linewidth of the fluorescence transition. The inset shows schematically the absorption rate on the  $|g\rangle \rightarrow |e\rangle$  transition, when the atom is strongly excited above resonance on the  $|r\rangle \rightarrow |e\rangle$  transition. (b) Absorption of cooling laser around  $\Delta_g = \Delta_r$  (solid line) and probabilities of carrier ( $|n\rangle \rightarrow |n\rangle$ ) and sideband ( $|n\rangle \rightarrow |n \pm 1\rangle$ ) transitions when  $\Delta_g = \Delta_r$  (dashed lines). [Mor00a]

In the following, we consider a three-level atom with ground state  $|g\rangle$ , stable or metastable state  $|r\rangle$ , and excited state  $|e\rangle$  in  $\Lambda$ -configuration [Mor00a], see Fig. 3.9(a). In case of  $^{40}\text{Ca}^+$  ions, such a lambda system can e.g. be formed by the states  $4^2\text{S}_{1/2}$ ,  $4^2\text{P}_{1/2}$  and  $3^2\text{D}_{3/2}$  or by using the Zeeman structure of the  $4^2\text{S}_{1/2} \leftrightarrow 4^2\text{P}_{1/2}$  transition, see also chapter 3.3.1. The excited state  $|e\rangle$  has the linewidth  $\Gamma$  and is coupled to both  $|g\rangle$  and  $|r\rangle$  by dipole transitions. The transition  $|r\rangle \rightarrow |e\rangle$  is thereby excited by an intense coupling laser field of frequency  $\omega_r$ , Rabi frequency  $\Omega_r$  and detuning  $\Delta_r = \omega_r - \omega_{re}$ , where  $\omega_{re}$  is the frequency of the bare atomic transition  $|r\rangle \rightarrow |e\rangle$ . The absorption spectrum observed by exciting the transition  $|g\rangle \rightarrow |e\rangle$  with another cooling laser at frequency  $\omega_{ge} + \Delta_g$  and Rabi frequency  $\Omega_g$  can thereby be described by a Fano-like profile [Lou92], whose zero corresponds to the case  $\Delta_g = \Delta_r$  and which is asymmetric for  $\Delta_r \neq 0$ , see also inset of Fig. 3.9(a).

In the case  $\Delta_r > 0$ , the two components of the absorption spectrum, i.e. the broad resonance at  $\Delta_g \simeq 0$  with linewidth  $\gamma'' \simeq \Gamma$  and the narrow resonance at  $\Delta_g \simeq \Delta_r$  with linewidth  $\gamma' \ll \Gamma$  correspond to so-called *dressed states*, which are formed due to the interaction of the coupling laser with the atom. These dressed states, and hence the maxima of the absorption spectrum, are shifted from  $\Delta_r$  by  $+\delta$  and from  $-\Delta_r$  by  $-\delta$ , respectively, with

$$\delta = \frac{1}{2} \left( \sqrt{\Delta_r^2 + \Omega_r^2} - |\Delta_r| \right) \quad (3.93)$$

being the ac Stark shift induced by the coupling laser. Taking the harmonic motion into account, the minimum of the Fano-like profile at  $\Delta_g = \Delta_r$  corresponds to the carrier transition  $|n, n\rangle \rightarrow |e, n\rangle$ , which is therefore canceled. Hence, by choosing  $\Delta_r > 0$  and a suitable Rabi frequency  $\Omega_r$ , the spectrum can be designed in such a way, that the transition  $|g, n\rangle \rightarrow |e, n-1\rangle$  on the red sideband corresponds to the maximum of the narrow resonance, whereas the blue sideband ( $|g, n\rangle \rightarrow |e, n+1\rangle$ ) falls into the region of the spectrum of small excitation probability, see also Fig. 3.9(b). The condition on the laser parameters for enhancing the red sideband absorption while eliminating the carrier is therefore

$$\Delta_g = \Delta_r, \quad \delta \simeq \omega_z, \quad (3.94)$$

with the achievable mean phonon number  $\langle n \rangle_{\text{EIT}}$  being given by

$$\langle n \rangle_{\text{EIT}} = \frac{\langle n \rangle_{\text{SC}}}{1 + \frac{4\xi}{\cos^2(\Theta)}}. \quad (3.95)$$

Here,  $\Theta$  again denotes the angle between the motional axis and the direction of the laser beam, with  $\xi = \frac{2}{3}$  and  $\langle n \rangle_{\text{SC}}$  being the minimal achievable mean phonon number in case of sideband cooling. Thus, given the same cooling rate,  $\langle n \rangle_{\text{EIT}} < \langle n \rangle_{\text{SC}}$ . By tuning the absorption spectrum in such a way, that red sidebands of higher order are also covered by the narrow resonance, EIT cooling not only allows for cooling larger ion crystals, but it is even possible to cool mixed ion crystals to the motional ground state due to the simultaneous cooling of several vibrational modes with different frequencies of oscillation [Roo00b]. As the implementation of this scheme is comparatively easy, i.e. only a few additional laser beams are needed with the exact location of the motional sidebands being not as crucial as in case of sideband cooling, EIT cooling thus is the prime candidate for cooling prospective doping atoms to the motional ground state.

## Chapter 4

# Experimental setup

In this chapter, we will focus on the experimental setup which is used for trapping, imaging and manipulating the  $^{40}\text{Ca}^+$  and prospective dopant ions. One of the main goals in the early stages of development was to come up with a modular setup which allows one to quickly exchange the substrate used for implantation without compromising the vacuum of the whole system. At the same time, a rather compact setup was needed in order to minimize the flight distance of the extracted ions, leading to a reduced broadening of the generated single-ion beam. After a description of the experimental setup including the vacuum setup (4.1), the utilized laser sources (4.2), the optical setup (4.3) as well as the imaging system (4.4), the required trap voltage supplies (4.5) will be discussed in detail and the dynamic experimental control system will be presented (4.6).

### 4.1 Ultra high vacuum setup

The core piece of the ultra high vacuum (UHV) setup is a Magdeburg hemisphere from Kimball Physics<sup>1</sup> with an inner diameter of 91.5 mm and a total length of 106 mm. It features a total of seven different access ports with flange sizes ranging from DN16CF<sup>2</sup> up to DN63CF which are labeled A-D2 in the following, see also Fig. 4.1. A specifically designed segmented linear ion trap (see chapter 5) is mounted inside of the hemisphere, with the trap axis being located 165 mm above the optical table, see also Fig. 4.2(b) and inset of Fig. 4.7.

---

<sup>1</sup> *MCF450-MH10204/8-A*, Kimball Physics Inc., Wilton, NH, USA, <http://www.kimballphysics.com>

<sup>2</sup> The abbreviation DNXXCF denotes a UHV compatible flange which is based on the Conflat design, locating and capturing a copper gasket between two symmetrical ‘knife edge’ sealing surfaces, with the XX indicating the inner diameter of the flange in millimeters.

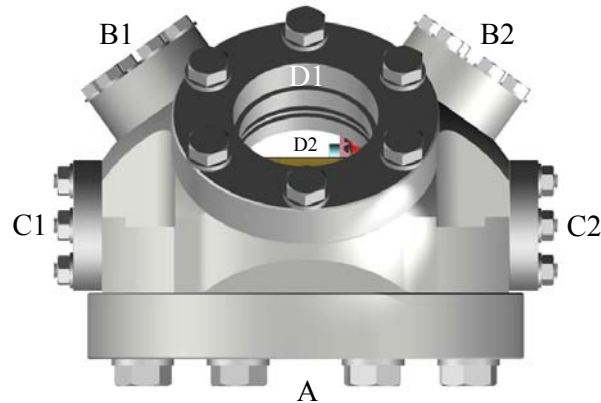


**Figure 4.1:** Technical drawing of the main vacuum chamber featuring seven different access ports (labeled A-D2). The available flange sizes vary from DN16CF (ports B1, B2, C1 and C2) over DN35CF (ports D1 and D2) up to DN63CF (port A).

The access ports A, B1 and B2 are all equipped with fused silica ( $\text{SiO}_2$ ) windows, allowing for optical access with laser beams and for imaging the ions, see also Fig. 4.6. A 20-pin vacuum feedthrough for the dc electrodes and the ovens is connected via a T-piece to port D1 whereas the power supply for the rf electrodes is managed using a 4-pin vacuum feedthrough which is mounted on a four-way cross connected to access port C1. Using port C2, the main vacuum chamber is connected to a separate detector chamber (see also chapter 6) via an all-metal gate valve<sup>3</sup>. The complete setup measures 850 mm in length with a depth of 480 mm and a total height of about 380 mm, see Fig. 4.2 for some schematic drawings. The pressure is held by a 201/s Vaclon *Plus* StarCell ion getter pump and a titanium sublimation pump (TSP) from Varian<sup>4</sup> which are connected to the main vacuum vessel via port D2. In addition, both the main vacuum and the detector chamber are connected via all-metal angle valves<sup>5,6</sup> to a turbomolecular pump from Oerlikon<sup>7</sup>. The base pressure of the UHV setup equals  $5 \times 10^{-10}$  mbar which is measured using a Varian<sup>4</sup> UHV-24p Bayard-Alpert type ionization gauge tube.

<sup>3</sup> 48124-CE01, VAT Deutschland GmbH, Grasbrunn, Germany, <http://www.vatvalve.com>

<sup>4</sup> Varian Inc., Palo Alto, CA, USA, <http://www.varianinc.com>

<sup>5</sup> ZCRD43R, VG Scienta Inc., Newburyport, MA, USA, <http://www.vgscienta.com>

<sup>6</sup> 54032-GE02, VAT Deutschland GmbH, Grasbrunn, Germany, <http://www.vatvalve.com>

<sup>7</sup> Oerlikon Leybold Vacuum GmbH, Cologne, Germany, <http://www.oerlikon.com>

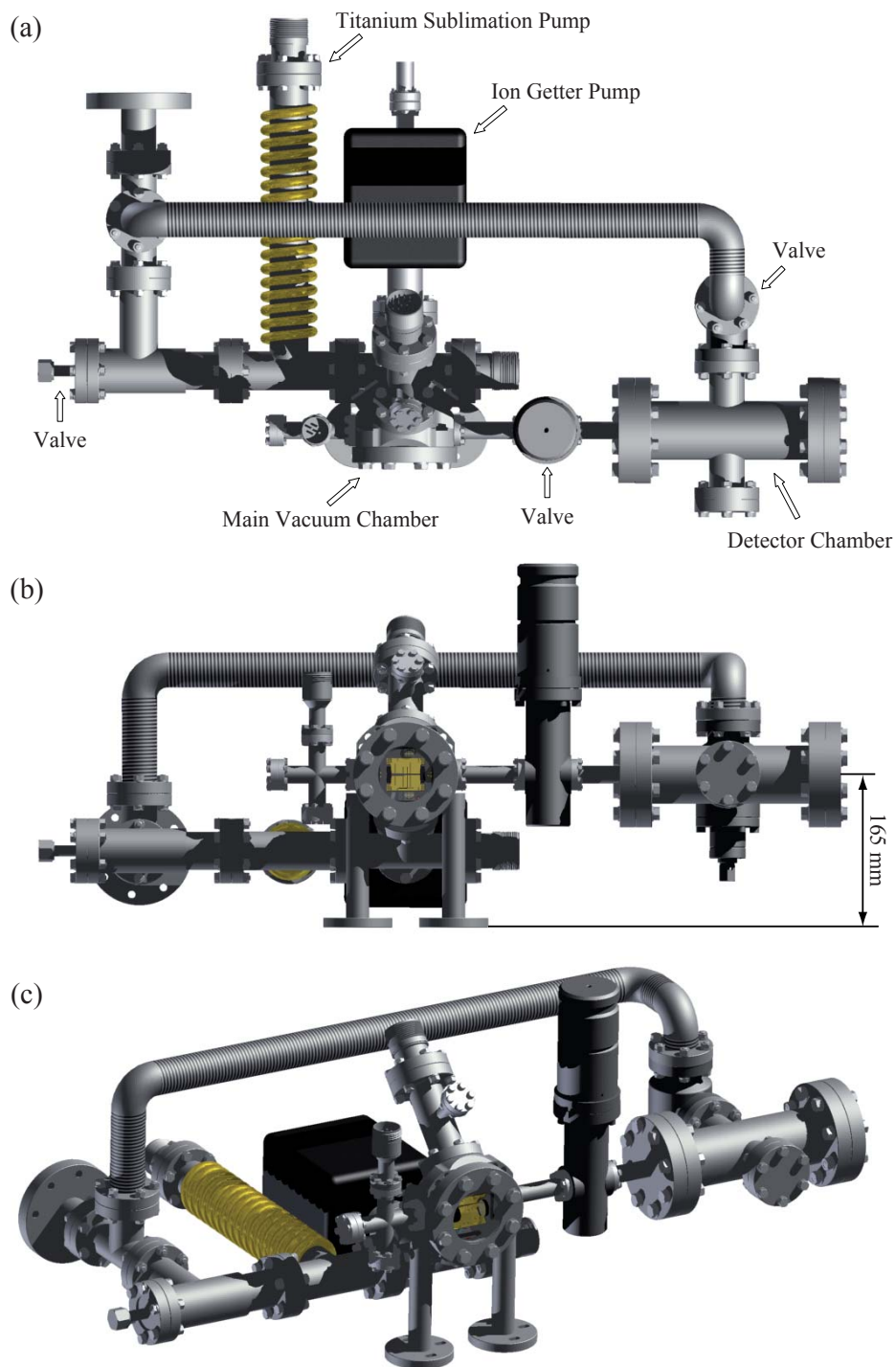


**Figure 4.2:** Schematic drawings of the ultra high vacuum setup. (a) Top view: The setup consists of a main vacuum chamber (see also Fig. 4.1) and a detector chamber which are connected via an all-metal gate valve. The pressure is held by an ion getter, a titanium sublimation and a turbomolecular pump (not pictured). (b) Front view: The trap axis is located 165 mm above the optical table. (c) Isometric view.

## 4.2 Diode laser systems

The generation of the necessary laser beams at the wavelengths 375 nm, 397 nm, 423 nm as well as 854 nm and 866 nm is done by using commercial grating stabilized diode laser systems from TOPTICA<sup>8</sup>. In contrast to complex and maintenance intensive laser systems like dye or titanium-sapphire lasers, the main advantages of diode laser systems are their compact and easy to maintain design, the low electric power consumption as well as the long lifetime of the utilized laser diodes.

### 4.2.1 Grating stabilized diode laser DL 100

Free-running laser diodes normally have a linewidth of almost 100 MHz. Their emission frequency can either be changed by adjusting the injection current or the ambient temperature of the pn-junction.

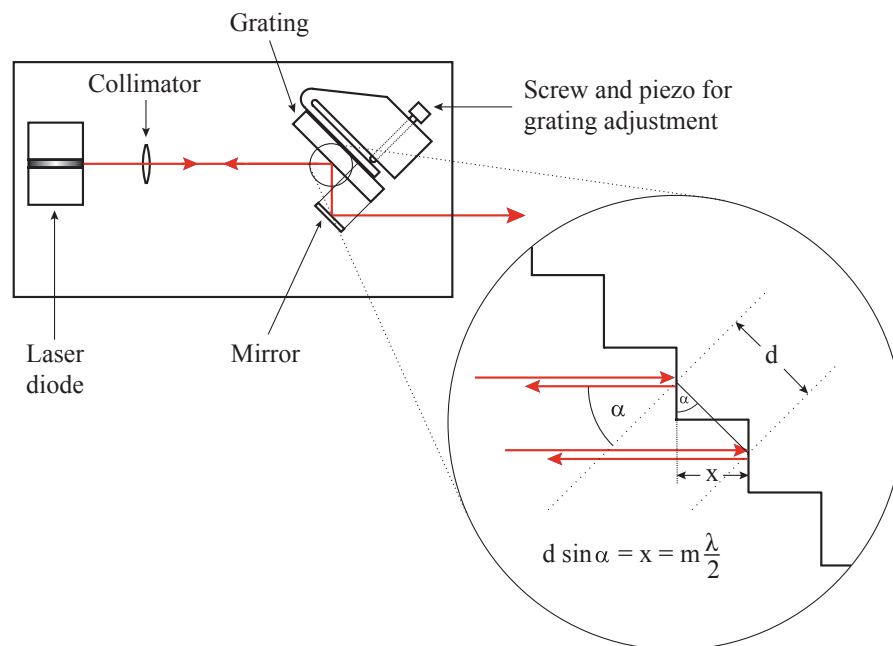


**Figure 4.3:** Schematic drawing of the diode laser DL 100 from TOPTICA<sup>8</sup>. [Ebl06]

However, in many cases it is not possible to reach the desired wavelength by means of current and temperature alone as so-called mode hops will occur, i.e. a hop over a relatively large wavelength interval followed by a short continual dependence of the basic wavelength on the current. Grating stabilized diode laser systems like the DL 100 from TOPTICA<sup>8</sup> circumvent these problems, see Fig. 4.3 for a schematic drawing.

<sup>8</sup> TOPTICA Photonics AG, Graefelfing (Munich), Germany, <http://www.toptica.com>

The light emitted from the front facet of the laser diode is collimated by a multi-element lens with a very short focal length and then hits a reflection grating which is adjusted in the so-called *Littrow* setup: The first diffraction order of the grating is focused back into the laser diode, creating a resonator out of the laser diodes' rear facet and the external grating. As the feedback of the grating is considerably higher than the feedback from the front facet of the laser diode, the laser diode is 'forced' to further emit light at the back reflected wavelength. The free spectral range of this new resonator is substantially smaller than the one of the laser diode and shows a higher finesse, reducing the typical linewidth of such a grating stabilized laser to about 1 MHz with typical output powers ranging from 5 to 50 mW.

The Littrow angle  $\alpha$  for a given wavelength  $\lambda$  is determined by the equation

$$d \sin \alpha = m \frac{\lambda}{2}, \quad (4.1)$$

where  $m$  denotes the diffraction order and  $d$  the grating constant. The angle  $\alpha$  is defined with reference to the grating normal, see also Fig. 4.3. As can be seen from equation (4.1), a change of the incident angle  $\alpha$  leads to a variation of the wavelength  $\lambda$  or the diffraction order  $m$  for a fixed grating constant  $d$ . A change of the grating position allows one to directly adjust the laser frequency within a frequency range of about 10 GHz. Subsequent adjustment will lead to mode hops where the diffraction order  $m$  is changed. The grating can either be adjusted using a micrometer screw (coarse adjustment) or a piezo actuator (fine adjustment) which is integrated in the grating holder. By simultaneously adjusting the laser diode current, the mode hop free tuning range can be increased up to 30 GHz. An additionally installed temperature stabilization ensures that the laser diode is not subject to temperature fluctuations.

### 4.2.2 Frequency-doubled diode laser system DL-SHG 110

In order to generate high laser powers in the ultraviolet wavelength domain, one utilizes systems which frequency double infrared laser light by using a resonant doubling cavity. Figure 4.4 shows the schematic drawing of such a system.

The fundamental laser light at 846 nm is generated by a grating stabilized DL 100 diode laser (Master Oscillator, see chapter 4.2.1), which passes through an optical isolator and is then matched to an external ring resonator in order to increase the fundamental laser power. A small part of the infrared laser light is transmitted through a semitransparent

mirror and is guided to a wavemeter (see also chapter 4.3) in order to control the wavelength. The optical isolator consists of a double-stage Faraday rotator and serves to avoid feedback of laser radiation into the DL 100 Master Oscillator, insuring its stable operation. The second harmonic laser light at a wavelength of 423 nm is produced by a temperature stabilized bismuth borate ( $\text{BiB}_3\text{O}_6$ ) crystal mounted inside of the external ring resonator which frequency doubles the infrared laser light by exploiting a nonlinear effect.

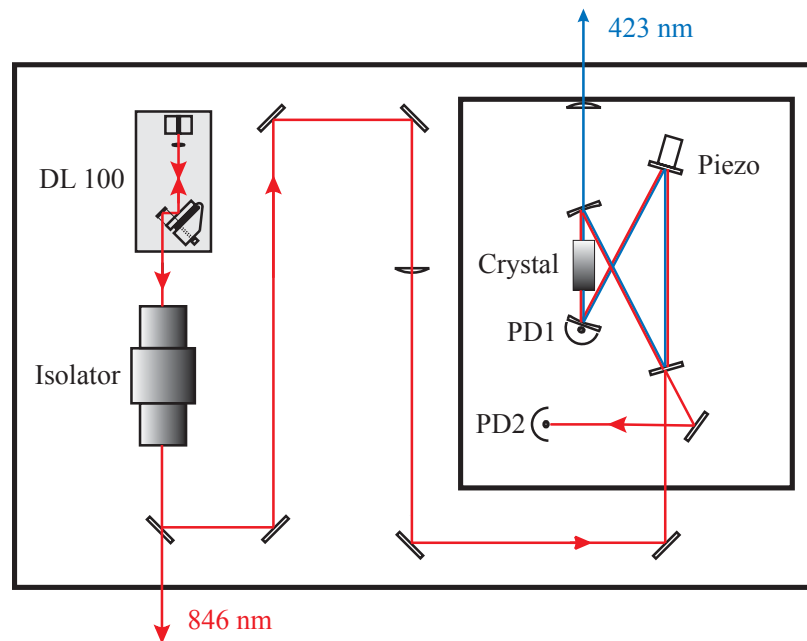


**Figure 4.4:** Schematic drawing of the frequency-doubled diode laser system DL-SHG 110 from TOPTICA<sup>8</sup>. [Ebl06]

The design of the cavity follows the idea of Boyd and Kleinman [Boy68] in order to achieve a maximum conversion efficiency for the fundamental wavelength. It has to be stabilized to a multiple of the fundamental wavelength in order to achieve increasing constructive interference and therefore intensity stability of the circulating wave. An electronic feedback control ensures that the length of the resonator is matched to the laser wavelength by adjusting one of the cavity mirrors which is mounted on a piezo stage. The corrective error signal is generated by using the Pound-Drever-Hall stabilization technique [Dre83] (see chapter 4.2.3) utilizing photo diode PD2. Another photo diode (PD1) is located behind one of the resonator mirrors and monitors the internal mode spectrum. The recorded signal is proportional to the intra-cavity laser power and allows one to adjust the ring resonator by eliminating the higher order Gaussian beam modes. In the end, the frequency-doubled laser light at 423 nm is transmitted through a semitransparent cavity mirror and exits the laser housing through an anti-reflexion-coated lens.

### 4.2.3 Pound-Drever-Hall frequency stabilization

In order to guarantee the long-term stability of the adjusted laser frequency, an active stabilization is needed. In our group, this is accomplished by using the Pound-Drever-Hall stabilization method [Dre83], see also Fig. 4.5 for a schematic drawing.

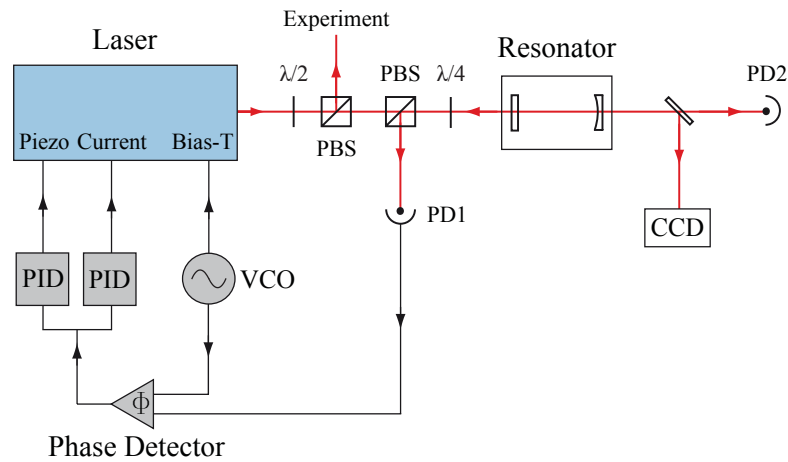


**Figure 4.5:** Schematic drawing of the Pound-Drever-Hall frequency stabilization.

Here, a small part of the laser light is coupled into a stable resonator with the aid of a CCD camera and a photo diode (PD2), which allow one to monitor the resonator mode as well as the transmitted laser intensity. Depending on the frequency of the irradiated light, the reflected and transmitted laser intensities vary. Using a PBS (**P**olarized **B**eam **S**plitter) and a fast photo diode (PD1), the back reflected laser light is utilized to generate an error signal which is a measure for the deviation from the desired frequency. In order to retrieve the necessary phase information for the feedback control, the frequency of the laser light is modulated via a Bias-T input (see also chapter 5.2.2) using a voltage controlled oscillator (VCO) which generates a sinusoidal ac voltage with a typical frequency of about 80 MHz. For this reason, the intensity of the back reflected light also undergoes a sinusoidal change and thus the electronic signal from photo diode PD1. The phase difference between the back reflected and the modulated laser light can then be obtained using a phase detector<sup>9</sup> which mixes both signals, generating the aforementioned error signal which is proportional to the deviation from the set point value. This error signal is then transferred to a fast PID (**P**roportional plus **I**ntegral plus **D**erivative) control loop which regulates the current of the laser diode and allows one to compensate disturbances ranging from a few kHz up to several MHz. Another PID control loop with a high integral portion is utilized to counter-balance slow drifts and disturbances of up to 10 kHz via the piezo of the laser [Tha99].

<sup>9</sup> ZRPD-1, Mini-Circuits, New York, NY, USA, <http://www.minicircuits.com>

### 4.3 Optical setup

Figure 4.6 shows a schematic drawing of the experimental setup consisting of the UHV chamber (4.1), the various diode lasers (4.2) as well as the imaging system (4.4) and a Fabry-Perot reference cavity used for frequency stabilization. The complete setup is located on an air-suspended optical table which is situated in a temperature stabilized laboratory in order to suppress vibrations of the building and to reduce thermal elongations to a minimum.

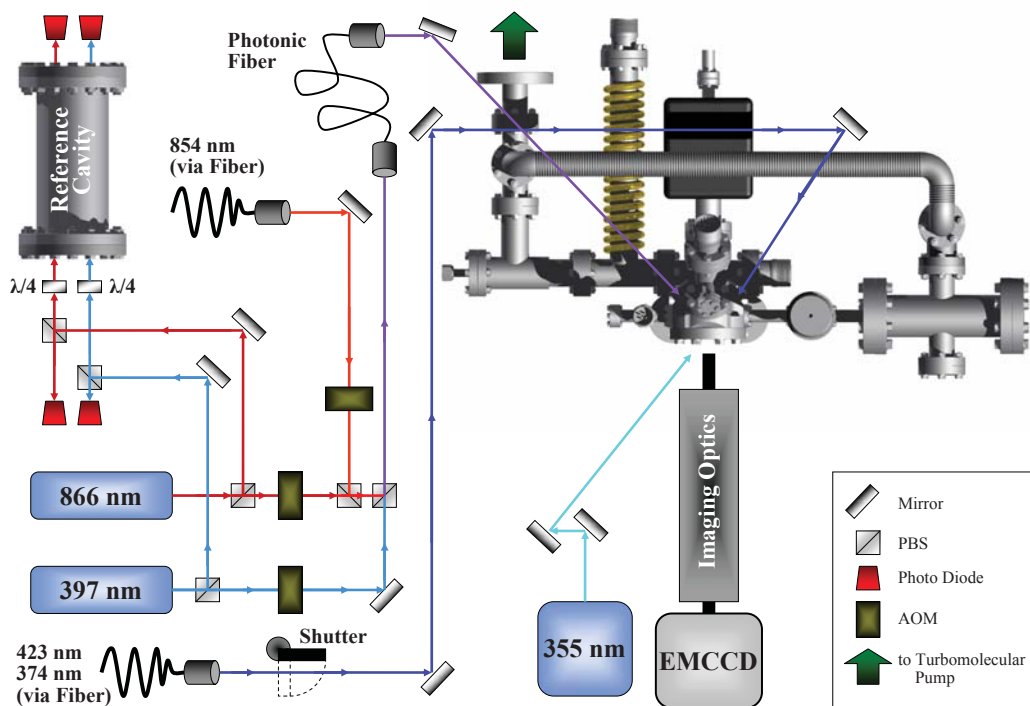


**Figure 4.6:** Schematic drawing of the experimental setup. See text for further details.

The lasers at 397 and 866 nm, which are used for Doppler cooling and repumping, are located directly on the optical table whereas the repumping laser at 854 nm as well as the photoionization lasers at 374 and 423 nm are provided via fibers from a different lab. Using polarized beam splitters, a small part of the laser light at 397 and 866 nm is coupled into a Fabry-Perot reference cavity which is used for the Pound-Drever-Hall frequency stabilization as described in the previous chapter. Afterwards, the laser beams at the wavelengths 397, 854 and 866 nm are superimposed and coupled into a photonic fiber<sup>10</sup> which guides the laser beams directly to the main vacuum vessel. Using a lens with a

<sup>10</sup> *LMA-10-UV*, NKT Photonics A/S, Birkerød, Denmark, <http://www.nktphotonics.com>

focal length of 150 mm, the beams are focused and enter the vacuum chamber via access port B1, see also Fig. 4.1. In order to adjust the intensities of the different laser beams,  $\lambda/2$  wave plates are installed in front of the polarized beam splitters (which are omitted in Fig. 4.6 for reasons of clarity). The photoionization lasers are already superimposed when they exit the multi-mode fiber and are guided to the chamber by multiple mirrors. There, they are focused using a 500 mm lens and enter the chamber through access port B2. A pulsed frequency-tripled Nd-YAG laser<sup>11</sup> at a wavelength of 355 nm also stands directly on the optical table and is used for the generation of prospective dopant ions, see also chapter 6.2.1. In order to achieve a higher focal intensity, the beam diameter is enlarged using a telescope before the beam is again focused by a 150 mm lens and enters the chamber via access port A.

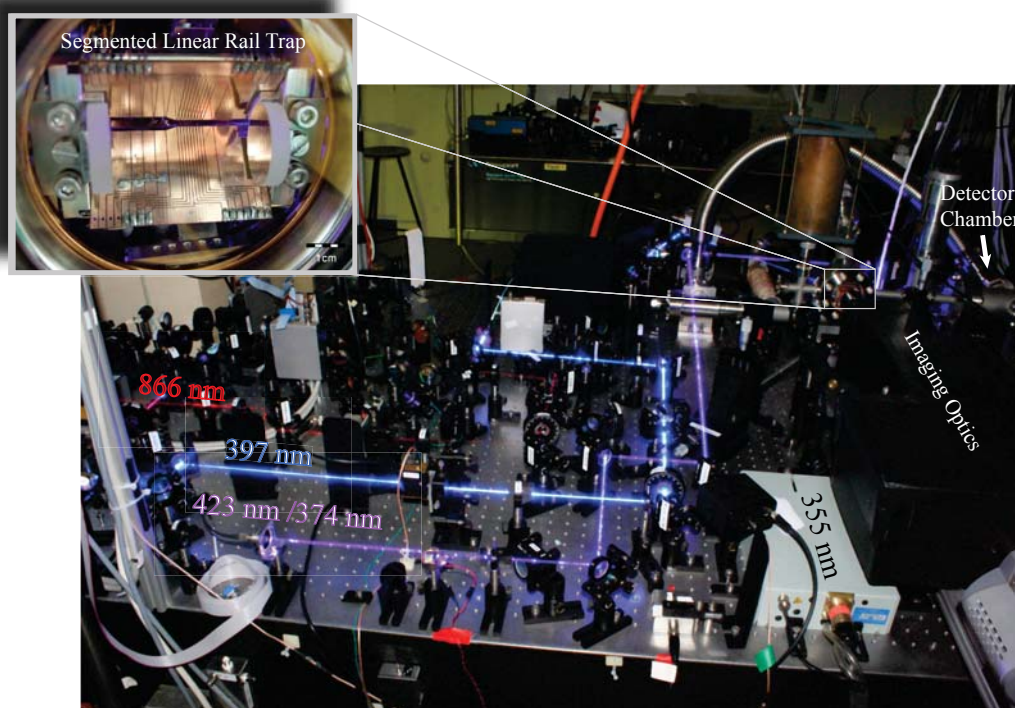


**Figure 4.7:** Picture of the experimental setup including the paths of the different lasers (which were made visible by taking a photograph with long term exposure). The inset shows a close-up view of the main vacuum vessel and the therein residing segmented linear ion trap. [Fic09a]

The switching of the lasers at the wavelengths 397, 854 and 866 nm is done using acousto-optical modulators (AOMs) which allow one to switch the laser beams on and off with an accuracy of a few ns. The photoionization lasers are switched using a conventional

<sup>11</sup> *Continuum Minilite I*, Continuum, Santa Clara, CA, USA, <http://www.continuumlasers.com>

mechanical shutter which is based on a personal computer loudspeaker following the design described in [Sin02] and allows for switching times in the  $\mu\text{s}$  regime. Figure 4.7 shows a picture of the experimental setup including the paths of the different lasers, with the inset showing a close-up view of the main vacuum vessel and the therein residing segmented linear ion trap. As the dimensions of the main vacuum chamber prevent that all of the necessary laser beams pass unobstructed through the chamber, mirrors have been installed on each side of the trap in order to guide the laser beams out again. The imaging of the ions is done through access port A by using a specifically designed lens system in combination with an EMCCD<sup>12</sup> camera from Andor<sup>13</sup>, see chapter 4.4 for further details.

However, as the imaging of the ions is done through the same access port which is also used for guiding the laser beams in and out of the main vacuum chamber, another problem arises. Especially the laser at 397 nm causes lots of stray light when it hits the fused silica window upon leaving the chamber through access port A. The generation of this unintentional stray light can be mainly ascribed to the surface roughness of the glass substrate causing some internal reflections which are also picked up by the imaging optics and therefore cannot be reduced by applying an anti-reflexion coating. The solution to this problem is twofold: First of all, the beam is irradiated into the chamber at a slightly tilted angle with respect to the horizontal plane, lowering the point of impact on the window relative to the optical axis of the imaging optics. This not only reduces the amount of stray light which is collected by the imaging optics, but also allows one to Doppler cool more than one oscillation direction of the ions as the effective k-vector of the irradiated beam features components in all three spatial directions. Secondly, the beam is p-polarized upon entering the chamber and adjusted in such a way that it hits the fused silica window of access port A at Brewster's angle<sup>14</sup>, effectively canceling the internal reflections and reducing the stray light to a minimum. For a wavelength of 397 nm, the refractive index of fused silica equals  $n_{\text{SiO}_2} = 1.47045$ <sup>15</sup>, resulting in a Brewster angle of  $\Theta_{\text{B}} = 55.78^\circ$ .

<sup>12</sup>Electron-Multiplying Charge-Coupled Device

<sup>13</sup>Andor Technology, Belfast, Northern Ireland, <http://www.andor.com>

<sup>14</sup>Also known as the polarization angle, Brewster's angle is an angle of incidence at which p-polarized light is perfectly transmitted through a surface without reflection. The angle  $\Theta_{\text{B}}$  at which this occurs is given by the equation  $\Theta_{\text{B}} = \arctan(n_2/n_1)$ , where  $n_1$  and  $n_2$  denote the refractive indices of the two media.

It is named after the Scottish physicist, Sir David Brewster (1781–1868).

<sup>15</sup>Refractive Index Database, <http://refractiveindex.info>

## Acousto-optical modulators

Acousto-optical modulators (AOMs) are optical components which allow one to diffract laser beams by modulating the refractive index of a crystal using a piezo element. By applying a sinusoidal ac voltage with a typical frequency ranging from 80 up to 160 MHz to the piezo, acoustic waves are generated inducing density modulations in the crystal which in turn cause a modulation of the refractive index. A moving diffraction grating is formed, leading to a diffraction of the incoming laser beam. Due to interference effects, different diffraction orders are formed, with the frequency of the  $n$ th diffraction order being detuned by  $n$  times the piezo drive frequency. In most cases, the 1st diffraction order of the AOM is used as the diffraction efficiency is lessened with each order of diffraction. If an aperture is now placed in such a way that only the 1st order of diffraction can pass through, switching the piezo drive frequency on and off allows one to turn the laser beam on and off. The switching time is thereby given by the velocity of the acoustic waves in the utilized crystal (4.2 km/s) and equals about 55 ns.

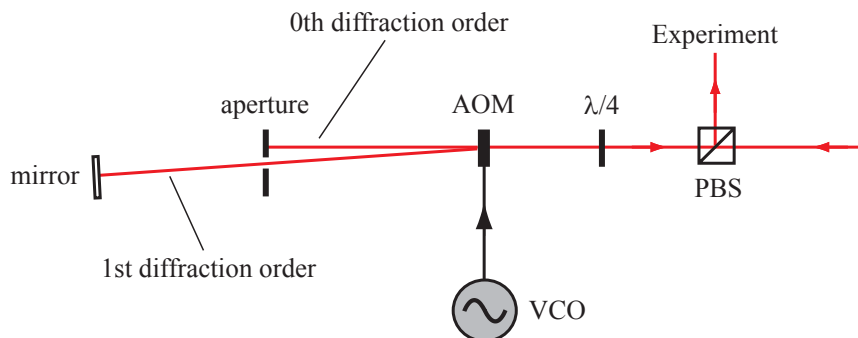


**Figure 4.8:** Schematic drawing of a double pass used for switching and detuning. [Zie08]

Figure 4.8 shows another application of an AOM. The so-called double pass configuration allows for compensating shifts of the laser beam which are induced by a variation of the piezo drive frequency. Here, the laser beam passes the AOM twice, thus leading both times to a diffraction by the same angle but in opposite directions. The outgoing laser beam therefore leaves the AOM in the direction of the incoming beam. In order to separate both beams, a  $\lambda/4$  wave plate in combination with a PBS is used. As the laser beam passes the  $\lambda/4$  wave plate twice, the overall polarization is shifted by  $90^\circ$ , leading to a reflection of the outgoing beam at the PBS. However, due to the double pass configuration the frequency of the outgoing laser beam is now detuned by two times the piezo drive frequency.

## Fabry-Perot reference cavities

As already stated in chapter 4.2.3, most of the utilized laser systems are frequency-stabilized by locking them onto a stable external resonator using the Pound-Drever-Hall stabilization method. In our experiment, this is achieved by using optical Fabry-Perot cavities with an adjustable cavity length. Figure 4.9(a) shows pictures of the ‘low finesse’ cavities showcasing the utilized piezo rings and mirrors as well as the overall assembly.

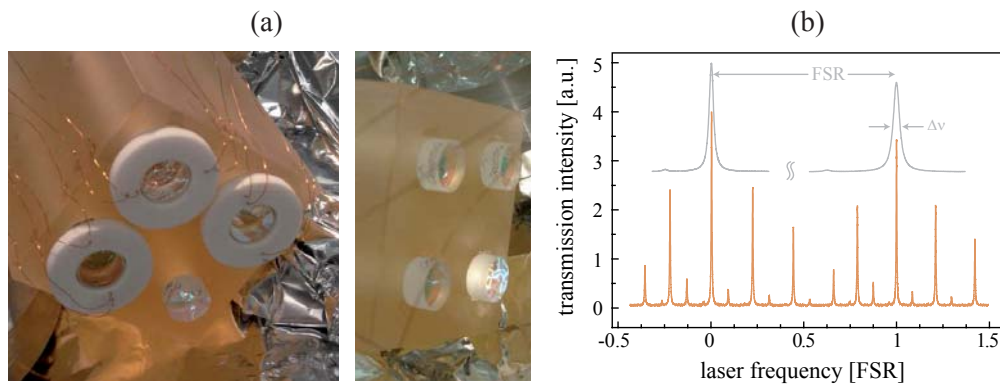


**Figure 4.9:** Assembly and mode spectrum of the ‘low finesse’ cavities. (a) The cavity base material consists of Zerodur which features a very low thermal expansion coefficient. Three of four cavities are adjustable in length using two independent piezo rings. The glued-on mirrors are plane-concave with a curvature of 250 mm on the movable side and plane-plane on the fixed side. A total reflectivity of 99.1% is achieved by an anti-reflexion coating at 397 nm and 866 nm. (b) Because of the cavity design, the transversal modes are separated. The free spectral range (FSR) thereby equals 1.5 GHz for the TEM<sub>00</sub> mode, with a measured finesse of 250. [Sch09b]

The cavity base material with a total length of 100 mm consists of Zerodur which features a very low thermal expansion coefficient. It accommodates a total of four cavities, with three cavities being adjustable in length using two independent piezo rings which are made out of *Pz27* material<sup>16</sup>. The thermal expansion of the cavities is thereby compensated by the special assembly of the piezo rings. The glued-on mirrors are plane-concave with a curvature of 250 mm on the movable side and plane-plane on the fixed side, resulting in a free spectral range (FSR) of 1.5 GHz and a finesse of 250, see also Fig. 4.9(b). A total reflectivity of 99.1% is achieved by an anti-reflexion coating at 397 nm and 866 nm. In order to prevent frequency shifts caused by temperature fluctuations, the cavities are operated under vacuum conditions at a base pressure of  $10^{-6}$  mbar which is held by a 21/s ion getter pump from Varian<sup>4</sup>. An additional acoustic insulation is achieved by embedding the vacuum chamber with the cavities in construction foam.

<sup>16</sup>Ferroperm Piezoceramics, Kvistgård, Denmark, <http://www.ferroperm-piezo.com>

The detuning of the lasers is now realized by a variation of the cavity length using the aforementioned piezo rings. For a coarse static adjustment to the atomic resonance, a high precision voltage supply<sup>17</sup> with a maximum output voltage of 1 kV and a noise level of  $< 10 \text{ mV}_{\text{pp}}$  is used, see also chapter 4.5. The fine adjustments are implemented by a fast multi-channel high voltage amplifier<sup>18</sup> with a maximum output voltage of 150 V at a ripple of  $< 50 \text{ mV}_{\text{pp}}$ .

### Photonic crystal fiber

In contrast to standard single- or multi-mode fibers, photonic crystal fibers use a micro-structured cladding region with air holes in order to guide light in a pure silica core. The utilized *LMA-10-UV* fiber from NKT Photonics<sup>19</sup> is a UV/VIS optimized single-mode large mode area fiber which combines a large effective mode field area ( $\sim 40 \mu\text{m}^2$ ) and low loss to allow high power delivery without nonlinear effects or material damage. It features a core size of  $10 \mu\text{m}$  with a cladding diameter of  $230 \mu\text{m}$  and a coating diameter of  $400 \mu\text{m}$ . Figure 4.10(a) shows the attenuation as a function of the wavelength.

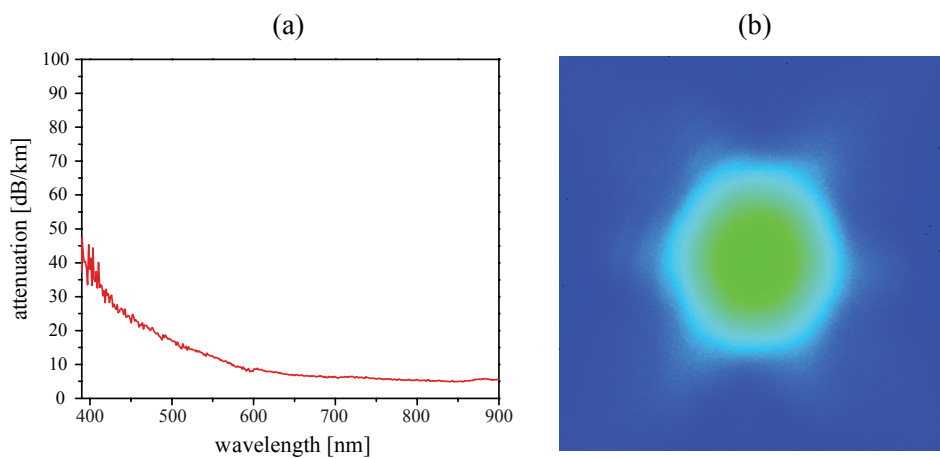


**Figure 4.10:** Characteristics of a photonic crystal fiber (Source: Manufacturer<sup>19</sup>). (a) Attenuation as a function of the wavelength. (b) Picture of the near field intensity profile.

In our experiment, the lasers at the wavelengths 397, 854 and 866 nm are coupled into the photonic crystal fiber in order to guarantee that the different beams are perfectly superimposed upon leaving the fiber, and to easily guide them to the main vacuum chamber (see also Fig. 4.6). Figure 4.10(b) shows a picture of the near field intensity profile of the utilized fiber.

<sup>17</sup> *EHQ-8610p*, iseg Spezialelektronik GmbH, Radeberg, Germany, <http://www.iseg-hv.de>

<sup>18</sup> *miniPiA 103*, TEM Messtechnik GmbH, Hannover, Germany, <http://www.tem-messtechnik.de>

<sup>19</sup> NKT Photonics A/S, Birkerød, Denmark, <http://www.nktphotonics.com>

## Wavelength meter

The measurement of the different wavelengths is done by using a *WS/Ultimate-30* wavelength meter from High Finesse<sup>20</sup> in conjunction with an opto-mechanical switching device (multi-channel switcher) which allows for the measurement of up to 8 different wavelengths almost simultaneously. The different lasers are guided to the multi-channel switcher via single- or multi-mode fibers which then couples the laser light into the wavemeter via an additional fiber. Upon entering the wavelength meter, the laser light gets collimated by a mirror before it enters 6 solid-state Fizeau-based interferometers with varying accuracy. The generated interference pattern is projected by a cylindrical lens onto an array of CCD photo diodes and the recorded pattern is transferred to a computer via a high-speed USB 2.0 connection which allows for data acquisition rates of up to 500 Hz. The software then fits and compares the pattern to a previously recorded calibration data in order to calculate the corresponding wavelength, allowing for measuring wavelengths ranging from 350 nm up to 1120 nm with a relative accuracy of  $3 \times 10^{-8}$ . For a frequency of 350 THz, this corresponds to an absolute accuracy of 10 MHz, which is mainly achieved by a good thermal insulation and an optical setup which does not include any moving mechanical parts. For an exposure time of 1 s, the necessary minimal laser intensity varies from 0.06  $\mu$ W (UV) up to 15  $\mu$ W (IR). In order to guarantee the high accuracy of the utilized wavelength meter, it is necessary to calibrate it on a regular basis using a frequency-stabilized HeNe laser.

## 4.4 Imaging system

The imaging of the ions is done by using a custom-made lens system<sup>21</sup> in combination with an EMCCD camera from Andor<sup>22</sup> which are both mounted on a specifically designed translation stage, allowing one to move the complete imaging system in all three spatial directions. The translation stage consists of different item<sup>23</sup> profiles which are attached to a *PT3/M* XYZ translation stage from Thorlabs<sup>24</sup> using a ball-and-socket joint. The lens system itself comprises 5 fused silica lenses which are covered with an anti-reflexion coating for light at 397 nm and 729 nm, with the spherical aberration of the 6 mm thick fused silica viewport already being included in the numerical optimization. Figure 4.11 shows a schematic drawing of the lens system.

<sup>20</sup>HighFinesse GmbH, Tübingen, Germany, <http://www.highfinesse.com>

<sup>21</sup>The lens system was originally developed by J. Benhelm and F. Schmidt-Kaler and was manufactured by Sill Optics GmbH, Wendelstein, Germany, <http://www.silloptics.de>.

<sup>22</sup>*iXon DV885KCS-VP*, Andor Technology, Belfast, Northern Ireland, <http://www.andor.com>

<sup>23</sup>item Industrietechnik GmbH, Solingen, Germany, <http://www.item.info/de/>

<sup>24</sup>Thorlabs, Newton, NJ, USA, <http://www.thorlabs.com>

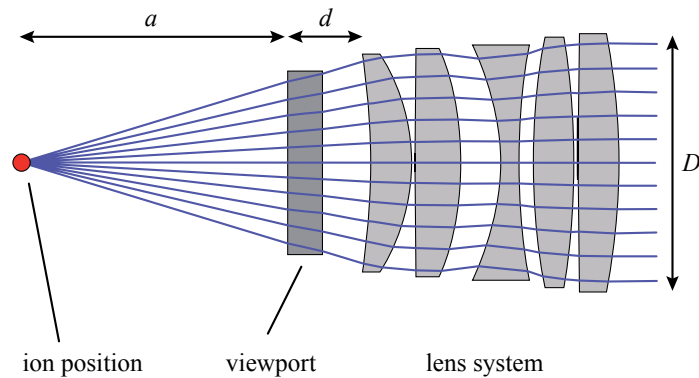


**Figure 4.11:** Schematic drawing of the custom-made lens system<sup>21</sup> used for ion imaging. It is placed at a distance of  $d = 30$  mm from the viewport with a remaining distance of  $a = 35$  mm on the vacuum side. The diameter  $D$  of the lens aperture equals 38 mm. The blue lines depict an exemplary optical path through the lens system. [Sch09b]

The focal length equals  $f = 66.8$  mm with a distance of  $g = 45.1$  mm from the object to the principal plane of the lens system, resulting in an image distance of  $b = 1436.5$  mm. With an f-number of 1.76 the numerical aperture amounts to 0.27, limiting the optical resolution for a wavelength of 397 nm according to the Rayleigh criterion<sup>25</sup> to  $0.85 \mu\text{m}$ . The depth of field has been calculated to be  $18.5 \mu\text{m}$ , see also [Mai06] for a detailed description.

As one can imagine, the lens system is the most critical optical component of the imaging system as the readout time is dominated by the collection efficiency of the custom-made lens. The photon collection efficiency is thereby determined by the solid angle  $\Delta\Omega$  of the utilized lens system. At a working distance of  $a + d$  and with an entrance diameter  $D$  (see also Fig. 4.11), the solid angle  $\Delta\Omega$  is given by [Mai06]

$$\frac{\Delta\Omega}{4\pi} = \frac{1}{2} \left( 1 - \sqrt{1 - \frac{1}{1 + (2(a+d)/D)^2}} \right). \quad (4.2)$$

With a total working distance of  $a + d = 65$  mm and a diameter of  $D = 38$  mm, the detected signal therefore is reduced by a factor of

$$\frac{\Delta\Omega}{4\pi} \approx 0.02 = \frac{1}{50}. \quad (4.3)$$

The utilized EMCCD camera features a CCD chip from Texas Instruments<sup>26</sup> with a total number of  $1004 \times 1002$  pixels and a pixel size of  $8 \times 8 \mu\text{m}$ , resulting in an effective chip

<sup>25</sup> The Rayleigh criterion states that the images of two different points are regarded as just resolved when the principal diffraction maximum of one image coincides with the first minimum of the other. For an ideal lens of focal length  $f$  and light with the wavelength  $\lambda$ , the Rayleigh criterion yields a minimum spatial resolution  $\Delta l = 1.220(f\lambda/D)$ , with  $D$  being the diameter of the lens' aperture. It is named after the English physicist John William Strutt, 3rd Baron Rayleigh (1842-1919).

<sup>26</sup> *Tx285SPD*, Texas Instruments, Dallas, TX, USA, <http://www.ti.com>

size of  $8 \times 8$  mm. The quantum efficiency at a wavelength of 397 nm equals 40 % with a maximum readout rate of 35 MHz. Using a Peltier element, the CCD chip can be cooled down to a temperature of  $-70$  °C, effectively reducing the dark current to 0.028 electrons per pixel and second. In order to reduce the number of detected photons which are generated by the infrared and photoionization lasers, a Chroma *D405/30m*<sup>27</sup> bandpass filter has been placed in front of the EMCCD camera featuring a total transmission of 52.9 % at a wavelength of 397 nm, with all other wavelengths being nearly completely suppressed<sup>28</sup>.

The overall detection efficiency  $\eta$  at a wavelength of 397 nm can now be calculated by using the solid angle  $\Delta\Omega/4\pi$  of the lens system given by equation (4.3), the corresponding lens and filter transmissions as well as the quantum efficiency of the EMCCD camera. For a measured lens transmission of 96 %, this leads to a total efficiency of  $\eta = 0.004$ . As one can see, several hundreds of photons are required to trigger a single event. However, this is still sufficient as the scattering rate on the  $S_{1/2} \leftrightarrow P_{1/2}$  optical dipole transition used for Doppler cooling and fluorescence detection equals about  $10^8$  photons per second, see also chapter 3.3.1.

## 4.5 Trap voltage supplies

In order to operate the segmented rail trap, three different types of voltage supplies are needed: A stable radio frequency voltage supply at a fixed frequency of several MHz and an amplitude of  $400 V_{pp}$ , a programmable multi-channel voltage supply with a range of  $-10$  V to  $10$  V for the micromotion compensation and the deflection electrodes, and a stable high voltage supply for the trap electrodes, the extraction setup, the ion optics and the electron multiplier tube used for ion detection.

### Single-channel rf voltage

The rf voltage is generated by a Marconi *2019* signal generator<sup>29</sup> followed by a Mini-Circuits *ZHL-5W-1* amplifier<sup>30</sup> with a fixed gain of 40 dB which is used for preamplification. The final amplification step is achieved by using a helical resonator [Mac59] which is directly connected to the rf vacuum feedthrough. A power meter<sup>31</sup> between the pream-

<sup>27</sup>Chroma Technology Corp., Rockingham, VT, USA, <http://www.chroma.com>

<sup>28</sup>Complete list of transmissions: 374 nm: 0.02 %, 397 nm: 52.9 %, 423 nm: 2.0 %, 854/866 nm: 0 %

<sup>29</sup>Marconi Instruments Ltd., London, United Kingdom

<sup>30</sup>Mini-Circuits, New York, NY, USA, <http://www.mini-circuits.com>

<sup>31</sup>*CN101L* SWR & Power Meter, Daiwa

plifier and the helical resonator allows one to monitor the power in forward and reverse direction in order to optimize the coupling into the resonator. Figure 4.12 shows the typical layout of a helical resonator.

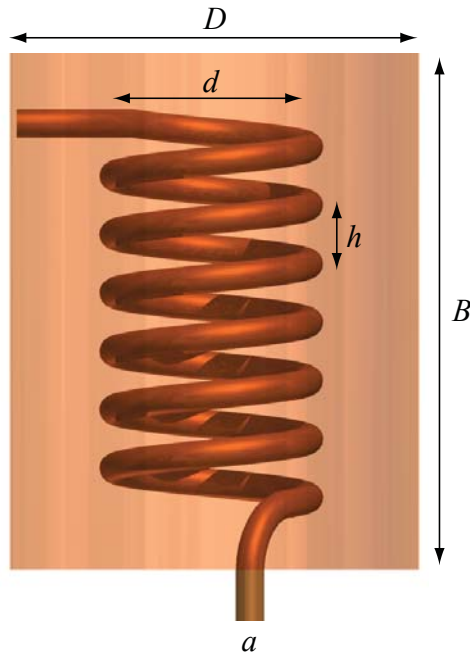


**Figure 4.12:** Layout of a helical resonator. A helix with diameter  $d$  and  $N$  turns with pitch  $h$  is placed inside of a copper tube with diameter  $D$  and length  $B$ . The helix is made out of copper wire with thickness  $a$ . [Deu07]

A helix with diameter  $d$  and  $N$  turns with pitch  $h$  is placed inside of a copper tube with diameter  $D$  and length  $B$ . The helix is made out of copper wire with thickness  $a$ . The length of the copper solenoid thereby equals approximately a quarter-wave of the input frequency, with the upper end being grounded to the copper tube while the lower end is directly connected to the rf feedthrough of the main vacuum chamber, see also chapter 4.1. A movable clip contact on the first turn of the helix allows for adjusting the coupling into the resonator.

According to [Zve61], the resonator can be characterized by the unloaded resonance frequency  $f_0$  and the quality factor  $Q_0$ . As the electrical energy is stored in the helix, the quality factor  $Q_0$  is limited due to energy dissipation in the resonator which is caused by losses in the conductor, the windings, the outer copper shielding as well as dielectric losses. Upon connecting the helical resonator to the vacuum chamber, the total inductivity  $L_{\text{load}}$  and capacitance  $C_{\text{load}}$  of the vacuum feedthrough, the copper wires and the trap electrodes act as a load for the resonator, effectively reducing the resonance frequency to  $f < f_0$ .

The final frequency  $f$  of the helical resonator is then given by [Gul03]

$$\frac{1}{f} = \frac{1}{f_0} + \frac{1}{f_{\text{load}}}. \quad (4.4)$$

Dependent on the dimensions, one can now calculate the unloaded resonance frequency  $f_0$  and the quality factor  $Q_0$  of the helical resonator. As per [Mac59], it is recommended that the diameter  $D$  of the copper tube is about twice as large as the helix diameter  $d$ :

$$\frac{d}{D} = 0.55 \quad (4.5)$$

The unloaded resonance frequency  $f_0$  is now determined by the total number of turns  $N$ :

$$f_0 = \left( \frac{48260}{ND} \right) \text{MHz mm}. \quad (4.6)$$

In order to achieve a high quality factor  $Q_0$  in the region of a few hundred, the minimum number of turns  $N$  should be larger than 5, with the helical pitch  $h$  being approximately twice as large as the wire thickness  $a$ :

$$\frac{a}{h} \approx 0.5 \quad (4.7)$$

As mechanical vibrations of the helix lead to a jitter of the resonance frequency and therefore to fluctuations of the rf amplitude, another prerequisite is a high mechanical stability of the chosen resonator design.

In our experiment, a helical resonator with a total number of  $N = 15$  turns and a helix diameter  $d = 55$  mm is used. The pitch equals  $h = 6$  mm with a wire thickness of  $a = 3$  mm. The utilized copper tube has a diameter of  $D = 100$  mm and a length of  $B = 200$  mm. It is characterized by an unloaded resonance frequency  $f_0 = 16$  MHz which is reduced to  $f = 12.155$  MHz upon connecting the resonator to the trap. Under typical operating conditions, the rf electrodes are supplied with a voltage of  $U_{\text{rf}} = 400$  V<sub>pp</sub>.

### Multi-channel dc voltages

The multi-channel dc voltage sources are experimentally realized by *TI8814* digital-to-analog converters<sup>32</sup> from Texas Instruments<sup>33</sup>, each providing a total of 4 independent channels featuring a voltage range from -10 V to 10 V with a resolution of 16-bit. The serial SPI-compatible programming interface allows update rates of up to 2.5 MSPS per channel at clock frequencies of 50 MHz. A self-developed printed circuit board<sup>34</sup> provides

<sup>32</sup>DAC, Digital-to-Analog Converter

<sup>33</sup>Texas Instruments, Dallas, TX, USA, <http://www.ti.com>

<sup>34</sup>The printed circuit board carries a total of 8 DACs and was developed by K. Singer and M. Bürzele.

32 output voltages which are individually connected via BNC cables to the corresponding trap electrodes using a 20-pin vacuum feedthrough, see also chapter 4.1. The  $\pm 12$  V supply voltage for the DACs is generated by two standard car batteries providing a stable and low noise voltage supply circumventing ac line noise. The DACs are interfaced with a personal computer by using the parallel port which is galvanically insulated via optocouplers in order to avoid any pickup of arbitrary noise.

In case of our segmented linear rail trap, the DACs are utilized to supply voltage to the deflection electrodes as well as to the electrodes which are used for the compensation of the micromotion. The detuning of the different lasers is achieved by using the DACs in combination with a high voltage amplifier<sup>18</sup>.

### High voltage supply

The necessary high voltages are generated by two high precision voltage supplies from iseg<sup>35</sup>. The *EHQ-8610p* supply module features a total of 8 output channels with a maximum output voltage of 1 kV and a noise level of  $< 10$  mV<sub>pp</sub>. As already stated in chapter 4.3, it is used for the coarse adjustment of the laser detuning. The *EHQ-8210p* supply module is identical to the *EHQ-8610p* version but features a slightly lower ripple and noise of  $< 5$  mV<sub>pp</sub>. Due to the lower noise level, this module is used for the extraction setup, the ion optics as well as for the trap electrodes which are used to generate the axial confinement of the segmented linear rail trap. A *Harrison 6516A* dc power supply from HP<sup>36</sup> with a maximal output voltage of  $\pm 3$  kV and a ripple and noise of 5 mV<sub>pp</sub> is used to supply the electron multiplier tube used for ion detection.

## 4.6 Dynamic experimental control

The control of the experimental setup is mainly done using a special software library called MCP (**M**aster **C**ontrol **P**rogram<sup>37</sup>), which was developed in our group<sup>38</sup>. Featuring a modular setup, the software is highly customizable, not only allowing for implementing new features and devices but also for changing the GUI<sup>39</sup> according to the needs at hand.

<sup>35</sup> iseg Spezialelektronik GmbH, Radeberg, Germany, <http://www.iseg-hv.de>

<sup>36</sup> Hewlett-Packard, Palo Alto, CA, USA, <http://www.hp.com>

<sup>37</sup> Note that the name match with the main villain of the 1982 Disney movie 'Tron' is purely coincidental.

At least, that is what we are being told...

<sup>38</sup> Programmers: R. Maiwald (MPI für die Physik des Lichts, Erlangen), F. Ziesel, G. Huber and K. Singer (Institut für Quanteninformationsverarbeitung, Universität Ulm)

<sup>39</sup> **G**eneral **U**ser **I**nterface

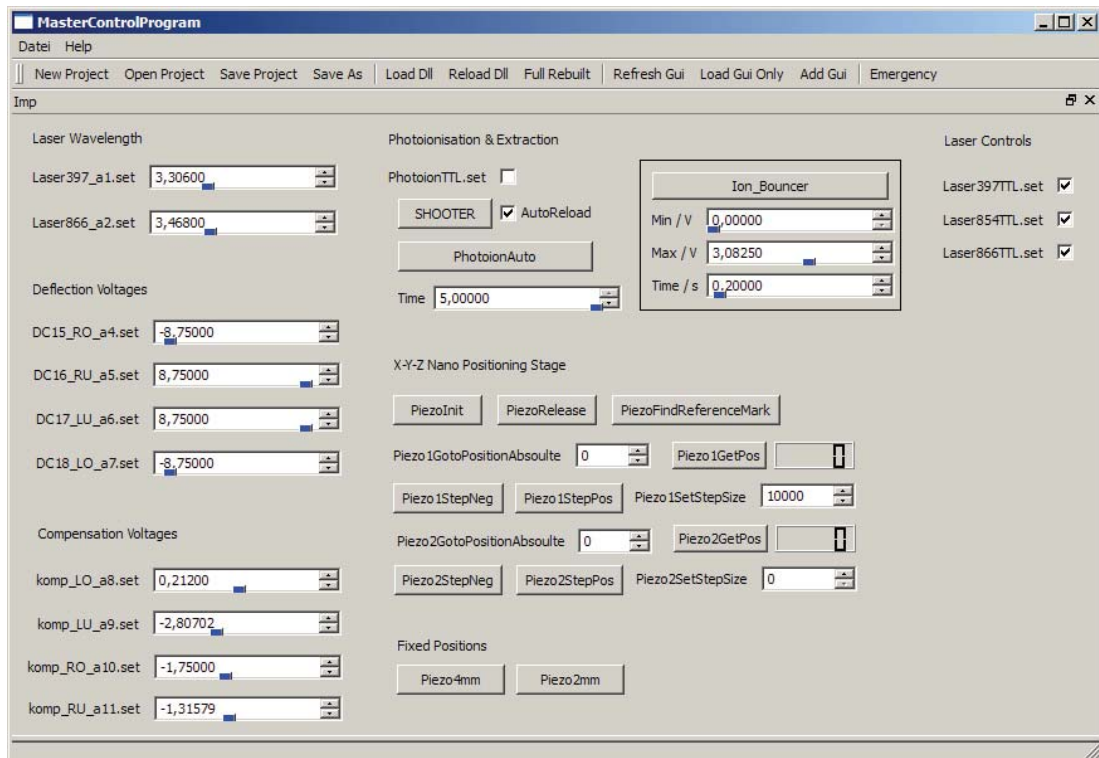


**Figure 4.13:** GUI of the experimental control software MCP.

As already stated in chapter 4.5, the software is used to control the digital-to-analog converters which generate the voltages for the laser detuning, the deflection electrodes as well as for the micromotion compensation. The switching of the different lasers is done by supplying TTL signals to the corresponding AOMs or conventional shutters (see chapter 4.3), which are either generated by the computer or a PCI card from National Instruments<sup>40</sup>. Using a TTL signal, it is also possible to trigger the extraction process (see chapter 6.1.1). Furthermore, the software allows for controlling the utilized EMCCD camera<sup>22</sup> as well as the nano positioning stage, see also chapter 7.2.6. Figure 4.13 shows a picture of the GUI of the experimental control software.

<sup>40</sup> NI PCI-6035E, National Instruments, Austin, TX, USA, <http://www.ni.com>

# Chapter 5

## Ion trap

In chapter 3.1, it was shown that a linear Paul trap is a versatile tool to spatially trap charged particles without contact to the environment. However, in order to manipulate trapped ions more efficiently, i.e. to transport strings of ions or to split ion crystals, more complex trap designs are required than the one depicted in Fig. 3.1. Especially for the usage as deterministic ion source, numerous changes have to be made to the fundamental layout of the dc and rf electrodes. After an in-depth description of the design and fabrication process (5.1), the operating conditions of the specifically designed rail trap will be illustrated in detail (5.2).

### 5.1 Segmented linear rail trap

As we utilize our ion trap as deterministic single-ion source, one of the main challenges in the development process was to come up with a design which not only allowed for trapping and manipulating different species of ions, but which at the same time permitted to extract single ions or larger ion crystals in a controlled way. In addition, the ions need to arrange in a linear crystal such that they can be counted and that the ion species can be identified using laser induced fluorescence. On the basis of these prerequisites, the design process was initiated, resulting in the trap design described in the following chapter.

#### 5.1.1 Trap design

The trap consists of four copper plated polyimide blades which are arranged in an x-shaped manner. A technical drawing of one of these blades is shown in Fig. 5.1. It features a total

of 15 independent dc electrodes which can be assigned to three different trap sections: A wide loading zone (electrodes 1-4) is connected via a taper (electrode 5) to a narrow experimental zone (electrodes 6-14). A deflection electrode (electrode 15) is used to alter the trajectories of ions which are extracted out of the trap. In order to generate the radial confinement an additional electrode is running along the inner front face of each blade which will be referred to as rail in the following. The blade itself has a total length of 65 mm and a thickness of 410  $\mu\text{m}$ . Electrodes 2-5 as well as electrode 14 have a width of 2.8 mm, electrodes 6-13 have a width of 0.7 mm, respectively. In order to efficiently deflect ions by targeted applying of low voltages, the deflection electrode has been elongated in extraction direction featuring a total length of 20.6 mm. The distance between the rf rail and the dc electrodes as well as between adjacent dc electrodes equals 0.1 mm.

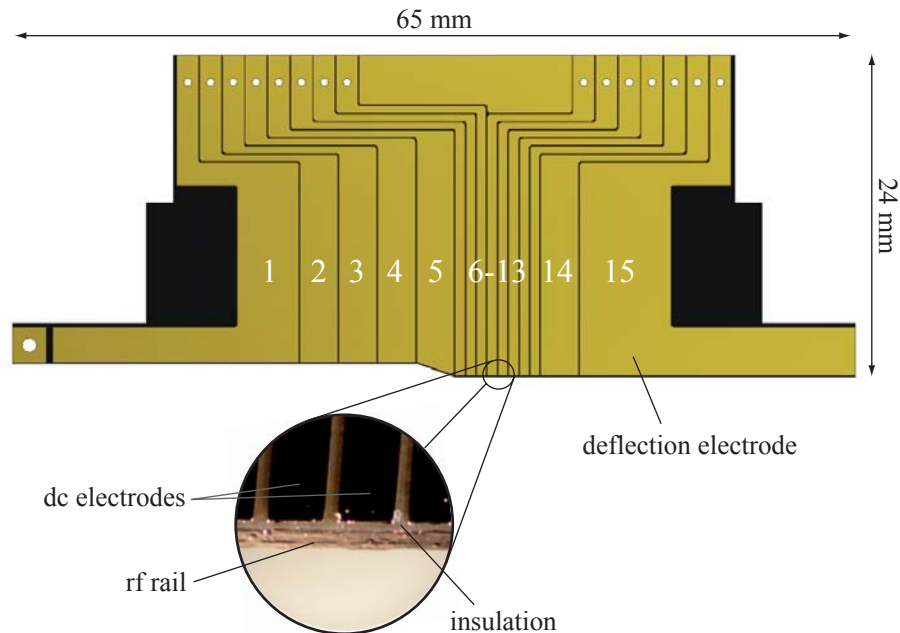


**Figure 5.1:** Technical drawing of one of the four trap blades featuring a total of 15 independent dc electrodes. A wide loading zone (electrodes 1-4) is connected via a taper (electrode 5) to a narrow experimental zone (electrodes 6-14). The rf rail has a thickness of about 22  $\mu\text{m}$  and covers the whole front of the blade. Insulated parts are colored black. The close-up view shows a microscope image of the front part of the blade. [Sch10]

Figure 5.2(a) shows a sketch of the assembled rail trap. The distance between the inner front faces of opposing blades equals 4 mm in the loading zone and 2 mm in the experimental zone, respectively. In case of a standard Paul trap (as described in chapter 3.1), the rf voltage is supplied to two of the four blades. The other two blades are used for the

axial confinement and are therefore divided into several electrodes. However, in case of our rail trap, all four blades are identical. Apart from the deflection electrodes, corresponding electrodes on all four blades (e.g. electrode 1 of each of the blades) are electrically connected, resulting in a stronger and more symmetrical axial confinement than in the standard case.

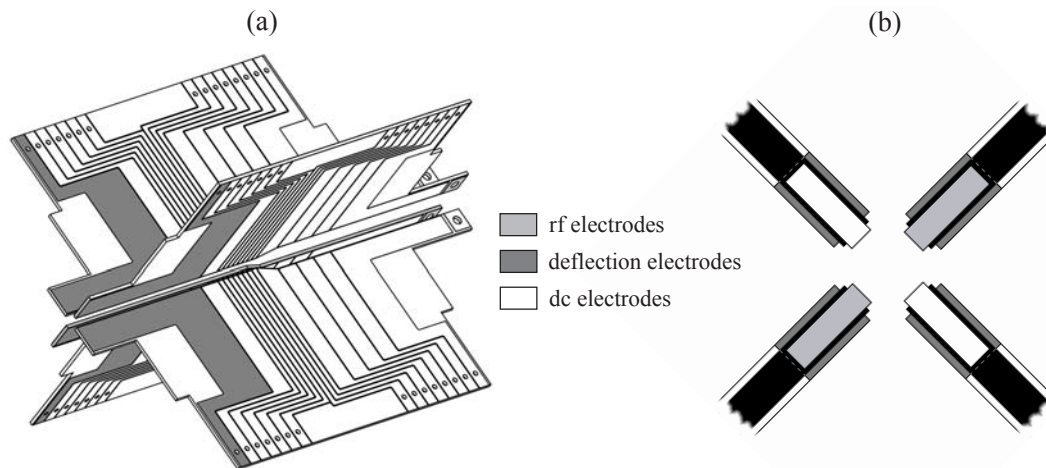


**Figure 5.2:** Sketch of the segmented linear rail trap with dc electrodes depicted in white and rf electrodes depicted in light gray, respectively. Deflection electrodes (dark gray) are used to alter the trajectories of ions which are extracted out of the trap. Insulated parts are colored black. (a) Perspective view. (b) Front view showing that rf and rf-ground electrodes (generating the radial confinement) are only covering the two  $410\ \mu\text{m}$  wide front faces of the blades and are continuing round the corner at the end of the blades. [Fic09a]

The rf voltage is only applied to the rails of two opposing blades; the front faces of the other blades are grounded, generating the quadrupole potential for the radial confinement. As these rails are running along the whole trap axis and are continuing round the corner at the end of each blade, the radial confinement is sustained during the whole extraction process and a targeted shooting is facilitated, see Fig. 5.2(b). The contacting of the electrodes is done by using a UHV compatible silver lead<sup>1</sup> in combination with silver and capton-insulated wires with a thickness of 0.5 mm and 0.55 mm, respectively.

Apart from the blade design described above, additional designs were created which are either already used in other experiments [Deu07, Eblxx] or will be put into operation in the near future. A selection of these designs can be seen in Fig. 5.3.

<sup>1</sup> *Stay-Brite, 505 Neutral Flux*, Harris, Mason, OH, USA, <http://www.harrisproductsgroup.com>

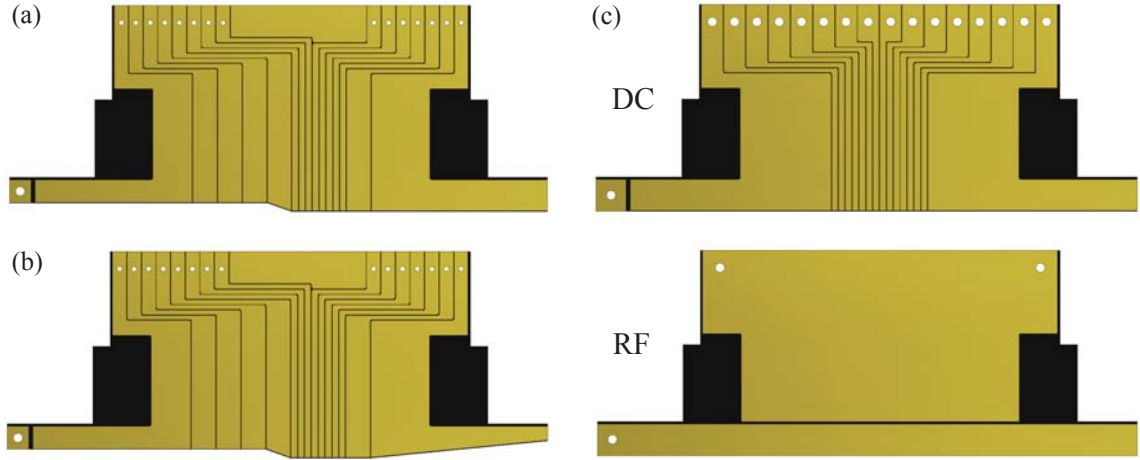


**Figure 5.3:** Technical drawings of different blade designs. (a) Standard blade design as shown in Fig. 5.1 consisting of a wide loading zone and a narrow experimental zone with an rf rail at the front of the blade. (b) Same blade design as shown in (a) but with a reamed up rf rail, leading to a smaller rf field gradient at the end of the trap. (c) DC version: Same blade as shown in (a) but without loading zone and taper. It features a total of 16 different electrodes with a main electrode width of 0.7 mm. RF version: Blade featuring an rf rail which not only covers the front but also part of the surface of the blade. An additional single large dc electrode can be utilized as compensation electrode. By combining both versions one can build a more conventional trap as described in chapter 3.1 consisting of two dc and two rf blades.

## Trap potentials

Under typical operating conditions, the rf electrodes are supplied with a voltage of  $U_{\text{rf}} = 400 \text{ V}_{\text{pp}}$  at the frequency  $\Omega = 2\pi \times 12.155 \text{ MHz}$ , leading to a radial pseudopotential with a depth of  $0.66 \text{ eV}$  and a radial secular frequency  $\omega_{\text{rad}} = 2\pi \times 476 \text{ kHz}$ . Using equation (3.7), this yields a q-parameter of 0.11 and a geometric factor  $\alpha' = 0.66$ . Figure 5.4 shows a simulation of the radial pseudopotential at the center of electrode 10.

In order to simulate the axial trapping potential, each individual dc electrode is supplied with a voltage of  $1 \text{ V}$  whereas all remaining electrodes are grounded, for example  $\{U_1, U_2, U_3, \dots, U_{15}\} = \{0, 1, 0, \dots, 0\} \text{ V}$ . The final trapping potential is then generated by a superposition of all these potentials. Figure 5.5 shows the corresponding potentials for all the dc electrodes.

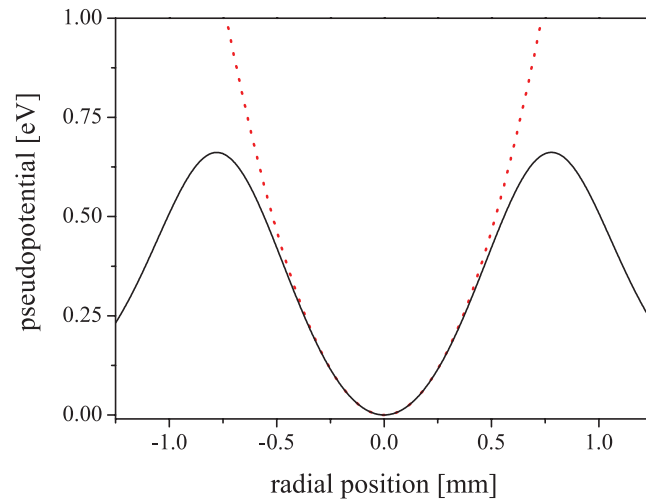


**Figure 5.4:** Simulated radial pseudopotential at the center of electrode 10 for an rf frequency of  $2\pi \times 12.155$  MHz and a voltage of  $400$  V<sub>pp</sub>. The depth of the pseudopotential equals  $0.66$  eV with a radial secular frequency  $\omega_{\text{rad}} = 2\pi \times 476$  kHz.

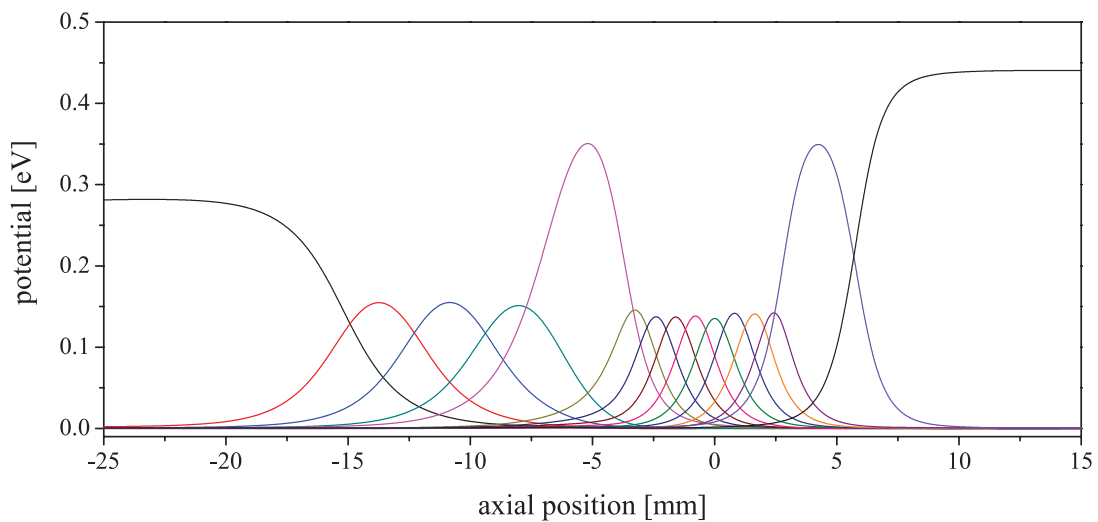


**Figure 5.5:** Simulated axial potentials. The different graphs illustrate the axial potentials along the trap axis generated by a voltage of  $1$  V for each of the 15 electrodes. The center of electrode 10 is used as point of reference for the axial position.

By supplying the dc-electrode trap segments 7 and 13 with a voltage of  $35$  V and the remaining electrodes with  $0$  V, an axial trapping potential with a trap depth of about  $4$  eV and an axial trapping frequency  $\omega_{\text{ax}} = 2\pi \times 295$  kHz is generated, see also Fig. 5.6.

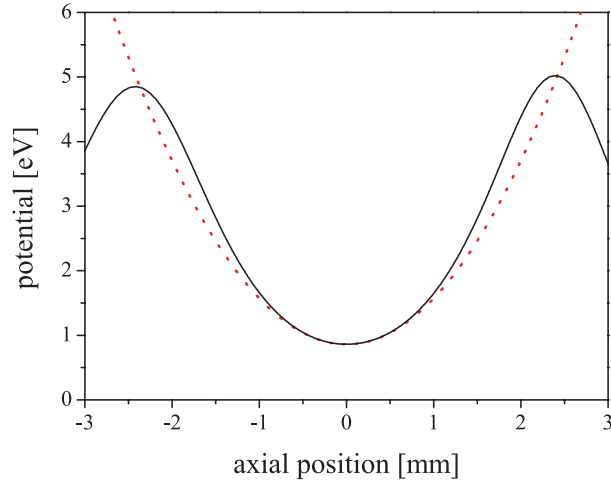


**Figure 5.6:** Simulated axial trapping potential. The potential is generated by supplying dc electrodes 7 and 13 with a voltage of 35 V and all remaining electrodes with 0 V, resulting in an axial trapping frequency  $\omega_{\text{ax}} = 2\pi \times 295$  kHz and a trap depth of about 4 eV. The center of electrode 10 is again the point of reference for the axial position.

### 5.1.2 Fabrication of the printed circuit board ion trap

One of the main goals in the development process was to find a manufacturing technique which not only was well established but also allowed one to produce new types of traps in short periods of time. Simultaneously, the processable materials needed to fulfill certain prerequisites such as being mechanically stable and UHV compatible. Using printed circuit board (PCB) technology not only offers a cheap and mainstream manufacturing technique, but also allows for rapid prototyping, representing the perfect choice for the needs at hand.

The starting point of the PCB blades is a printed circuit board consisting of polyimide with a thickness of 410  $\mu\text{m}$  which is plated with 18  $\mu\text{m}$  of copper on both sides<sup>2</sup>. After structuring the silhouette of the circuit board, the inner front face of each blade was also plated with copper, building the foundation for the rf rails. The featured strip lines were produced using standard lithography and etching techniques<sup>3</sup>. Some of the properties of the polyimide bulk material are listed in table 5.1.

The trap holder is manufactured from stainless steel and consists of two end caps which are connected by four rods with a diameter of 5 mm. Each end cap features various indentations and stoppers, allowing one to accurately place the blades with respect to each other.

<sup>2</sup> P96, Isola AG, Duren, Germany, <http://www.isola.de>

<sup>3</sup> micro pcb AG, Thundorf, Switzerland, <http://www.micro-pcb.ch/>

Property	P96 value
$T_g$	260 °C
Volume Resistivity	$1.5 \times 10^9$ M $\Omega$ /cm
Surface Resistivity	$3.0 \times 10^6$ M $\Omega$
Electric Strength	$5.6 \times 10^4$ V/mm

**Table 5.1:** Some properties of the polyimide bulk material (P96). Listed are the glass transition temperature  $T_g$ , the volume and surface resistivity as well as the electric strength.

The fastening of the blades is done by utilizing copper blocks which are pressed on the insulated surfaces on both ends of each blade (see also Fig. 5.1) and clamp the blades to the corresponding end cap. Figure 5.7 shows an image of the assembled trap holder with four unpolished blades for test fitting purposes. As can be seen, each end cap features three indentations at the front which are used to fasten the trap holder to the main vacuum chamber (threaded hole in the middle) and to align the trap axis by tilting the holder in horizontal and vertical direction (indentations at the top and bottom). In order to reduce the influence of the end caps on the ion during the extraction process, the blades stick out of the trap holder, effectively shielding the ion from the ground potential of the end cap.

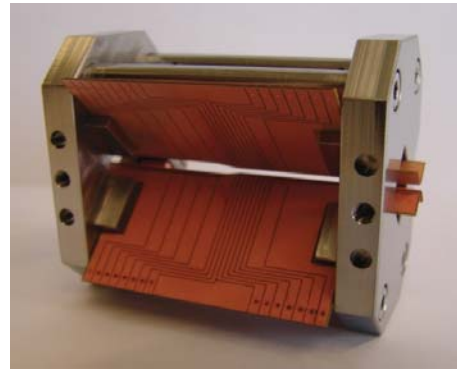


**Figure 5.7:** Picture of the trap holder with four unpolished blades for test fitting purposes.

## 5.2 Operation of the trap

By utilizing the segmented linear rail trap described in chapter 5.1, a variety of different ionized particles can be trapped. In principle, the only restrictions are the technical feasibility of a proper oven in order to generate an atom beam of the desired species as well as the availability of appropriate laser systems which not only allow one to ionize the neutral atoms but also to drive optical transitions for cooling and imaging purposes. As stated in chapter 3.2, we are using  $^{40}\text{Ca}^+$  ions in our experiment as these have already proven of value in quantum information experiments in ion traps [Hub08, Sch08, Pos09].

After a brief description of the employed photoionization scheme and the low current oven, which is used for the generation of the neutral atom beam, possible micromotion compensation methods will be presented.

### 5.2.1 Photoionization schemes for ion generation

In our group, the ionization of the particles is done by utilizing a multi-stage photoionization process called REMPI (**R**esonant **E**nhanced **M**ulti-**P**hoton **I**onization). Bound electrons are resonantly excited to higher states in multiple steps before they are finally excited into the continuum. By driving resonant transitions, the technique allows one to even ionize specific isotopes while at the same time the generation of multiply charged ions or impurity ions is circumvented, making it highly efficient and selective.

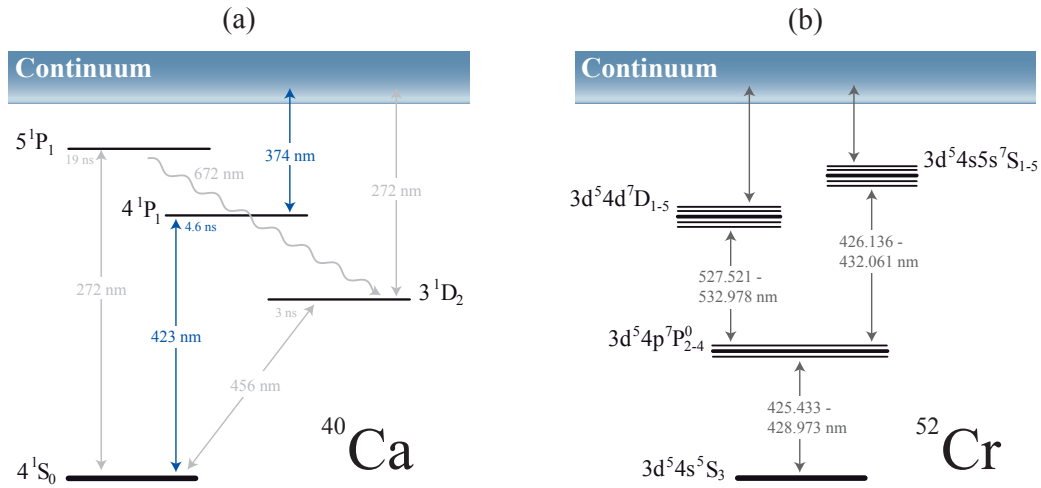


**Figure 5.8:** (a) Transitions in neutral  $^{40}\text{Ca}$  and lifetimes of the different states [Ebl06]. The colored transitions at the wavelengths 423 nm and 374 nm are used for photoionization. (b) Options for the multi-photon ionization of  $^{52}\text{Cr}$  [Paq98].

In case of  $^{40}\text{Ca}$ , two different two-photon ionization schemes are possible which are called 1+1-REMPI, see Fig. 5.8(a). By utilizing a laser with a wavelength of 274 nm, the electron is initially excited from the ground state  $4^1\text{S}_0$  to the excited state  $5^1\text{P}_1$  from where it decays into the  $3^1\text{D}_2$  state by spontaneous emission of a photon at the wavelength 672 nm. In a second step, it is excited by the same laser into the continuum [Kja00]. Although only one laser is needed for the realization of this scheme, it is not favorable as the required laser is expensive and difficult to handle due to the low wavelength. Due to this reason, the second scheme is employed in our experiment which is depicted in blue in Fig. 5.8(a).

In the first step, a laser with a wavelength of 423 nm resonantly excites the electron from the ground state  $4^1S_0$  into the excited state  $4^1P_1$ . From there, a second laser at 374 nm excites the electron into the continuum. Similar ionization schemes are also conceivable for other elements: Figure 5.8(b) depicts the energy levels of neutral  $^{52}\text{Cr}$  together with the wavelengths which can be used for multi-photon ionization.

Apart from photoionization, there is also the possibility to ionize neutral particles by the use of electron bombardment. However, if isotopic pure samples are needed, this method can cause problems, since the energetic electrons can ionize atoms from the residual gas in the vacuum chamber as well as unwanted isotopes in the atomic beam. Moreover, several charge states can often be formed. In addition, the creation of unintentional electric patch charges on the insulated surfaces of the trap due to the utilized electron beam is way more likely than in the case of stray light caused by the photoionization lasers [Kja00].

### Low current oven

In order to generate the calcium ions which are needed for the experiments, metallic calcium is vaporized by utilizing a custom-built calcium oven. The resulting neutral atom beam is collimated by the shape of the oven tube which is aimed at the trap center. Figure 5.9 shows the layouts of two different calcium ovens. Originally developed by D. Rotter [Rot03], the design depicted in Fig. 5.9(a) [Deu07] consists of a stainless steel tube with a length of 53 mm and a diameter of 3 mm with a wall thickness of  $1.15\text{ mm}^4$ . The electric contacting and mechanical mounting is implemented by stainless steel rods with a diameter of 2.5 mm. Whereas the first rod extends into the rear part of the oven tube for mechanical stability, the second rod and the middle part of the oven tube are connected via a tantalum foil with a thickness of 0.05 mm. In order to achieve a good electric contacting between the different components all parts were connected using spot-welding. The heating is achieved by exploiting the high electric resistivity of the thin-walled oven tube. As the tantalum foil not only serves as electric contact but also for heat dissipation, the oven tube only heats up between the tantalum foil and the stainless steel rod at the rear end of the oven tube. Under typical operating conditions, the oven is supplied with a current between 3 and 6 A. However, due to space restrictions the implementation of the design described above was not possible as a current as high as 13 A would have been necessary in order to vaporize the calcium due to the downsized dimensions of the oven. As the used vacuum feedthrough cannot sustain such high currents, a new design was developed which is shown in Fig. 5.9(b).

<sup>4</sup> R. Helwig GmbH, Berlin, Germany, <http://www.hero-berlin.de>

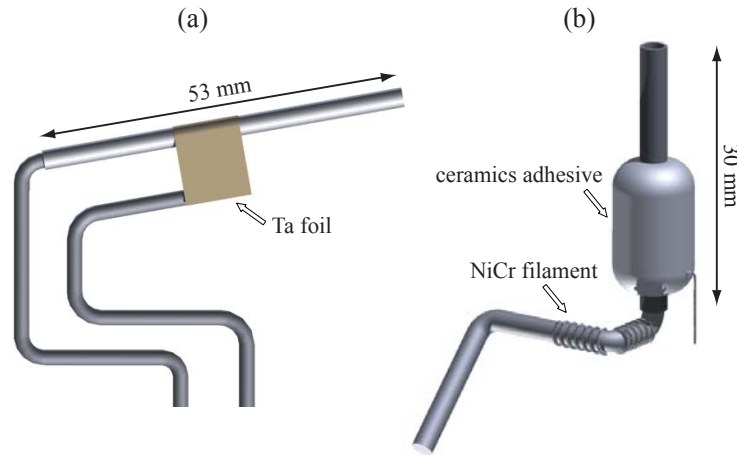


**Figure 5.9:** Layouts of two different calcium ovens. (a) Design as originally developed by D. Rotter [Rot03]: A stainless steel tube is filled up to the end of the tantalum foil with metallic calcium granules. Two stainless steel rods are used as conductors and as mechanical support for the oven tube. Under typical operation conditions, the oven is supplied with a current between 3 and 6 A [Deu07]. (b) Low current oven: A NiCr filament is used in conjunction with a ceramics adhesive to heat up a stainless steel tube which is filled with metallic calcium granules. The bent stainless steel rod is again used as conductor and mechanical support. In contrast to the oven design shown in (a), a maximum current of 0.37 A is used to generate a neutral calcium beam.

The oven consists of a stainless steel tube with a length of 30 mm and a diameter of 3 mm with a wall thickness of 1.15 mm. Again, the rear end of the oven tube is connected with a stainless steel rod with a diameter of 2.5 mm which is used as conductor and mechanical support. In contrast to the oven design shown in Fig. 5.9(a), the heating of the oven tube is achieved by using a NiCr filament<sup>5</sup> with a diameter of 0.2 mm and a resistance of  $34.46 \Omega/\text{m}$  in conjunction with a ceramics adhesive<sup>6</sup>. After initially coating the surface of the oven tube with a thin layer of the ceramics adhesive, the NiCr filament is coiled onto the tube with alternating coil directions in order to avoid the generation of unintentional magnetic fields. Adjacent layers of wound up filament are electrically insulated by a layer of the ceramics adhesive. The oven itself is filled with metallic calcium granules<sup>7</sup> with a purity of 99.5% and a grain size of maximal 1.2 mm (*16 mesh*). By applying a current of maximal 0.37 A, the oven is heated with a thermal output of about 3 W.

<sup>5</sup> *Cronix 80E*, Krupp VDM GmbH, Werdohl, Germany, <http://www.thyssenkruppvdm.de>

<sup>6</sup> *Ultra-Temp 516*, Kager GmbH, Dietzenbach, Germany, <http://www.kager.de>

<sup>7</sup> Alfa Aesar GmbH & Co KG, Karlsruhe, Germany, <http://www.alfa-chemcat.com>

### 5.2.2 Micromotion compensation methods

A compensation of the micromotion is not only necessary for an efficient cooling, but it is also a prerequisite in order to successfully extract ions out of the trap. Only when being compensated, the extraction position of the ions is well defined, allowing for generating a single-ion beam with a small velocity fluctuation and spatial divergence, see also chapter 7. The amplitude of the micromotion, which is caused by the radio frequency and oscillates at the trap drive frequency  $\Omega/2\pi$ , is thereby directly proportional to the displacement out of the minimum of the radial pseudopotential, with small displacements already leading to an oscillation of the ions, see also Fig. 5.10(a). In the experiment, the ions are mostly not located in the rf minimum, which is mainly due to asymmetries of the ion trap itself and patch electric charges on the insulated surfaces between the electrodes. Therefore, in order to reduce the induced micromotion to a minimum, it is necessary to place the ions in the rf minimum as accurately as possible by means of static electric fields.

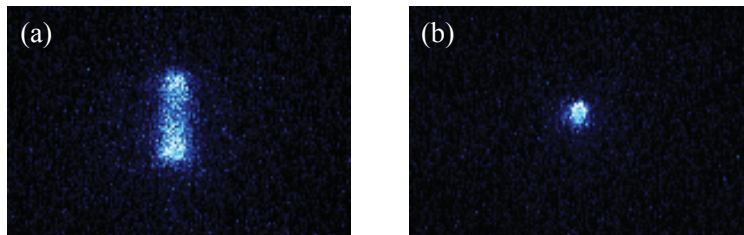


**Figure 5.10:** Micromotion compensation. (a) EMCCD image of a single  $^{40}\text{Ca}^+$  ion without any compensation voltages applied. One can clearly see the oscillation in vertical direction as the ion is not located in the rf minimum. (b) Same ion as shown in (a) but with compensation voltages applied. Under typical operating conditions, voltages in the range of  $\pm 2\text{ V}$  are needed for compensation.

In case of our segmented linear rail trap, the compensation of the micromotion is achieved by using a so-called Bias-T circuit for supplying a dc offset voltage  $U_{\text{dc}}$  to the rf rails. As can be seen in Fig. 5.11, the usage of a resistance ( $R = 10\text{ M}\Omega$ ) in the dc junction of the Bias-T circuit prevents the rf voltage from ending up in the dc power supply whereas the capacitance<sup>8</sup> ( $C = 680\text{ pF}$ ) in the rf branch guarantees that no dc voltage arrives at the rf power supply, respectively<sup>9</sup>. By applying proper offset voltages to all four rails, it is possible to shift the ion in both radial directions, effectively allowing for moving the ion into the minimum of the radial pseudopotential.

<sup>8</sup> Due to their superior characteristics (e.g. low loss, high capacitance stability, low temperature coefficient), polystyrene film capacitors ('Styroflex') are used.

<sup>9</sup> Depending on the frequency of the ac voltage, it is also possible to use an inductance instead of a resistance in the dc branch of the Bias-T circuit.

Figure 5.10(b) shows the EMCCD image of a fully compensated  $^{40}\text{Ca}^+$  ion by applying compensation voltages in the range of  $\pm 2$  V.

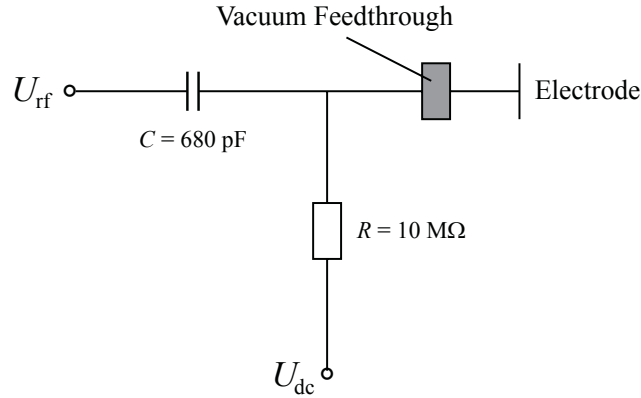


**Figure 5.11:** Bias-T circuit for supplying an offset voltage  $U_{\text{dc}}$  to the rf rails in order to compensate the micromotion.

There are various ways in order to measure and compensate the micromotion [Ber98]. A rather coarse method relies on a change of the average ion position as the trap potentials are changed. Starting from a linear ion crystal consisting of well-separated ions, a coarse estimate for the position of the rf minimum can be obtained by raising the amplitude of the rf voltage in order to check whether the position of the ions is altered due to the stronger confinement in radial direction. The higher the chosen amplitude, the more exact the ions will be located in the minimum of the radial pseudopotential. Hence, an optimal compensation is achieved when the ions are no more moving upon lowering or raising the rf amplitude. Using these compensation voltages as starting point, a more exact compensation can be achieved by reducing the spectral linewidth of the micromotion broadened  $S_{1/2} \leftrightarrow P_{1/2}$  transition which is used for Doppler cooling and imaging the ions. After the transition has been desaturated, the laser at 397 nm is red-detuned in such a way that only half of the resonance fluorescence is observed. Thus, improving the compensation, i.e. lowering the amplitudes of the micromotion sidebands by adjusting the compensation voltages, also reduces the linewidth of the  $S_{1/2} \leftrightarrow P_{1/2}$  transition, effectively leading to a further reduction of the photon scattering rate. After a readjustment of the laser detuning, the process is repeated until no further improvement is achieved.

Another compensation method, which was already successfully implemented in one of our traps [Deu07], is based on the modulation of the ion's fluorescence signal due to the first-order Doppler shift of the  $S_{1/2} \leftrightarrow P_{1/2}$  transition [Die87, Höf97]. Due to the micromotion, the ions preferably scatter photons at a particular phase of their oscillation which depends on the frequency detuning of the cooling laser at 397 nm. As the lifetime of the excited

---

$P_{1/2}$  state ( $\approx 8$  ns) is small compared to the period of the radio frequency ( $\approx 82$  ns), the scattering rate depends on the velocity of the ions and therefore on the phase of the radio frequency. Using a time interval and frequency counter<sup>10</sup>, it is now possible to measure the dependency by conducting a correlation measurement between the arrival time of the scattered photons and the zero-crossing of the rf voltage. Hence, an optimal compensation is achieved when no correlation between the scattering rate and the rf phase is observed.

---

<sup>10</sup> *SR620*, Stanford Research Systems, Sunnyvale, CA, USA, <http://www.thinksrs.com>



## Chapter 6

# Ion trap as deterministic ion source

In this chapter, we will mainly focus on how to utilize the segmented linear rail trap presented in chapter 5 as a deterministic ion source. Although most of the experimental results presented so far revolved around the manipulation of  $^{40}\text{Ca}^+$  ions, the main focus of attention lies on the deterministic implantation of dopant ions in order to improve the electrical properties of semiconductor devices or to generate systems which can be used for solid state quantum computing. After a description of the extraction mechanism and the employed detection scheme (6.1), the generation, cooling and identification of prospective dopant ions will be discussed in detail (6.2).

### 6.1 Ion extraction

#### 6.1.1 Extraction mechanism

Initially, the ion is trapped at the center of electrode 10 by supplying a voltage of 35 V to electrodes 7 and 13, see Fig. 6.1(a). However, due to the large distance of the electrodes to the trap center, the generated axial trapping potential only features a depth of about 4 eV, not representing a large barrier during the extraction process. A simulation of the trapping potential in axial direction can be seen in Fig. 6.1(b).

The extraction process is then initiated by increasing the dc voltages on electrodes 9 and 10 to 500 V within a few tens of nanoseconds, see Fig. 6.2(a). The extraction voltage generates a repulsive potential at the position of the ion, effectively canceling the axial

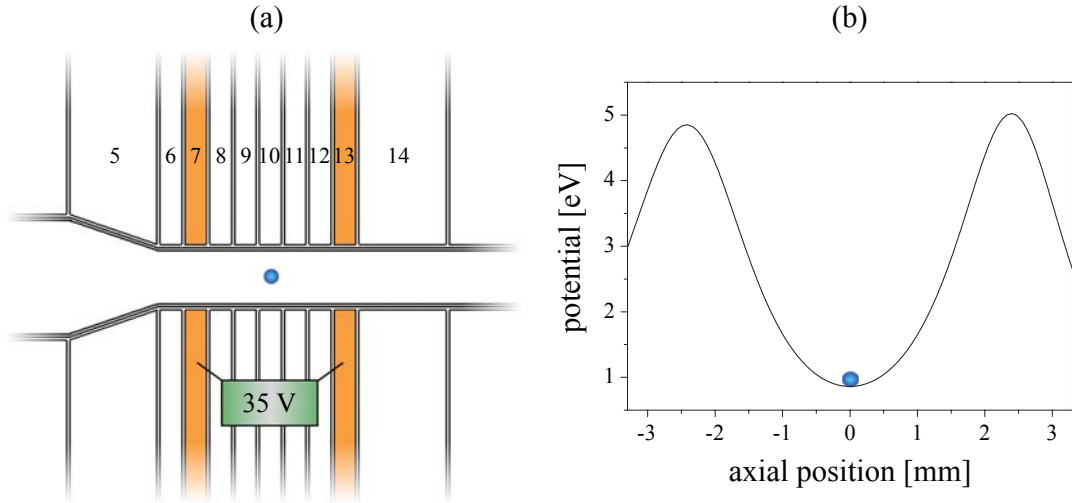


**Figure 6.1:** Schematic drawing of the axial trapping potential [Fic09a]. (a) The axial confinement is experimentally generated by supplying 35 V to electrodes 7 and 13. (b) Simulated trapping potential in axial direction. The ion (depicted in blue) is trapped above the center of electrode 10 which also serves as point of reference for the axial position.

confinement, see Fig. 6.2(b). However, as the ion already gets accelerated by the developing potential during the switching process, the ion does not sense the full potential strength and the effective energy transfer is lessened. In addition, due to the asymmetric voltage configuration the peak voltage is not at the position of the ion and it is only accelerated by the shoulder of the generated potential, reducing the kinetic energy even further. From a time-of-flight analysis, one can deduce a final kinetic energy of about 80 eV for the extracted  $^{40}\text{Ca}^+$  ions (see also chapter 7.2.5).

Figure 6.3 shows a schematic drawing of the extraction setup. After a specific number of ions has been loaded into the trap (in this case an ion crystal consisting of four  $^{40}\text{Ca}^+$  ions), the extraction process is triggered via a computer-controlled TTL signal which is fed into a phase synchronization circuit (phase delay trigger). The phase synchronization circuit delays the TTL signal such that a constant delay to the next zero crossing of the trap drive frequency  $\Omega$  is ensured as the synchronization is crucial in order to minimize shot to shot fluctuations of the velocity and position of the extracted ions. The measured delay time shows a  $1\sigma$ -spread of 0.34 ns. A circuit diagram of the phase synchronization circuit can be found in appendix A [Fic09a]. The switching of the extraction voltage<sup>1</sup> is experimentally realized by two high voltage switches<sup>2</sup> which can switch voltages of up to

<sup>1</sup> supplied by isec inc., Model *EHQ-8210p* (see also chapter 4.5)

<sup>2</sup> *HTS 41-06-GSM*, Behlke Power Electronics GmbH, Kronberg, Germany, <http://www.behlke.de>

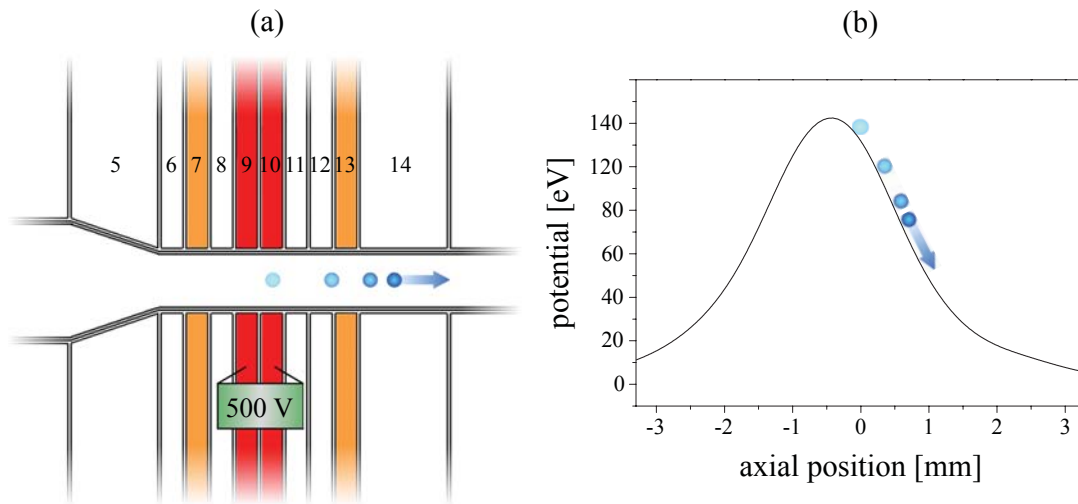


**Figure 6.2:** Schematic drawing of the utilized extraction mechanism [Fic09a]. (a) Experimental voltage configuration for the extraction. By increasing the dc voltages on electrodes 9 and 10 to 500 V within a few tens of nanoseconds, the ion overcomes the axial trapping potential and gets shot out of the trap. (b) Simulated trapping potential during extraction. The center of electrode 10 is again the point of reference for the axial position.

4 kV within a timespan of 10 ns. However, as the extraction voltage leads to a temporary charging of the trap, the TTL trigger signal is only supplied for a few ms to the high voltage switches, reducing the unintentional charging to a minimum.

### 6.1.2 Detection of extracted ions

The detection of the extracted ions is performed via an electron multiplier tube<sup>3</sup> (EMT) with 20 dynodes and a main entrance aperture of 20 mm which can detect positively charged ions with a specified quantum efficiency of about 80% and a specified gain of  $5 \times 10^5$ . After a positively charged particle enters the EMT through the main aperture, it gets deflected onto the first dynode where a certain number of electrons is released due to the ion impact. These electrons then generate secondary electrons as they hit adjacent dynodes, resulting in an electron cascade leading to an electrical signal which is detected via an oscilloscope<sup>4</sup>. At typical operating conditions, the detector is supplied with a voltage of -2.5 kV leading to detection signals with a width of 10 to 15 ns and an amplitude of about 100 mV. As already stated in chapter 4.1, the detector is housed in a

<sup>3</sup> AF553, ETP electron multipliers, Ermington, NSW, Australia, <http://www.sge.com>

<sup>4</sup> Agilent infiniium 54832D MSO, Agilent Technologies, Böblingen, Germany, <http://www.agilent.de>

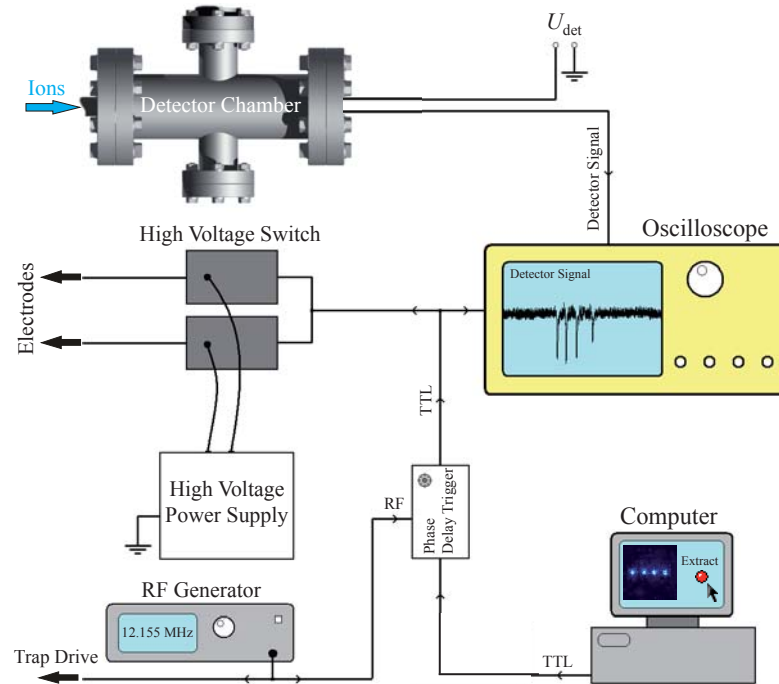


**Figure 6.3:** Schematic drawing of the extraction setup. After a certain number of ions has been loaded into the trap, the extraction process is triggered via a TTL signal which is synchronized to the trap drive frequency  $\Omega$  using a phase synchronization circuit (phase delay trigger). Two high voltage switches then increase the dc voltages on electrodes 9 and 10 to 500 V within a few tens of nanoseconds, leading to the extraction of the trapped ions. Upon entering the detector chamber, the extracted ions are detected using an electron multiplier tube leading to signal dips on an oscilloscope. [Sch10]

separate vacuum chamber with a distance of 287 mm<sup>5</sup> from the trap. Figure 6.4 shows a picture of the EMT as well as a technical drawing showcasing the internal structure with the different dynodes.

## 6.2 Dopant ions

### 6.2.1 Generation and sympathetic cooling

In our experiment, dopant ions (e.g. nitrogen, nickel, chromium) are generated by a pulsed frequency tripled Nd-YAG laser<sup>6</sup> at a wavelength of 355 nm with a pulse power of 7 mJ, a pulse duration of 5 ns and a maximum repetition rate of 15 Hz. Due to its high pulse power,

<sup>5</sup> For measurements conducted without the movable aperture plate (see chapter 7.2.6) and the electrostatic einzel-lens (see chapter 8.3), the distance between the trap center and the detector equals 247 mm.

<sup>6</sup> *Continuum Minilite I*, Continuum, Santa Clara, CA, USA, <http://www.continuumlasers.com>

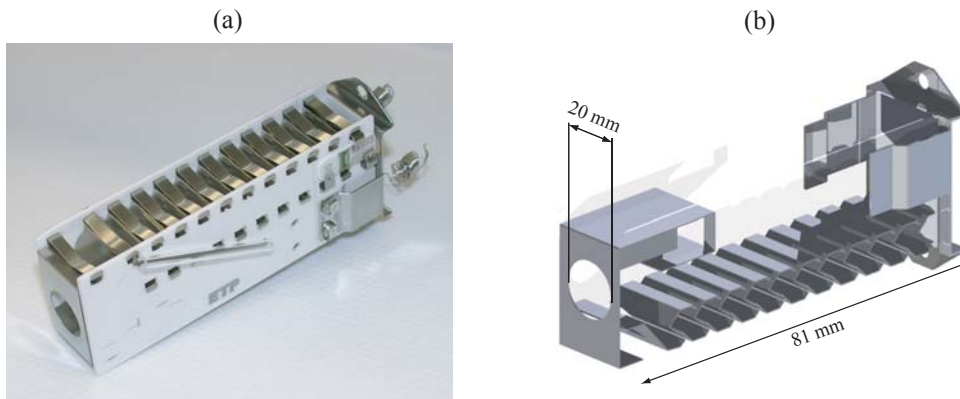


**Figure 6.4:** (a) Picture of the electron multiplier tube used for ion detection (Source: Manufacturer<sup>3</sup>). (b) Technical drawing showcasing the dimensions and the internal structure with the different dynodes.

the ionization of a broad spectrum of chemical elements can be achieved in a multi-photon process even though the wavelength does not match the electronic transitions. Similar to the photoelectric effect, the electrons can absorb the energy of one or more photons and are directly excited into the continuum. The maximum kinetic energy of an ejected electron is then given by the difference between the binding energy  $W_B$  and the energy of the absorbed photons:

$$E_{\text{kin}} = h\nu - W_B \quad (\text{Einstein equation}) \quad (6.1)$$

However, one of the main disadvantages of the described multi-photon ionization process is the lack to ionize selectively specific chemical elements, increasing the probability to ionize and load unwanted atoms from the background gas. The creation of unwanted electric patch charges on the insulated surfaces of the trap due to the high pulse power and low wavelength of the pulsed laser also has to be taken into account. Regardless of these problems, the multi-photon ionization is still the method of choice as it allows one to ionize a variety of chemical elements without the need to have a matched laser system for the respective species.

The supply of the various species of dopant atoms is either accomplished by utilizing an already installed NiCr oven which consists of a combination of ceramics tubes and the aforementioned NiCr filament (see chapter 5.2.1) or by leading in corresponding gases via a micro dosing valve, allowing one to adjust the gas pressure with an accuracy of  $10^{-11}$  mbar. Figure 6.5 shows an image of a mixed ion crystal consisting of  $10^{40}\text{Ca}^+$  ions and one dopant ion which can be identified from the void in the fluorescence image compared to that of a regular linear  $^{40}\text{Ca}^+$  crystal. Although the dopant ion cannot be directly laser cooled

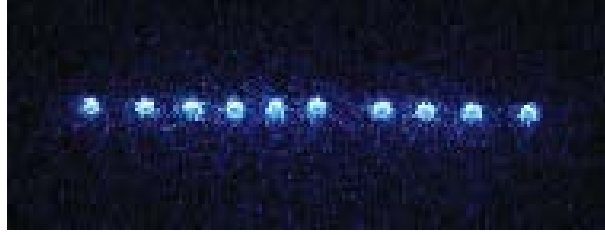


**Figure 6.5:** Mixed ion crystal consisting of 10  $^{40}\text{Ca}^+$  ions and one dark ion (5th from the right).

(either due to a non-existent closed cooling cycle or the non-availability of the necessary laser systems), it is still possible to sympathetically cool it due to the Coulomb interaction between the charged particles [Lar86].

### 6.2.2 Mass determination

In order to identify trapped dopant ions, one takes advantage of the difference in masses between the unknown dopant and the  $^{40}\text{Ca}^+$  ions by exciting collective vibrational modes of the mixed ion crystals [Mor00b]. For two equally charged ions close to their equilibrium positions, it can be shown that the two eigenfrequencies for their motion along the trap axis are given by [Kie00]

$$\omega_{\pm}^2 = \left[ (1 + \mu) \pm \sqrt{1 - \mu + \mu^2} \right] \omega_z^2, \quad (6.2)$$

with  $\mu = m/m_x$ , where  $m$  and  $m_x$  are the masses of the two ions, and  $\omega_z$  is the oscillation frequency of a single ion with mass  $m$ . In analogy to chapter 3.1.3,  $\omega_+$  stands for the eigenfrequency of the center-of-mass mode, whereas  $\omega_-$  denotes the eigenfrequency of the breathing mode. By measuring  $\omega_z$  for an ion with the known mass  $m$  (in our case for a  $^{40}\text{Ca}^+$  ion), the unknown mass  $m_x$  of the dopant ion can be deduced from a measurement of either the COM mode frequency  $\omega_+$  or the breathing mode frequency  $\omega_-$ . In the case of two identical ions with mass  $m$ , the COM mode frequency equals  $\omega_z$  [Dre04]. The excitation of the vibrational modes is experimentally realized by applying an ac voltage to one of the trap electrodes at a frequency near one of the eigenfrequencies of the two-ion crystal. In our case, the ac voltage is supplied by an R&S SML01 signal generator<sup>7</sup> to dc electrode 8.

Figure 6.6(a) shows an image of a mixed two-ion crystal consisting of one  $^{40}\text{Ca}^+$  ion (left) and one non-fluorescing dopant ion (right). Here, the dopant ion again is sympathetically cooled by the  $^{40}\text{Ca}^+$  ion. However, once in a while the dopant ion can change its position

<sup>7</sup> ROHDE & SCHWARZ GmbH & Co. KG, Munich, Germany, <http://www.rohde-schwarz.de>

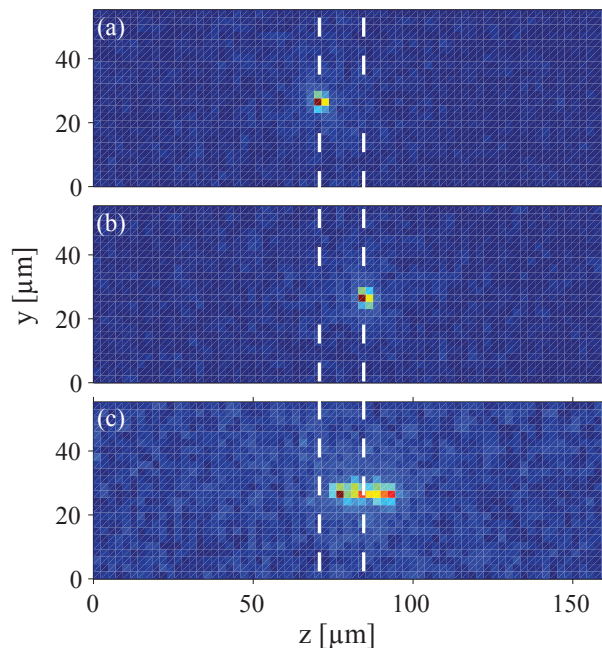


**Figure 6.6:** Mass determination of prospective dopant atoms. The dashed lines represent the positions of the two ions. (a) Mixed two-ion crystal consisting of one  $^{40}\text{Ca}^+$  ion (left) and one non-fluorescing dopant ion (right). (b) Same picture as in (a), but the dopant ion is now located on the left hand side due to a position exchange with the  $^{40}\text{Ca}^+$  ion. (c) Same situation as in (b), but with a modulated voltage applied to one of the trap electrodes at a frequency near the COM-mode of the mixed two-ion crystal. Due to the perturbation, the  $^{40}\text{Ca}^+$  ion appears blurred and spatially smeared out on the CCD camera. Because of the different mass of the dopant ion, the eigenfrequencies of the mixed two-ion crystal differ from those measured for a pure  $^{40}\text{Ca}^+$  two-ion crystal. [Deu07]

due to a temporal ‘melting’ of the ion crystal, see also Fig. 6.6(b). By now applying an ac voltage near one of the eigenfrequencies  $\omega_+$  or  $\omega_-$  of the mixed two-ion crystal, the amplitude of the ions’ motion along the trap axis is enhanced, leading to a spatial smearing of the fluorescence signal as the exposure time of the CCD camera is longer than the oscillation period, see Fig. 6.6(c). Another way to detect the driven oscillation is to measure the fluorescence of the trapped ions, which decreases due to the induced Doppler shift, see Fig. 6.7.

In the present case, the measurement yielded a frequency of  $\omega_z = 2\pi \times 235.6(1)$  kHz for the COM mode of the pure  $^{40}\text{Ca}^+$  two-ion crystal and a frequency of  $\omega_- = 2\pi \times 212.2(1)$  kHz for the breathing mode of the mixed two-ion crystal, respectively. Here, an ac voltage with an amplitude of  $225 \mu\text{V}$  was used. As the mass of a  $^{40}\text{Ca}^+$  ion equals  $m = 39.97$  u (unified atomic mass unit), one can calculate the mass of the dopant ion to be  $m_x = 57.1(2)$  u

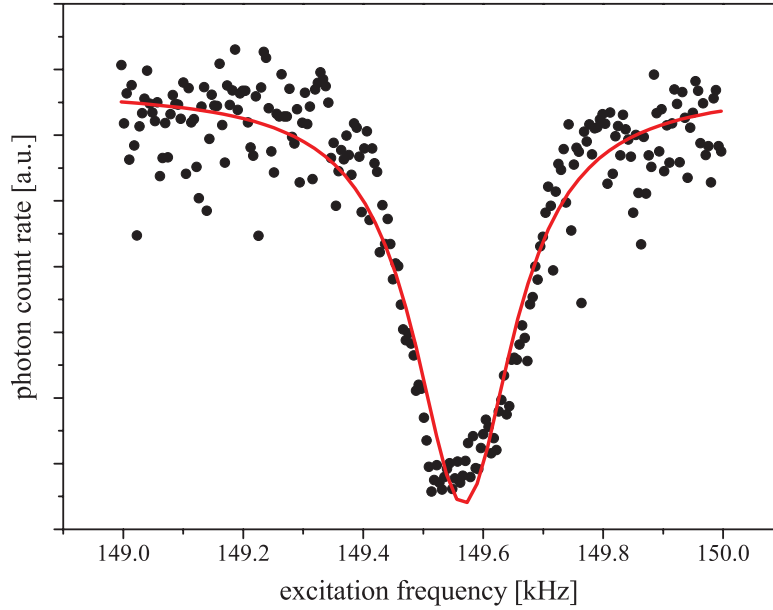


**Figure 6.7:** Fluorescence signal of a pure  $^{40}\text{Ca}^+$  two-ion crystal as a function of the excitation frequency of the axial COM mode. The observed dip features a width of 200 Hz (FWHM). [Deu07]

using equation (6.2), thus revealing with high probability that the dopant ion has to be a  $^{40}\text{Ca}^{17}\text{O}^+$  ion with a mass of 57.0 u. Due to the damping effect of the laser cooling force and the trap frequency, the mass resolution of this method is limited to about 1%.

However, to discriminate between equally charged atomic or molecular ions with the same total number of nucleons, a relative mass resolution of  $10^{-4}$  is typically needed. This can be achieved, if the oscillating electric field along the trap axis is generated by modulating the radiation pressure force on the laser cooled ions, which e.g. can be accomplished by modulating the laser intensity of a beam propagating along the trap axis using an electro-optical chopper<sup>8</sup>. Here, the position of the ions is monitored as a function of the frequency modulation. For a detailed description of this method, please see [Dre04].

<sup>8</sup> EOC, **E**lectro-**O**ptical **C**hopper

## Chapter 7

# Characterization of the ion source

The characterization of our novel single-ion source was done in two different ways: Using a numerical simulation software which was developed in our group, the properties of our segmented linear rail trap were simulated and the generated single-ion beam as well as its dependencies were studied in detail. Without these simulations, it would not have been possible to come up with the design which was presented in chapter 5. In addition, the simulations allow for a better understanding of the extraction process and give rise to further optimizations of the experimental setup. Experimentally, we characterized our ion source by measuring the beam divergence as well as the velocity distribution of the extracted ions, and by studying the influence of various parameters such as the rf trigger phase and the vacuum base pressure. After a brief description of the simulation software and an in-depth discussion of the numerical simulations (7.1), the experimental results will be presented (7.2) and a comparison with the simulations will be made (7.3).

### 7.1 Simulation of the ion source

One of the main goals during the development process of the simulation software was to come up with an algorithm, which was not only able to process macroscopic structures like our ion trap with a size of a few tens of millimeters, but also allowed for simulating electrostatic potentials and electric fields with an accuracy in the sub-nm regime. Simultaneously, the efficient calculation of the electric fields of complex structures and the therein occurring motion of charged particles was an important aspect. Commercially available software applications like FEMLAB, which e.g. is based on the finite element method<sup>1</sup>,

---

<sup>1</sup> FEM, Finite Element Method

were not sufficient to fulfill the needs at hand. On basis of the simulation software, it was also possible to develop a specifically designed einzel-lens [Sch10] which was adapted to the properties of the generated single ion beam (see chapter 8).

The calculation of the electrostatic potentials is performed by a high accuracy boundary-element solver package [Sin10] which is based on the boundary element method<sup>2</sup> [Bre92, Bec92] and is accelerated by the FMM<sup>3</sup> algorithm [Gre96, Of01, She07]. The simulation of the motion of the charged particles in the calculated electric field is done by using the Verlet integration method [Ver67].

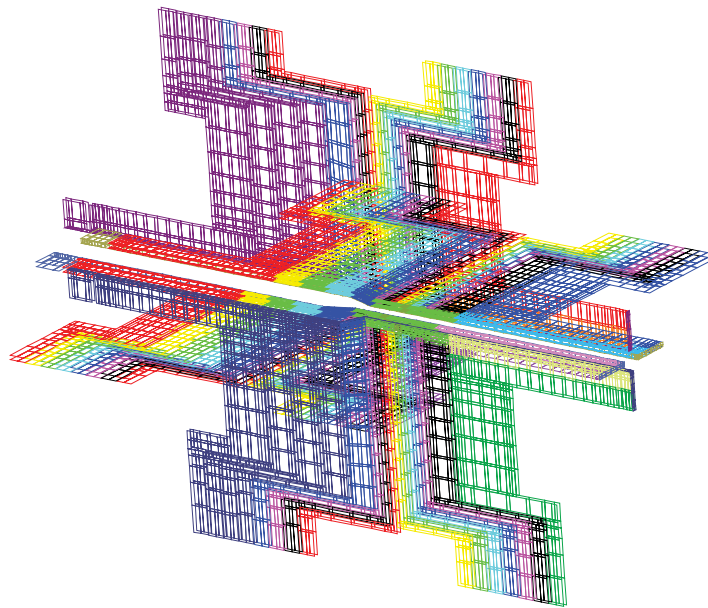


**Figure 7.1:** AutoCAD drawing of the segmented linear rail trap which is used for the numerical simulations. The colors define the different electrodes which can be independently supplied with voltages in the simulation. [Lin07]

At first, the geometry of the segmented linear rail trap was recreated using AutoCAD<sup>4</sup> and imported into the simulation software, see also Fig. 7.1. By virtually applying the same voltages as in the real experiment, it is possible to calculate the trajectories of the trapped particles with full time-dependent dynamics including the micromotion at the trap drive frequency  $\Omega$ . Figure 7.2(a) shows the simulated radial motion of the ion inside of the trap when a dc voltage of 35 V is supplied to electrodes 7 and 13 and the rf electrodes are supplied with a voltage of  $U_{\text{rf}} = 400 \text{ V}_{\text{pp}}$  at the frequency  $\Omega = 2\pi \times 12.155 \text{ MHz}$ .

<sup>2</sup> BEM, **B**oundary **E**lement **M**ethod

<sup>3</sup> **F**ast-**M**ultipole **M**ethod

<sup>4</sup> AutoCAD is a CAD (**C**omputer **A**ided **D**esign) software application for 2D and 3D design and drafting, developed and sold by Autodesk, Inc. For further details, please visit: <http://www.autodesk.com>.

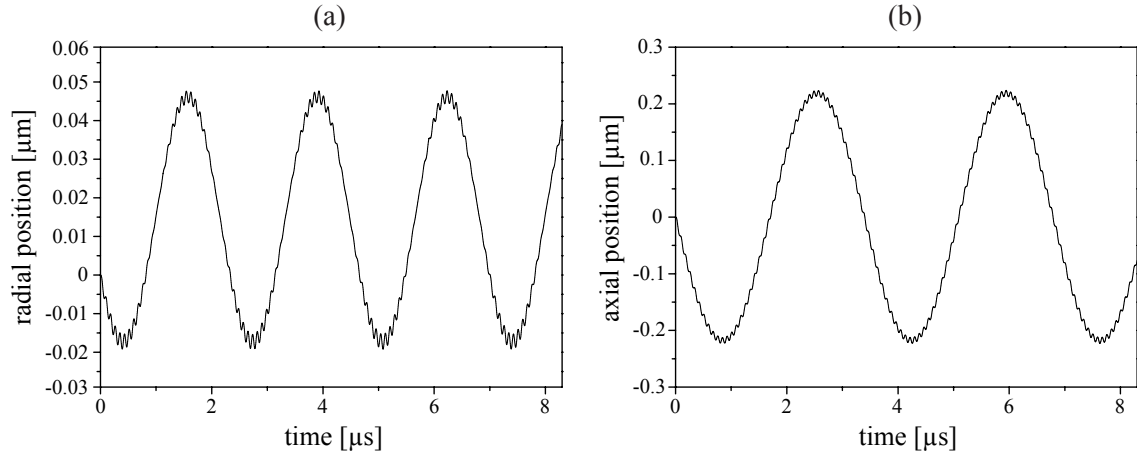


**Figure 7.2:** Simulated motion of the ions inside of the trap. (a) Simulated motion in radial direction. One can clearly see the superimposed micromotion with an amplitude of about 2 nm. The radial trapping frequency equals  $\omega_{\text{rad}} = 2\pi \times 476$  kHz. (b) Simulated motion in axial direction. The oscillations with an amplitude of 5 nm are caused by the finite step size of the numerical simulation and the layout of the trap electrodes. The axial trapping frequency amounts to  $\omega_{\text{ax}} = 2\pi \times 295$  kHz. [Fic09a]

One can clearly see the theoretically predicted micromotion with an amplitude of about 2 nm which is superimposed on the secular motion with an amplitude of 30 nm and a radial trapping frequency of  $\omega_{\text{rad}} = 2\pi \times 476$  kHz. The simulation of the axial motion also shows an oscillation which is superimposed on the secular motion with an axial trapping frequency of  $\omega_{\text{ax}} = 2\pi \times 295$  kHz, see Fig. 7.2(b). However, in contrast to the ‘real’ micromotion in radial direction, this oscillation features an amplitude of about 5 nm. Possible explanations for this unintentional oscillation are the finite step size of the used Verlet algorithm and the presence of the taper which connects the wide loading zone with the narrow experimental zone of the trap, see also Fig. 5.1. Furthermore, with an amplitude of 220 nm the secular motion in axial direction is also much larger than in the radial direction. The simulation of the axial motion also allowed for determining an optimal ‘starting point’ for the trapped ions which is shifted about 22 nm out of the middle of electrode 10. As there are no unintentional electric patch charges present in the simulation, this discrepancy from the ideal case has to be ascribed again to numerical errors and the layout of the trap electrodes.

### 7.1.1 Numerical simulation of the ion beam

Using the simulation software in combination with the CAD model depicted in Fig. 7.1, it is possible to simulate the extraction of single ions out of the trap and to visualize the

corresponding trajectories. In addition, one can study the influence of various parameters (e.g. initial ion temperature, start position) on the generated ion beam in order to better understand the behavior of the novel single-ion source.

As in the real experiment, the extraction process is initiated at a certain phase of the rf voltage by increasing the dc voltages on electrodes 9 and 10 to 500 V, effectively canceling the axial confinement (see also chapter 6.1.1). After a distance of 70 mm, the Verlet integration method used for calculating the trajectories is aborted as the ions have left the electric field which is generated by the ion trap. From there on, a ‘free flight’ can be assumed and the trajectories can be calculated by a linear extrapolation using the spatial coordinates and velocity vectors from the Verlet algorithm. After a distance of 247 mm from the trap center<sup>5</sup>, the corresponding positions and velocities of the extracted ions are recorded. By repeating the extraction process many times without changing the parameters, a so-called spot diagram is generated, see also Fig. 7.3(b).

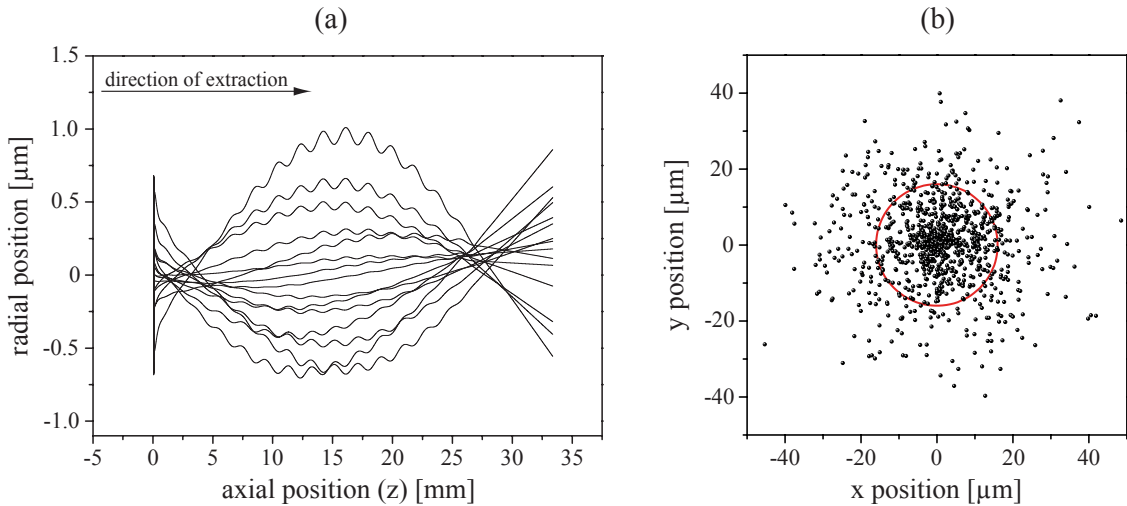


**Figure 7.3:** Numerical simulation of ion trajectories during extraction [Fic09b]. (a) Trajectories of 15  $^{40}\text{Ca}^+$  ions during the extraction from the trap with an initial temperature of 2 mK. (b) The resulting spot diagram at a distance of 247 mm from the trap center yields a beam divergence of  $134\ \mu\text{rad}$ . The red circle illustrates the  $1\sigma$ -spot radius of  $16.5\ \mu\text{m}$ .

The optimal trapping position, which has been determined from the simulations of the ion motion inside of the trap, is used as initial position for the simulation of the extraction whereas the initial velocities are randomly generated using a Monte Carlo simulation. As one can assume a thermal distribution, the momentum in all three spatial directions is

<sup>5</sup> Note that, depending on the type of measurement, this is either the location of the detector or of the movable aperture plate (see chapter 7.2.6) in the real experiment.

determined by the Maxwell-Boltzmann distribution at temperature  $T$ :

$$W(v) \sim v^2 \exp\left(-\frac{mv^2}{2k_B T}\right). \quad (7.1)$$

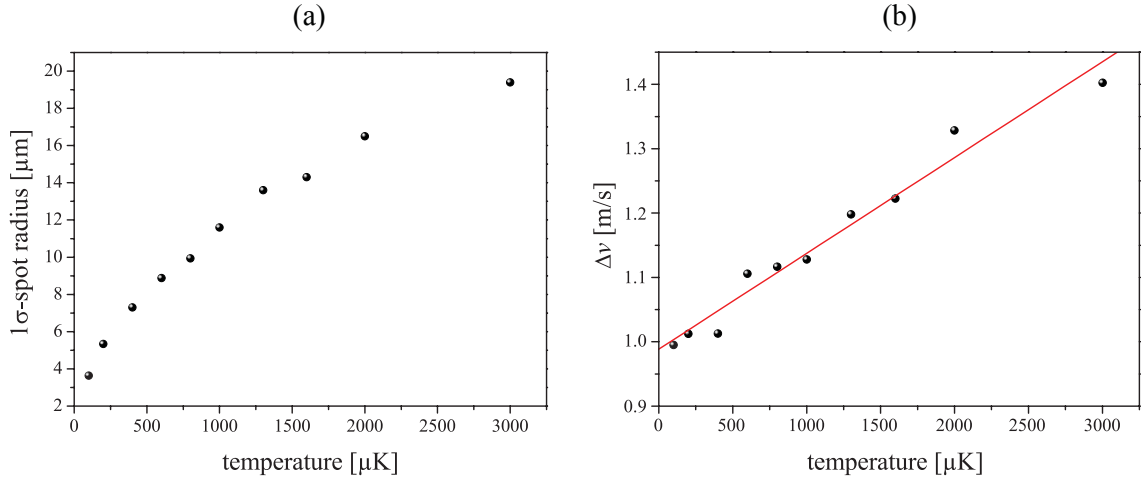
Symmetry properties of the trap are exploited to reduce numerical errors to a minimum, with minor numerical asymmetries, which still remain because of the finite mesh size of the utilized algorithms, being corrected by small compensation voltages on the rails just as in the real experiment. As a test, the measured trap frequencies  $\omega_{\text{ax}}$  and  $\omega_{\text{rad}}$  for various traps of different size and shape in our lab [Sch08] were compared to corresponding simulations, finding an agreement at the level of 2-3 %.

Figure 7.3(a) shows the trajectories of 15 ions during extraction. Due to the different initial velocities, one can clearly see the influence of the micromotion during the extraction and the resulting spread of the ion beam. As in the real experiment, each extraction was synchronized to a certain phase of the rf voltage. Here, the experimentally determined value of  $260^\circ$  was used for the simulation, see also chapter 7.2.3.

### 7.1.2 Impact of the initial ion temperature

With an initial ion temperature of 2 mK, the resulting spot diagram shows a  $1\sigma$ -spot radius of  $16.5\ \mu\text{m}$  at a distance of 247 mm from the trap center, which amounts to a full angle beam divergence of  $134\ \mu\text{rad}$ , see Fig. 7.3(b). The specified temperature of 2 mK is similar to the experimentally achieved value, with the deflection electrodes being grounded during the extraction simulation. The mean longitudinal velocity of the extracted ions at the target is calculated to be 22.1 km/s with an  $1\sigma$ -uncertainty of only 1.3 m/s. Therefore, the predicted ion beam shows promising characteristics for subsequent focusing with ion optics due to small spherical and chromatic aberration. The predictions are even better if sub-Doppler cooling methods are applied. These would lead to mean phonon expectation values below 1 and temperatures of about  $100\ \mu\text{K}$ . In this case, the full angle divergence of the generated ion beam shrinks to  $30\ \mu\text{rad}$ , effectively reducing the  $1\sigma$ -spot size at the target to  $3.7\ \mu\text{m}$ , see Fig. 7.4(a). However, as the extraction voltage remains the same, the mean longitudinal velocity is not influenced by the smaller initial temperature, but the  $1\sigma$ -velocity uncertainty decreases slightly to 1 m/s, see also Fig. 7.4(b).

Although these values are very promising, it has to be noted that these calculations are fully classical. As the ions are cooled to the motional ground state approaching the Heisenberg limit, quantum mechanical simulations describing the propagation of the wave packets of the extracted ions would be needed to get more exact values. Nevertheless, the simula-



**Figure 7.4:** Dependence of the ion beam on the initial ion temperature. Each data point consists of 1000 individually simulated shots. (a) Simulated  $1\sigma$ -spot radii as a function of the initial ion temperature. (b)  $1\sigma$ -velocity fluctuation  $\Delta v$  as a function of the initial ion temperature. [Fic09a]

tions show that by applying voltages to the deflection electrodes, the characteristics of the resulting spot shapes change enormously. For example, by applying deflection voltages of 7.5 V between two opposing blades and 9.1 V between the other two (which resembles a typical configuration in the experiment), the generated spot is shifted approximately 19.4 mm in the horizontal and 30.5 mm in the vertical direction. In addition to this expected deflection, the spot is also stretched from the former Gaussian to a cigar-shaped distribution, and therefore the  $1\sigma$ -spot size value cannot be calculated anymore, see inset of Fig. 7.6(b). This drastic change has been simulated for 2 mK cold ions as well as for sub-Doppler cooled ions.

### 7.1.3 Impact of the initial start position

Aside from the dependence on the initial temperature, the transversal expansion and the velocity of the ion beam strongly depend on the start position of the extracted ions. Whereas altering the initial position does not significantly change the size and the (Gaussian) spot shape at the target when the deflection electrodes are grounded, the velocity fluctuation is strongly affected, see Fig. 7.5(a). Although the mean longitudinal velocity  $\bar{v}$  stays at a constant 22 km/s ( $\pm 2\%$ ) for displacements up to  $\pm 400 \mu\text{m}$ , the velocity spread varies enormously: From an initial 1.3 m/s, it increases up to 1.5 km/s when the ions are displaced about  $420 \mu\text{m}$  out of the trap center before being extracted. As the trapped ions are no more located in the minimum of the trapping potential, the micromotion is

increased, leading to a highly varying initial momentum. A similar behavior can be observed in case of the achievable spot sizes. Here,  $1\sigma$ -spot sizes of about  $16\ \mu\text{m}$  are feasible if the ions are extracted out of the center of the trap, with a displacement of  $\pm 400\ \mu\text{m}$  resulting in an enlargement of the spot size by an additional  $2\ \mu\text{m}$ .

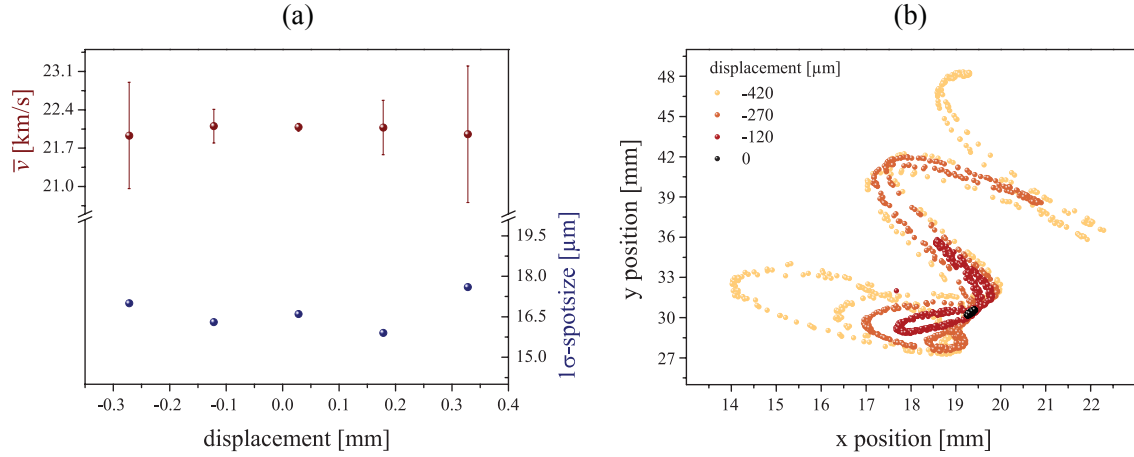


**Figure 7.5:** Dependence of the ion beam on the initial start position. Positive values denote a displacement in extraction direction. (a) Resulting mean longitudinal velocities  $\bar{v}$  and  $1\sigma$ -spot sizes after extraction at a distance of 247 mm from the trap center with deflection electrodes grounded. (b) Resulting spot diagrams, when the deflection electrodes are biased to 7.5 V between two opposing trap blades and 9.1 V between the other two blades, respectively. [Fic09b]

The influence of the start position on the properties of the ion beam becomes even more crucial when the deflection electrodes are supplied with a non-zero voltage. Due to slightly displaced trajectories during the extraction process, the ions start to oscillate in the rf drive field and therefore lose their originally well-defined extraction direction. In Fig. 7.5(b), the ions are again displaced up to  $420\ \mu\text{m}$  from the potential minimum before being extracted, meaning that they are effectively located between two electrodes. Thus, the extension of the former cigar shaped spot of around half a millimeter increases tremendously to about 10 to 20 mm. Additionally, the shape changes to a screw-like structure, making it nearly impossible to deterministically aim the extracted ions. The mean value of the longitudinal velocity thereby sums to around 22 km/s and changes only by 2% for different extraction positions, while fluctuations increase to a maximum of 1.6 km/s for ions being displaced  $420\ \mu\text{m}$  out of the minimum of the trapping potential.

### 7.1.4 Impact of the phase of the rf voltage

Similar results are calculated for the enlargement of the beam expansion when changing the phase of the rf voltage at the time of extraction, see Fig. 7.6(a). With deflection electrodes grounded, the  $1\sigma$ -spot size varies from  $16\ \mu\text{m}$  up to  $19\ \mu\text{m}$  over a whole period of the rf voltage but remains Gaussian distributed. The mean longitudinal velocity thereby oscillates in a sine-like manner with an amplitude of  $0.25\ \text{km/s}$  around  $22.2\ \text{km/s}$  whereas the velocity spread only varies negligibly between  $1.3\ \text{m/s}$  and  $2.3\ \text{m/s}$ .

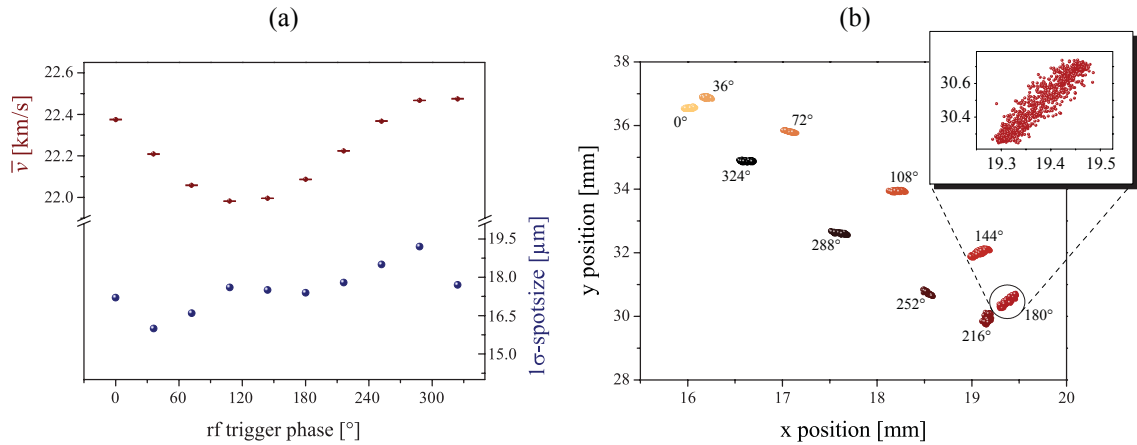


**Figure 7.6:** Dependence of the ion beam on the phase of the rf voltage for an initial ion temperature of  $2\ \text{mK}$ . All shown results are calculated for a distance of  $247\ \text{mm}$  from the trap center. (a) Resulting mean longitudinal velocities  $\bar{v}$  and  $1\sigma$ -spot sizes with deflection electrodes grounded. (b) Resulting spot diagrams, when the deflection electrodes are biased to  $7.5\ \text{V}$  between two opposing trap blades and  $9.1\ \text{V}$  between the other two blades, respectively. The inset shows a close-up view of one of the spots in order to show that a Gaussian distribution is no longer an accurate assumption if the ions are deflected during the extraction. [Fic09b]

Again, the exact trigger phase at the time of extraction becomes even more important when the deflection electrodes are used to alter the trajectories of the extracted ions. Figure 7.6(b) shows the simulated spots, when the deflection electrodes are biased to the same voltages as already mentioned above. For a constant trigger phase, the spot shape maintains its oval shape and size. However, when changing the phase the spots are distributed over an area of  $10\ \text{mm}$  by  $15\ \text{mm}$ . The mean velocity for each different trigger phase thereby stays within  $1\%$  at about  $22\ \text{km/s}$ , with the fluctuations only adding up to around  $2.5\ \text{m/s}$ .

Hence, in order to generate a deterministic single-ion beam suitable for implantation, it is important to accurately align the trap axis to the optical axis of the ion optics and to avoid the usage of the deflection electrodes. Furthermore, it is crucial to position the ion in the minimum of the radial pseudopotential and to synchronize the time of extraction with the phase of the rf field.

## 7.2 Experimental characterization

In order to characterize our novel single-ion source experimentally, it was necessary to determine at least two quantities, namely the velocity fluctuation of the extracted ions as well as the divergence of the generated single-ion beam. In addition, just like in the numerical simulations, we wanted to study the influence of various parameters, e.g. the rf trigger phase and the vacuum base pressure. Therefore, it was also necessary to experimentally determine the detection efficiency of the utilized EMT (see also chapter 6.1.2). After a brief description of the initial aiming procedure, the experimental results will be presented and discussed in detail.

### 7.2.1 Coarse aiming

As already stated in chapter 5.1.1, our segmented linear rail trap allows for a targeted shooting by applying low voltages to the deflection electrodes, effectively altering the trajectories of the ions during the extraction process. Although corresponding simulations were conducted beforehand, however, it was still unclear how the extracted ions would behave in the real experiment. Therefore, in order to increase the probability to detect the extracted ions, the first measurements were conducted with large ion clouds. Just like the shot pellets from a shotgun spread upon leaving the barrel, the extracted ion cloud contains a large amount of single ions which are widely spread upon leaving the ion trap. Hence, the likelihood to detect a single ion is proportional to the size of the extracted ion cloud. In order to extract ion clouds with an almost constant size, the loading procedure was stopped when a certain level of fluorescence was detected on the EMCCD camera. The optimal deflection voltages were then retrieved by gradually changing them, effectively maximizing the hit rate on the detector.

Figure 7.7(a) shows a typical detector signal in case of the extraction of an ion cloud. After an initial flight time of  $12.5 \mu\text{s}$ , a total of 25  $^{40}\text{Ca}^+$  ions have been detected within a time span of about  $2.5 \mu\text{s}$ . Note that the oscillations at the beginning are caused by the switching

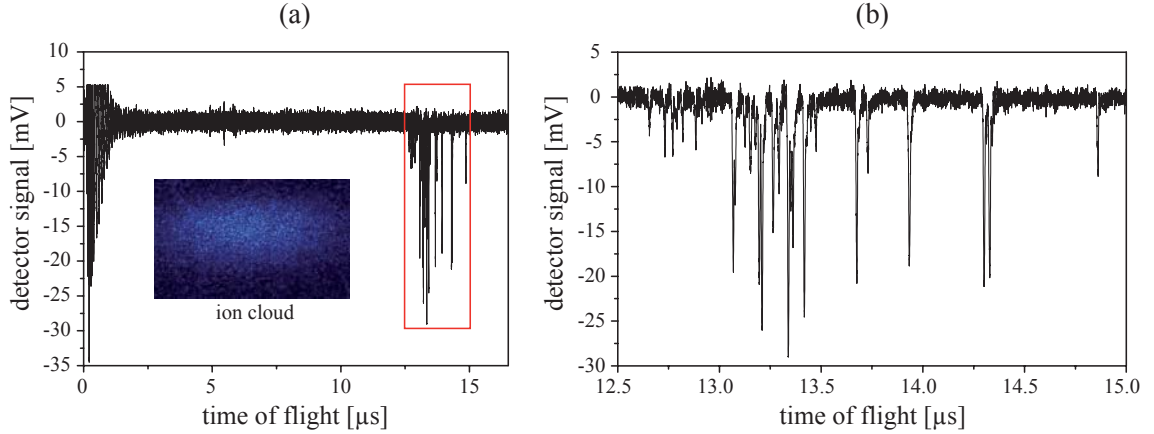


**Figure 7.7:** Typical detector signal in case of ion cloud extraction. (a) By extracting large ion clouds and adjusting the deflection voltages, a coarse aiming is accomplished by maximizing the number of the detected ions. The oscillations at the beginning are caused by the switching of the high voltage which is used for the extraction, see also chapter 6.1. The inset shows an EMCCD image of an ion cloud consisting of  $^{40}\text{Ca}^+$  ions. (b) Close-up view of the highlighted region (red rectangle) of the detector signal shown in (a). After an initial flight time of  $12.5\ \mu\text{s}$ , a total of 25  $^{40}\text{Ca}^+$  ions have been detected within a time span of about  $2.5\ \mu\text{s}$ .

of the high voltage which is used for the extraction, see also chapter 6.1. Figure 7.7(b) shows a close-up view of the highlighted region (red rectangle) of the detector signal shown in Fig. 7.7(a). The measurements were conducted without the movable aperture plate with an effective distance of 247 mm between the trap center and the detector.

### 7.2.2 Deterministic extraction of ion crystals

Using the optimal deflection voltages which were retrieved from the ion cloud measurements as starting point, the next step was to deterministically extract ion crystals with different sizes out of the trap in order to further improve the aiming onto the detector. In addition, the deterministic extraction of ion crystals allows us to experimentally determine the efficiency of the utilized EMT, see also chapter 7.2.4.

Figure 7.8(a) shows a typical fluorescence image of a single  $^{40}\text{Ca}^+$  ion with linear ion crystals consisting of two and four ions being depicted in Fig. 7.8(b) and (c), respectively. After the extraction, EMT detector traces are recorded with a single detection event (Fig. 7.8(e)), two events (Fig. 7.8(f)) and four events (Fig. 7.8(g)), correspondingly. As one can see, the arrival times for the different sized ion crystals are nearly the same,

only varying on a timescale of a few tens of nanoseconds. Taking a closer look at the EMT detector trace shown in Fig. 7.8(g), one can also see that the difference in arrival times between the first and the second as well as between the third and the last ion is slightly larger than the difference between the second and the third ion. This can be seen as evidence that the ion crystal is extracted in a linear manner as the ions slightly separate from each other due to the Coulomb interaction. If the ion crystal would be tilted during extraction, one would normally expect that the detected events were spaced more randomly and the differences in the arrival times were not as symmetrical.

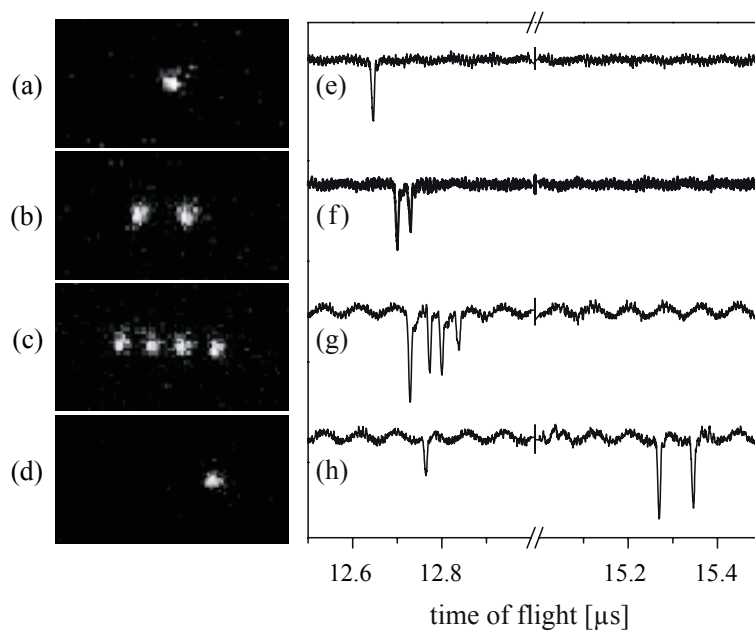


**Figure 7.8:** Deterministic extraction of ion crystals with varying size. (a) Typical fluorescence image of a single  $^{40}\text{Ca}^+$  ion, and linear ion crystals consisting of two (b) and four (c) ions. After the extraction, EMT detector signal traces are recorded with a single detection event (e), two events (f) and four events (g), respectively. The EMCCD image (d) shows fluorescence from a single  $^{40}\text{Ca}^+$  ion only; however, one can discover from its position that it is trapped in a linear crystal together with two dark ions at the left-hand side. As the mixed ion crystal is extracted, three events are detected, one from the  $^{40}\text{Ca}^+$  near  $12.8\ \mu\text{s}$  and two events near  $15.3\ \mu\text{s}$ . From this time-of-flight spectroscopy, one can deduce the mass of  $^{40}\text{Ca}^{17}\text{O}^+$  ions for both dark ions. All measurements were conducted without the movable aperture plate with an effective distance of  $247\ \text{mm}$  between trap center and detector. [Sch09a]

The EMCCD image depicted in Fig. 7.8(d) shows the fluorescence from a single  $^{40}\text{Ca}^+$  ion only. However, one can discover from its position that it is trapped in a linear crystal together with two dark ions at the left-hand side which are again sympathetically cooled

by the  $^{40}\text{Ca}^+$  ion, see also chapter 6.2.1. As the mixed ion crystal is extracted, three events are detected, one from the  $^{40}\text{Ca}^+$  near  $12.8\ \mu\text{s}$  and two events near  $15.3\ \mu\text{s}$ . As the mass of the  $^{40}\text{Ca}^+$  ion and the distance between the trap center and the detector is known, one can deduce the mass of  $^{40}\text{Ca}^{17}\text{O}^+$  ions for both dark ions from this time-of-flight spectroscopy.

### 7.2.3 Phase dependence

As already discussed in chapter 7.1.4, the time of extraction has to be accurately synchronized to the phase of the rf voltage in order to reduce position and velocity fluctuations of the extracted ions to a minimum. Especially in combination with the deflection electrodes, simulations predict a strong dependence of the hit rate on the rf trigger phase. Using the developed phase synchronization circuit (see also appendix A), it was possible to study the influence of the rf trigger phase on the measured hit rate by gradually changing the phase upon the time of extraction from  $0^\circ$  to  $360^\circ$ , see also Fig. 7.9.

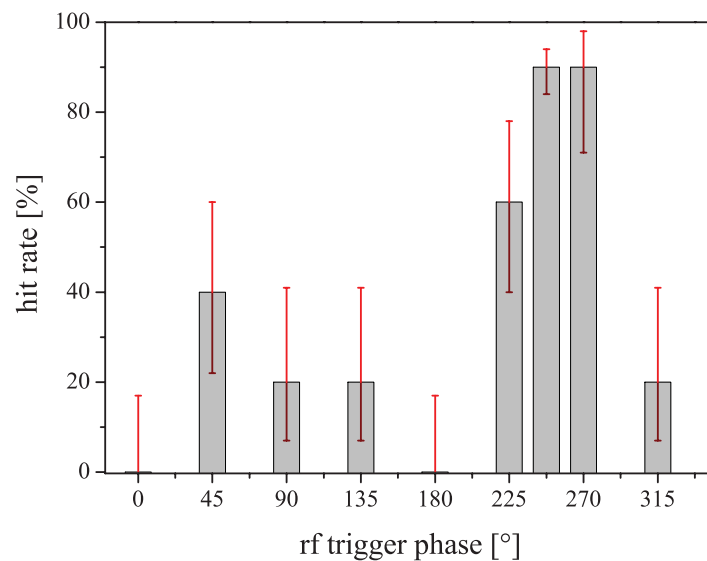


**Figure 7.9:** Hit rate for single ions as a function of the rf trigger phase upon the time of extraction [Lin07, Fic09b]. As a consequence, all following measurements were conducted with an rf trigger phase of  $260^\circ$ .

During all these measurements, the deflection voltages between opposing blades were kept constant at 22 V leading to a maximum hit rate of 90% for an rf trigger phase between  $250^\circ$  and  $270^\circ$ . However, as no additional apertures were placed in front of the detector at that time, the ion trajectories were only constricted by the main entrance aperture of the EMT which features a diameter of 20 mm, effectively leading to a broadening of the maximum. Taking into account the simulations depicted in Fig. 7.6, the non-zero hit rates

for rf trigger phases between  $45^\circ$  and  $135^\circ$  can also be explained. Here, the spot diagrams for the different phases were distributed over an area of 10 mm by 15 mm resembling the shape of an oval which, in principal, would allow two opposing spots to enter the EMT.

### 7.2.4 Pressure dependence

While studying the properties of our single-ion source, another important aspect was the dependence of the hit rate on the residual gas pressure. As already stated in chapter 4.1, the base pressure of our UHV setup equals  $5 \times 10^{-10}$  mbar. However, back when the measurement was conducted, the base pressure of the system equaled  $3 \times 10^{-9}$  mbar and rised as high as  $9 \times 10^{-9}$  mbar during the course of the measurement<sup>6</sup>. Figure 7.10 shows the hit rate for single ions as a function of the vacuum base pressure.

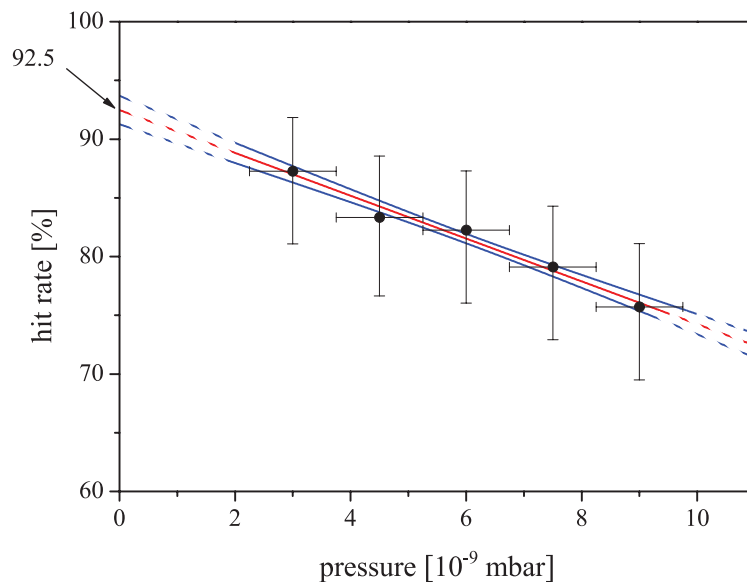


**Figure 7.10:** Hit rate for single ions as a function of the vacuum base pressure [Lin07, Fic09b]. A linear fit (red line) as well as the standard deviation (blue lines) have been added. For perfect vacuum, a maximum hit rate of 92.5% can be extrapolated. The measurement is based on 251 successful extractions out of 310 shots in total and was conducted with an rf trigger phase of  $260^\circ$  without any aperture in front of the detector.

At a pressure of  $9 \times 10^{-9}$  mbar, the hit rate only equals about 75% which is mainly due to collisions with the background residual gas particles. Furthermore, the stability of the ions in the trapping potential is lessened with higher pressure, leading to larger fluctuations

<sup>6</sup> The installation of a titanium sublimation pump and repeated bake-outs of the detector chamber allowed for reducing the base pressure to the aforementioned  $5 \times 10^{-10}$  mbar.

of the trajectories of the extracted ions. Reducing the pressure to  $3 \times 10^{-9}$  mbar already improves the measured hit rate to almost 90 % whereas for perfect vacuum, a maximum hit rate of as high as 92.5 % can be extrapolated. Regarding the manufacturer specified quantum efficiency of about 80 %, the measured hit rate for single ions is still about 10 % larger than the specified value, which means that all conducted measurements are mainly limited by the detector efficiency.

### 7.2.5 Time-of-flight measurements

Just like in classical optics, where an optical lens cannot focus light with different wavelengths to the same point due to dispersion effects, fluctuations in the velocity lead to chromatic aberration when using ion optics. Hence, the smaller the fluctuations, the better the extracted ions can be focused by using an electrostatic einzel-lens. Using our EMT, one cannot only measure whether an extraction process was successful or not, but at the same it is also possible to measure the time-of-flight distribution of the extracted ions, allowing for determining the corresponding velocity. Although the main focus of attention lies on the deterministic extraction of single ions, time-of-flight measurements were also conducted for ion crystals consisting of two  $^{40}\text{Ca}^+$  ions.

Figure 7.11(a) shows the time-of-flight distribution for two-ion crystals based on 93 successful extractions without any aperture plates in front of the detector, with the bin size of the histogram being 10 ns. The mean value for the first detected ion (white bins) equals  $12.699 \mu\text{s}$  with a  $1\sigma$ -error of 28 ns (light gray line) and  $12.725 \mu\text{s}$  with a  $1\sigma$ -error of 29.5 ns (gray line) for the second ion (gray bins), respectively. The difference in arrival time between the first and the second ion amounts to  $\overline{\Delta t} = 26.3 \text{ ns}$  which is mainly caused by the Coulomb interaction. Hence, the ions maintain their relative positions during the extraction which might be important for the implantation of a whole crystal with one extraction event or the post-separation of the  $^{40}\text{Ca}^+$  ions from prospective dopant ions utilizing the electrostatic einzel-lens (see also chapter 8.2.4). Additionally, the mean value for the time-of-flight for both detection events (dark gray bins) adds up to  $12.715 \mu\text{s}$  with a  $1\sigma$ -error of 26 ns (dark gray line).

The corresponding time-of-flight distribution for single ions is depicted in Fig. 7.11(b). It is based on 123 successful extractions out of 139 shots in total, resulting in a detection efficiency of  $88.5^{(+2.7)}_{(-3.3)} \%$ . The bin size of the histogram equals 2 ns. A Gaussian fit (red curve) of the data leads to an average flight time of  $14.74 \mu\text{s}$  with a  $1\sigma$ -error of 4.75 ns. As the measurements were conducted through the 1 mm aperture (see also chapter 7.2.6),

the effective distance between the trap center and the detector equals 287 mm, leading to an average velocity of  $\bar{v} = 19.47$  km/s with a  $1\sigma$ -velocity fluctuation of  $\Delta v = 6.3(6)$  m/s.

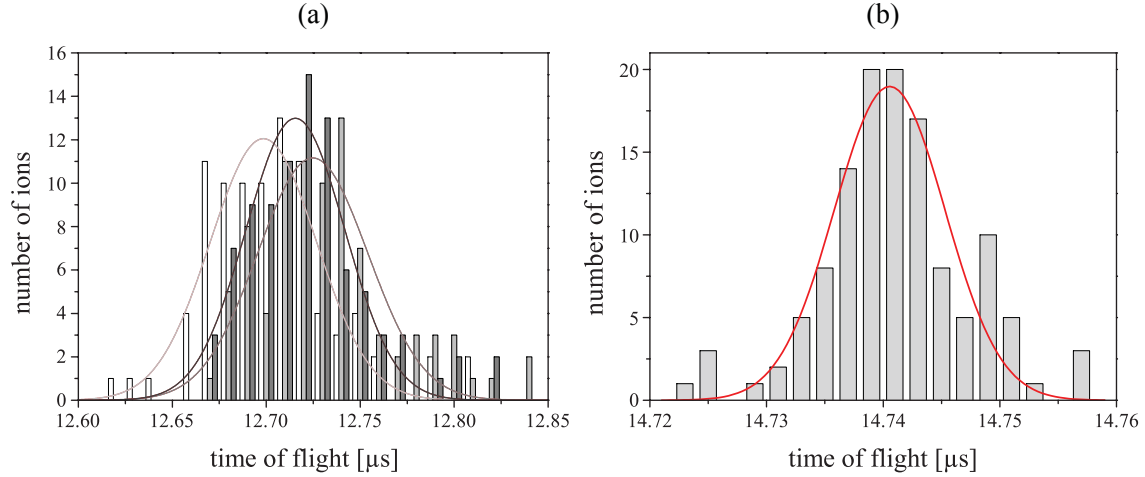
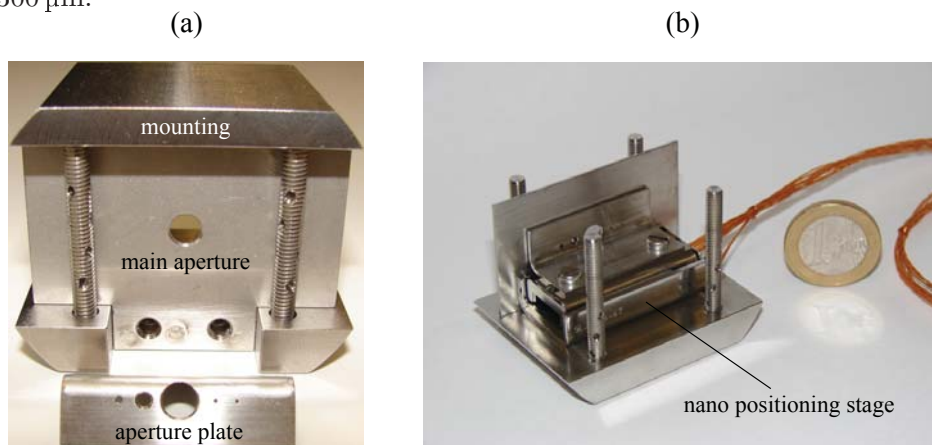


**Figure 7.11:** Time-of-flight measurements for ion crystals consisting of one and two  $^{40}\text{Ca}^+$  ions. All measurements were conducted with an rf trigger phase of  $260^\circ$ . (a) Time-of-flight distribution for two-ion crystals based on 93 successful extractions without any aperture plates in front of the detector [Fic09b]. The bin size of the histogram is 10 ns. The mean value for the first detected ion (white bins) amounts to  $12.699 \mu\text{s}$  with a  $1\sigma$ -error of 28 ns (light gray line) and for the second ion (gray bins) to  $12.725 \mu\text{s}$  with a  $1\sigma$ -error of 29.5 ns (gray line), respectively. The difference in arrival time between the first and the second ion equals  $\overline{\Delta t} = 26.3$  ns. Additionally, the mean value for the time-of-flight for both detection events (dark gray bins) adds up to  $12.715 \mu\text{s}$  with a  $1\sigma$ -error of 26 ns (dark gray line). (b) Time-of-flight distribution for single ions based on 123 successful extractions out of 139 shots in total through the 1 mm aperture [Sch09a]. The bin size of the histogram is 2 ns. A Gaussian fit (red curve) of the data leads to an average time of  $14.74 \mu\text{s}$  with a  $1\sigma$ -error of 4.75 ns. Note that the different average time with respect to (a) is caused by a repositioning of the detector backwards due to the installation of the movable aperture plate (see also chapter 7.2.6), and that the improvement of the  $1\sigma$ -error is mainly due to the enhancement of the electronics of the phase synchronization circuit (see also appendix A).

For the measurement at hand, the relative velocity uncertainty therefore amounts to  $\Delta v/v = 3.2 \times 10^{-4}$  with the possibility of further reduction by a post-acceleration of the extracted ions. Comparing the measured  $1\sigma$ -errors from Fig. 7.11(a) and (b) also shows, that it was possible to reduce the  $1\sigma$ -error by a factor of 6 which was mainly achieved by an enhancement of the electronics of the phase synchronization circuit (see also appendix A).

### 7.2.6 Determination of the beam divergence

In order to determine the beam divergence of our single-ion source, an additional movable aperture plate was installed in front of the detector. Consisting of stainless steel, the aperture plate features hole diameters ranging from 5 mm down to 300  $\mu\text{m}$ . It is mounted on a nano positioning stage from SmarAct<sup>7</sup> which allows for moving the aperture plate with an accuracy of a few tens of nanometers. An internal sensor module guarantees that the absolute position of the stage is kept constant. Using a special software library which was provided by the manufacturer, it is also possible to control the nano positioning stage via the experimental control system, allowing for a future automation of the alignment process. A fixed aperture with a diameter of 5 mm in front of the aperture plate and the nano positioning stage guarantees that the trajectories of the extracted ions are constricted to the chosen aperture. The distance between the fixed aperture and the aperture plate equals 300  $\mu\text{m}$ .



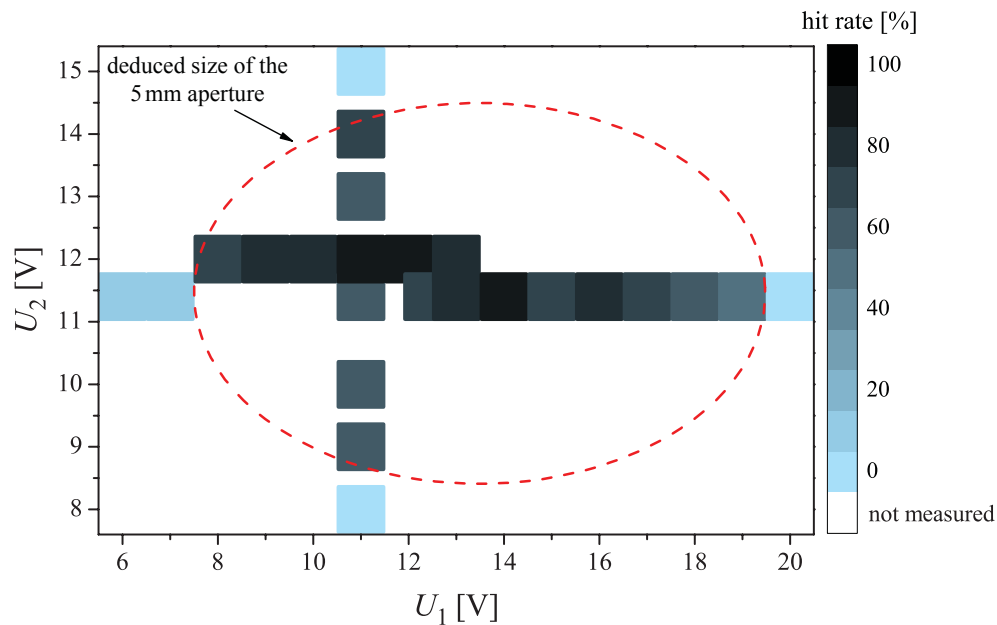
**Figure 7.12:** Movable aperture plate used for the determination of the beam divergence. (a) Front view showcasing the aperture plate which features hole diameters ranging from 5 mm down to 300  $\mu\text{m}$  (from left to right: 1 mm, 2 mm, 5 mm, 500  $\mu\text{m}$ , 300  $\mu\text{m}$ ), the main entrance aperture with a diameter of 5 mm as well as the mounting. (b) Rear view showing the aperture plate mounted on the nano positioning stage<sup>7</sup> with a 1 EUR coin for size comparison.

Figure 7.12 shows pictures of the aperture plate, the main entrance aperture, the mounting as well as the nano positioning stage with a 1 EUR coin for size comparison. Due to the installation of the movable aperture plate, the detector was repositioned backwards, effectively increasing the distance between the trap center and the detector from 247 mm to 287 mm. The beam divergence is then determined by scanning the beam over the different apertures by altering the deflection voltages.

<sup>7</sup> *SL-2040*, SmarAct GmbH, Oldenburg, Germany, <http://www.smaract.de>

### 5 mm aperture

Starting with the 5 mm aperture, the first step was to find the center of the aperture by gradually changing the deflection voltages. From there on, a consecutive reduction of the aperture size allows for determining the spatial expansion of the generated ion beam by simultaneously monitoring the hit rate on the detector. In the following, the voltage  $U_1$  indicates the potential between the two trap blades which carry the rf voltage, whereas  $U_2$  stands for the potential between the other two blades where the rails are only supplied with dc voltages for compensating the micromotion. Figure 7.13 shows the hit rate as a function of the deflection voltages. Each data point consists of a total of 10 individual measurements with ion crystals of varying size.



**Figure 7.13:** Hit rate as a function of the deflection voltages for the 5 mm aperture.  $U_1$  and  $U_2$  indicate the potential applied between two opposing blades. The scan clearly shows the edge of the aperture (dashed red circle) by a sharp decrease of the hit rate. All measurements were conducted with an rf trigger phase of  $260^\circ$ . [Fic09b]

As one can see, the scan clearly shows the edge of the aperture (dashed red circle) which is marked by a sharp decrease of the hit rate. By changing  $U_1$  and  $U_2$  over a voltage range of about 10 V and 5 V respectively, we were able to detect ion crystals consisting of up to 6  $^{40}\text{Ca}^+$  ions with an efficiency of more than 90 %. In addition, it was possible to determine the deflection voltages which were necessary in order to centrally shoot through the 5 mm aperture. Using these voltages as starting point, the next step was to reduce the size of the aperture from 5 mm down to 1 mm.

### 1 mm aperture

Figure 7.14 shows the corresponding scan for the 1 mm aperture, with the hit rate again being plotted as a function of the deflection voltages. As in case of the 5 mm aperture, the scan clearly shows the edge of the 1 mm aperture which is depicted as dashed red circle. Due to the reduced size of the aperture, the voltage range in which ions can be efficiently detected is also reduced to 2 V in case of  $U_1$  and 1 V in case of  $U_2$ , respectively.

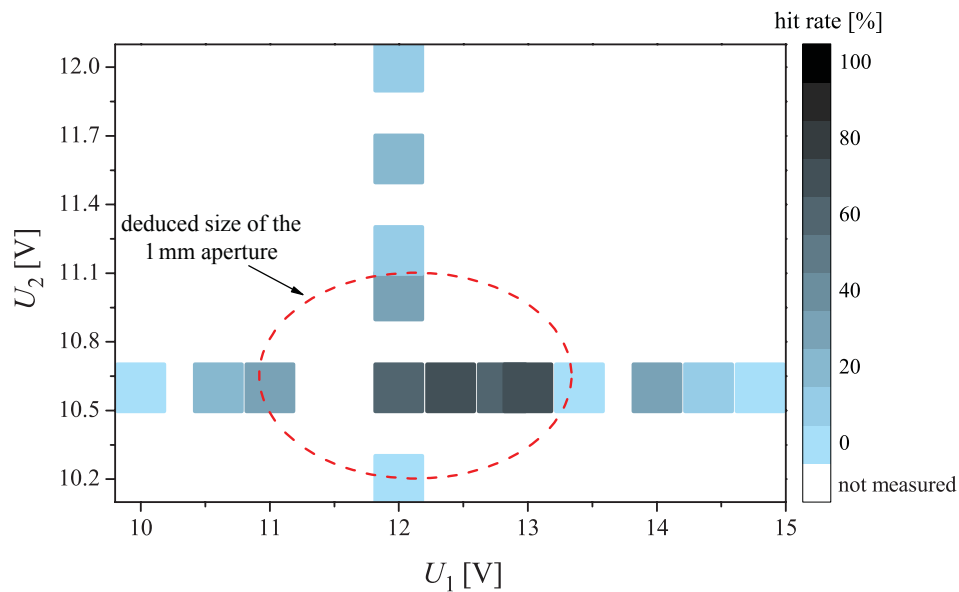


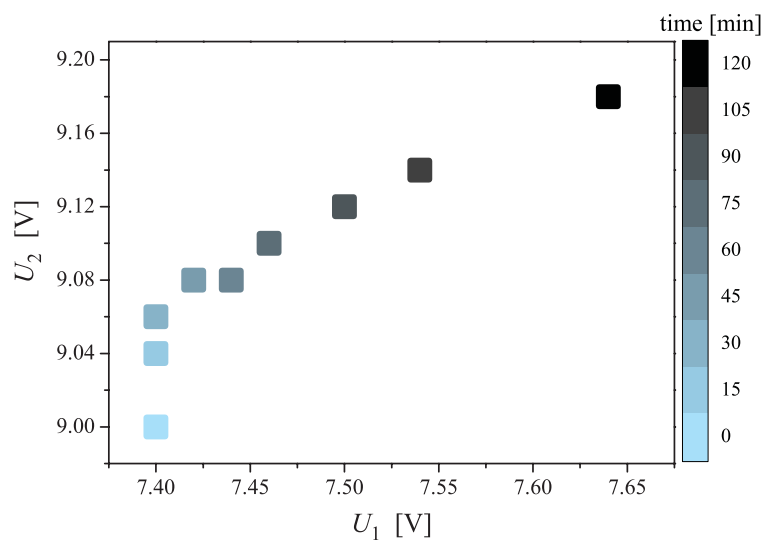
**Figure 7.14:** Hit rate as a function of the deflection voltages for the 1 mm aperture.  $U_1$  and  $U_2$  again indicate the potential applied between two opposing blades. As in case of the 5 mm aperture, the scan clearly shows the edge of the 1 mm aperture, which is depicted as dashed red circle. All measurements were conducted with an rf trigger phase of  $260^\circ$ . [Fic09b]

However, as ion crystals consisting of up to 7 ions were extracted out of the trap, the measured hit rate in the center of the aperture slightly decreased to 78 % as not all of the extracted ions passed through the 1 mm aperture and arrived at the detector. Taking only single ions into account, hit rates of up to 88.5 % were achieved, see also Fig. 7.11(b).

### 300 $\mu\text{m}$ aperture

Using the smallest available aperture with a diameter of only 300  $\mu\text{m}$ , a scan of the voltages is no more possible. Due to a partial cut-off of the ion beam by the aperture, the hit rate for single ions is reduced from about 90 % to 68.6 %. The value is based on 83 successful extractions of single ions out of 121 shots in total. However, taking into account the

detector efficiency of about 90 %, one can still deduce a  $1\sigma$ -spot radius of  $83^{(+8)}_{(-3)} \mu\text{m}$  for the trajectories of the extracted ions if one assumes a Gaussian spatial distribution for the generated single-ion beam, with the error being due to counting statistics. With an effective distance of 257 mm between the trap center and the movable aperture plate, this amounts to a full-angle beam divergence of  $600 \mu\text{rad}$ . It has to be noted that this value is an upper limit as the measurement was affected by a measured drift of the ion beam of about  $15 \mu\text{m}/\text{min}$ , possibly caused by temperature drifts of the setup or a displacement of the ions due to patch electric fields on the insulating surfaces between the electrodes.



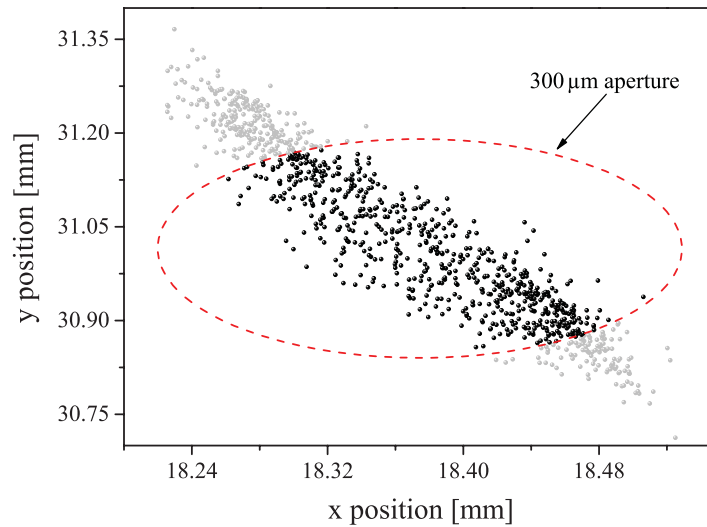
**Figure 7.15:** Variation of the optimal deflection voltages  $U_1$  and  $U_2$  during a time span of two hours. The change in voltages compensates for the drift of the ion beam, keeping the hit rate for single ions constant at about 70 %. The overall difference in the deflection voltages with respect to Fig. 7.13 and Fig. 7.14 is caused by long term drifts of the setup, as these measurements were conducted at different days. [Fic09b]

Figure 7.15 shows the variation of the optimal deflection voltages  $U_1$  and  $U_2$  during a time span of two hours in order to compensate for the drift of the ion beam, keeping the hit rate for single ions constant at about 70 %. The overall difference in the deflection voltages with respect to Fig. 7.13 and Fig. 7.14 is caused by long term drifts of the setup as not all measurements were conducted at the same day.

### 7.3 Comparison between simulation and experiment

In order to compare the numerical simulations with the experimental results, one has to conduct the simulations with the same set of parameters as used in the experiment,

namely an initial ion temperature of  $T = 2$  mK, an rf trigger phase of  $260^\circ$  and the optimal deflection voltages  $U_1 = 7.5$  V and  $U_2 = 9.1$  V for the  $300\ \mu\text{m}$  aperture. Using these parameters, the simulation yields a velocity fluctuation of  $\Delta v_{\text{sim}} = 2.7$  m/s which is by a factor of 2.3 smaller than the experimentally determined value of  $\Delta v_{\text{exp}} = 6.3(6)$  m/s. Comparing the corresponding mean velocities, the deviation is less, with the simulated value  $\bar{v}_{\text{sim}} = 22.36$  km/s being by a factor of 1.1 larger than the measured value  $\bar{v}_{\text{exp}} = 19.47$  km/s.



**Figure 7.16:** Comparison of the simulation with the experiment. The spot diagram has been enlarged by a factor 2.3 which was derived from a comparison of the simulated and experimentally determined velocity fluctuation. Black spots illustrate ions that would have passed the  $300\ \mu\text{m}$  aperture (dashed red circle) whereas gray spots are blocked by the aperture. According to the simulation, 65 % of the extracted ions can be detected after the aperture which is in good agreement with the experimental result yielding a detection efficiency of 68.6 %. Note that the spot diagram is not a Gaussian distribution and is displaced by a few millimeters due to the deflection voltages  $U_1 = 7.5$  V and  $U_2 = 9.1$  V. [Fic09b]

If one now assumes that the factor 2.3 also holds for the spatial spreading of the spot, it is also possible to compare the simulation with the measurements conducted through the  $300\ \mu\text{m}$  aperture by enlarging the simulated spot diagram by the same factor. Figure 7.3 shows the enlarged spot diagram with the  $300\ \mu\text{m}$  aperture being depicted as dashed red circle. Black spots illustrate ions that would have passed the aperture whereas gray spots are blocked. According to the simulation, 65 % of the extracted ions can be detected after the aperture which is in good agreement with the experimental result yielding a detection efficiency of 68.6 % (see also chapter 7.2.6). Taking into account that the simulated spot diagram again resembles the shape of an oval, this might be an indication that the real spot is also not Gaussian distributed.

In order to reduce the spatial spreading and to allow for an efficient focusing of the generated single-ion beam, it is therefore important to align the trap axis to the optical axis as accurately as possible while at the same time restricting the usage of the deflection electrodes to a minimum. As a consequence, the detector chamber has been attached to a specifically designed translation stage, see also Fig. 7.17. In combination with a membrane bellows, the translation stage allows for rotating the detector chamber in horizontal and vertical direction with respect to the trapping position of the ion, compensating any misalignment between the trap axis and the optical axis of the utilized electrostatic einzel-lens (see also chapter 8).

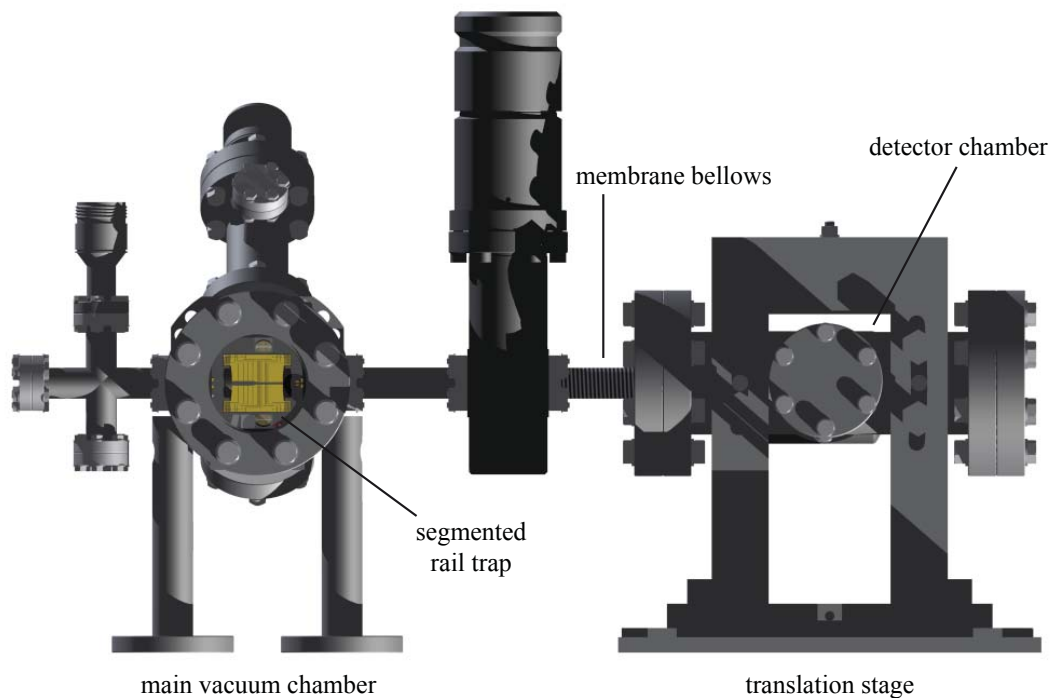


**Figure 7.17:** Schematic drawing of the enhanced UHV setup [Sch10]. A membrane bellows in combination with a specifically designed translation stage allows for rotating the detector chamber in horizontal and vertical direction with respect to the trapping position of the ion. For reasons of clarity, most of the remaining parts of the UHV setup have been omitted (see Fig. 4.2 for a complete view).

Despite the good agreement of the simulations with the experimental results, it has to be noted that a few inconsistencies still remain. From the simulation, one can deduce that the trap is tilted by an angle of  $4.2^\circ$  to the  $x$ -axis and  $7.2^\circ$  to the  $y$ -axis, respectively. However, such a huge misalignment should be visible to the naked eye. In addition, the location of the simulated spot diagram with a displacement of about 18.4 mm in  $x$ -direction and 30 mm in  $y$ -direction is rather unlikely, as the inner diameter of the connection pieces between the

main vacuum and the detector chamber only equals 16 mm. These inconsistencies, as well as the rather large difference in the velocity fluctuations, can be explained by the ideal nature of the numerical simulations, not taking into account the non-perfect vacuum and a large number of mechanical parts of the UHV setup. Potential asymmetries of the trap blades as well as of the assembly are not considered, neither are patch electric charges on insulated surfaces or external stray fields. Nevertheless, the simulations have proven to be a valuable tool in order to better understand the behavior of our deterministic single-ion source and to further improve the experimental setup.

# Chapter 8

## Focusing ion optics

In order to utilize our novel single-ion source as a deterministic implantation tool, it does not suffice to generate a single-ion beam with a small divergence and narrow velocity distribution: the ion trajectories have to be focused down to a few nm, too. We have realized this goal by developing ion optics, which should be able to focus down the generated single-ion beam to the required nanometer regime, with  $1\sigma$ -spot sizes of around 1 nm being feasible without the need of additional optical elements. After an initial description of the theoretical foundations (8.1), the properties of the developed ion optics will be discussed by means of numerical ray tracing simulations (8.2), including a brief description of the different operating modes of an electrostatic einzel-lens and a comparison of different lens designs. The experimental realization and results will be presented in the following chapter (8.3).

### 8.1 Theoretical foundations

The operating mode of an electrostatic einzel-lens can be best understood by studying the motion of charged particles in an electrostatic field<sup>1</sup>. As we only consider rotationally symmetric lenses in the following, cylindrical polar coordinates are used, with the  $z$ -axis being the axis of symmetry of the lens system. Hence, Laplace's equation is given by

$$\frac{\partial^2 \Phi}{\partial z^2} + \frac{1}{r} \frac{\partial}{\partial r} \left( r \frac{\partial \Phi}{\partial r} \right) = 0 \quad (8.1)$$

with  $\Phi(r, z)$  denoting the electric potential.

---

<sup>1</sup> For this purpose, the notation and approach of [Hed00] will be used.

Because of the rotational symmetry, one can make an expansion of the potential in even powers of  $r$ :

$$\Phi(r, z) = \sum_{n=0}^{\infty} A_n(z) r^{2n} \quad (8.2)$$

Hence, using this expansion, equation (8.1) becomes

$$\Phi(r, z) = A_0(z) - \frac{A_0''(z)r^2}{2^2} + \frac{A_0^{(4)}(z)r^4}{2^2 \cdot 4^2} + \dots, \quad (8.3)$$

where the primes ( $'$ ) are used to denote differentiation with respect to  $z$ .

### Paraxial approximation

In order to derive the equation of paraxial motion, only terms up to second order are retained in equation (8.3), with higher order terms being necessary when considering aberration effects. Thus, as the axial potential  $V(z)$  is just  $A_0(z)$ , one can write the axial and radial components of the electric field as

$$E_z = -\frac{\partial\Phi}{\partial z} = -\Phi' \quad E_r = -\frac{\partial\Phi}{\partial r} = \frac{r}{2}\Phi'', \quad (8.4)$$

where the explicit reference to  $z$  is omitted. The equation of radial motion for a particle with charge  $q$ , which has the opposite sign as the potential, is then given by

$$m \frac{d^2 r}{dt^2} = qE_r = \frac{qr}{2}\Phi''. \quad (8.5)$$

In addition, as the axial velocity is much larger than the radial in these circumstances, the total energy of the particle can be written as

$$\frac{1}{2}m \left( \frac{dz}{dt} \right)^2 + qV = 0. \quad (8.6)$$

Thus, using equations (8.5) and (8.6), the equation of motion reduces to

$$\frac{d^2 r}{dz^2} + \frac{1}{2} \frac{\Phi'}{\Phi} \frac{dr}{dz} = -\frac{r}{4} \frac{\Phi''}{\Phi} \quad (8.7)$$

As one can see, equation (8.7) contains neither the charge of the particle nor its mass and is therefore valid for all kinds of charged particles, with the only constraint being that the potential should have a sign opposite to that of the charge of the particle to ensure a positive total energy. By introducing a reduced radius  $R = r\Phi^{1/4}$  (where  $\Phi$  must be read as  $|\Phi|$  for positive particles), equation (8.7) becomes

$$\frac{d^2 R}{dz^2} = -\frac{3}{16} R \left( \frac{\Phi'}{\Phi} \right)^2, \quad (8.8)$$

which is also known as the Picht equation [Pic32]. Using this equation, it is not difficult to show that all electrostatic lenses, which have uniform potential regions to each side, are converging. In the following, we consider a ray incident parallel to the optical axis at a reduced radius  $R_1$  with the assumption, that this reduced radius does not change in passing through the lens. Naturally,  $r$ , the true radius, will change or there would be no lens action, but the change in  $\Phi$  will act in the opposite direction. A formal integration of the Picht equation yields

$$\int_{-\infty}^{\infty} R'' dz = R'_2 - R'_1 = -\frac{3}{16} R_1 \int_{-\infty}^{\infty} T^2 dz, \quad (8.9)$$

with  $T(z) = \Phi'(z)/\Phi(z)$ . As the incident ray is parallel to the optical axis,  $R'_1 = 0$  ( $R_1 = \text{const}$ ), with  $R_2$  thus having the opposite sign to  $R_1$ . Hence,  $R'_2$  can be written as

$$R'_2 = r'_2 \Phi_2^{1/4} + \frac{r_2}{4} \Phi_2^{-3/4} \Phi'_2, \quad (8.10)$$

where one can assume that  $\Phi'_2 \cong 0$  without loss of generality, with  $\Phi_2^{1/4}$  being intrinsically positive. Hence,  $r'_2$  has the same sign as  $R'_2$ , meaning that for rays incident above the optical axis, the emergent ray moves towards the optical axis, resulting in a convergent lens action.

### Aberration errors

Just as conventional optical lenses, electrostatic lenses are subject to the same optical aberrations, with the effects sometimes being even worse as it is not possible to use materials of different dispersion to reduce chromatic aberration or to grind surfaces of special forms to reduce spherical and other aberrations. In case of our electrostatic einzel-lens, the main aberration errors are spherical and chromatic aberration, see Fig. 8.1.

Spherical aberration is caused by a displacement of the trajectories of the extracted ions with respect to the optical axis of the einzel-lens, either due to a radial velocity component or because of a misalignment of the generated ion beam, see also Fig. 8.1(a). On the other hand, chromatic aberration is generated by velocity fluctuations of the extracted particles (see Fig. 8.1(b)), which – in our case – are mainly caused by minor variations of the time of extraction with respect to the phase of the rf voltage, see also chapter 7. Although it is not possible to avoid such spherical and chromatic aberration with rotationally symmetric electrostatic einzel-lenses in a charge-free space according to Scherzer's theorem [Sch36], our setup still allows for correcting these errors by utilizing time-dependent electrostatic fields, see chapter 8.2.3. For a more detailed discussion of aberration errors, see [Hed00].

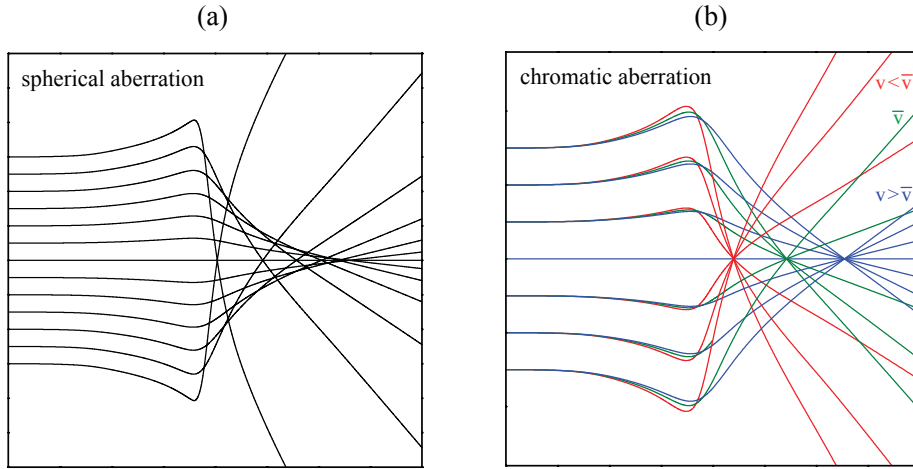


**Figure 8.1:** Simulated ion trajectories illustrating aberration errors occurring at the electrostatic einzel-lens. (a) Spherical aberration. (b) Chromatic aberration. [Fic09a]

## 8.2 Ion ray tracing simulations

Due to the small beam divergence and narrow velocity distribution of our single-ion source, the focusing optics can be kept simple without sophisticated aberration corrections [Wei01, Wei02, Sze88, Haw89], with a rotationally symmetric simple electrostatic einzel-lens already yielding adequate results. This type of ion lens consists of three electrodes where the first and the third electrode are on the same potential. The electrostatic potential thereby resembles a saddle surface and can be generated in two different modes: the decel-accel and the accel-decel mode, see also Fig. 8.2. The former mode is achieved when the center electrode is biased to a voltage with the same sign as the charged particle (in our case a positive voltage), with the lens operating with a voltage of opposite sign with respect to the charged particles in the accel-decel mode, respectively.

Both modes offer different advantages [Lie08]: In the accel-decel mode, the undesirable chromatic and spherical aberration is smaller than in the decel-accel mode. The chromatic aberration is thereby reduced due to higher velocities of the particles inside of the lens, resulting in a lower relative velocity spread  $\Delta v/v$ . Additionally, spherical aberration is smaller because the ion trajectories are closer to the optical axis during their passage through the lens [Shi83] as they are always deflected towards the optical axis (see Fig. 8.2(b)), whereas in the decel-accel mode the ions diverge at first before being focused to the center (see Fig. 8.2(a)). On the other hand, the decel-accel mode offers three essential advantages: Firstly, the lens requires lower center electrode voltages for reaching a similar focal length. In addition, by applying positive voltages, it is possible to correct

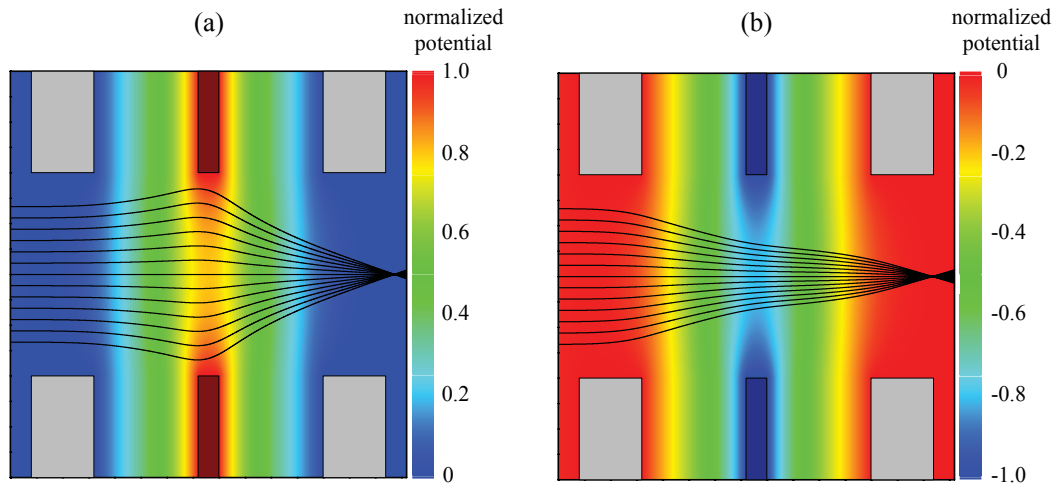


**Figure 8.2:** Operating modes of an electrostatic einzel-lens. Depicted are schematic drawings of the cross-section of the einzel-lens with the corresponding potential distribution and ion trajectories. Grounded electrodes are colored light gray. (a) In the decel-accel mode, the center electrode (dark red) is biased to a voltage with the same sign as the charged particles (in our case a positive voltage). (b) In the accel-decel mode, the center electrode (dark blue) is supplied with a voltage of the opposite sign with respect to the charged particles. [Fic09a]

for spherical aberration by switching the lens to a higher voltage, i.e. by increasing the potential while the particle is passing through the lens [Sch02], see chapter 8.2.3. A further increase of the potential will even allow for utilizing the lens as a deflector for different ion species, see also chapter 8.2.4.

### 8.2.1 Comparison of different lens designs

Various electrode shapes have been developed and discussed in order to optimize the properties of electrostatic einzel-lenses [Haw89, Lie08, Shi83, Rid78, Sep60]. Generally, the most important feature is a perfect alignment of the electrodes in combination with voltage stability, which, on the one hand, depends on the voltage supply, and on the other hand on the insulating material between the electrodes. As for the properties of the lens, one can assume that the smaller the dimensions of the lens, the better its focusing properties are. However, the possibility to reduce the lens dimensions is limited by the extension of the ion beam as spherical aberration effects become more noticeable when the size of the beam approaches the lens diameter. In order to assure that the extracted ions easily pass through the lens and spherical aberration is not dominant, lenses with a minimal entrance aperture of 1 mm were designed.

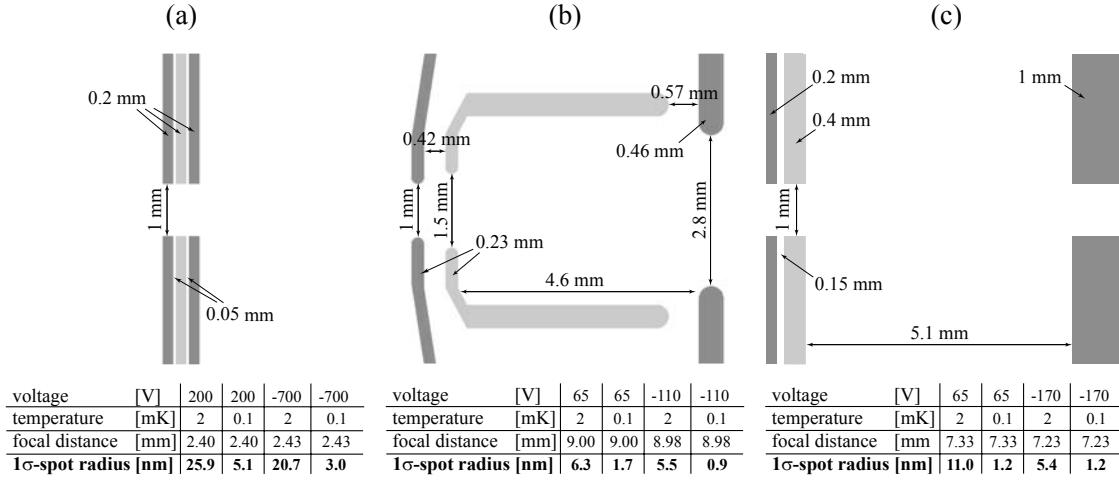


**Figure 8.3:** Comparison of three einzel-lenses with different electrode shapes. Dc electrodes are depicted in light gray, whereas grounded electrodes are colored dark gray, respectively. (a) Non-optimized simple einzel-lens, allowing for focusing down the generated single-ion beam by a maximum factor of about 1200. (b) Specially shaped einzel-lens featuring a design developed by Septier [Sep60], where the minimal achievable  $1\sigma$ -spot radius is more than three times smaller than the one of the non-optimized einzel-lens depicted in (a). (c) Custom-made einzel-lens, which has been implemented in our setup. The focusing properties are similar to the lens design depicted in (b). Aside from a maximum focusing factor of approximately 3000, simulations predict optimal results for the decel-accel mode (center electrode repulsive), which is important for the implementation of spherical aberration correction and for using the einzel-lens as an ion deflector. [Fic09b]

As a rule of thumb, the properties of the lens improve when the first electrode is thinner than the second one, with a minimal gap spacing in between. Conversely, the distance between the second and the third electrode has to be much larger in order to minimize the focal spot size, see Fig. 8.3(a) and (c). Another possibility to improve the focusing properties is to change the shape of the electrodes, e.g. to a special design developed by Septier [Sep60]. The design is based on a lens with hyperbolic field distribution which has good imaging characteristics even for steeply inclining beams, but has been modified to reduce spherical aberration, see Fig. 8.3(b). Each of the three electrodes has a different aperture and a completely different shape. For an optimal adjustment of the lens to our single-ion source, a huge range of different lenses was developed and the achievable spot sizes were simulated. Figure 8.3 shows three different types of einzel-lenses to demonstrate the enormous influence of the lens design, each with the focal distance and the appropriate optimized focal spot size at different voltages and temperatures.

A non-optimized einzel-lens made out of three equivalent electrodes, which is operated in the decel-accel mode, allows for focusing the non-deflected ion beam down to a  $1\sigma$ -spot radius of 25.9 nm for an initial ion temperature of 2 mK (5.1 nm @ 100  $\mu$ K), see Fig. 8.3(a). Slightly better results are obtained in the accel-decel mode, where the  $1\sigma$ -spot radius amounts to 20.7 nm for 2 mK laser-cooled ions (3.0 nm @ 100  $\mu$ K). Although this simple einzel-lens already achieves nanometer spot sizes, the required voltages, especially in the accel-decel mode, are too high to ensure the insulating property of the spacer between the electrodes. Using a design resembling the one developed by Septier, the lens depicted in Fig. 8.3(b) is able to achieve a focal  $1\sigma$ -spot radius of 6.3 nm in the decel-accel mode for an initial ion temperature of 2 mK, with the simulated spot radius decreasing to 1.7 nm for ions cooled to the motional ground state (100  $\mu$ K). Even better are the results for the accel-decel mode, where the  $1\sigma$ -spot radius amounts to 5.5 nm for an initial ion temperature of 2 mK and only 0.9 nm for 100  $\mu$ K, respectively. However, the experimental realization of this lens is quite difficult because of the different apertures, inclined electrodes and rounded edges. Hence, we developed a more simple design with similar focusing properties, which will be discussed in detail in the following chapter, see also Fig. 8.3(c) for a schematic drawing.

### 8.2.2 Characterization of the einzel-lens

The developed einzel-lens consists of three stainless steel electrodes, which feature an outer diameter of 27 mm. The first electrode has a thickness of 0.2 mm with an inner diameter of 1 mm, the second electrode has a thickness of 0.4 mm and an inner diameter of 1 mm, respectively. The third electrode consists of two parts: The first part is a cylindrical shaped spacer with an inner diameter of 16 mm and a thickness of 4.95 mm whereas the second part consists of a stainless steel plate with a thickness of 1 mm, featuring a 1 mm aperture which is also used as mounting for all other electrodes. The first and third electrode are conductively interconnected whereas the second electrode is electrically insulated by using Kapton sheets with a thickness of 0.15 mm, see also Fig. 8.3(c) for a schematic drawing. Figure 8.4 shows pictures of the experimental realization: Depicted are the different components, the assembled einzel-lens with a one-cent coin for size comparison as well as a picture of the einzel-lens mounted inside of the detector chamber.

For the accel-decel mode, it is possible to reach a  $1\sigma$ -spot radius of 1.2 nm for 100  $\mu$ K laser-cooled ions (5.4 nm @ 2 mK), which is comparable to the results for the special shaped lens from Septier. Although the numerical results in the accel-decel mode for 2 mK laser-cooled ions are better than in the decel-accel mode, meaning that this mode exhibits larger

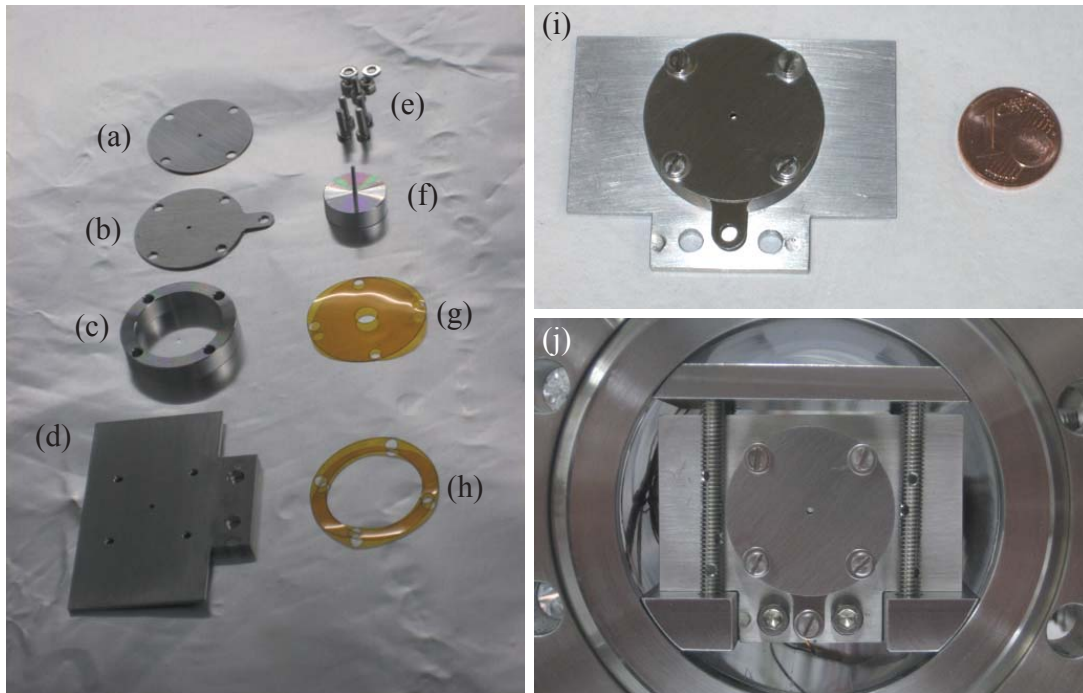


**Figure 8.4:** Pictures of the developed electrostatic einzel-lens. (a) First electrode. (b) Second electrode. (c) Spacer. (d) Third electrode. (e) Mounting screws. (f) Alignment pin. (g) Kapton sheet between 1st and 2nd electrode. (h) Kapton sheet between 2nd and 3rd electrode. (i) Picture of the assembled einzel-lens with a one-cent coin for size comparison. Under typical operating conditions, the center electrode is supplied with a voltage of 65 V. (j) Picture of the assembled einzel-lens mounted inside of the detector chamber.

chromatic aberration effects, we have chosen to operate the lens in the decel-accel mode in order to be able to implement spherical aberration correction and to utilize the lens as a switchable deflector for ions. For an initial ion temperature of 2 mK, one can achieve a  $1\sigma$ -spot radius of 11.0 nm, with a  $1\sigma$ -spot radius of 1.2 nm being feasible for ground-state cooled ions, respectively. Figure 8.5 shows the induced potential for the developed einzel-lens, when a voltage of 65 V is supplied to the center electrode, illustrating the function in the decel-accel mode.

Before the ions enter the lens, they are slowed down and deflected slightly away from the optical axis. After a further defocusing, the ions reach the highest point of the potential which equals approximately 60 V, thus having the slowest velocity. Afterwards, the ions are accelerated out of the lens and are strongly focused towards the optical axis. The focusing effect thereby relies on the different ion velocities inside of the lens potential: The longitudinal velocity of the ion is higher during the defocusing period while climbing to

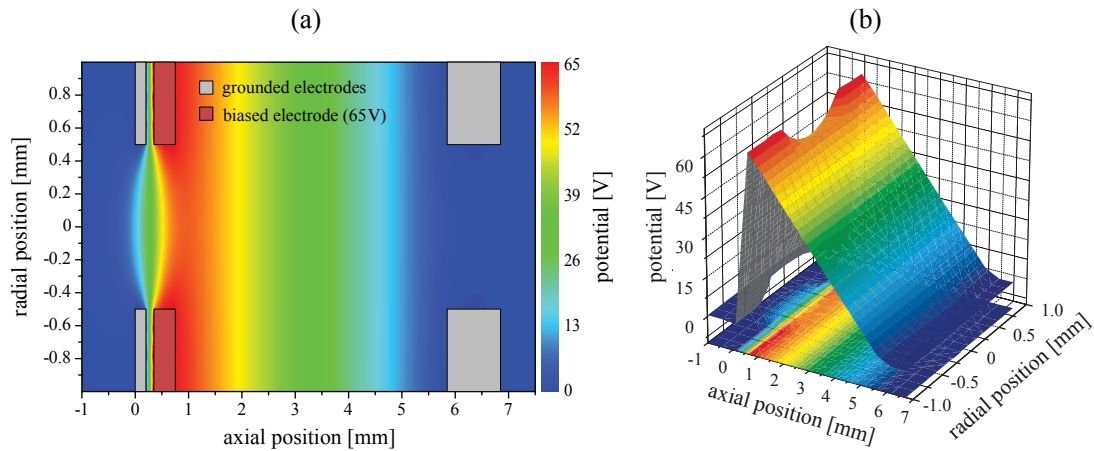


**Figure 8.5:** Potential distribution of the electrostatic einzel-lens. (a) Potential distribution of the lens from Fig. 8.3(c), when the central electrode (dark red) is biased to 65 V. Grounded electrodes are colored light gray. (b) Three-dimensional view of the potential distribution. [Fic09b]

the maximum potential, whereas it is lower during the focusing period thereafter. Hence, a focusing force is generated even for completely symmetric lens constructions as shown in Fig. 8.3(a), also explaining the lower voltages for lens designs, where the focusing space is stretched by positioning the last electrode further away from the center electrode, see Fig. 8.3(b) and (c).

Figure 8.6(a) shows the trajectories of extracted  $^{40}\text{Ca}^+$  ions passing through the electrostatic einzel-lens, with Fig. 8.6(b) depicting the resulting spot diagram in the focal plane at a distance of 7.33 mm from the main entrance aperture. When the ions are extracted with an initial temperature of 2 mK and the lens is biased to 65 V, the focal spot occurs half a millimeter after the last electrode and shows a  $1\sigma$ -spot radius of only 11 nm. Reducing the voltage of the center electrode moves the focal plane further behind the lens, almost without impairment of the focusing properties. For instance, lowering the voltage to 50 V generates the spot 8.5 mm after the last electrode but the spot radius is hardly affected and remains at 12 nm. Hence, the focal distance can be adjusted over a few mm without a severe loss in performance by simply changing the voltage of the center electrode. However, the varying range should be kept as small as possible since a further decrease in voltage increases the spot radius, see also Fig. 8.7(a). A reduction to 25 V, for example, enlarges the spot radius to 52 nm, with the focal plane already being located 110 mm behind the entrance aperture of the einzel-lens.

As already mentioned in previous chapters, our ion source is able to alter the trajectories of the extracted ions by biasing the deflection electrodes, allowing for correcting small

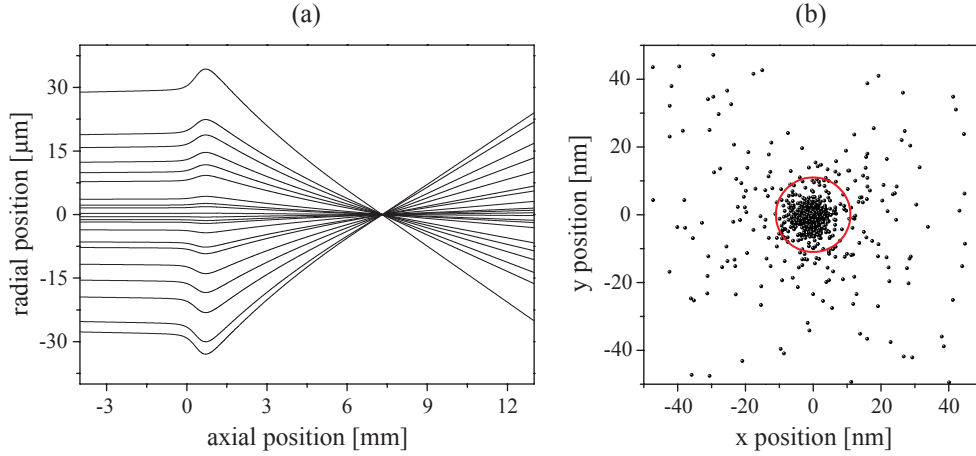


**Figure 8.6:** Ion trajectories passing through the electrostatic einzel-lens. (a) Trajectories of 2 mK cold  $^{40}\text{Ca}^+$  ions which are focused by the lens depicted in Fig. 8.3(c) to a  $1\sigma$ -spot radius of 11 nm. The lens is operated in the decel-accel mode at 65 V. (b) Resulting spot diagram in the focal plane around 0.5 mm after the last electrode of the lens. The red circle illustrates the  $1\sigma$ -spot radius. [Fic09b]

discrepancies in the alignment of the setup by a slight deflection of the beam towards the optical axis. The importance of shooting through the lens without even a small initial displacement of the ion beam is highlighted in Fig. 8.7(b). For example, a displacement of the incoming beam of half the aperture radius ( $250\ \mu\text{m}$ ) already annihilates the focusing properties: Besides a displacement of the outgoing beam in the opposite direction, the beam also diverges to similar spot dimensions as without ion optics. A further displacement even enlarges the spot size in the intended focal plane. Hence, for the required precise alignment, the deflection electrodes present the best way to aim the generated ion beam at the center of the lens aperture. A displacement of  $250\ \mu\text{m}$ , for example, can already be neutralized by applying a potential of 0.36 V to two opposing trap blades, only leading to a small increase of the  $1\sigma$ -spot radius from  $16.1\ \mu\text{m}$  to  $17.2\ \mu\text{m}$ . However, as already discussed in chapter 7.3, the course alignment should be done mechanically by moving the detector chamber itself (see also Fig. 7.17), restricting the usage of the deflection electrodes to a minimum.

### 8.2.3 Correction of the spherical aberration

One of the most advantageous properties of our setup is the fact, that the extraction process is synchronized to the phase of the rf voltage, with the relative velocity uncertainty being extremely low. Thus, the ions are well-defined in space and time during the whole extraction, as well as during the focusing process. With that, it is possible to switch the

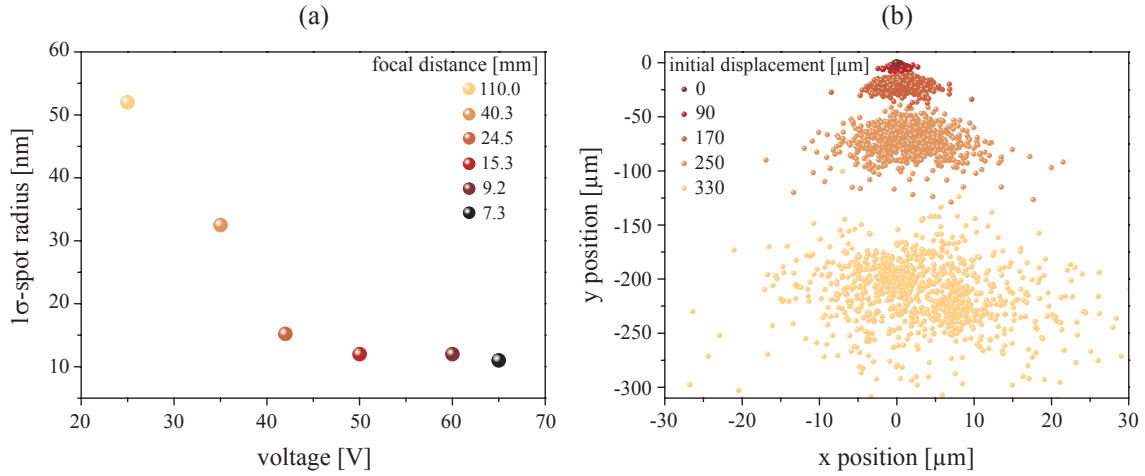


**Figure 8.7:**  $1\sigma$ -spot radius as a function of the lens voltage and the initial displacement of the ion beam. (a) Enlargement of the  $1\sigma$ -spot radius by applying smaller voltages to the center electrode of the lens. The focal plane moves away from the lens, with 65 V being the upper limit as higher voltages would generate a focus inside of the lens. (b) If the initial beam is displaced out of the center of the lens, the focusing properties of the lens worsen or even annihilate. Here, the focal plane as well as the lens voltage are kept constant at 0.5 mm and 65 V respectively, with the incoming beam being displaced in positive  $x$ -direction. [Fic09b]

lens to different voltages at different points in time, which allows for correcting aberration effects. When compared to the lens from Septier, our design shows a larger spherical aberration which slightly enlarges the spot radius from 6.3 nm to 11.0 nm for 2 mK cold ions, see also Fig. 8.3(b) and (c). According to Scherzer's theorem, it is not possible to avoid such spherical and chromatic aberration with rotationally symmetric electrostatic einzel-lenses in a charge-free space [Sch36]. Another way of interpreting the theorem is by stating the impossibility of the realization of a diverging lens. One way of circumventing this theorem is to utilize time-dependent electrostatic fields [Sch02] by simply switching the lens to another voltage at a well-defined time. This leads to the same forces a diverging lens would create, thus allowing for reducing the spherical aberration. Due to the fast increase of the lens potential at a specific time, the particle is accelerated and therefore slightly diverges. Hence, ions with outer trajectories react stronger to the potential variation and subsequently intersect the optical axis further away. However, the switching time, where the lens voltage is altered from one value to another, has to be accurately chosen and has to be as short as possible.

Utilizing our high voltage switches (see also chapter 6.1.1), we are able to vary the voltage within 5 to 10 ns, which is short enough to neglect additional energy broadening due to a

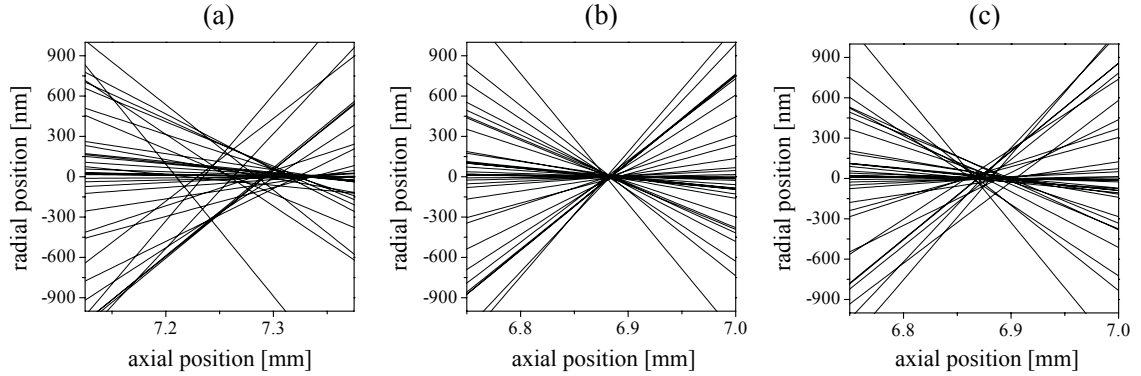


**Figure 8.8:** Zoom of the focal regions to show the effect of spherical aberration correction. All diagrams were calculated with an incoming beam featuring a  $1\sigma$ -spot radius of  $36\ \mu\text{m}$ . For the first two diagrams (a) and (b), the chromatic aberration effect is artificially removed by setting the velocity fluctuations of the ions to zero. (a) The uncorrected spot is achieved when the lens is constantly biased to  $65\ \text{V}$ , resulting in a  $1\sigma$ -spot radius of  $52\ \text{nm}$ . (b) The spherically corrected spot has a  $1\sigma$ -spot radius of only  $12\ \text{nm}$ .  $210\ \text{ns}$  after the ions have entered the lens, the voltage of the center electrode is switched from  $35\ \text{V}$  to  $85\ \text{V}$ . (c) The same incoming beam and correction settings of the lens as in (b) are used for the calculation of the trajectories, but with an added velocity fluctuation of  $6.3\ \text{m/s}$  to show the negative effect of the chromatic aberration of the lens. Here, the  $1\sigma$ -spot radius amounts to  $57\ \text{nm}$ . [Fic09b]

finite rise time of the electric field. However, the spherical aberration correction has to be adjusted to the incoming single-ion beam. According to simulations, the best results for  $2\ \text{mK}$  cold ions are obtained, when the lens is initially grounded, then being biased to  $60\ \text{V}$  exactly  $170\ \text{ns}$  after the ions have passed the first aperture. Thus, the  $1\sigma$ -spot radius in the focal plane can be nearly reduced by a factor of 2 from  $11.0\ \text{nm}$  down to  $6.0\ \text{nm}$ , with the same switching time and voltage reducing the focal  $1\sigma$ -spot radius for ground-state cooled ions from  $1.2\ \text{nm}$  to  $0.9\ \text{nm}$ , respectively.

If the dimensions of the ion beam are increased, the factor of improvement also increases slightly. For example, beam characteristics similar to the ones we expect in our experiment after perfectly aligning the the trap axis to the optical axis of the einzel-lens ( $1\sigma$ -spot radius of  $36\ \mu\text{m}$  and a maximum velocity uncertainty of only  $6.3\ \text{m/s}$ ) require different settings for the switching time and voltage, but the focal spot size is reduced by more than a factor of 2, see Fig. 8.8. Here, the voltage is switched from  $35\ \text{V}$  to  $85\ \text{V}$  exactly  $210\ \text{ns}$  after the ions have entered the lens, reducing the  $1\sigma$ -spot radius from  $138\ \text{nm}$  (when the lens is constantly biased to  $65\ \text{V}$ ) to  $57\ \text{nm}$ , see Fig. 8.8(c). The additional spread of the focal spot is therefore mainly due to the remaining chromatic aberration of the lens, which is caused by velocity fluctuations.

In order to show solely the improvement induced by the spherical aberration correction, the velocity fluctuations have been artificially removed in Fig. 8.8(a) and (b). Here, the  $1\sigma$ -spot radius is reduced from 52 nm to 12 nm. Note, that the spot in Fig. 8.8(a) does not show an accurate Gaussian distribution and therefore the measured value of 68.3% within 52 nm obviously cannot be read out from the plot. But Fig. 8.8(a) and (b) provide a good insight into the enhancement due to spherical aberration correction, whereas Fig. 8.8(c) shows the effect of chromatic aberration. So far, chromatic errors are not corrected by the developed ion optics, but this can also be implemented by using time-dependent electric fields [Sch02].

#### 8.2.4 Ion reflection and post-acceleration

Another advantage of the deterministic, triggered extraction is the possibility to reflect the cooling ions during the implantation process. Because of unavoidable heating processes during a possible separation of the ions inside of the trap [Row02], it is preferable to separate the  $^{40}\text{Ca}^+$  ions from the prospective dopant ions by reflecting them at the einzel-lens. Due to the different mass of the additionally loaded, sympathetically cooled ions compared to the  $^{40}\text{Ca}^+$  ions, the velocities of the extracted ions differ from each other. As the  $^{40}\text{Ca}^+$  ions arrive at different times at the einzel-lens, they can be easily reflected by applying higher voltages. Nitrogen, for instance, is accelerated in the simulation up to 36.2 km/s due to its smaller mass, thus arriving approximately 4.3  $\mu\text{s}$  earlier at the lens than the  $^{40}\text{Ca}^+$  ions. Hence, the lens has to be switched to a higher potential after the nitrogen particles have passed. According to simulations, the required voltage for reflection needs to be at least 115 V, a value which is experimentally feasible, see also Fig. 8.9.

By switching the lens voltage, it will also be possible to post-accelerate the extracted ions which will improve the focusing results even further as the chromatic aberration is reduced due to a smaller relative velocity fluctuation. A simple, cylindrical tube which is biased to a voltage of 10 kV already shows promising focusing effects when being switched off after the ions have entered the tube. First simulated results predict velocities above 200 km/s and focal  $1\sigma$ -spot sizes of less than 0.4 nm for ions cooled to the motional ground state. However, switching times have to be even more precise due to higher velocities and therefore shortened timescales, with the gained increase in spatial resolution being partly neutralized by straggling effects of the implanted ions inside of the target material.

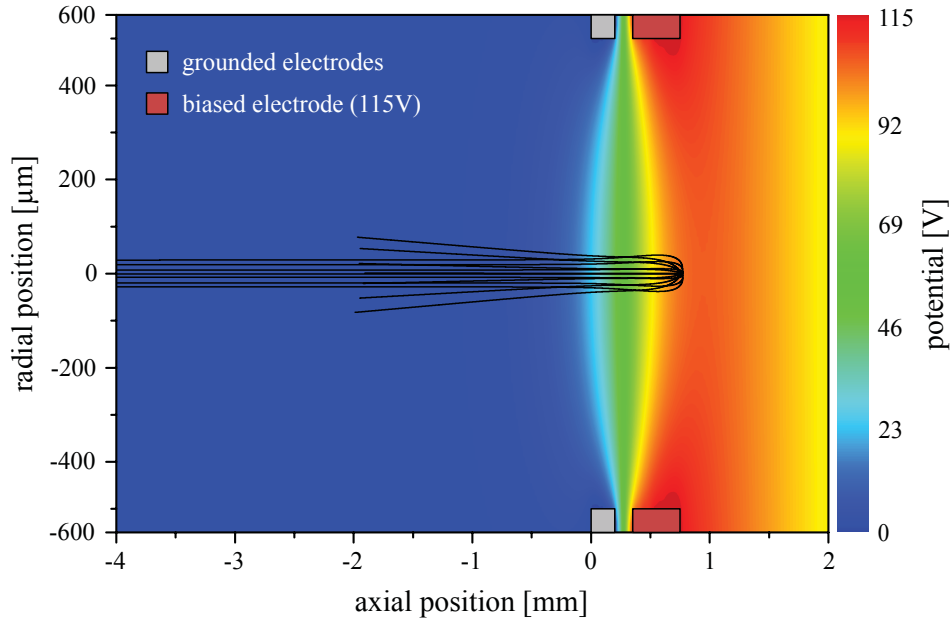


**Figure 8.9:** Trajectories of reflected  $^{40}\text{Ca}^+$  ions and potential distribution of the electrostatic einzel-lens for a voltage of 115 V at the center electrode (red). Grounded electrodes are depicted in light gray. [Fic09b]

## 8.3 Experimental results

### 8.3.1 Experimental determination of the spot size

To achieve an optimal alignment with respect to the optical axis of the einzel-lens, the radial adjustment of the ion beam is performed by utilizing the deflection electrodes of our segmented rail trap. Using the 1 mm aperture behind the einzel-lens, the optimal deflection voltages are retrieved by gradually changing them, maximizing the hit rate on the detector. As it turns out, the hit rate is very sensitive to changes of the deflection and compensation voltages, i.e. a minor change in the range of a few mV is already sufficient to miss the 1 mm aperture, effectively reducing the measured hit rate to zero. Hence, all presented measurements were conducted with a fixed set of deflection and compensation voltages in order to keep adjacent measurements consistent to each other.

For determining the spot size of the ion beam in the focal plane of the installed ion optics, a razor blade was attached behind the 2 mm aperture, effectively creating a well defined tearing edge. By stepwise moving the razor blade into the path of the generated ion beam, a gradual cut-off of the ion trajectories is achieved, leading to a reduction of the overall hit rate on the detector. The  $1\sigma$ -spot radius can then be derived by fitting these points with

an error function, which itself is obtained by integrating a Gaussian distribution which will be assumed for the radial cross-section of the single-ion beam:

$$f(x) = \int_{-\infty}^x \frac{c}{\sigma_r \sqrt{2\pi}} e^{-\frac{1}{2}\left(\frac{y-a}{\sigma_r}\right)^2} dy = \frac{c}{2} \left( 1 + \operatorname{erf} \left( \frac{x-a}{\sigma_r \sqrt{2}} \right) \right). \quad (8.11)$$

Here,  $\sigma_r$  denotes the radius of the ion beam measured with the razor blade, with  $a$  being the offset in  $x$ -direction. The parameter  $c$  is used as a scaling factor in order to account for the detector efficiency which has been experimentally measured to be 0.87 [Sch09a]. Note that in former measurements, the size of the ion beam was determined by shooting single ions through the 300  $\mu\text{m}$  aperture, yielding a  $1\sigma$ -spot radius of  $83^{(+8)}_{(-3)} \mu\text{m}$  and a full-angle beam divergence of 600  $\mu\text{rad}$  at a distance of 257 mm from the trap center, see also chapter 7.2.6. Here, 68.3 % of all detected ions were located inside of the stated  $1\sigma$ -spot radius. Hence, in order to compare these values with the current measurements, one has to convert them according to equation (8.11), resulting in a  $1\sigma_r$ -spot radius of  $55^{(+5)}_{(-2)} \mu\text{m}$ .

Because the exact focal distance of our einzel-lens is unknown, one would normally have to repeat the measurement described above for different spacings between the einzel-lens and the razor blade. However, our nano positioning stage is only capable of moving perpendicular to the ion beam, which means that the location of the focal plane of the einzel-lens has to be adjusted by changing the lens voltage. Measuring the spot radius for different lens voltages in the plane of the razor blade therefore should allow for obtaining the minimal spot radius. Since the time span needed for doing a single measurement is considerably long ( $\approx 0.5$  incidents per minute), the number of measurements taken for each blade position was reduced to a total of 10 individual shots with ion crystals consisting of up to six  $^{40}\text{Ca}^+$  ions. This was done in order to avoid changes of the deflection and compensation voltages, which would have been necessary to counteract long term drifts caused by a thermal expansion of the trap.

Figure 8.10 shows the hit rate as a function of the blade position for the optimal lens voltage of 62.5 V, yielding a  $1\sigma_r$ -spot radius of  $(1.2 \pm 0.5) \mu\text{m}$ . Compared to the original beam diameter of 55  $\mu\text{m}$ , our einzel-lens thus would be capable of focusing the ion beam by a factor of 46. However, in order to check whether the ion beam drifted during the course of the measurement, additional data points ( $\Delta$ ) were taken, revealing a drift in the range of a few tens of  $\mu\text{m}$ . In addition, as the measurement is based on the extraction of ion crystals (which was done because the loading of single ions was not possible in an acceptable time span), this also influences the behavior of the generated ion beam, not only changing the beam divergence but also the focusing characteristics at the electrostatic einzel-lens. Hence, we have come up with a very simple and robust procedure to facilitate the deter-

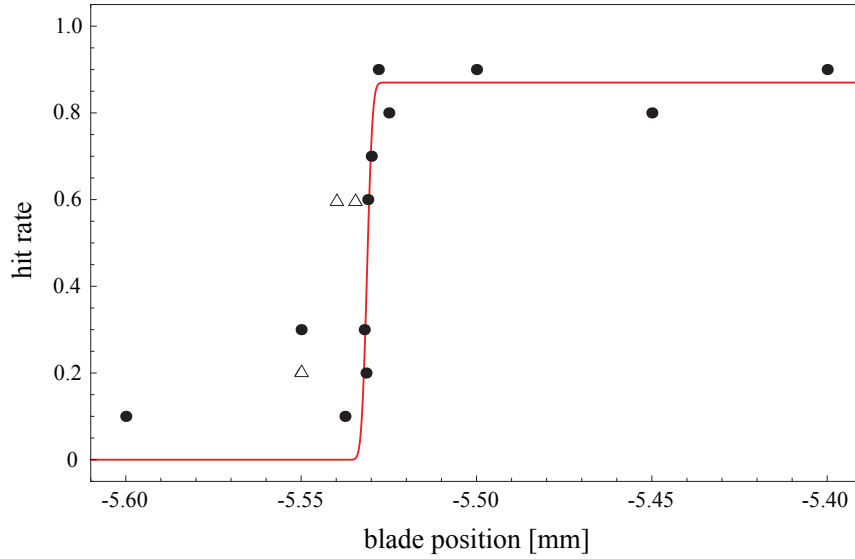


**Figure 8.10:** Hit rate as a function of the blade position for the optimal lens voltage of 62.5 V. Each data point consists of 10 individual shots with ion crystals consisting of up to six  $^{40}\text{Ca}^+$  ions, with the red curve representing the error function fit according to equation (8.11). The data points (●) were taken in one continuous measurement, whereas the data points (△) were measured afterwards in order to check for a drift of the ion beam.

ministic loading of single ions and to speed up the measurement process, which will be described in the following chapter. Furthermore, the lens design depicted in Fig. 8.3(c) was modified to increase the working regime of the einzel-lens, see also chapter 8.3.3.

### 8.3.2 Deterministic single-ion loading

In order to reduce the divergence of the ion beam to a minimum, it is necessary to ensure that only one ion is extracted out of the trap with each shot. In case of a Paul trap, there are in principal two options to achieve this goal: The first one is to avoid the loading of more than one ion at a time. Since this is not feasible due to the fact that the number of loaded ions varies for equal loading times, one needs to implement a feedback control in order to stop the ionization after one ion has been loaded into the trap. As it turned out, it was not possible to implement this method in our setup as the time which elapses between the ionization and the crystallization of an one-ion crystal has to be much shorter than the average time between ionization incidents of two different ions. Therefore, we have chosen the second possibility, namely to get rid of the redundant ions after the crystallization process.

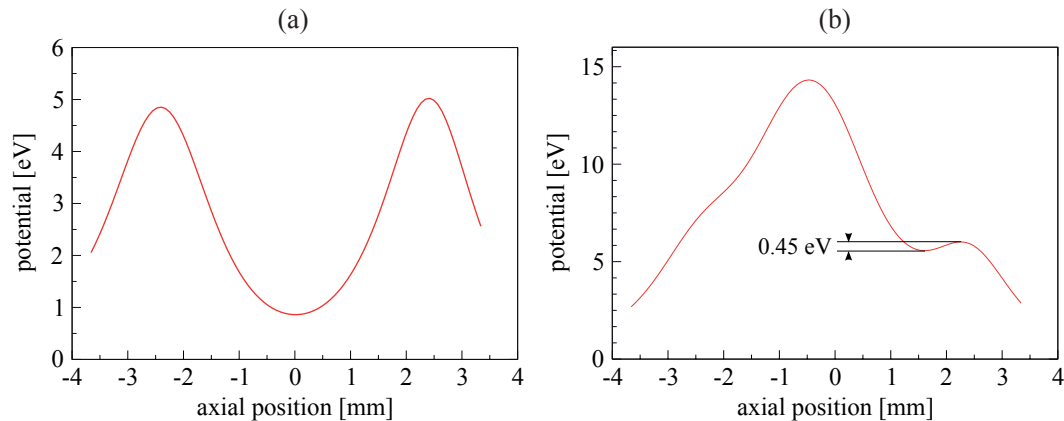


**Figure 8.11:** Deterministic single-ion loading [Sch10]. (a) Simulated trapping potential in axial direction. The potential is generated by supplying dc electrodes 7 and 13 with a voltage of 35 V and all remaining electrodes with 0 V, resulting in an axial trapping frequency  $\omega_{\text{ax}} = 2\pi \times 295$  kHz and a trap depth of about 4 eV, see also chapter 5.1.1. The center of electrode 10 is used as the point of reference for the axial position. (b) Same potential as in (a) but with a voltage of 54.8 V applied to electrodes 9 and 10, reducing the axial trap depth to about 0.45 eV in order get rid of the surplus ions.

To drop the surplus ions, we exploit the potential shaping capabilities offered by our segmented linear rail trap (see also chapter 5.1). At the beginning, the ions are trapped above electrode 10 by supplying a voltage of 35 V to electrodes 7 and 13, leading to an axial trapping potential with a trap depth of about 4 eV, see also Fig. 8.11(a). By using the offset input of our high voltage switches (see also chapter 6.1.1), the voltage supplied to electrodes 9 and 10 is linearly ramped up from 0 V to 54.8 V within a time span of about 50 ms before it is again linearly reduced to 0 V after a waiting time of 200 ms. As a consequence, the depth of the axial trapping potential is reduced to about 0.45 eV, thus becoming shallow enough so that only one ion will remain inside of the trap, see also Fig. 8.11(b). In order to determine the reproducibility of our method, the procedure described above was repeated with ion crystals of various sizes yielding a total efficiency of 96.7(7) % for reducing the amount of ions to exactly one. By means of this approach, it is also possible to reduce the number of ions to an arbitrary predefined quantity (e.g. from 5 to 4) by adjusting the maximum voltage and waiting time of the utilized voltage ramp.

### 8.3.3 Modified einzel-lens and single-ion focusing

The modified einzel-lens resembles the one presented in chapter 8.2.2, still consisting of three stainless steel electrodes with an outer diameter of 27 mm and varying thickness.

Whereas the original einzel-lens featured three 1 mm apertures, the modified design consists of two 8 mm apertures and one 4 mm aperture, effectively increasing the area of the main entrance aperture by a factor of 64. In addition, the thickness of the utilized Kapton sheets was reduced from 150  $\mu\text{m}$  to 50  $\mu\text{m}$ , see Fig. 8.12(a) for a schematic drawing of the updated lens design.

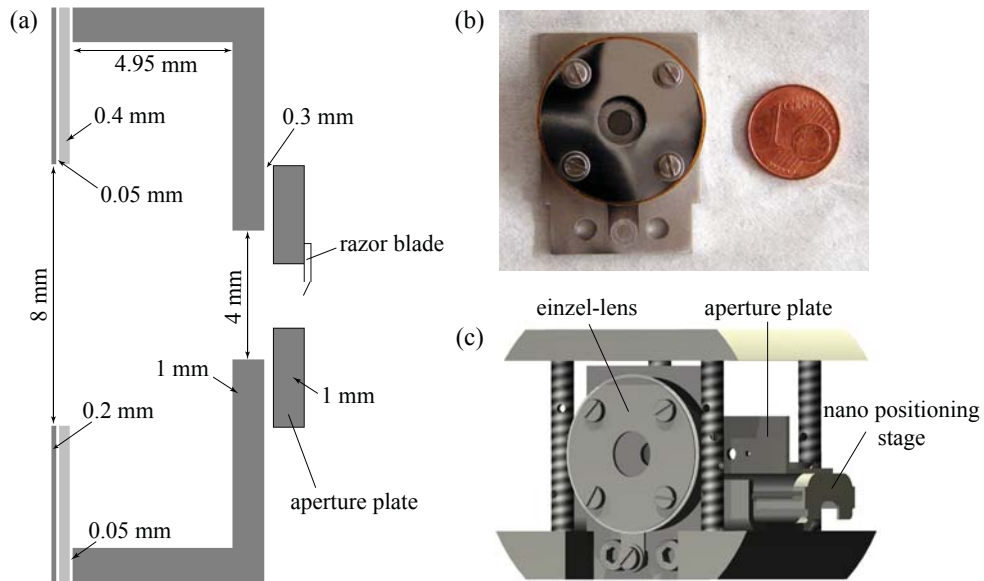


**Figure 8.12:** Modified electrostatic einzel-lens featuring two 8 mm apertures and one 4 mm aperture. (a) Schematic drawing of the einzel-lens with the dc electrode depicted in light gray and grounded electrodes colored dark gray, respectively. The razor blade (depicted in white), which is mounted behind the 2 mm aperture of the movable aperture plate, is also included. (b) Picture of the assembled einzel-lens with a one-cent coin for size comparison. Under typical operating conditions, the dc electrode is supplied with a voltage of 150 V. (c) Schematic drawing of the einzel-lens and the nano positioning stage, which are located at the beginning of the detector chamber directly in front of the EMT. [Sch10]

All parts were electropolished in order to remove ridges which were formed during the manufacturing process and to reduce the overall surface roughness. The electropolishing was done using a solution consisting of phosphoric acid ( $\text{H}_3\text{PO}_4$ ), methanesulfonic acid ( $\text{CH}_3\text{SO}_3\text{H}$ ) and triethanolamine ( $\text{C}_6\text{H}_{15}\text{NO}_3$ )<sup>2</sup>. All parts were polished for a time span of 15 min at a temperature of 65 °C using an anodic current density of 5 A/dm<sup>2</sup>. Figure 8.12(b) shows a picture of the assembled einzel-lens with a one-cent coin for size comparison. Under typical operating conditions, the center electrode is supplied with a voltage of 150 V whereas the other two electrodes are grounded.

<sup>2</sup> patent specification DE102006050317B3

Starting from these prerequisites, the measurements described in chapter 8.3.1 were repeated, utilizing the modified einzel-lens for focusing single  $^{40}\text{Ca}^+$  ions. Although the deterministic loading of single ions allowed to speed up the measurement process, the overall time span needed for doing a single measurement is still quite long ( $\approx 3$  incidents per minute). Hence, the number of measurements taken for each blade position was kept constant at a total of 10 individual shots. Figure 8.13(a) shows the hit rate for single ions as a function of the blade position for the optimal lens voltage of 150 V, yielding a  $1\sigma_r$ -spot radius of  $(4.6 \pm 1.3) \mu\text{m}$ . Compared to the original beam diameter of  $55 \mu\text{m}$ , our einzel-lens thus is capable of focusing the single-ion beam by a factor of 12. Figure 8.13(b) shows the corresponding curve for a lens voltage of 153 V.

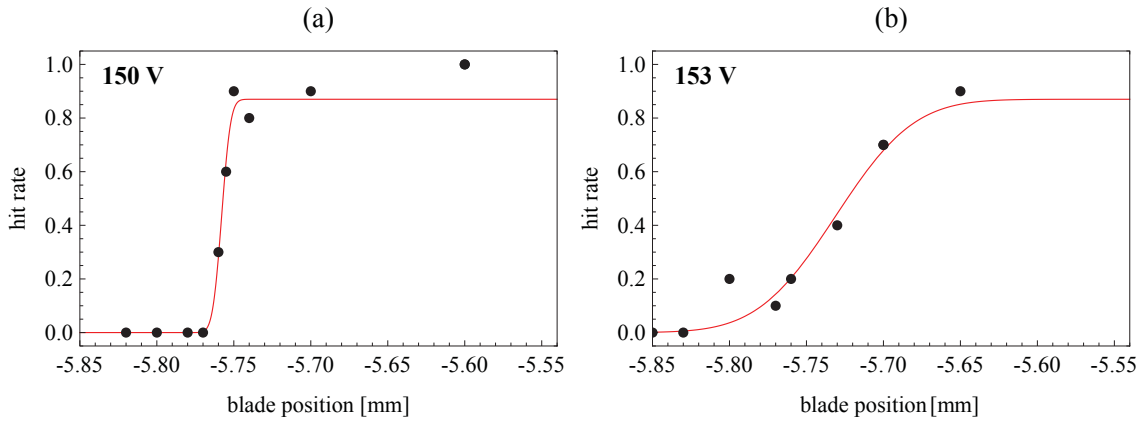


**Figure 8.13:** (a) Hit rate for single ions as a function of the blade position for the optimal lens voltage of 150 V [Sch10]. Each data point consists of 10 individual measurements, with the red curve representing the error function fit according to equation (8.11). (b) Same curve as in (a), but for a lens voltage of 153 V.

Although the experimental results are already very promising, numerical simulations predict that a much higher resolution should be feasible. In case of ground-state cooled ions with a temperature of  $100 \mu\text{K}$ , simulations predict a  $1\sigma_r$ -spot radius of  $1 \text{ nm}$ , which is enlarged to  $45 \text{ nm}$  for a temperature of  $2 \text{ mK}$ . However, in the experiment, additional deflection voltages are needed in order to align the ion beam with respect to the optical axis of the utilized einzel-lens. Including these deflection voltages in the numerical simulations leads to a further decline in resolution, resulting in a  $1\sigma_r$ -spot radius of about  $270 \text{ nm}$ . Only taking into account a spatial displacement of the incident ion beam in the principal plane of the lens, numerical simulations predict that a mismatch of  $520 \mu\text{m}$  with respect to the optical axis is already sufficient in order to obtain a spot size of  $4.6 \mu\text{m}$  in the focal plane of the lens, see also Fig. 8.14.

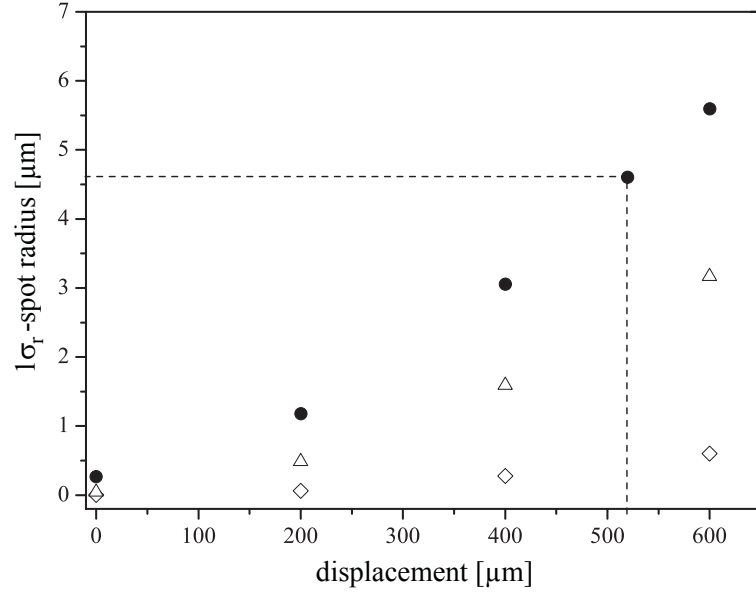


**Figure 8.14:** Simulated  $1\sigma_r$ -spot radii as a function of the spatial displacement of the ion beam in the principal plane of the lens. The radii were calculated for an initial ion temperature of 2 mK with (●) and without ( $\Delta$ ) deflection voltages as well as for an initial ion temperature of 100  $\mu\text{K}$  without deflection voltages ( $\diamond$ ). In order to explain the experimentally measured  $1\sigma_r$ -spot radius of 4.6  $\mu\text{m}$  for 2 mK laser-cooled ions, a displacement of half a millimeter is already sufficient (dashed lines). Note, that the initial ion temperature and deflection voltages for the simulated data set (●) match the experimental conditions whereas the spatial displacement was not determined experimentally. [Sch10]

In case of our experiment, this displacement is caused by a mechanical misalignment of the center of the aperture with respect to the optical axis of the einzel-lens as well as a displacement of the ion beam itself within the 1 mm aperture. The former can be ascribed to manufacturing imperfections, which are estimated to be about 200  $\mu\text{m}$ . The latter is caused by the initial adjustment of the ion beam using the 1 mm aperture. By taking into account the original beam diameter, a displacement of less than 400  $\mu\text{m}$  can be assumed. Hence, both errors result in a maximum total deviation of 600  $\mu\text{m}$ , explaining the numerically predicted deviation.

## Chapter 9

# Detection of implanted ions

As already stated in the previous two chapters, our single-ion source excels by the possibility to deterministically implant single ions with very low energies and an expected resolution of a few nm. After the implantation event, however, the main challenge is to prove that the implantation was indeed successful and that the placement and the spacing of the dopant ions match the expected values. In the following chapters, different systems and approaches will be described and the assets and drawbacks of each system will be discussed.

### 9.1 Implantation through nano apertures

In chapter 7.2.6, it was described that we used a movable aperture plate with different hole diameters in order to determine the initial beam divergence of our ion source. A similar approach can be followed to determine the final resolution of the single-ion beam after the electrostatic einzel-lens by utilizing a nano aperture. Figure 9.1 shows such an aperture realized by a pierced AFM tip consisting of SiN. In a first step, a hollow nitride pyramid is produced by standard molding techniques with a thickness of about 150 nm which is then glued onto the cantilever of an atomic force microscope<sup>1</sup>. By utilizing focused ion beam<sup>2</sup> milling, a hole is drilled into the hollow tip, resulting in typical hole diameters in the range of 30 nm or below [Mei06, Mei08b]. A Faraday cup<sup>3</sup> behind the AFM tip ensures that the beam is turned off just at the moment when the transmission current indicates that a hole was drilled.

---

<sup>1</sup> AFM, **A**tomic **F**orce **M**icroscope

<sup>2</sup> FIB, **F**ocused **I**on **B**eam

<sup>3</sup> A Faraday cup is a conductive cup designed to catch charged particles in vacuum.

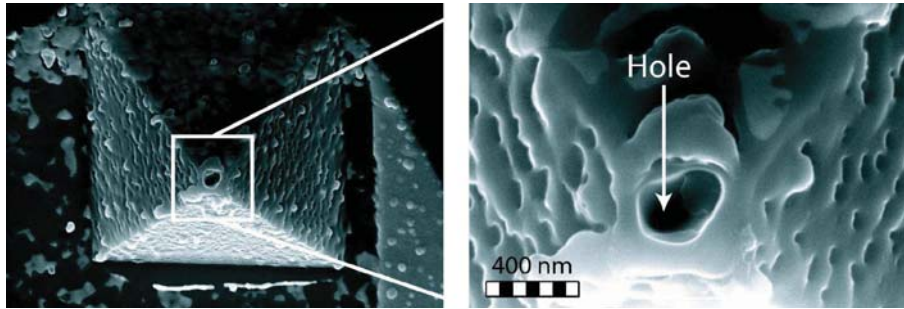


**Figure 9.1:** Pierced AFM-tip consisting of SiN [Mei06]. The hole in the hollow pyramid was fabricated by FIB milling. The crater shaped pit on top of the pyramid ends in a 30 nm hole.

## 9.2 Color centers

As mentioned in chapter 2.1.2, color centers in diamond are a promising candidate for the development of a solid state quantum computer. However, apart from the possibility to encode qubits in the internal energy levels of such defect centers, one can also use the optical properties of such systems to detect the spatial position of the dopant ions. Although there exists a huge amount of elements which can be used to generate color centers in diamond [Zai01], the applicability of only one of these systems will be discussed in more detail, namely the NV color center.

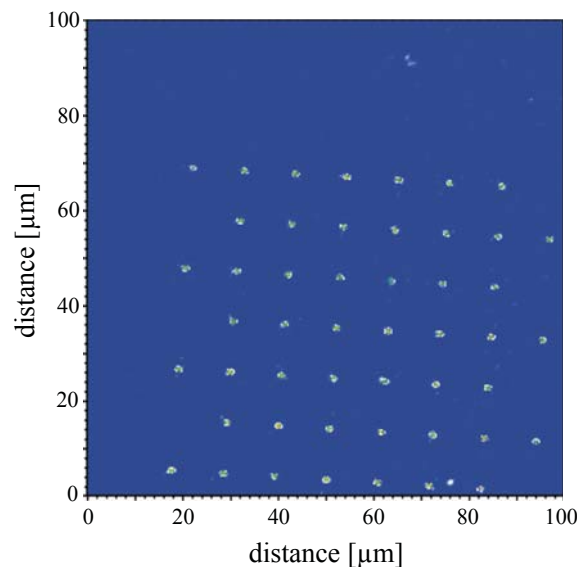


**Figure 9.2:** Fluorescence image of an NV color center pattern generated by implanting nitrogen ions into diamond with an energy of 2 MeV. [Pez10]

Figure 9.2 shows the fluorescence image of an NV pattern, which was generated by implanting nitrogen ions into diamond with an energy of 2 MeV by focusing the ion beam below  $1\ \mu\text{m}$  [Pez10]. Although the created color centers cannot be resolved within a confocal spot, it is still possible to determine their number by measuring the emitted photon statistics if the spots only contain a few NV centers. As a single two-level system cannot emit two photons at the same instant, one can determine the number of emitters in a confocal spot by measuring the second-order autocorrelation function

$$g^{(2)}(\tau) = \frac{\langle I(t)I(t+\tau) \rangle}{\langle I(t) \rangle^2}, \quad (9.1)$$

where  $I(t)$  and  $I(t+\tau)$  denote the fluorescence intensities at times  $t$  and  $t+\tau$ , respectively. Figure 9.3 shows the autocorrelation function for a single and a double NV center, where at a delay of  $\tau = 1.5\ \mu\text{s}$  a dip is observed (anti-bunching), dropping to zero in case of a single NV center or to one half in case of a double NV center. Hence, by repeating this measurement for all implanted NV centers, one can precisely determine the corresponding creation efficiency.

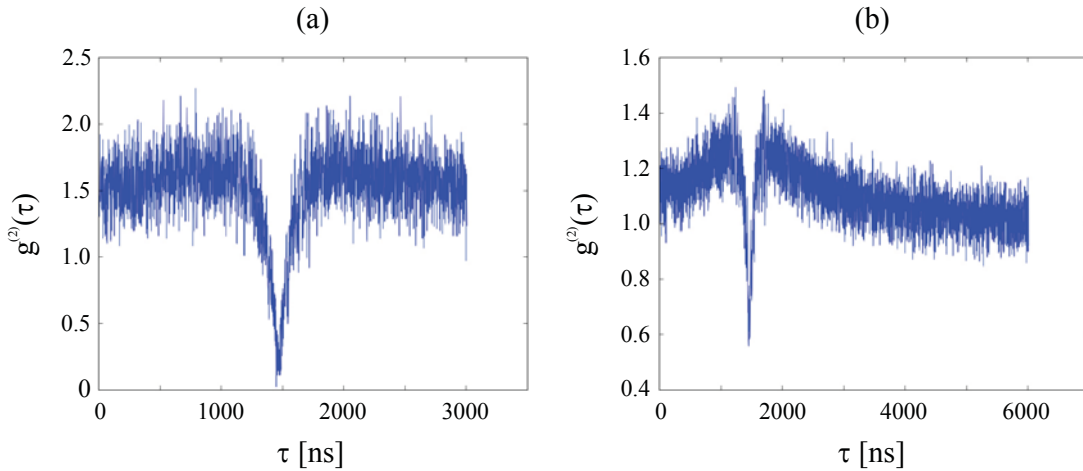


**Figure 9.3:** Second order auto-correlation function measurement showing a single (a) and double (b) NV center. [Pez10]

However, the main drawback of this detection method is the conversion efficiency, i.e. the probability that an NV center is generated upon the implantation of a nitrogen ion. Figure 9.4 shows the measured yield for NV color center creation as a function of the implantation energy. While up to 45 % of all implanted nitrogen ions will form an NV color center if the implantation occurs with energies of 18 MeV, the conversion efficiency drops down below 1 % for implantation energies lower than 5 keV [Pez10].

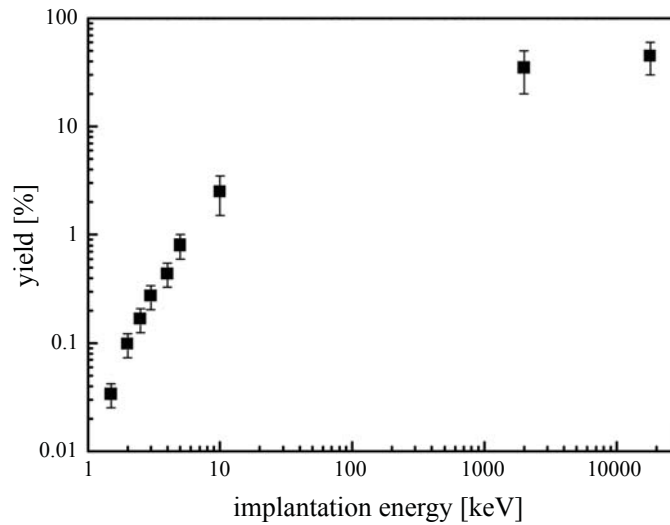


**Figure 9.4:** Measured yield for NV color center creation as a function of the energy of the implanted  $^{15}\text{N}^+$  ions. [Pez10]

According to SRIM<sup>4</sup> simulations, nm resolution in lateral and vertical direction will only be achievable if the implantation energy will be of the order of about 1 keV, resulting in an implantation depth of only 1-2 atom layers, see also Fig. 9.5(a). However, with such a low implantation energy, the number of generated vacancies per implanted  $^{15}\text{N}^+$  ion is only about 10, with the implanted nitrogen atoms being located close to the surface. Thus, some of these vacancies will get lost due to the necessary annealing process after the implantation and the associated diffusion of the vacancies to the surface. If a higher implantation energy is utilized, the number of additionally generated vacancies increases, but the resolution in lateral direction will decrease at the same time as the straggling inside of the diamond host material will increase correspondingly, see also Fig. 9.5(b).

One possible cure for this problem could be to implant  $^{12}\text{C}^+$  ions prior to the main implantation of the  $^{15}\text{N}^+$  ions in order to generate additional vacancies in the diamond host crystal. In order to yield higher numbers of vacancies, the implantation of these  $^{12}\text{C}^+$  ions could then be done with higher energies in the MeV range. However, the drawback of this pre-implantation is that due to the high implantation energy of the  $^{12}\text{C}^+$  ions, the surface of the diamond host crystal will get damaged, altering the placement accuracy of post-implanted  $^{15}\text{N}^+$  ions. Therefore, it would be preferable to generate color centers which do not need an additional vacancy near the implanted impurity atom in order to

<sup>4</sup> SRIM (The **S**topping and **R**ange of **I**ons in **M**atter), which was developed by James Ziegler, is a collection of software packages which calculate many features of the transport of ions in matter. Typical applications include the stopping and range of ions in targets, ion implantation, ion sputtering as well as ion transmission and ion therapy. For further information, please visit: <http://www.srim.org/>.

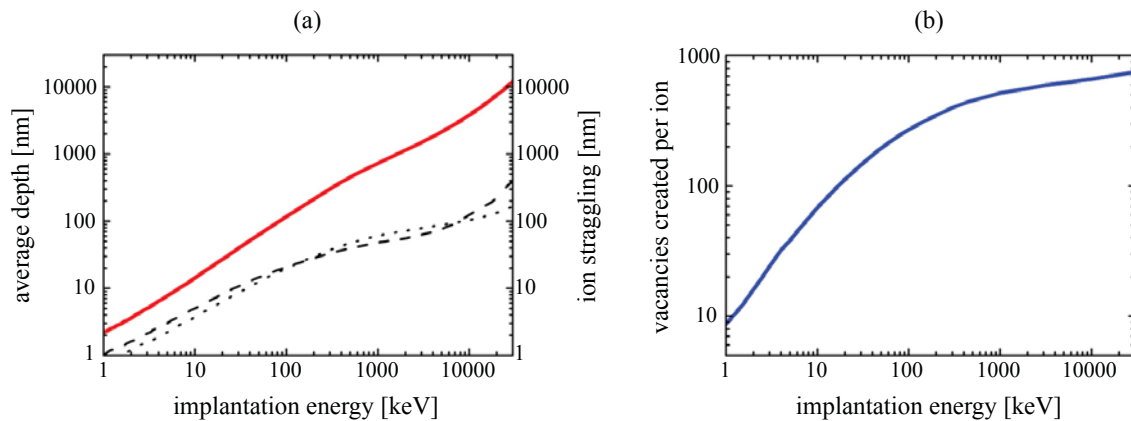


**Figure 9.5:** (a) Average depth (red line) as well as longitudinal (dotted line) and transverse (dashed line) straggling of implanted  $^{15}\text{N}^+$  ions as a function of the implantation energy (simulated with SRIM). (b) Number of vacancies created per implanted  $^{15}\text{N}^+$  ion as a function of the implantation energy (simulated with SRIM). [Pez10]

be formed. Two systems, which are currently under consideration, are chromium atoms in diamond and cerium atoms in yttrium silicate<sup>5</sup>. However, as these systems are not as well characterized as NV color centers in diamond, additional preliminary studies have to be made to determine their feasibility.

## 9.3 Microscopy techniques

### 9.3.1 STED microscopy

STED<sup>6</sup> microscopy is a technique, that utilizes the non-linear de-excitation of fluorescent dyes in order to overcome the resolution limit imposed by diffraction with standard confocal laser scanning microscopes and conventional far-field optical microscopes. So far, STED microscopy provided a resolution of 16-80 nm, which has been used for mapping proteins in cells [Don06], and for the real-time imaging of colloidal particles or synaptic vesicles in living neurons [Wes08]. In these systems, the fluorescent markers used were organic molecules or fluorescent proteins having a singlet ground state ( $S_0$ ) and a first excited state ( $S_1$ ), each featuring vibrational sublevels. Here, the de-excitation of the excited state either occurs due to fluorescence emission after an average period  $\tau_{\text{spont}}$  or by using a so-called STED beam, which switches the molecules off by forcing them down to the  $S_0$  state. This can be achieved, if the stimulated emission rate  $\Gamma_{\text{stim}}$  is much larger

<sup>5</sup>  $\text{Y}_2\text{SiO}_5$ , often abbreviated as YSO.

<sup>6</sup> **ST**imulated **E**mission **D**epletion

than the spontaneous decay rate  $\Gamma_{\text{spont}}$ :

$$\begin{aligned} \Gamma_{\text{stim}} &\gg \Gamma_{\text{spont}} \\ \frac{\sigma I_{\text{STED}} \lambda_{\text{STED}}}{hc} &\gg \frac{1}{\tau_{\text{spont}}} \end{aligned} \quad (9.2)$$

Here,  $\sigma$  denotes the cross-section of the stimulated emission, with  $I_{\text{STED}}$  being the STED beam intensity. The wavelength  $\lambda_{\text{STED}}$  has to be chosen in such a way, that the fluorophore is pumped into a rapidly decaying higher vibrational sublevel of the  $S_0$  state, which makes de-excitation predominant. Hence, for a certain intensity of the STED beam, the fluorophore is essentially switched off.

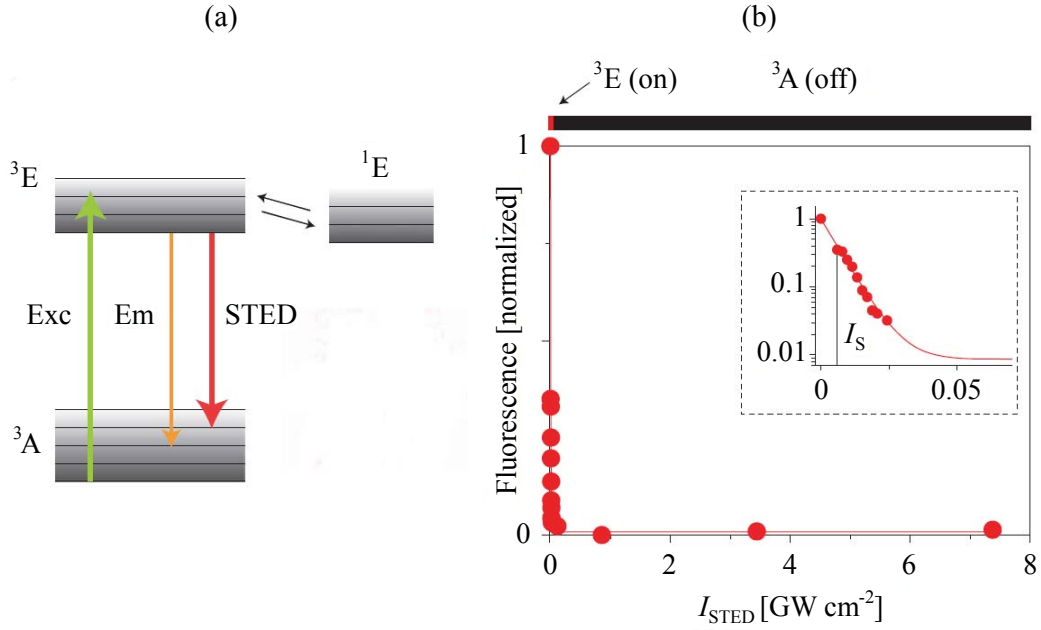


**Figure 9.6:** Principle of STED microscopy in case of an NV color center. The fluorescence is ‘switched off’ due to the stimulated emission depletion of the excited state. (a) Energy diagram sketching the ground ( $^3A$ ), the excited ( $^3E$ ) and the dark singlet state ( $^1E$ ) along with the excitation (Exc), emission (Em) and stimulated emission (STED) transitions. (b) Fluorescence of the excited state ( $^3E$ ) as a function of the intensity  $I_{\text{STED}}$  of the STED beam, with the inset confirming the exponential suppression of the excited state. For  $I_{\text{STED}} > 20 \text{ MW cm}^{-2}$ , the center is deprived of its ability to fluoresce (switched off). [Rit09]

The same technique can now also be applied for imaging individual NV color centers with high spatial resolution. Figure 9.6(a) shows the principle of STED microscopy in case of an NV color center, see also chapters 2.1.2 and 9.2. By using an additional STED beam, the fluorescence of the  $^3E$  state can be ‘switched off’ due to the stimulated emission depletion of the excited state. Figure 9.6(b) shows the fluorescence of the excited state as a function

of the intensity  $I_{\text{STED}}$  of the STED beam, where one can observe a steep exponential drop of the fluorescence. In order to utilize this nearly ‘rectangular’ depletion curve for imaging purposes, one can then generate a STED beam with a doughnut-shaped focal intensity distribution  $I_{\text{STED}}^{\text{d}}(x, y)$  and a central minimum  $I_{\text{STED}}^{\text{min}}(0, 0) \approx 0$ . Overlapping the Airy disk of the excitation beam with the doughnut hence switches off all the centers covered by the Airy disk except for those at the doughnut minimum.

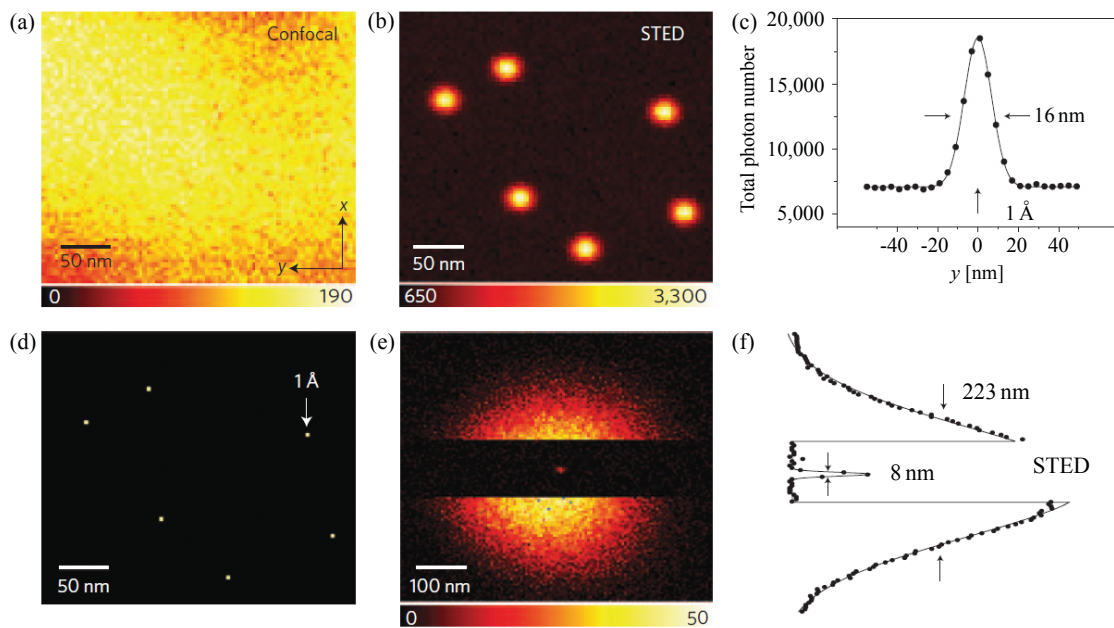


**Figure 9.7:** STED microscopy of  $\text{NV}^-$  color centers. (a) Confocal image. (b) STED image from the same crystal region as shown in (a). In contrast to the confocal image, one can clearly resolve the individual color centers. (c) A measurement of the  $y$ -profile of one of the color centers shown in (b) yields a  $\text{FWHM}^7$  of  $\Delta y = 16.0$  nm. (d) Using STED microscopy, the  $xy$ -coordinate of each center can be derived with a precision of 1-2 Å. (e),(f): Applying a STED beam with an intensity  $I_{\text{STED}} = 3.7 \text{ GW cm}^{-2}$  shrinks a confocal spot of 223 nm diameter (FWHM) down to 8 nm. [Rit09]

Figure 9.7 compares a confocal image (Fig. 9.7(a)) with the corresponding STED image (Fig. 9.7(b)), which was taken at  $I_{\text{STED}}^{\text{max}} = 1.4 \text{ GW cm}^{-2}$  [Rit09]. Although the confocal image does not show any details, the corresponding STED image resolves each NV center, with the images of individual centers yielding a  $\text{FWHM}^7$  of  $\Delta x = 18.3 \text{ nm}$  and  $\Delta y = 16.0 \text{ nm}$ , see Fig. 9.7(c). Scanning over the sample together with the excitation beam, the doughnut-shaped STED beam only allows for imaging a single NV center at a time, with all others being either switched off or simply not excited. STED microscopy thus not only allows for resolving individual NV color centers, but it is also possible to reg-

<sup>7</sup> Full Width Half Maximum

ister them sequentially in time. Once all the centers have been resolved, there is no need to further increase the resolution as their positions can be calculated from the centroid of their subdiffraction-sized spot, allowing for deriving the  $xy$ -coordinates of each center with a precision of 1-2 Å [Rit09], see also Fig. 9.7(d). Figure 9.7(e) again shows a confocal image of an isolated NV center, but with the STED beam being momentarily engaged near its middle, producing a spot of 8 nm FWHM, see also Fig. 9.7(f). By extending STED into the third dimension, it is even possible to incorporate depth information.

Hence, by avoiding scanning distortions and drift, STED microscopy is capable of mapping individual NV color centers with nanometric resolution and sub-nanometer precision. Taking into account the straightforward implementation, STED microscopy thus is the prime candidate for imaging single implanted color centers with unprecedented spatial resolution.

### 9.3.2 Scanning tunneling microscopy

Another method for imaging single implanted impurities relies on a low-temperature scanning tunneling microscope<sup>8</sup>. So far, scanning tunneling microscopy has been used to manipulate atoms and to create structures that allow for visualizing standing electron wave patterns [Cro93]. Extending this line of investigations, C. R. Moon *et al.* succeeded in 2008 in retrieving quantum-phase information in nanostructures utilizing an STM [Moo08]. Also in 2008, F. Meier *et al.* measured the exchange interaction between Co adatoms<sup>9</sup> and wires on a platinum surface [Mei08a]. All of these effects thereby depend on a rearrangement of the electron sea in order to minimize the disturbance caused by foreign atoms.

By using single buried impurities, it is thus possible to visualize a directional propagation of electrons inside of the host material. A. Weismann *et al.* [Wei09] combined an STM experiment and density functional theory<sup>10</sup> calculations to demonstrate the existence of unusually strong anisotropies in the resulting charge densities caused by the shape of the Fermi surface, which focuses electrons in very narrow directions, see also Fig. 9.8. For this purpose, isolated subsurface Cobalt impurities were prepared in single crystals of Cu(100) and Cu(111), and their influence on the local density of states<sup>11</sup> was investigated with the use of low-temperature STM.

---

<sup>8</sup> STM, Scanning Tunneling Microscope

<sup>9</sup> An adatom is an atom which is located on a crystal surface, and can be thought of as the opposite of a surface vacancy.

<sup>10</sup>DFT, Density Functional Theory

<sup>11</sup>LDOS, Local Density Of States

Figure 9.9(a) shows a 9 by 9 nm STM-topography of four Co-atoms, which were embedded in different depths (6, 7, 9 and 10 monolayers) by simultaneous deposition of the host metal and the impurity compound from two electron-beam evaporators, illustrating the influence on the electron's spectral density at the surface. One can clearly observe four ringlike structures, which correspond to short-wavelength oscillations with an amplitude of about 2 pm. According to [Wei09], the long-wavelength standing wave-pattern is caused by surface state electrons scattered at a monoatomic step-edge, which is located in the upper left corner. Figure 9.9(b) shows the STM topography of a single Co atom below the Cu(100) surface, elucidating the propagation of electrons in the Cu host crystal from another perspective. Here, the LDOS is only influenced in a squarelike region above the impurity and within four beamlike regions extending diagonally outside the four vertices, reflecting the symmetry of the underlying band structure (i.e. threefold symmetry for (111) and fourfold symmetry for (100) surfaces)<sup>12</sup>.

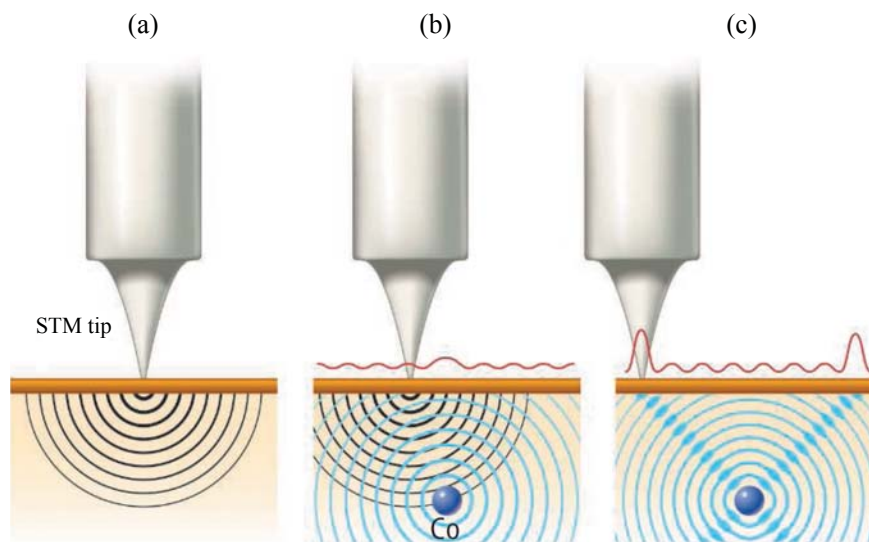


**Figure 9.8:** Principle of nanoscale electron focusing. (a) In a typical STM experiment performed on metal, an electron tunnels into the surface and becomes a bulk electron wave whose amplitude decays with distance. (b) When a scatterer is present under the surface, the electron wave can be reflected. In case of a spherical Fermi surface, this results in a weak interference pattern at the surface. (c) When the Fermi surface is not spherical, electron focusing is observed along certain directions, which can give rise to a pronounced interference pattern observable at the surface. [Hei09]

Although this method offers the prospect to image single dopant atoms with high spatial resolution, a few drawbacks still remain. So far, measurements have only been conducted with Co impurities, which were embedded in the Cu host metal by using chemical vapor

<sup>12</sup>For a more detailed description, please see [Wei09].

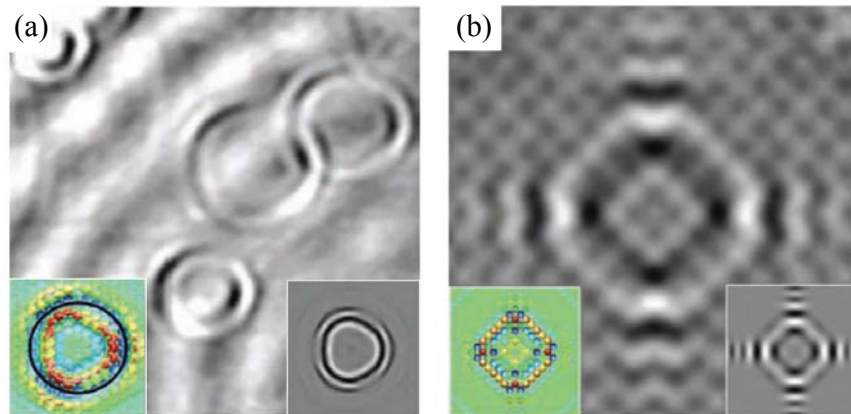


**Figure 9.9:** Localization of single Co dopant atoms by utilizing nanoscale electron focusing. The left insets thereby refer to DFT<sup>10</sup> calculations, with the right insets showing the calculated LDOS<sup>11</sup>, respectively. (a) STM topography of four Co atoms below the Cu(111) surface. The size of the image equals 9 by 9 nm. (b) STM topography of one Co atom below the Cu(100) surface. The size of the image equals 3.5 by 3.5 nm. [Wei09]

deposition. As a result, the Cu host crystal does not feature any surface defects, which are normally generated due to the implantation event. The formation of vacancies inside of the Cu crystal is also prevented. Hence, it remains to be seen whether this method can also be applied to other dopant atoms and host metals, and to which degree crystal imperfections influence the detection efficiency and overall achievable resolution.

## Chapter 10

# Summary and Outlook

The work presented in this thesis revolved around the development, assembly, operation and characterization of a new type of ion source with the ability to deterministically implant single doping atoms into solid state materials with nanometer spatial resolution. This technique can e.g. be applied to generate color centers in diamond or to implant P into Si. Both systems provide a possible way for the realization of a solid state quantum computer. Another challenge is to circumvent the breakdown of Moore's law due to Poissonian dopant fluctuations in nanometer scaled semiconductor devices, where the deterministic implantation of single ions can greatly enhance the electrical properties.

Based on a segmented linear Paul trap, numerical simulations were used to optimize the layout of the dc and rf trap electrodes, resulting in a design which not only allows for trapping and manipulating different species of ions but which at the same time permits to extract single ions or larger ion crystals in a controlled way. The trap itself consists of four copper plated polyimide blades which were manufactured in printed circuit board (PCB) technology and are arranged in an x-shaped manner. Each blade features a total of 15 independent dc electrodes, with large deflection electrodes being used for altering the trajectories of the extracted ions. The rf electrodes are designed in such a way, that the radial confinement is sustained during the whole extraction process and a targeted shooting is facilitated.

A complete new setup was built for the implantation experiments. Apart from installing laser sources and optics, an ultra high vacuum (UHV) vessel was designed and installed with the trap, featuring a modular setup which allows one to quickly exchange the substrate used for implantation without compromising the vacuum of the whole system.

Experiments were mainly performed with mK laser-cooled  $^{40}\text{Ca}^+$  ions, which were deterministically extracted from the trap and detected via an electron multiplier tube. The total detection efficiency thereby amounts to nearly 90 %. For single-ion extraction, we have measured a mean velocity of 19.47 km/s with a  $1\sigma$ -spread of only 6.3 m/s and a beam divergence of 600  $\mu\text{rad}$  at a distance of 257 mm from the trap center. The influence of various parameters such as the rf trigger phase and the vacuum base pressure was studied as well. Apart from measurements with single-ion crystals, we also conducted experiments with crystals consisting of two and more  $^{40}\text{Ca}^+$  ions. The extraction of mixed ion crystals containing other dopant ions was demonstrated, too. By utilizing the potential shaping capabilities of our ion trap, we were able to deterministically load a predetermined number of ions which will allow for further automation of the loading and extraction procedure, resulting in orders of magnitude increased repetition rates.

Using a custom-built electrostatic einzel-lens, we have demonstrated the focusing of an ion beam consisting of single  $^{40}\text{Ca}^+$  ions to a spot size of a few  $\mu\text{m}$ . Due to the small beam divergence and narrow velocity distribution of the generated single-ion beam, chromatic and spherical aberration at the einzel-lens is strongly reduced, presenting a promising starting point for focusing single ions on their way to the substrate. Numerical simulations predict, that if the ions are cooled to the motional ground state (Heisenberg limit), nanometer spatial resolution can be achieved. In addition, as the time of extraction as well as the velocity and the trajectories of the extracted ions are well-defined, it is possible to correct aberration effects using time-dependent electrostatic fields by simply switching the lens to another voltage at a specific time.

In future experiments, efforts will be made to avoid the usage of the deflection electrodes by aligning the beam mechanically and to implement more sophisticated cooling techniques like sideband or EIT cooling in order to reduce the divergence of the ion beam. Moreover, the utilized nano positioning stage will be exchanged by a modular setup consisting of three independent stages in order to move apertures and substrates in all three spatial directions. The additional degrees of freedom will not only allow for a more precise alignment with respect to the optical axis of the einzel-lens but will also allow us to determine the optimal focal length and spot size more accurately. Using two perpendicular edges of the substrate as well defined tearing edges will then allow for approaching a specific location on the substrate relative to the corner formed by the two edges. Alternatively, one could think of mounting the einzel-lens on the tip of an AFM, thus allowing for determining the implantation position with respect to potential surface structures. A new lens design, which is currently in development, will facilitate a better focusing of the single-ion

beam, and additionally allow for post-accelerating the extracted ions in order to reach higher implantation energies of a few keV, i.e. improving the conversion efficiency for the generation of color centers in diamond. Due to the high spatial and temporal resolution of the focused single-ion beam, one might also consider to shoot ions from one ion trap into another. This would allow one to transport quantum information stored in the internal, electronic states of the ions in a much faster way and over larger distances than currently possible when performing a standard ion transport in multi-segmented micro ion traps. A further possible application might be as on-demand source for matter-wave interferometry with ultracold slow ions.



## Appendix A

# Phase synchronization circuit

In order to successfully extract the ions out of the trap, the time of extraction has to be matched with a certain phase of the radio frequency. Originally developed by K. Singer and built by N. M. Linke, the presented phase synchronization circuit was further enhanced by R. Fickler during his diploma thesis. By utilizing the circuit at hand, a computer-controlled TTL signal is delayed in such a way that a constant delay to the next zero-crossing of the trap drive frequency  $\Omega$  is ensured. In order to reduce the charging of the trap due to the extraction voltage to a minimum, the TTL trigger signal is only supplied for a few ms to the high voltage switches. The precision of the circuit was experimentally measured showing a  $1\sigma$ -spread of 0.34 ns.



# Appendix B

## Scientific publications

### B.1 Physical Review Letters

#### **Deterministic Ultracold Ion Source Targeting the Heisenberg Limit**

---

W. Schnitzler, N. M. Linke, R. Fickler, J. Meijer, F. Schmidt-Kaler and K. Singer

Published on 19 February 2009 in the scientific journal:

**Physical Review Letters**

(Volume: 102 / Page: 070501 / Year: 2009)

### Deterministic Ultracold Ion Source Targeting the Heisenberg Limit

W. Schnitzler,<sup>1</sup> N. M. Linke,<sup>1</sup> R. Fickler,<sup>1</sup> J. Meijer,<sup>2</sup> F. Schmidt-Kaler,<sup>1</sup> and K. Singer<sup>1,\*</sup>

<sup>1</sup>*Institut für Quanteninformationsverarbeitung, Universität Ulm, Albert-Einstein-Allee 11, 89081 Ulm, Germany*<sup>†</sup>

<sup>2</sup>*RUBION, Ruhr-Universität Bochum, 44780 Bochum, Germany*

(Received 26 September 2008; revised manuscript received 2 December 2008; published 19 February 2009)

The major challenges to fabricate quantum processors and future nano-solid-state devices are material modification techniques with nanometer resolution and suppression of statistical fluctuations of dopants or qubit carriers. Based on a segmented ion trap with mK laser-cooled ions we have realized a deterministic single-ion source which could operate with a huge range of sympathetically cooled ion species, isotopes or ionic molecules. We have deterministically extracted a predetermined number of ions on demand and have measured a longitudinal velocity uncertainty of 6.3 m/s and a spatial beam divergence of 600  $\mu$ rad. We show in numerical simulations that if the ions are cooled to the motional ground state (Heisenberg limit) nanometer spatial resolution can be achieved.

DOI: 10.1103/PhysRevLett.102.070501

PACS numbers: 03.67.-a, 29.25.Ni, 81.16.Rf, 85.40.Ry

The miniaturization of semiconductor devices has reached length scales of a few tens of nanometers, where statistical Poissonian fluctuations of the number of doping atoms in a single transistor significantly affect the characteristic properties, e.g., gate voltage or current amplification [1]. Further miniaturization will even cause statistical device failure. Particularly fatal are statistical dopant fluctuations for a future solid state quantum processor based on single implanted qubit carriers like color centers in diamond or phosphorous dopants in silicon [2–5]. So far, the only known methods to control the number of dopants utilize statistical thermal sources followed by a postdetection of the implantation event, either by the observation of Auger electrons, photoluminescence, phonons, the generation of electron-hole pairs, or changes in the conductance of field effect transistors [6–10]. To make the detection of such an event successful the methods require either highly charged ions or high implantation energies which, as a down side, generate defects in the host material. In these systems resolutions of less than 10 nm are achieved by means of masks and apertures shielding the substrate from incident ions and leading to compulsory losses of dopants. Another fabrication method, specific for Si surfaces, uses hydrogen terminated surfaces structured with the tip of a tunneling microscope, followed by a chemical reactive surface binding of doping atoms [11–15]. With this technique sub-nm resolution can be achieved but the applicability is mainly limited to specific substrates and impurities in the background gas can cause severe impairment.

Here, we present the experimental proof of a novel ultracold ion source which can be used for the deterministic implantation of a predetermined number of single ions [16]. Our technique is based on a segmented linear Paul trap with laser-cooled  $^{40}\text{Ca}^+$  ions similar to setups used for scalable quantum information processing with ions [17]. Additionally loaded doping ions of different elements or ionic molecules cannot be directly laser cooled but could be sympathetically cooled by  $^{40}\text{Ca}^+$  ions. Although invis-

ible to the laser light they are still identified [18,19] and counted by exciting collective vibrational modes. Our segmented ion trap allows for the separation of the cooling ion from the dopant ion, which is finally extracted by a tailored electric field. The implantation method is in principle independent of the dopant species and the target substrate. For 2 mK laser-cooled ions accelerated to 80 eV the measured longitudinal velocity distribution shows a  $1\sigma$  spread of 6.3(6) m/s [20] and a spatial  $1\sigma$ -spot radius of  $83^{(+3)}_{(-3)} \mu\text{m}$  at a distance of 257 mm (beam divergence: 600  $\mu$ rad). These properties reduce chromatic and spherical aberration of any focusing ion optics. The resolution of our system is thereby not enforced by additional masks or apertures but is an intrinsic property of our setup.

The core of the experimental setup is a Paul trap—a universal tool for trapping charged particles such as atomic and molecular ions or charged clusters using a combination of static (dc) and alternating (rf) electric fields. A pseudopotential of a few eV depth is generated with a properly chosen rf amplitude and frequency  $\Omega$ .

For our application it is necessary that the ions arrange as a linear crystal such that they can be identified and counted using laser induced fluorescence. During the extraction we apply voltages to additional dc segments tailoring the axial potential. In a conventional linear segmented Paul trap this would lead to a loss of the radial confinement because the applied extraction potential exceeds the radial pseudopotential. We have developed a special design of our trap, in which the ions are radially guided even during the axial extraction. Our trap consists of four copper plated polyimide blades of 410  $\mu\text{m}$  thickness and 65 mm length which are arranged in a  $x$ -shaped manner [21] (see Fig. 1 for a schematic view). The rf is applied to the inner front faces of two opposing blades; the front faces of both other blades are grounded. The distance between inner front faces of opposing blades is 2 mm. dc voltages are applied to eight segments of 0.7 mm width which are placed on the top and bottom areas of all four blades. Under typical

PRL 102, 070501 (2009)

PHYSICAL REVIEW LETTERS

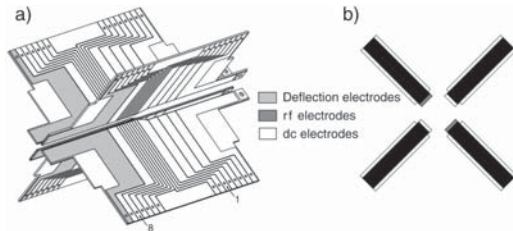
week ending  
20 FEBRUARY 2009

FIG. 1. (a) Sketch of the segmented linear Paul trap with dc electrodes (white) and rf electrodes (dark grey). Deflection electrodes (light gray) are used to alter the trajectories of ions which are extracted out of the trap. (b) Front view showing that rf and rf-ground electrodes (generating the radial confinement) are only covering the two  $410 \mu\text{m}$  wide front faces of the blades.

operating conditions we apply to the rf electrodes an amplitude of 200 V at the frequency of  $\Omega/2\pi = 12.155 \text{ MHz}$  leading to a radial secular frequency  $\omega_{\text{rad}}/2\pi = 430 \text{ kHz}$  for a  $^{40}\text{Ca}^+$  ion. The dc-electrode trap segments 2 and 8 are supplied with 35 V and the remaining electrodes with 0 V resulting in an axial potential with  $\omega_{\text{ax}}/2\pi = 280 \text{ kHz}$ . The location of trapped ions is above electrode 5. The trap assembly is housed in a stainless steel vacuum chamber with enhanced optical access held by a turbomolecular pump and an ion-getter pump at a pressure of  $3 \times 10^{-9}$  mbar. Ions are illuminated by resonant laser light near 397 and 866 nm for Doppler cooling. Scattered photons are collected by a  $f/1.76$  lens on an EMCCD camera to image individual  $^{40}\text{Ca}^+$  ions; see Figs. 2(a)–2(c). From the width of the laser excitation spectrum on the  $S_{1/2}$ – $P_{1/2}$  laser cooling transition, we deduce a temperature of about 2 mK slightly above the Doppler cooling limit.

Calcium and dopant ions are generated in a multiphoton ionization process by a pulsed frequency tripled Nd-YAG laser at 355 nm with a pulse power of 7 mJ. Dopant ions are sympathetically cooled and identified from the voids in the fluorescence image compared to that of a regular linear  $^{40}\text{Ca}^+$  crystal. Figure 2(d) shows the fluorescence of an ion crystal consisting of a single  $^{40}\text{Ca}^+$  and two molecular  $\text{CaO}^+$  ions resulting from a chemical reaction with background residual gas [18]. We identify the species of dark ions by exciting collective vibrational modes with an ac voltage applied to electrode 4 and observing a blurring of the  $^{40}\text{Ca}^+$  fluorescence image at the resonance frequency  $\omega_{\text{ax}}$  [19]. Alternatively, amplitude modulated resonant laser light is used [18] to determine the charge to mass ratio of trapped particles at a precision of better than 0.2%. Before extraction, the sympathetically cooled doping ions may be separated from the  $^{40}\text{Ca}^+$  ions. This is achieved by converting the axial trapping potential into a double well. The doping ions are further transported away from the  $^{40}\text{Ca}^+$  ions by time dependent dc-electrode voltages [21]. As heating generated during this separation process [17] cannot be cooled away anymore an alternative separation

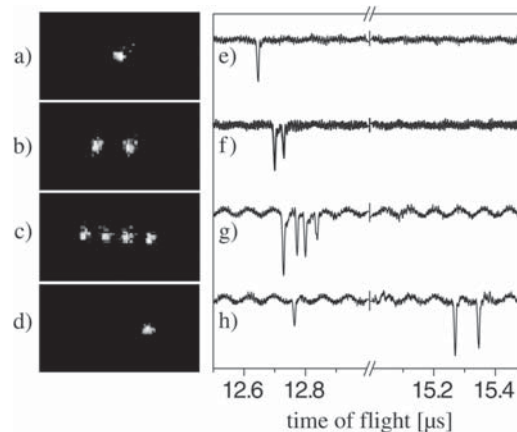


FIG. 2. Typical fluorescence image of a single  $^{40}\text{Ca}^+$  ion (a), and linear ion crystals of two (b) and four (c) ions. After the extraction we record EMT detector signal traces with a single-ion detection event (e), two events (f) and four events (g), correspondingly. The EMCCD image (d) shows fluorescence from a single  $^{40}\text{Ca}^+$  ion only; however, we can discover from its position that it is trapped in a linear crystal together with two dark ions at the left-hand side. As the mixed ion crystal is extracted, we detect three events, one from the  $^{40}\text{Ca}^+$  near  $12.8 \mu\text{s}$  and two events near  $15.3 \mu\text{s}$ . From this time-of-flight spectroscopy, we reveal the mass of  $\text{CaO}^+$  ions for both dark ions. All measurements were conducted without the movable aperture plate with an effective distance of 247 mm between trap center and detector.

method would deflect the unwanted  $^{40}\text{Ca}^+$  ions after extraction, e.g., by increasing the electrode voltages of an einzel-lens. For the extraction we increase the dc voltage of segments 4 and 5 to 500 V within a few tens of nanoseconds. The switching of the extraction voltage (supplied by iseg inc., Model EHQ-8010p) is performed by two high voltage switches (Behlke inc., HTS 41-06-GSM) triggered via a computer-controlled TTL signal and synchronized with the rf-field phase. Synchronization is crucial in order to minimize shot to shot fluctuations of velocity and position. An electronic phase synchronization circuit delays the TTL signal for extraction such that a constant delay to the next zero crossing of the trap drive with frequency  $\Omega$  is ensured. We found the optimum extraction parameters by matching the time of extraction with a certain phase of the radio frequency and by adjusting the dc voltages on the deflection electrodes, which alter the ion trajectory during extraction. All measurements described below use these settings. The detection of the extracted ions is performed via an electron multiplier tube (EMT) with 20 dynodes from ETP inc., model AF553, which can detect positively charged ions with a specified quantum efficiency of about 80%. The detector is housed in a separate vacuum chamber at a distance of 287 mm from the trap. At typical operating conditions the detector is supplied with a voltage of

–2.5 kV. The gain is specified with  $5 \times 10^5$  and we observe an electrical signal of about 100 mV. The detection events show a width of 10 to 15 ns. In order to measure the beam divergence a movable aperture plate was installed in front of the detector. This plate, mounted on a nanopositioning stage from Smaract, model SL-2040, features hole diameters ranging from 5 mm down to 300  $\mu\text{m}$ .

Typical EMT detector signals for different numbers of ions are shown in Figs. 2(e)–2(g). Figure 2(h) displays the detector events for one  $^{40}\text{Ca}^+$  ion and two  $\text{CaO}^+$  ions, which arrive at  $t = 15.3 \mu\text{s}$ . From a time-of-flight analysis through the 1 mm aperture we deduce a mean ion velocity of 19.47 km/s for the  $^{40}\text{Ca}^+$  ions. At  $3 \times 10^{-9}$  mbar we detect  $87_{(-11)}^{(+7)}\%$  of all extracted single ions within a  $1\sigma$ -confidence interval. We found that the efficiency slightly depends on the residual gas pressure but is mainly limited by the detector efficiency (which we measure to be higher than specified). The measured longitudinal velocity distribution (see Fig. 3) shows a  $1\sigma$ -spread of 6.3(6) m/s which is about a factor of 10 larger than the velocity distribution inside the trap at  $T = 2$  mK. This leads to a relative velocity uncertainty  $\Delta v/v$  of  $3.2 \times 10^{-4}$  which may be further reduced by post-accelerating the ions after extraction. From measurements conducted with the smallest aperture (300  $\mu\text{m}$ ) we deduce a  $1\sigma$ -spot radius of  $83_{(-3)}^{(+8)} \mu\text{m}$  for the trajectories of the extracted ions. Here we assume a Gaussian spatial distribution and the error is due to counting statistics. Note that this value is an upper limit as our measurements are currently affected by a measured drift of the ion beam of about 15  $\mu\text{m}/\text{min}$  possibly caused by temperature drifts of the setup.

For a comparison of measured data with numerical Monte Carlo simulations we need accurate electrostatic potentials which we deduce from a complete CAD-model of the trap geometry created with AUTOCAD. Electrostatic potentials and fields are calculated by using a boundary

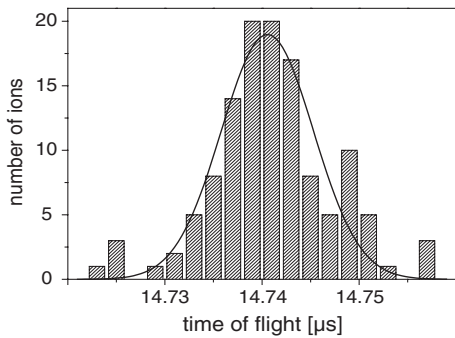


FIG. 3. Time-of-flight distribution for single ions based on 123 successful extractions out of 139 shots in total through the 1 mm aperture. The bin size of the histogram is 2 ns. A Gaussian fit of the data yields an average velocity of 19.47 km/s with a  $1\sigma$ -spread of 6.3(6)m/s.

element method accelerated by the fast multipole method [22]. Symmetry properties of the trap are exploited to reduce numerical errors. The ion trajectories are obtained by applying the Verlet integration method. The initial momentum and position is determined from the thermal Boltzmann distribution in the trapping potential. As a test, we have compared measured trap frequencies  $\omega_{\text{ax}}$  and  $\omega_{\text{rad}}$  for various traps of different size and shape in our lab [23] with corresponding simulations and found an agreement at the level of 2% to 3%. The ion trajectory calculation takes into account the full time dependent dynamics, including the micromotion at frequency  $\Omega$  yielding a  $1\sigma$ -velocity spread of 12 m/s and a beam divergence of 130  $\mu\text{rad}$ . Simulated velocity uncertainty and beam divergence agree within 1 order of magnitude with experimental results (see Table I).

In order to implant single ions into solid state materials with nanometer spatial resolution, the detector will be replaced by a simple electrostatic einzel-lens [24] with a diameter of 1 mm and a focal length of 9 mm. Simulations predict a  $1\sigma$ -spot radius of 7 nm for 2 mK and 2 nm for 100  $\mu\text{K}$ , respectively (see Fig. 4 and Table I).

We attribute the discrepancies between experimental results and numerical simulations to patch electric fields on insulating surfaces, geometrical imperfections of the electrodes and fluctuations of the extraction voltage power supply (specified with  $\Delta U/U = 10^{-3}$ ). The aforementioned drift of the ion beam will be reduced in future experiments by installing magnetic shielding and a temperature stabilization.

Currently, our initial mean spatial and momentum spread is a factor of 10 larger than at the Heisenberg limit. An ideally suited cooling method for reaching this fundamental limit uses the electromagnetically induced transparency, as it allows cooling of all degrees of freedom at different oscillation frequencies even for mixed ion crystals [25,26]. This would lead to the perfect single-ion single-mode matter-wave source. By changing the trapping parameters we can freely adjust the ratio between the variance of the spatial components versus variance of the momentum components.

Thus, the spot size would be limited by the diffraction of the matter wave, which results in a spot size of  $10^{-10}$  m if we assume a numerical aperture of 0.001 for the ion lens and an energy of 80 eV. To assure the proper alignment of a short focal length lens system with respect to the substrate

TABLE I. Comparison between experimental and numerical  $1\sigma$ -longitudinal velocity uncertainty  $\Delta v$ , beam divergence  $\alpha$  (full angle) and  $1\sigma$ -focal spot radius  $r_f$  for different initial ion temperatures  $T$ .

	T	$\Delta v$	$\alpha$	$r_f$
Meas.	2 mK	6.3 m/s	600 $\mu\text{rad}$	...
Calc.	2 mK	12 m/s	130 $\mu\text{rad}$	7 nm
Calc.	100 $\mu\text{K}$	1 m/s	30 $\mu\text{rad}$	2 nm

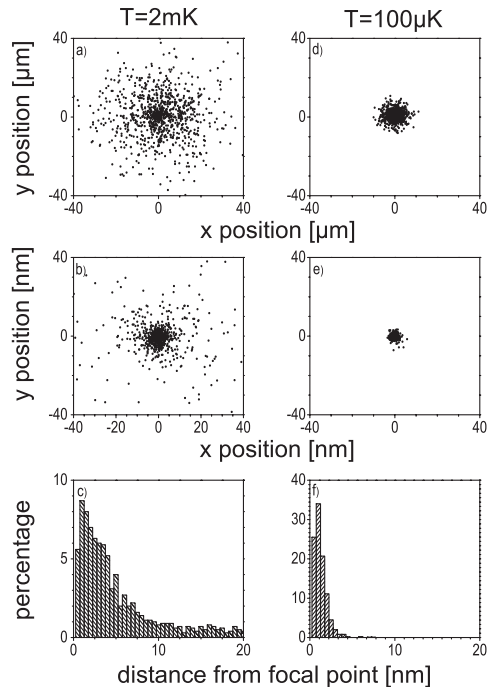


FIG. 4. Monte Carlo simulation of extracted ions. Left side: (a) Spot diagram at a distance of 247 mm from the trap center for an initial ion temperature of 2 mK. (b) Focal spot diagram generated by an einzel-lens with a  $1\sigma$ -spot radius of 7 nm. (c) Histogram of radial distribution of spots in the focal plane. Right side: (d)–(f) Similar diagrams as on the left side but for a temperature of 100  $\mu$ K.

we propose to implant through a hole in the tip of an atomic force microscope [27,28]. This would bring along the additional advantage that the charged particle could be placed with respect to surface structures (such as gate electrodes) in deterministic doping applications. A further possible application of our system is as on-demand source for matter-wave interferometry with ultracold slow ions, which until now was only possible with electrons, neutrons, and neutral atoms and molecules [29–32]. Being compatible with state of the art ion trap quantum processors, our setup may be used to convey qubits directly from one trap to the other by transmitting the qubit carrier itself.

In conclusion, we have experimentally realized a deterministic ultracold source for single ions and ionic molecules. For an ion temperature of a few mK we measured a longitudinal velocity distribution of extracted ions which shows a  $1\sigma$ -spread of a few meters per second which is a promising starting point for the application of ion optical elements. Ion ray tracing simulations predict nm resolution

for our setup when combined with an electrostatic einzel-lens. If the ions are further cooled to the motional ground state our setup could realize the perfect matter-wave source at the Heisenberg limit.

We acknowledge financial support by the Landesstiftung Baden-Württemberg in the framework “atomics” (Contract No. PN 63.14), the European commission within EMALI (Contract No. MRTN-CT-2006-035369) and the Volkswagen Stiftung.

\*kilian.singer@uni-ulm.de

†URL: <http://www.quantenbit.de>

- [1] T. Shinada, S. Okamoto, T. Kobayashi, and I. Ohdomari, *Nature (London)* **437**, 1128 (2005).
- [2] M. V. Gurudev Dutt *et al.*, *Science* **316**, 1312 (2007).
- [3] P. Neumann *et al.*, *Science* **320**, 1326 (2008).
- [4] B. E. Kane, *Nature (London)* **393**, 133 (1998).
- [5] A. D. Greentree, B. A. Fairchild, F. M. Hossain, and S. Praver, *Mater. Today* **11**, 22 (2008).
- [6] T. Shinada, H. Koyama, C. Hinshita, K. Imamura, and I. Ohdomari, *Jpn. J. Appl. Phys.* **41**, L287 (2002).
- [7] A. Persaud *et al.*, *Quant. Info. Proc.* **3**, 233 (2004).
- [8] M. Mitic *et al.*, *Microelectron. Eng.* **78**, 279 (2005).
- [9] A. Batra *et al.*, *Appl. Phys. Lett.* **91**, 193502 (2007).
- [10] T. Shinada *et al.*, *Nanotechnology* **19**, 345202 (2008).
- [11] J. L. O’Brien *et al.*, *Phys. Rev. B* **64**, 161401(R) (2001).
- [12] S. R. Schofield *et al.*, *Phys. Rev. Lett.* **91**, 136104 (2003).
- [13] F. J. Ruess *et al.*, *Nano Lett.* **4**, 1969 (2004).
- [14] W. Pok *et al.*, *IEEE Trans. Nanotechnol.* **6**, 213 (2007).
- [15] F. J. Ruess *et al.*, *Small* **3**, 563 (2007).
- [16] J. Meijer *et al.*, *Appl. Phys. A* **83**, 321 (2006).
- [17] M. A. Rowe *et al.*, *Quantum Inf. Comput.* **2**, 257 (2002).
- [18] M. Drewsen, A. Mortensen, R. Martinussen, P. Staunum, and J. L. Sørensen, *Phys. Rev. Lett.* **93**, 243201 (2004).
- [19] H. Nägerl *et al.*, *Opt. Express* **3**, 89 (1998).
- [20] Y. Lee *et al.*, *J. Vac. Sci. Technol. B* **16**, 3367 (1998) reports measurements of a narrow ion velocity distribution in nondeterministic sources with additional velocity filtering. Our measured velocity uncertainty is more than 1 order of magnitude smaller.
- [21] G. Huber *et al.*, *New J. Phys.* **10**, 013004 (2008).
- [22] L. Greengard, *The Rapid Evaluation of Potential Fields in Particle Systems* (M.I.T. Press, Cambridge, Massachusetts, 1988).
- [23] S. Schulz, U. Poschinger, F. Ziesel, and F. Schmidt-Kaler, *New J. Phys.* **10**, 045007 (2008).
- [24] A. Septier, CERN Report No. 60-39 (1960).
- [25] C. F. Roos *et al.*, *Phys. Rev. Lett.* **85**, 5547 (2000).
- [26] F. Schmidt-Kaler *et al.*, *Appl. Phys. B* **73**, 807 (2001).
- [27] A. Persaud *et al.*, *Nano Lett.* **5**, 1087 (2005).
- [28] J. Meijer *et al.*, *Appl. Phys. A* **91**, 567 (2008).
- [29] C. Jönsson, *Z. Phys.* **161**, 454 (1961).
- [30] O. Carnal and J. Mlynek, *Phys. Rev. Lett.* **66**, 2689 (1991).
- [31] M. Arndt *et al.*, *Nature (London)* **401**, 680 (1999).
- [32] H. Rauch, W. Treimer, and U. Bonse, *Phys. Lett. A* **47**, 369 (1974).



## B.2 Journal of Modern Optics

### **Optimized focusing ion optics for an ultracold deterministic single ion source targeting nm resolution**

---

R. Fickler, W. Schnitzler, F. Schmidt-Kaler and K. Singer

Published on 18th August 2009 in the scientific journal:

**Journal of Modern Optics**

(Volume: 56 / Pages: 2061 - 2075 / Year: 2009)

### Optimised focusing ion optics for an ultracold deterministic single ion source targeting nm resolution

Robert Fickler<sup>a</sup>, Wolfgang Schnitzler<sup>a</sup>, Norbert M. Linke<sup>a,b</sup>, Ferdinand Schmidt-Kaler<sup>a</sup> and Kilian Singer<sup>a\*</sup>

<sup>a</sup>Institut für Quanteninformationsverarbeitung, Universität Ulm, Ulm, Germany; <sup>b</sup>Department of Physics, University of Oxford, Clarendon Laboratory, Oxford, UK

(Received 11 March 2009; final version received 11 July 2009)

Using a segmented ion trap with mK laser-cooled ions we have realised a novel single ion source which can deterministically deliver a wide range of ion species, isotopes or ionic molecules [Schnitzler et al. *Phys. Rev. Lett.* **2009**, *102*, 070501]. Experimental data is discussed in detail and compared with numerical simulations of ion trajectories. For the novel ion source we numerically investigate the influence of various extraction parameters on fluctuations in velocity and position of the beam. We present specialised ion optics and show from numerical simulations that a nm spatial resolution is achievable. The Paul trap, which is used as a single ion source, together with the presented ion optics, constitutes a promising candidate for a deterministic ion implantation method for applications in solid state quantum computing or classical nano-electronic devices.

**Keywords:** laser cooling; deterministic single ion source; ion optics

#### 1. Motivation

Over the last few years, integrated semiconductor devices have reached structure sizes in the order of a few tens of nanometres, and further miniaturisation is expected. Thus, it is becoming more and more important to dope the devices in an exact predetermined and reproducible manner. In the next few years, the amount of doping atoms in the active region of a field effect transistor might drop below 100, then statistical Poissonian fluctuations which arise from conventional doping techniques will be significant. At nanometre length scales, only small fluctuations in the number of doped atoms are sufficient such that the assumption of homogeneously distributed doping atoms is no longer valid and the electronic characteristics are disturbed [1]. But not only conventional solid state devices would benefit from an accurate quantity of doping atoms, a future solid state quantum computer fully relies on precisely placed single dopant atoms; at well-defined distances and depths. In those quantum devices, single embedded impurity atoms, e.g. phosphorus dopants in silicon [2] or colour centres in diamond [3], are used to retain and process information in a quantum mechanical way. Nowadays it is possible to address single quantum devices like nitrogen-vacancy (NV) colour centres in diamond and to manipulate them coherently over several  $\mu\text{s}$  or even ms [4,5]. However, when it comes to scalable quantum computers with more than a few qubit carriers, one of the most important challenges

is to place the dopant atoms at an exact position and with uniform separation at nm resolution. One method proposed for the fabrication of these assemblies uses lithography based on scanning tunnelling microscopy (STM) [6–10]. A hydrogen terminated silicon surface is structured with an STM, followed by chemical reactive surface binding of the doping atoms. Although the positioning of the incorporated single phosphorous dopants is realised with sub-nm accuracy, the technique is limited to silicon surfaces and unavoidable impurities in the background gas can lead to functional impairment. Another method for controlling the amount of doping atoms is the direct implantation of atoms or ions. Here, the common approach utilises statistical thermal sources which provide a dense ion beam that has to be thinned out by several choppers and apertures. To ensure single ion implantation it is necessary to detect the implantation event by observing the generated Auger electrons, photoluminescence, phonons, electron–hole pairs or changes in the conductance of a field effect transistor [11–15]. Therefore, the implantation only works if the ions are either highly charged or implanted with large kinetic energies. With both systems it is possible to achieve a resolution of less than 10 nm, but their use is limited to cases where either highly charged states or high kinetic energies are available, and therefore deep implantation is unavoidable. Both methods lead to surface damage and additional inaccuracies in depth and lateral position

\*Corresponding author. Email: kilian.singer@uni-ulm.de

2062

R. Fickler et al.

due to statistical straggling. Our method is universally applicable to a wide range of doping atoms and it allows implanting at very low energies, thus avoiding the problems described above.

## 2. Ultracold deterministic ion point source

We have realised a novel system for direct implantation of ions into solid state surfaces by using a Paul trap as an ultracold deterministic ion source [16–18].

### 2.1. Specialised linear Paul trap

Central component of our technique is a linear segmented Paul trap with laser cooled  $^{40}\text{Ca}^+$  ions similar to those utilised for scalable quantum information processing [19]. A Paul trap is a well known tool for trapping single, charged particles by using static (dc) electric fields and an alternating (rf) field, thereby producing a pseudo-potential of around 1 eV depth. With various laser cooling techniques, the trapped ions can be cooled to the motional ground state [20,21]. In addition, it is possible to trap other charged particles or even molecules that cannot be directly laser cooled but can be sympathetically cooled due to their electrostatic interaction. Identification of those additionally loaded doping ions, which are invisible to laser light, can be conducted by exciting collective vibrational modes [22,23]. The segmented trap design is capable of separating and transporting ions over a distance of a few cm [24]. Our design consists of four copper-plated polyimide blades of 410  $\mu\text{m}$  thickness and 65 mm length arranged in an x-shaped manner with a distance of 2 mm between opposing blades [18]. The dc voltages are applied to eight segments of 0.7 mm width on the top and bottom of each blade. A unique feature of our design is that it is capable of shooting out ions in a well-defined axial direction by switching two of the electrode segments to a higher voltage. Unlike conventional linear Paul traps, our design does not lose its radial confinement even when biasing the dc trap potential to high voltages. This is realised by applying the rf to the electrodes at the inner front edges of two opposing blades, while the other two are grounded. Furthermore, the trap features an additional broader deflection electrode on every blade, which is used to aim the extracted ions in the demanded direction. This special arrangement enables the exact axial extraction of the cooled  $^{40}\text{Ca}^+$  ions and sympathetically cooled dark ions due to the preservation of the radial confinement during the extraction sequence. The development and numerical investigation of this special design was feasible with our custom-designed simulation software (see Section 3). Characteristic working conditions are an rf voltage with

an amplitude of 200 V at a frequency of  $\Omega/2\pi = 12.155$  MHz, which yields a radial secular frequency  $\omega_{\text{rad}}/2\pi = 430$  kHz for a  $^{40}\text{Ca}^+$  ion. The required dc potential is generated by a voltage of 35 V which is applied to trap segments 2 and 8 and leads to a frequency of the axial potential of  $\omega_{\text{ax}}/2\pi = 280$  kHz. The vacuum chamber itself is made out of stainless steel and evacuated down to a base pressure of  $3 \times 10^{-9}$  mbar by a turbo molecular pump, an ion-getter pump and a titanium sublimation pump. Calcium and dopant ion generation is induced via a multiphoton process, e.g. by a pulsed frequency tripled Nd-YAG laser with a wavelength of 355 nm and a pulse power of 7 mJ.

### 2.2. Observation of ions

With this setup the trapped  $^{40}\text{Ca}^+$  ions are located above segment 5, where they are Doppler cooled and illuminated by laser light near 397, 866 and 854 nm. In order to image single ions or ion crystals we collect the scattered photons by a f/1.76 lens on an electron multiplying charge coupled device (EMCCD) camera. While the calcium ions can be directly cooled by the installed laser system and identified on the image from the camera, the additionally loaded doping ions are sympathetically cooled and can be easily identified by the voids in the image of the ion crystal [18] as they are not excited by the applied laser fields at 397, 866 and 854 nm. By applying an alternating voltage to an electrode located under the ion crystal we can resonantly stimulate collective vibrational modes with characteristic resonance frequencies  $\omega_{\text{ax}}$  and therefore specify the exact species of these dark ions [22]. Another determination of the additionally loaded doping ions can be implemented by measuring the mass ratio with amplitude modulated resonant laser light [23]. So far, the trapped particles are simply Doppler cooled down to  $T \approx 2$  mK, which is slightly above the Doppler limit and was deduced from the width of the excitation spectrum on the  $S_{1/2} - P_{1/2}$  laser cooling transition. With further cooling methods using electromagnetically induced transparency, which is currently implemented in our lab, it is possible to cool the broad band of vibrational frequencies of an ion crystal simultaneously and thereby reach the motional ground state [20,25]. Under these initial conditions the ion trap would operate at the fundamental limit given by the Heisenberg uncertainty relation. In order to exclusively implant doping ions they can be separated from the cooling  $^{40}\text{Ca}^+$  ions in two different possible implementations. Firstly, by splitting the ions inside the trap before the extraction is performed and which can be achieved by converting the axial potential into a double well and transporting

the doping ion away by subsequently applying time dependent dc voltages [24]. The second possible separation process can be implemented after the extraction of the mixed ion crystal by deflecting unwanted ions, e.g. by increasing the voltage of an einzel-lens (see Section 3.2).

### 2.3. Extraction of ions

The extraction process itself is induced by biasing segments 4 and 5 with 500 V (supplied by Iseg Inc., Model EHQ-8010p) within a few nanoseconds. This fast switching is achieved by two high voltage switches (Behlke Inc., HTS 41-06-GSM) which are triggered by a TTL signal from our control computer. In addition, we synchronised the switching event with the rf field phase in order to reduce fluctuations of velocity and position of the ion by implementing an electronic phase synchronisation circuit which delays the TTL signal to a well-defined constant time period after the zero crossing of the rf. The experimentally measured standard deviation of the delay time equals 0.34 ns. For the detection of the extracted ions or dopants we use an electron multiplier tube (EMT) with 20 dynodes (ETP Inc., Model AF553) which is supplied with a voltage of  $-2.5$  kV and has a specified quantum efficiency of about 80% for positively charged particles. The gain is specified with  $5 \times 10^5$  and provides a 100 mV electrical signal which is 10 to 15 ns wide for each detection event. The EMT is accommodated in a second vacuum chamber which is located at 247 mm from the trap and can be completely separated by a valve to facilitate prospective changes of target probes.

### 3. Numerical simulation of the ion source and specialised ion optics

For designing an optimised trap and ion optics we developed a simulation software package which is based on a fast multipole solver [26,27] with additional high accuracy solvers respecting symmetry properties of the trap and the ion optics. The software allows deducing accurate electrostatic potentials from any CAD model. With this simulation software we describe the trajectories during the extraction and the expected spots at the target. We analyse the dependence of the spatial dimension and the velocity fluctuation of the single ion beam on the initial ion temperature, the start position inside the trap and the phase of the rf voltage at the extraction event. Additionally, we compare different designs of possible einzel-lenses and study the simulated focusing properties as well as the ability of our system to correct spherical aberration of the lens and to deflect the cooling ions during the implantation process.

To verify our simulation with experimental data we have checked different trap geometries and found an agreement of the axial and radial trapping frequencies within 2 to 3%.

#### 3.1. Deterministic ion point source

For an exact simulation of the trap potentials we have sketched the complete trap geometry as a full three-dimensional CAD model. By virtually applying the same voltages as we do in the real experiment (values mentioned above) we are able to calculate the trajectories of the trapped particles with full time dependent dynamics including micro motion at frequency  $\Omega$ . The initial momentum and position of the ion inside the trap is determined from the thermal Boltzmann distribution at a selectable temperature. The extraction process is triggered by switching two segments on every trap blade to 500 V synchronised to a well-defined phase of the rf voltage. The plotted trajectories show the influence of the micro motion during the extraction and the resulting spread of the ion beam (see Figure 1(a)). Slight numerical asymmetries, which appear despite the symmetrisation procedure, are corrected by small compensation voltages on the rails as in the real experiment.

##### 3.1.1. Dependence of the ion beam on the initial ion temperature

With an initial ion temperature of 2 mK the results show a  $1\sigma$ -spot<sup>1</sup> radius of  $16.5 \mu\text{m}$  at a distance of 247 mm between trap centre and target which amounts to a full angle beam divergence of  $134 \mu\text{rad}$  (see Figure 1(b)). The specified temperature of 2 mK is similar to the experimentally achieved value and the deflection electrodes are grounded during the extraction simulation. The mean longitudinal velocity of the extracted ions at the target is calculated to be  $22.1 \text{ km s}^{-1}$  with an  $1\sigma$ -uncertainty of only  $1.3 \text{ ms}^{-1}$ . Therefore, the predicted ion beam shows promising characteristics for subsequent focusing with ion optics due to small spherical and chromatical aberration. The predictions are even better if sub-Doppler cooling methods are applied. This would lead to mean phonon expectation values below 1 and temperatures of  $100 \mu\text{K}$  for the ions inside the trap, respectively. Then the setup would work at the Heisenberg limit. The full angle divergence of the generated ion beam shrinks to  $30 \mu\text{rad}$ . This means the  $1\sigma$ -spot size at the target amounts to  $3.7 \mu\text{m}$  and therefore the beam improves significantly. However, as the extraction voltage remains the same, the mean longitudinal velocity is not influenced by the smaller initial temperature, but the  $1\sigma$ -velocity uncertainty decreases slightly to  $1 \text{ ms}^{-1}$ . Although these values are

2064

R. Fickler et al.

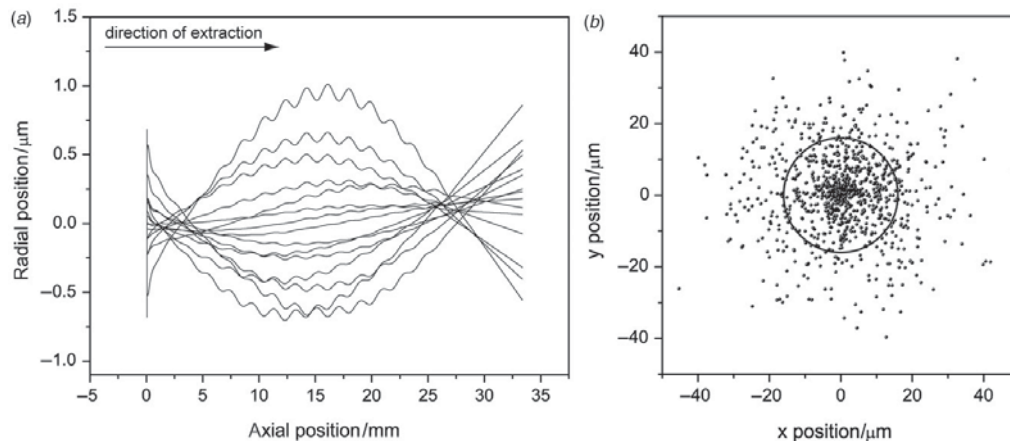


Figure 1. (a) Trajectories of  $^{40}\text{Ca}^+$  ions during extraction from the trap with an initial temperature of 2 mK. (b) Resulting spot diagram at a distance of 247 mm between trap centre and target amounts to a beam divergence of  $134\mu\text{rad}$  (grey circle illustrates the  $1\sigma$ -spot radius of  $16\mu\text{m}$ ).

very promising it has to be noted that these calculations are fully classical. As the ions are cooled to the motional ground state quantum mechanical simulations describing the propagation of the wave packets of the extracted ions would be needed to get more exact values. Nevertheless, these simulations show that by applying voltages to the deflection electrodes, the characteristics of the resulting spot shapes change enormously. For example, if we apply 7.5 V between two opposing deflection electrodes and 9.1 V between the others, respectively (which resembles our experimental setup), the spot is approximately shifted 19.4 mm in the horizontal and 30.5 mm in the vertical direction. In addition to this expected deflection the spot is stretched from the former Gaussian to a cigar-shaped distribution and therefore the  $1\sigma$ -spot size value cannot be calculated (see Section 3.1.3, Figure 3(b), zoomed area). This drastic change is simulated for 2 mK cooled ions as well as for sub-Doppler cooled ions.

### 3.1.2. Dependence of the ion beam on the initial start position

Aside from the dependence on the initial temperature, the transversal expansion and the velocity of the ion beam with its uncertainty strongly depends on the start position of the extracted ion. Whereas altering the initial position does not change the size and the (Gaussian) spot shape at the target significantly when deflection electrodes are grounded, the velocity fluctuation is strongly affected (see Figure 2(a)). For displacements up to  $\pm 400\mu\text{m}$  the mean longitudinal velocity for the different displacements has a constant

value of  $22\text{ km s}^{-1}$  ( $\pm 2\%$ ). Conversely, the velocity spread at each displacement varies enormously: from only  $1.3\text{ m s}^{-1}$  when the ions are extracted from the theoretical minimum of the axial potential, it increases up to  $1.5\text{ km s}^{-1}$  when they are shifted around  $420\mu\text{m}$  out of the centre of the potential before being extracted. This is caused by a strong increase of the micro motion of a trapped ion when it is no longer in the minimum of the trapping potential, and therefore has a highly varying initial momentum. For the  $1\sigma$ -spot sizes it is also advantageous to extract the ion out of the potential minimum. Then, a  $1\sigma$ -spot of about  $16\mu\text{m}$  can be achieved. However, a displacement of  $\pm 400\mu\text{m}$  only leads to an enlargement of the  $1\sigma$ -spot size by an additional  $2\mu\text{m}$ . The influence of the start position on the ion beam properties becomes more crucial when the deflection electrodes are supplied with a non-zero voltage. Due to slightly displaced trajectories during the extraction process, the ions start to oscillate in the rf drive field and therefore lose their well-defined extraction direction. In Figure 2(a) the ions are displaced up to  $420\mu\text{m}$  from the potential minimum before extraction which means that the ion is trapped in the middle of two electrodes. The former cigar-shaped extension of the spot of around half a millimetre increases tremendously to about 10 to 20 mm. Additionally, the shape changes to a screw-like structure (see Figure 2(a)) and deterministic aiming becomes nearly impossible. The mean value of the longitudinal velocity sums to around  $22\text{ km s}^{-1}$  and changes only by 2% for different extraction positions, while fluctuations increase to a maximum of  $1.6\text{ km s}^{-1}$  for ions shifted  $420\mu\text{m}$  out of the trapping potential minimum.

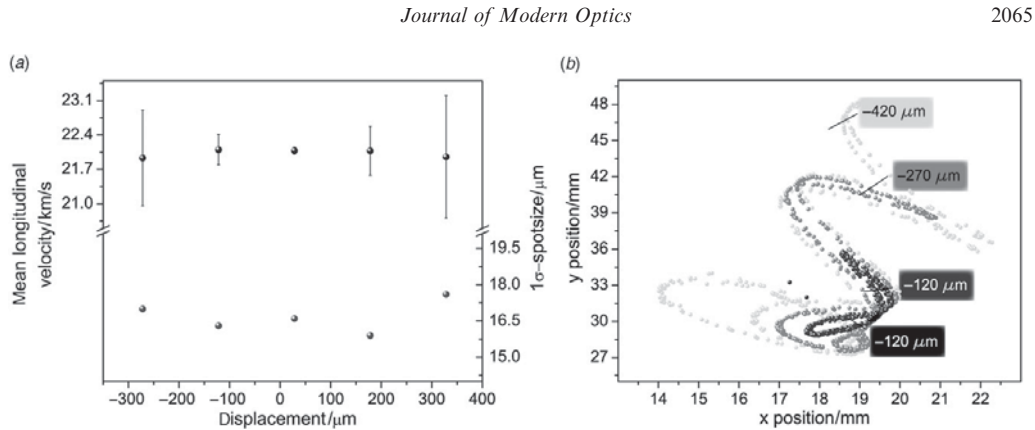


Figure 2. Dependence of the ion beam on the start position (positive values mean towards the extraction direction). (a) Resulting mean longitudinal velocities and  $1\sigma$ -spot sizes after extraction at a distance of 247 mm from the trap centre with deflection electrodes grounded. (b) Resulting spot diagrams of extracted ions when the deflection electrodes are biased to 7.5 V between two opposing trap blades and 9.1 V between the other two blades, respectively.

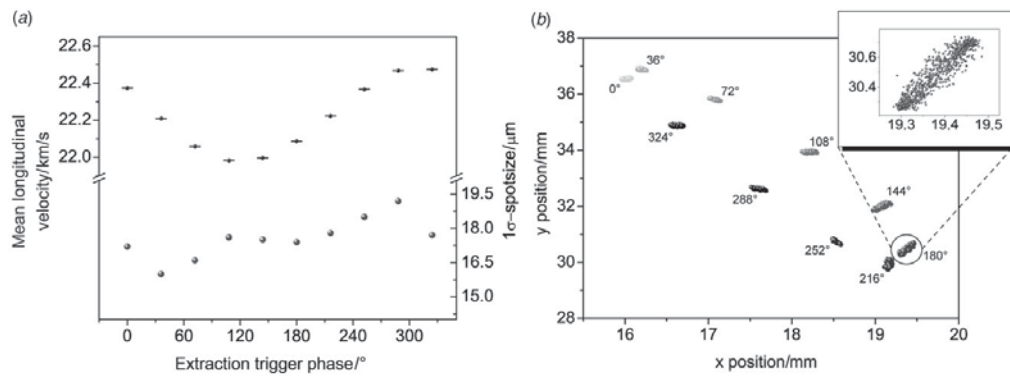


Figure 3. Dependence of the ion beam on the phase of the rf voltage. Initial temperature of the ions inside the trap is kept constant at 2 mK and the distance is set to 247 mm from the trap centre for all shown results. (a) Resulting mean longitudinal velocities and  $1\sigma$ -spot sizes with deflection electrodes grounded. (b) Resulting spot diagrams of extracted ion when the deflection electrodes are biased to 7.5 V between two opposing trap blades and 9.1 V between the other two blades, respectively. In (b) one spot is zoomed in to show that a Gaussian distribution is no longer an accurate assumption if the ions are deflected during extraction.

### 3.1.3. Dependence of the ion beam on the phase of the rf voltage at the instance of extraction

Similar results are calculated for the enlargement of the beam expansion while changing the phase of the rf voltage at the time of the extraction event (see Figure 3(b)). Here, the  $1\sigma$ -spot size varies from 16 to 19  $\mu\text{m}$  over a whole period of the radio frequency voltage but remains Gaussian distributed. The mean longitudinal velocity oscillates in a sine-like manner over an interval of  $0.5 \text{ km s}^{-1}$  around  $22.2 \text{ km s}^{-1}$  during the different trigger phases. The velocity spread only varies negligibly between  $1.3$  and  $2.3 \text{ m s}^{-1}$ . This shows

that with deflection electrodes grounded, the trigger phase at the extraction event is important to reach a single ion beam featuring the promising characteristics of a narrow velocity fluctuation and a small beam divergence. Again, the exact triggering phase becomes even more important when the deflection electrodes are used to aim the ions during the extraction process. In Figure 3(b) the simulated spots are shown for altering the trigger phase and deflecting the ions with the same voltages mentioned above. The spot shape for a constant trigger phase maintains its oval shape and size. When changing the phase the spots are distributed over

2066

R. Fickler et al.

an area of 10 mm by 15 mm. The mean velocity for each different trigger phase stays within 1% at around  $22 \text{ km s}^{-1}$ , and the fluctuations only add up to around  $2.5 \text{ m s}^{-1}$ . Hence, to achieve a beam of single deterministic extracted ions suitable for implantation it is important to align the trap axis to the ion optical axis as accurately as possible and therefore avoid the usage of the deflection electrodes. Besides the alignment, it is also crucial to position the ion into the radial pseudo-potential minimum. Furthermore, the extraction itself has to be synchronised to the rf field as exactly as possible.

### 3.2. Ion optics

In order to use our specially designed ion trap as a deterministic implantation tool it does not suffice to shoot the ions out of the trap with the aforementioned small values of beam divergence and velocity fluctuations: the ion trajectories have to be focused down to a few nm. To realise this goal we have developed ion optics which should be able to focus the beam down to the required nanometre regime, even to a  $1\sigma$ -spot size of around one nm without additional optical elements to reduce aberration errors. Due to the narrow ion trajectories and the low fluctuations in the velocity of the ions, the focusing optics can be kept simple without sophisticated aberration corrections [28–31]. A rotationally symmetric simple electrostatic einzel-lens yields adequate results. This type of ion lens consists of three electrodes where the first and the third electrode are on the same potential. The electrostatic potential resembles a saddle surface and can be generated in two different modes, decel-accel and accel-decel mode. The former mode is achieved when the middle electrode is biased to a voltage with the same sign as the charged particle (in our case a positive voltage) while the lens operates in the accel-decel mode with a voltage of opposite sign with respect to the charged particles. Both modes offer different advantages [32]. In the accel-decel mode the undesirable chromatical and spherical aberrations are smaller than in the decel-accel mode. The chromatic aberration is reduced due to higher velocities of the particles inside the lens and a therefore lower relative velocity spread  $\Delta v/v$ . Additionally, spherical aberration is smaller because the ion trajectories are closer to the optical axis during their passage through the lens [33] since they are always deflected towards the axis, while in the decel-accel mode the ions diverge at first before being focused to the centre. On the other hand, the decel-accel mode offers three essential advantages. Firstly, the lens requires lower centre electrode voltages for reaching a similar focal length. In addition,

by applying positive voltages it is possible to correct spherical aberration by switching the voltage to a higher potential while the particle is going through the lens [34] and in our setup the lens can be used as a deflector for different ion species (both will be discussed in more detail below).

#### 3.2.1. Comparison of different lens designs

In order to optimise the properties of the lens, different shapes are possible and have been discussed [31–33, 35, 36]. Generally, the most important feature is a perfect alignment of the electrodes in connection with voltage stability which depends, on the one hand, on the voltage supply, and on the other hand, on the insulating material between the electrodes. For the properties of the lens it can be presumed that the smaller the dimensions of the lens, the better its focusing properties are. However, the decreasing of the lens dimension is limited by the extension of the ion beam because spherical aberration effects become stronger when the size of the beam approaches the lens diameter. To assure that all ions easily go through the lens and spherical aberration is not dominant, we designed lenses with an entrance aperture of 1 mm. Usually the lens' properties improve when the first electrode is thinner than the second one and the gap spacing between them is minimal. Conversely, the distance between the second and the third electrode has to be much larger to minimise the focal spot size (see Figures 4(a) and (c)). Another possibility to improve the focusing properties is to change the shape of the electrodes, e.g. to a special design developed by Septier [36]. The design is based on a lens with hyperbolic field distribution which has good imaging characteristics even for steeply inclining beams, but has been modified to reduce spherical aberration (see Figure 4(b)). Each of the three electrodes has a different aperture and a completely different shape. For an optimal adjustment of the lens to our single ion source we have developed a huge range of different lenses and simulated the achievable spot sizes. In Figure 4 we present three different types to demonstrate the enormous influence of the lens design, each with the focal distance and the appropriate optimised focal spot size at different voltages and temperatures. A non-optimised einzel-lens made out of three equivalent electrodes and gaps in between in the decel-accel mode (see Figure 4(a)) allows one to focus down the non-deflected ion beam to a  $1\sigma$ -spot radius of 25.9 nm with 2 mK cooled ions (5.1 nm @ 100  $\mu$ K). Slightly better results are obtained in the accel-decel mode, where the  $1\sigma$ -spot size produces 20.7 nm for ion beams of 2 mK cooled ions (3.0 nm @ 100  $\mu$ K). Although this simple einzel-lens already achieves nanometre spot sizes, the required voltages, especially in the accel-decel mode, are

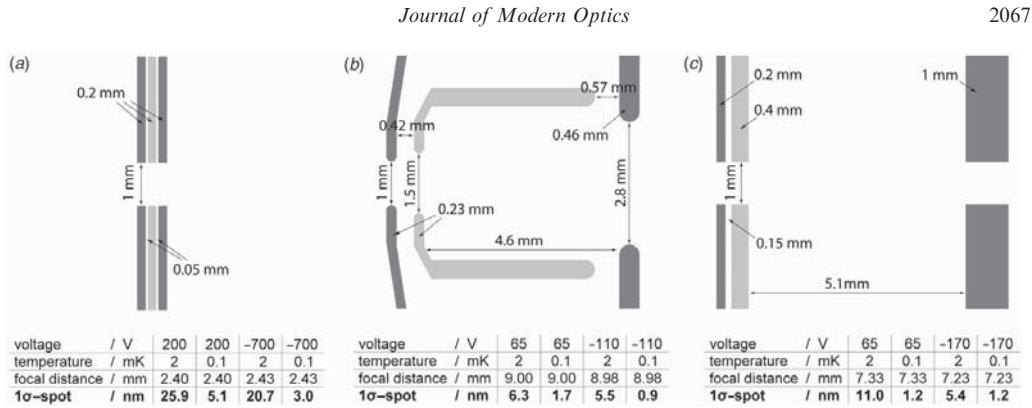


Figure 4. Comparison of three different shapes of einzel-lenses. Non-optimised simple lens (a) which is able to focus down the beam by a maximum factor of about 1200. Special shaped einzel-lens (b) with a design developed by Septier [36] where the minimal achievable  $1\sigma$ -spot size is more than three times smaller than the one of the non-optimised einzel-lens. Custom-made einzel-lens (c) which is implemented in our setup due to realisable electrode shapes with similar focusing properties as the special shaped lens (b). Aside from a maximum focusing factor of approximately 3000, the simulation predicts for the decel-accel mode (middle electrode repulsive) optimal results which is important for further implementation of spherical aberration correction and utilisation of the lens as an ion deflector. Voltages are applied to the centre electrode (light grey) while the outer ones are grounded (dark grey).

too high to ensure the insulating property of the spacer between the electrodes. Conversely, the lens in Figure 4(b), which resembles the one developed by Septier, is able to achieve (in decel-accel mode) a focal  $1\sigma$ -spot radius of 6.3 nm, even with ions of 2 mK temperature before extraction. With ions cooled to the motional ground state (100  $\mu$ K) the simulated spot size decreases down to 1.7 nm. Even better are the results for the accel-decel mode where the  $1\sigma$ -spot size amounts to 5.5 nm for 2 mK and only 0.9 nm for 100  $\mu$ K. This proves the desired qualities of our achieved ion beam and shows explicitly that our setup is able to operate at nm resolution. However, the realisation of this lens is quite difficult because of different apertures, the inclined electrodes and the rounded edges. For this reason we have developed a design with similar focusing properties but which is easily realisable (see Figure 4(c)).

### 3.2.2. Analysis of the developed einzel-lens

The apertures of all three electrodes of our developed einzel-lens equal 1 mm, which facilitates exact alignment. The gaps between the electrodes are 150  $\mu$ m wide to ensure the required insulation. For the accel-decel mode it is possible to reach a  $1\sigma$ -spot size of 1.2 nm for 100  $\mu$ K cooled ions (5.4 nm @ 2 mK) which is comparable to the results for the special shaped lens from Septier. Although the outcomes in the accel-decel mode for 2 mK are better than in the decel-accel mode, which means this mode shows bigger chromatical aberration effects, we have chosen to use the lens in the

decel-accel mode to be able to implement spherical aberration correction and to utilise the lens as a switchable deflector for ions. With 2 mK cooled ions inside the trap we can achieve a  $1\sigma$ -spot size of the extracted ions after focusing through the lens of 11.0 and 1.2 nm for ground state cooled ions, respectively.

In Figure 5, the induced potential for the lens of Figure 4(c) is plotted when the centre electrode is biased to 65 V. The potential plot illustrates the function of an einzel-lens in the decel-accel mode. Before the ions enter the lens, they are slowed down and deflected slightly away from the axis. After further defocusing, the ions reach the highest point of the potential which is approximately 60 V and therefore have the slowest velocity. Afterwards the ions are accelerated out of the lens and focused strongly to the axis. The focusing effect relies on the different ion velocities inside the lens potential. The longitudinal velocity of the ion is higher during the defocusing period while climbing to the maximum potential and it is lower during the focusing period thereafter. This generates the focusing force even for complete symmetric lens constructions as shown in Figure 4(a), and explains the lower voltages for lens designs where the focusing space is stretched by positioning the last electrode further away from the centre electrode (see Figures 4(b) and (c)). In Figure 6, trajectories of extracted  $^{40}\text{Ca}^+$  ions through the lens are shown, as well as the focal spot at a distance of 7.33 mm after entering the lens. When the ions are extracted with 2 mK initial temperature and the lens is biased to 65 V,

2068

R. Fickler et al.

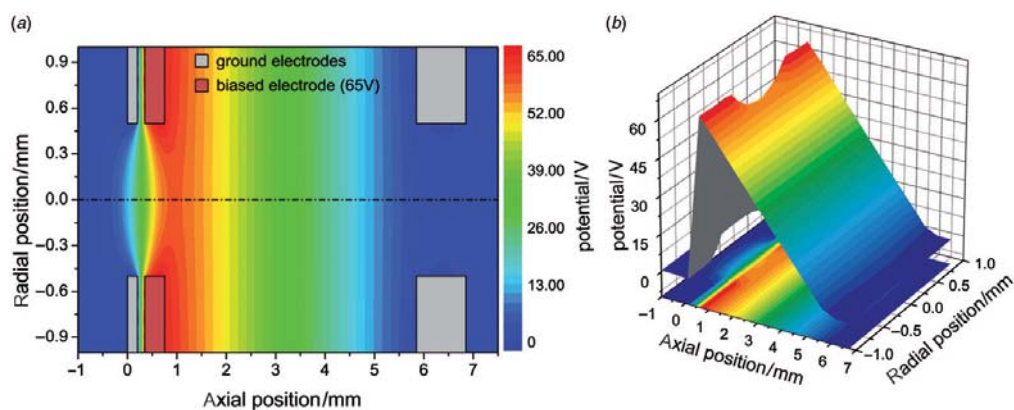


Figure 5. (a) Potential of the lens from Figure 4(c) where the central electrode is biased to 65 V. (b) Three-dimensional view of the potential distribution. (The colour version of this figure is included in the online version of the journal.)

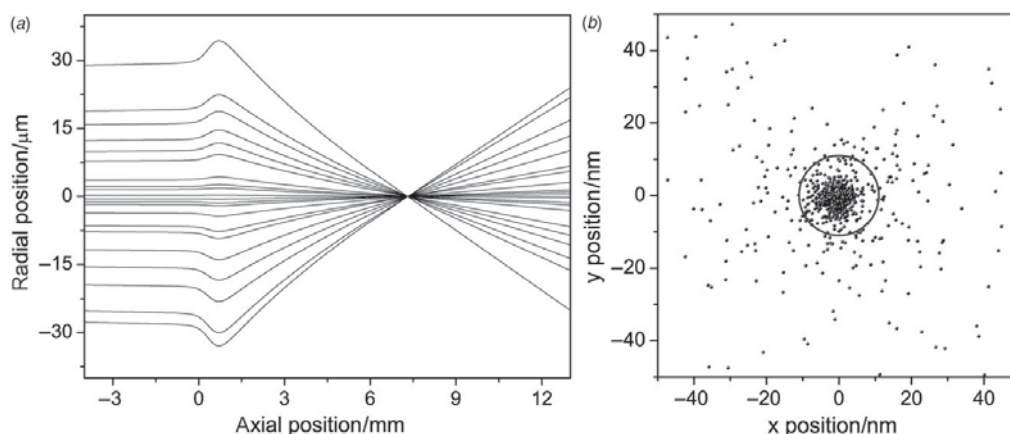


Figure 6. (a) Trajectories of extracted  $^{40}\text{Ca}^+$  ions at 2 mK which are focused by the lens of Figure 4(c) in the decel-accel mode (65 V) to a  $1\sigma$ -spot size of 11 nm. (b) Resulting spot diagram in the focal spot around 0.5 mm after the last electrode of the lens (grey circle illustrates the  $1\sigma$ -spot radius).

the focal spot occurs half a millimetre after the last electrode and shows a  $1\sigma$ -spot size of only 11 nm. Reducing the voltage of the centre electrode moves the focal spot size further behind the lens almost without impairment of the focusing properties. Lowering the voltage, for instance to 50 V, generates the spot 8.5 mm after the last electrode, but the spot size is hardly affected and remains at 12 nm. Therefore, the focal distance can be adjusted over a few mm without a severe loss in performance by simply changing the voltages of the centre electrode. However, the varying range should be as small as possible since further

decreasing of the voltage increases the spot size (see Figure 7(a)). A further reduction to 25 V, for example, enlarges the spot size up to 52 nm by a movement of around 100 mm. As described above, our ion source is able to deflect the ions during extraction by biasing the deflection electrodes. Small discrepancies in the alignment of the setup can be corrected by slight deflection of the beam into the optical axis. The importance of shooting through the lens without even small initial dislocation of the ion beam is shown in Figure 7(b). For example, a displacement of the incoming beam of half the aperture radius ( $250\mu\text{m}$ ) annihilates the

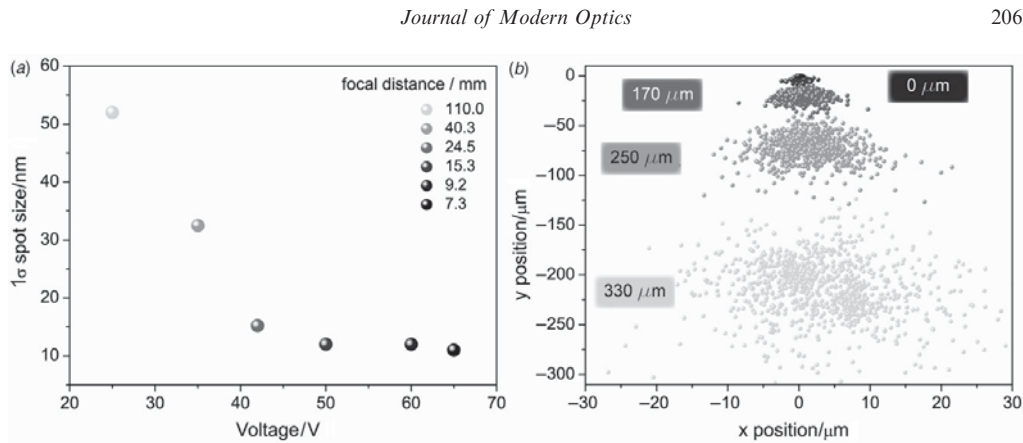


Figure 7. (a) Enlargement of the  $1\sigma$ -spot size by applying smaller voltages to the centre electrode of the lens. The focal plane moves away from the lens. 65 V is the upper limit for the lens voltage because even higher voltages would generate a focus of the beam inside the lens. (b) If the initial beam is dislocated out of the centre of the lens, the focusing properties of the lens worsen or even annihilate. Here, the focal plane is kept constant at 0.5 mm after the lens as well as the voltage of 65 V. The incoming beam is displaced upward in the positive  $x$ -axis to different distances.

focusing property. Besides the displacement of the outgoing beam in the opposite direction, it also diverges to similar spot dimensions as it has without any ion optics. With further shifting of the ion beam the lens even enlarges the spot size in the intended focal plane. Hence, for this required precise alignment, the deflection electrodes present the best way to aim the extracted ion beam to the centre of the lens aperture. A displacement in one direction of the trap axis of 250  $\mu\text{m}$  for example is neutralised by applying a potential of 0.36 V to two opposing trap blades and leads only to a small increase of the  $1\sigma$ -spot size from 16.1 to 17.2  $\mu\text{m}$ . However, when our setup is adjusted accurately, it is, in combination with the specially developed einzel-lens, a perfect implantation source, where nearly every species of charged particles or molecules can be deterministically implanted to any substrate with nanometre resolution.

### 3.2.3. Correction of the spherical aberration

One of the most advantageous properties of our setup is the fact that the ion extractions are synchronised to the rf voltage and the relative velocity uncertainty is extremely low. Thus, the ions are well defined in space and time during the whole extraction, as well as during the focusing process. With that, it is possible to switch the lens to different voltages at different points in time, which enables the correction of aberration effects. When compared to the lens from Septier our design shows a larger spherical aberration which enlarges the spot size a little bit. According to Scherzer's theorem,

it is not possible to avoid such spherical and chromatical aberration with rotationally symmetric electrostatic einzel-lenses in a charge free space [37]. Another way of interpreting the theorem is by stating the impossibility of the realisation of a diverging lens. One way of circumventing this theorem is to use time-dependent electrostatic fields [34] simply by switching the lens to another voltage at a well-defined time. This leads to forces a diverging lens would create and therefore spherical aberration can be reduced. Because of a fast increase of the lens potential at a well-defined time, the particle is accelerated and therefore slightly diverged. Ions with outer trajectories react stronger to the potential shift and subsequently intersect the optical axis further away. The switching time, where the lens voltage is altered from one value to another, has to be accurately chosen and has to be as short as possible. With our high voltage switches mentioned above we are able to vary the voltage within 5 ns, which is short enough to neglect additional energy broadening due to finite rise time of the electric field. However, the spherical aberration correction has to be adjusted to the incoming single ion beam. Simulation shows that for 2 mK cooled ions (which means a  $1\sigma$ -spot size of 16.1  $\mu\text{m}$ ) the best results are obtained when the lens is primarily grounded then biased to 60 V, 170 ns after the ions have passed the first aperture. Thus, the  $1\sigma$ -spot in the focal plane can be nearly reduced by a factor of 2 from 11 nm down to 6.0 nm. The same switching time and voltage reduces the focal  $1\sigma$ -spot size for ground state cooled ions from 1.2 to 0.9 nm. If the ion beam dimensions are

2070

R. Fickler et al.

increased, the factor of improvement also increases slightly. For example, beam characteristics similar to the ones we expect in our experiment after perfectly aligning the lens axis to the trap axis ( $1\sigma$ -spot of  $36\ \mu\text{m}$  and a maximum velocity uncertainty of only  $6\ \text{ms}^{-1}$ ) requires a different setting for the switching time and voltage, but the reduction of the focal spot increases by more than a factor of 2 (see Figure 8). Here, the voltage is switched from 35 V during the entering of the ions to 85 V after 210 ns. The focused spot amounts to 138 nm when the lens is constantly biased to 65 V and decreased down to 57 nm for the spherical aberration corrected lens due to switching of the voltage (see Figure 8(c)). The remaining spread of the focal spot is therefore mainly due to the remaining chromatic aberration of the lens because of the velocity fluctuation. In order to show solely the enhancement of the correction of the spherical aberration, the velocity fluctuations have been artificially removed in Figures 8(a) and (b). Here, the spot improves with the spherical aberration correction from a  $1\sigma$ -spot size of 52 nm down to 12 nm. Note that the spot in Figure 8(a) does not show an accurate Gaussian distribution and therefore the measured value of 68% within 52 nm obviously cannot be read out from the plot. But Figures 8(a) and (b) give a good insight of the enhancement due to spherical aberration correction, whereas Figure 8(c) shows the effect of chromatic aberration. So far chromatic errors will not be corrected by the presented ion optics, but this can be also implemented with time-dependent electric fields [34].

### 3.2.4. Reflection of the cooling ions and post acceleration of the doping ions

Another advantage of the triggered extraction is the possibility to reflect the cooling ions during the implantation process. Because of unavoidable heating processes during a possible separation of the ions inside the trap [19], it is preferable to separate the cooling  $^{40}\text{Ca}^+$  ions from the implantation particles by reflecting the cooling ions at the einzel-lens. Due to different masses of the additionally loaded, sympathetically cooled ions compared to the  $^{40}\text{Ca}^+$  ions, the flight velocities differ from each other. Therefore, the cooling ions arrive at different times at the lens and can be easily reflected by applying higher voltages. Nitrogen, for instance, is accelerated in the simulation up to  $36.2\ \text{km s}^{-1}$  due to its smaller mass, and thus arrives approximately  $4.3\ \mu\text{s}$  earlier at the lens than the  $^{40}\text{Ca}^+$  ions. Hence, the lens has to be switched to a higher potential after the nitrogen particles have passed. The required voltage for reflection has to be at least 115 V, which is experimentally feasible (see Figure 9). Also worth mentioning is that post acceleration will even improve the focusing results by reducing the chromatic aberration due to a smaller *relative* velocity fluctuation. A simple cylindrical tube positioned in the ion beam axis and biased to 10 kV shows promising focusing effects when switched off after the ions are inside the tube. First simulated results predict velocities above  $200\ \text{km s}^{-1}$  and focal  $1\sigma$ -spot sizes of less than 0.4 nm for ground-state cooled ions. However, switching times have to be even more precise due to higher velocities and therefore shortened timescales.

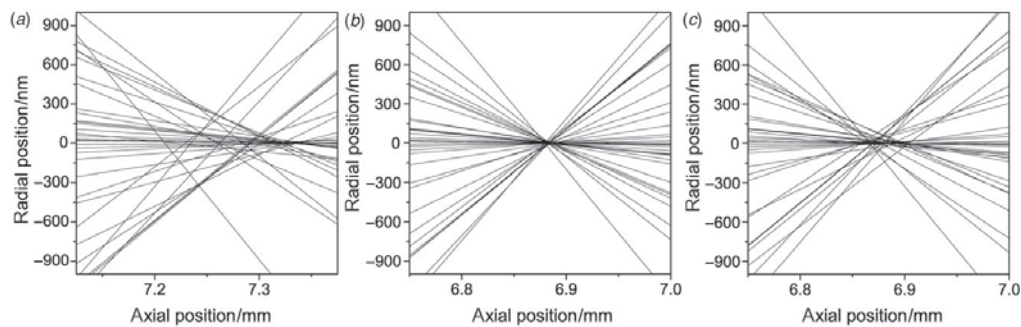


Figure 8. Zoom of the focal regions to show the effect of spherical aberration correction. All diagrams were calculated with an incoming beam with a  $1\sigma$ -spot radius of  $36\ \mu\text{m}$ . For the first two diagrams (a) and (b) the chromatical aberration effect is artificially removed by setting the velocity fluctuations of the ions to zero. The uncorrected spot (a) is achieved with the lens constantly being biased to 65 V and shows a  $1\sigma$ -spot radius of 52 nm. Conversely, the spherical corrected spot (b) only has  $1\sigma$ -size of 12 nm. 210 ns after the ions have entered the lens, the voltage of the centre electrode is switched from 35 to 85 V. The same incoming beam and correction settings of the lens are used for the trajectories in diagram (c), only with an added velocity fluctuation of  $6.3\ \text{ms}^{-1}$  to show the negative effect of the chromatic aberration of the lens. Here, 68% of all simulated ion trajectories lie within a spot radius of 57 nm.

Moreover, the gained reduction of the spatial resolution is partly neutralised by straggling effects of the implanted ions inside the target material.

#### 4. Experimental results of the novel ion source

We have implemented a linear segmented Paul trap as a novel ion source which is deterministic and has promising characteristics in velocity fluctuations and spot sizes for focusing the beam to nanometre resolution [18]. As mentioned above, the source has to be accurately synchronised to the phase of the rf trap drive voltage. We have therefore developed electronics that synchronise the TTL signal from the lab computer to the rf phase. The dependence of the hit rate on the extraction trigger phase is shown in Figure 10(a) where the detection probability has a maximum at a rf phase of around  $250^\circ$  to  $270^\circ$ . During all these measurements, the deflection voltages were kept constant and no additional apertures were placed in front of the detector (entrance aperture of the detector equals 20 mm). With smaller apertures, the contrast between detecting 90% of the extracted ions and missing the detector would be even stronger. Additionally, the experiment shows a weak dependence on the pressure in the vacuum chamber (see Figure 10(b)). When improving the vacuum down to a few  $10^{-9}$  mbar, the detection rate again improves to almost 90% as well. A linear extrapolation leads to a maximum detection probability of 92.5%. The dependency on the pressure is mainly based on possible collisions with the background residual gas particles. Furthermore, the stability of the ions in the trapping potential is lessened with higher pressure, which leads to higher fluctuations of the extraction trajectories. However, our measured hit rate lies above the specified quantum efficiency of 80% of the detector.

#### 4.1. Determination of the velocity fluctuation

In order to get information concerning the velocity fluctuation of the extracted ions we have measured the time of flight of each detected ion or ion crystal. The time of flight spectrum for ion crystals consisting of two ions is depicted in Figure 11(a). The difference between the arrival times of the first and the second ion results in  $\overline{\Delta t} = 26.3$  ns, which is mainly based on the Coulomb interaction. The spectrum shows that the ions remain in their crystalline structure during the extraction, which is important for the above-mentioned post-separation of the  $^{40}\text{Ca}^+$  ions from possible dopant ions or the implantation of a whole crystal with one extraction event. In order to characterise the spatial divergence of the ion beam, a movable aperture plate was installed in front of the detector. Along with this modification, a faster and more stable trigger phase electronic unit was also implemented. The subsequent measurements of the time of flight spectra are shown in Figure 11(b). With the improvement of the phase delay trigger the  $1\sigma$ -width reduces from the previous 50 ns down to 9.5 ns. The movement of the detector of about 30 mm further away from the trap causes an elongation of the time of flight from around  $12.7 \mu\text{s}$  up to  $14.74 \mu\text{s}$ . Therefore, the mean velocity of the extracted single  $^{40}\text{Ca}^+$  ions is measured to be  $19.47 \text{ km s}^{-1}$  with a  $1\sigma$ -width of  $6.3 (6) \text{ m s}^{-1}$ , meaning that the velocity uncertainty is a factor of 10 larger than inside the trap for the 2 mK cooled ions. The relative velocity uncertainty  $\Delta v/v$  is only  $3.2 \times 10^{-4}$  with the possibility of further reduction due to post-acceleration.

#### 4.2. Determination of the spatial beam dimension

The beam divergence is determined by scanning the beam over different apertures of 5 mm, 1 mm and

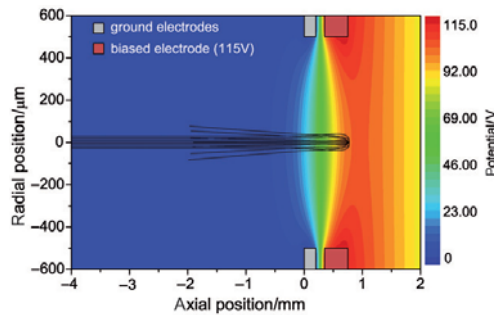


Figure 9. Trajectories of reflected  $^{40}\text{Ca}^+$  ions and potential distribution of the lens set to 115 V at the centre electrode (red). (The colour version of this figure is included in the online version of the journal.)

2072

R. Fickler et al.

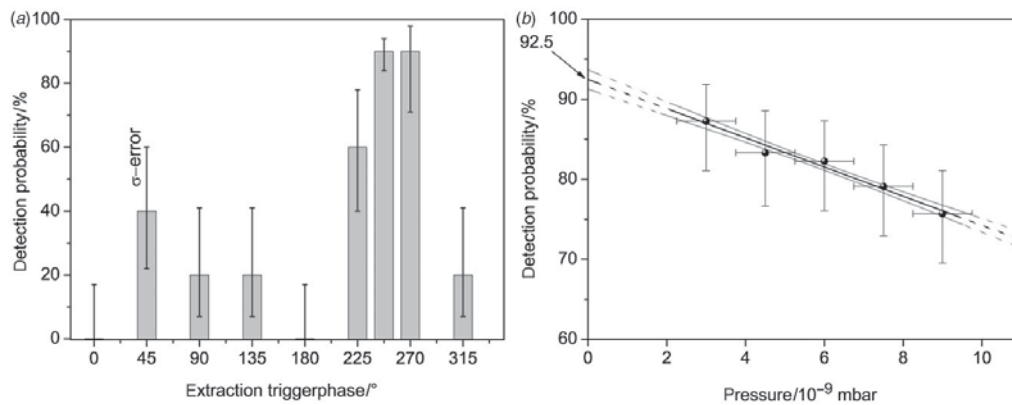


Figure 10. (a) Dependence of detection probability on different extraction trigger phases. (b) Detection probability during the extraction of single ions while the pressure changes. A linear fit is added (black line) as well as the standard deviation (grey line). The measurement is based on 251 successful extractions out of 310 shots. Both diagrams are measured without any aperture in front of the detector.

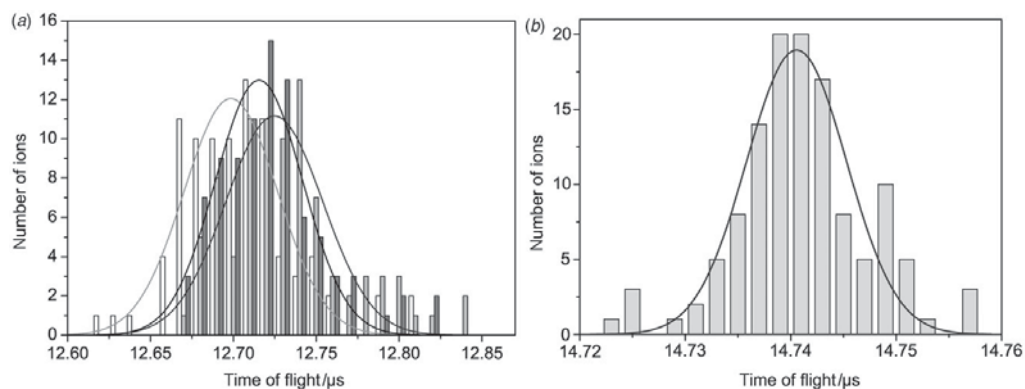


Figure 11. (a) Time of flight spectrum for two-ion crystals based on 93 successful detections without any aperture plates in front of the detector. The mean value for the first detected ion (white bins) amounts to  $12.699 \mu\text{s}$  with a  $1\sigma$ -spread of 56 ns (light grey line) and for the second ion (grey bins) to  $12.725 \mu\text{s}$  with a  $1\sigma$ -spread of 59 ns, respectively (grey line). The difference in arrival time between the first and the second ion amounts to  $\Delta t = 26$  ns. Additionally, the mean value (dark grey bins) for the time of flight for both detection events adds up to  $12.715 \mu\text{s}$  with a  $1\sigma$ -spread of 52 ns (dark grey line). The bin size of the histogram is 10 ns. (b) Time of flight spectrum for single ion crystals based on 123 successful detections out of 139 shots through the 1 mm aperture. Gaussian fit of the data leads to an average time of  $14.74 \mu\text{s}$  with a  $1\sigma$ -spread of 9.5 ns. The bin size of the histogram equals 2 ns. Note that the different average times in (a) and (b) are caused by a repositioning of the detector backwards due to the installation of an aperture plate, and that the improvement of the  $1\sigma$ -spread is mainly due to the enhancement of the electronics of the phase delay trigger.

$300 \mu\text{m}$  diameter by altering the deflection voltages. Measurements conducted with the 5 mm aperture have shown that over a voltage range of 5 V between two opposing blades and 10 V between the other two opposing blades we are even able to detect ion crystals of up to 6 ions with an efficiency above 90%

(see Figure 12(a)). The edge of the aperture is also clearly recognisable in the scan diagram due to a sharp decrease of the detection rate. When reducing the aperture diameter to 1 mm the scanning range of the deflection voltages are scaled down to 1 and 2 V, respectively (see Figure 12(b)). In the centre of the

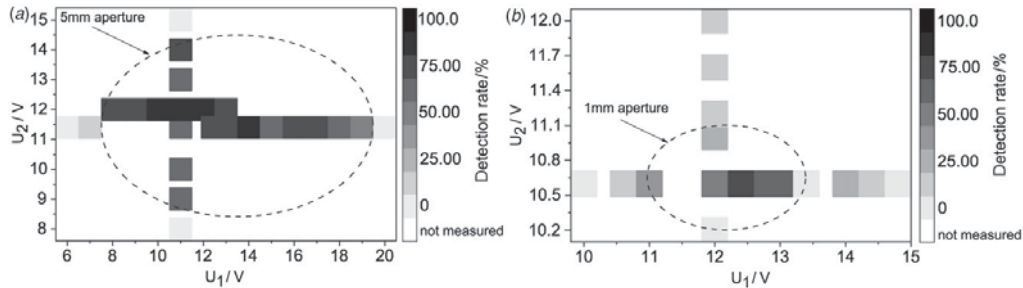


Figure 12. Detection probabilities as a function of the deflection voltages.  $U_1$  and  $U_2$  indicate the potential applied between two opposing blades. The scan clearly shows the edge of the aperture by a sharp decrease of the detection rate. (a) The range can be varied over 10 V and 5 V for the 5 mm aperture. (b) For the 1 mm hole the range where ions can be efficiently detected decreases to 2 and 1 V, respectively.

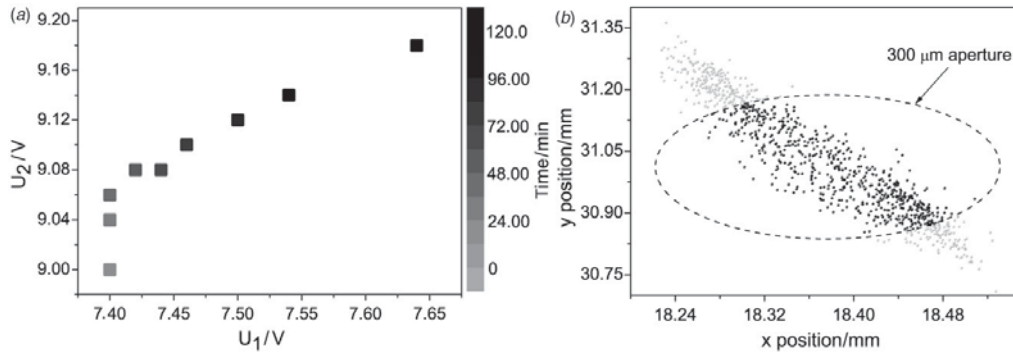


Figure 13. (a) Experimentally measured variation of optimal voltages  $U_1$  and  $U_2$  for the two pairs of opposing blades during measurements of two hours duration. The change in voltages compensates for the drift of the ion beam. Therefore, the detection probability could be kept constant at 68%. (b) Simulation of the spot with experimental settings. Black spots illustrate ions that would have passed the 300  $\mu\text{m}$  aperture whereas grey spots are blocked by the aperture. Therefore, 65% of the extracted ions can be detected after the aperture which is in good agreement with our experimental result (68%). Note that the spot is not a Gaussian distribution and is displaced by a few millimetres due to deflection voltages  $U_1 = 7.5$  V and  $U_2 = 9.1$  V.

scanned voltage range we detect 87% of the single extracted ions while the detection of ions which are extracted in a crystal shows a reduced detection rate of 78%. Note that the detection rate of nearly 90% for single ions lies above the specified quantum efficiency of the detector and is mainly limited by its performance. However, further downsizing of the dimension of the aperture to 300  $\mu\text{m}$  reduces the detection rate to 68% which indicates the cut-off of the spot by the edge of the aperture. By scanning over the 5 mm aperture at two different times we observed a drift of the ion beam of  $15 \mu\text{m min}^{-1}$ , possibly caused by temperature drifts or a displacement of the ions due to patch electric fields on the insulating surface between the electrodes. When using the 300  $\mu\text{m}$  aperture, the drift becomes more significant, which we compensated by adjusting the deflection voltages (see Figure 13).

#### 4.3. Comparison of the experiment and the simulation

For a comparison of the experimental results with the findings from the simulations it is useful to obtain the simulated spot shape with all experimentally used settings. The resulting simulated spot again shows an oval shape. The velocities have a Gaussian distribution (similar to the experiment) with a  $1\sigma$ -spread of  $2.7 \text{ m s}^{-1}$ . The experimentally measured values are by a factor of 2.2 larger than the simulated results. If it is assumed that the same holds true for the spatial spreading of the spot, it is possible to compare the results of the experiment and the simulation. With the cigar-shaped spot that is enlarged by a factor of 2.2, about 65% of the extracted ions would pass through the 300  $\mu\text{m}$  aperture (see Figure 13(b)). In our experiment we are able to detect 68% of the single ions

2074

R. Fickler et al.

behind the 300  $\mu\text{m}$  hole, with adjustment of the deflection voltages during the extractions. From the simulation, we can also deduce that our trap is tilted by an angle of  $4.2^\circ$  at the  $x$ -axis and  $7.2^\circ$  for the  $y$ -axis.

### 5. Outlook

We have shown that our setup is able to deterministically extract single ions on demand. With additional optimised ion optics, the numerical simulation predicts a spot size with nm dimension. For an experimental confirmation of the predicted focal spot, different methods are conceivable. Similar to the previous measurements of the spatial beam divergence, it is possible to implement an aperture with less than 30 nm, which can be drilled, for example, by a focused ion beam (FIB) [16,17]. Another possibility to confirm the expected nm resolution of our combined system of ion trap and ion optics is to measure the achieved resolution after implanting the ions into solid state surfaces. With a STM, it is possible to identify subsurface impurities with nm resolution, produced by cobalt particles in a copper bulk material, for example [38]. A further method to confirm the resolution of single implanted ions makes use of generated NV colour centres in diamond [5]. Dipolar coupling of single nuclei localised close to the defect can be used to measure the achieved implantation resolution.

### Acknowledgements

We acknowledge financial support by the Landesstiftung Baden-Württemberg in the framework 'atomics' (Contract No. PN 63.14) and the 'Eliteprogramm Postdoktorandinnen und Postdoktoranden', the European commission within EMALI (Contract No. MRTN-CT-2006-035369) and the VolkswagenStiftung.

### Note

- Note that the  $1\sigma$ -expression is always used to express that 68% of the studied data lies within the given interval, although some results are not perfectly reproduced by a Gaussian distribution.

### References

- [1] Shinada, T.; Okamoto, S.; Kobayashi, T.; Ohdomari, I. *Nature* **2005**, *437*, 1128–1131.
- [2] Kane, B.E. *Nature* **1998**, *393*, 133–137.
- [3] Greentree, A.D.; Fairchild, B.A.; Hossain, F.M.; Praver, S. *Materials Today* **2008**, *11*, 22–31.
- [4] Gurudev Dutt, M.V.; Childress, L.; Jiang, L.; Togan, E.; Maze, J.; Jelezko, F.; Zibrov, A.S.; Hemmer, P.R.; Lukin, M.D. *Science* **2007**, *316*, 1312–1316.
- [5] Neumann, P.; Mizuochi, N.; Rempp, F.; Hemmer, P.; Watanabe, H.; Yamasaki, S.; Jacques, V.; Gaebel, T.; Jelezko, F.; Wrachtrup, J. *Science* **2008**, *320*, 1326–1329.
- [6] O'Brien, J.L.; Schofield, S.R.; Simmons, M.Y.; Clark, R.G.; Dzurak, A.S.; Curson, N.J.; Kane, B.E.; McAlpine, N.S.; Hawley, M.E.; Brown, G.W. *Phys. Rev. B* **2001**, *64*, 161401(R).
- [7] Schofield, S.R.; Curson, N.J.; Simmons, M.Y.; Ruess, F.J.; Hallam, T.; Oberbeck, L.; Clark, R.G. *Phys. Rev. Lett.* **2003**, *91*, 136104.
- [8] Ruess, F.J.; Oberbeck, L.; Simmons, M.Y.; Goh, K.E.J.; Hamilton, A.R.; Hallam, T.; Schofield, S.R.; Curson, N.J.; Clark, R.G. *Nano Lett.* **2004**, *4*, 1969–1973.
- [9] Pok, W.; Reusch, T.C.G.; Scappucci, G.; Rueb, F.J.; Hamilton, A.R.; Simmons, M.Y. *IEEE Trans. Nanotech.* **2007**, *6*, 213.
- [10] Ruess, F.J.; Pok, W.; Reusch, T.C.G.; Butcher, M.J.; Goh, K.E.J.; Oberbeck, L.; Scappucci, G.; Hamilton, A.R.; Simmons, M.Y. *Small* **2007**, *3*, 563–567.
- [11] Shinada, T.; Koyama, H.; Hinosihta, C.; Imamura, K.; Ohdomari, I. *Jpn. J. Appl. Phys.* **2002**, *41*, L287–L290.
- [12] Persaud, A.; Park, S.J.; Liddle, J.A.; Rangelow, I.W.; Bokor, J.; Keller, R.; Allen, F.I.; Schneider, D.H.; Schenkel, T. *QIP* **2004**, *3*, 233–245.
- [13] Mitic, M.; Andresen, S.E.; Yang, C.; Hopf, T.; Chan, V.; Gauja, E.; Hudson, F.E.; Buehler, T.M.; Brenner, R.; Ferguson, A.J.; Pakes, C.I.; Hearne, S.M.; Tamanyan, G.; Reilly, D.J.; Hamilton, A.R.; Jamieson, D.N.; Dzurak, A.S.; Clark, R.G. *Microelectron. Eng.* **2005**, *78*, 279–286.
- [14] Batra, A.; Weis, C.D.; Reijonen, J.; Persaud, A.; Schenkel, T.; Cabrini, S.; Lo, C.C.; Bokor, J. *Appl. Phys. Lett.* **2007**, *91*, 193502.
- [15] Shinada, T.; Kurosawa, T.; Nakayama, H.; Zhu, Y.; Hori, M.; Ohdomari, I. *Nanotechnology* **2008**, *19*, 345202.
- [16] Meijer, J.; Vogel, T.; Burchard, B.; Rangelow, I.W.; Bischoff, L.; Wrachtrup, J.; Domhan, M.; Jelezko, F.; Schnitzler, W.; Schulz, S.A.; Singer, K.; Schmidt-Kaler, F. *Appl. Phys. A* **2006**, *83*, 321–327.
- [17] Meijer, J.; Pezzagna, S.; Vogel, T.; Burchard, B.; Bukow, H.H.; Rangelow, I.W.; Sarov, Y.; Wiggers, H.; Plümel, I.; Jelezko, F.; Wrachtrup, J.; Schmidt-Kaler, F.; Schnitzler, W.; Singer, K. *Appl. Phys. A* **2008**, *91*, 567–571.
- [18] Schnitzler, W.; Linke, N.M.; Fickler, R.; Meijer, J.; Schmidt-Kaler, F.; Singer, K. *Phys. Rev. Lett.* **2009**, *102*, 070501.
- [19] Rowe, M.A.; Ben-Kish, A.; DeMarco, B.; Leibfried, D.; Meyer, V.; Beall, J.; Britton, J.; Hughes, J.; Itano, W.M.; Jelenkovic, B.; Langer, C.; Rosenband, T.; Wineland, D.J. *Quant. Inf. Comp.* **2002**, *2*, 257–271.
- [20] Roos, C.F.; Leibfried, D.; Mundt, A.; Schmidt-Kaler, F.; Eschner, J.; Blatt, R. *Phys. Rev. Lett.* **2000**, *85*, 5547–5550.
- [21] King, B.E.; Wood, C.S.; Myatt, C.J.; Turchette, Q.A.; Leibfried, D.; Itano, W.M.; Monroe, C.; Wineland, D.J. *Phys. Rev. Lett.* **1998**, *81*, 1525–1528.
- [22] Nägerl, H.; Blatt, R.; Eschner, J.; Schmidt-Kaler, F.; Leibfried, D. *Opt. Express* **1998**, *3*, 89–96.

- [23] Drewsen, M.; Mortensen, A.; Martinussen, R.; Staunum, P.; Sørensen, J.L. *Phys. Rev. Lett.* **2004**, *93*, 243201.
- [24] Huber, G.; Deuschle, T.; Schnitzler, W.; Reichle, R.; Singer, K.; Schmidt-Kaler, F. *New J. Phys.* **2008**, *10*, 013004.
- [25] Schmidt-Kaler, F.; Eschner, J.; Morigi, G.; Roos, C.F.; Leibfried, D.; Mundt, A.; Blatt, R. *Appl. Phys. B* **2001**, *73*, 807–814.
- [26] Greengard, L. *The Rapid Evaluation of Potential Fields in Particle Systems*; MIT Press: Cambridge, MA, 1988.
- [27] Nabors, K.; Kormeyer, F.T.; Leighton, F.T.; White, J. *SIAM J. Sci. Stat. Comp.* **1994**, *15*, 713–735.
- [28] Weißbäcker, Ch.; Rose, H. *Jpn. Soc. Elec. Microscopy* **2001**, *50*, 383.
- [29] Weißbäcker, Ch.; Rose, H. *Jpn. Soc. Elec. Microscopy* **2002**, *51*, 45.
- [30] Szep, J.; Szilagy, M. *IEEE* **1988**, *35*, 1181–1183.
- [31] Hawkes, P.W.; Kasper, E. *Principles Of Electron Optics*; Academic Press: London, 1989.
- [32] Liebl, H. *Applied Charged Particle Optics*; Springer: Berlin, 2008.
- [33] Shimizu, K. *Jpn. J. Appl. Phys.* **1983**, *22*, 1623–1626.
- [34] Schönhense, G.; Spiecker, H. *J. Vac. Sci. Technol. B* **2002**, *20*, 2526–2534.
- [35] Riddle, G.H.N. *J. Vac. Sci. Technol.* **1978**, *15*, 857–860.
- [36] Septier, A. Septier CERN report: Aberation spherique de quelques lentilles electrostatiques a symetrie de revolution pour des faisceaux de grande ouverture; CERN Report, No. 60-39, Geneva, 1960.
- [37] Scherzer, O. *Z. Phys.* **1936**, *101*, 593–603.
- [38] Weismann, A.; Wenderoth, M.; Lounis, S.; Zahn, P.; Quaas, N.; Ulbrich, R.G.; Dederichs, P.H.; Blügel, S. *Science* **2009**, *323*, 1190–1193.

## B.3 Applied Physics A - Materials Science & Processing

### **Towards the implanting of ions and nanoparticles with nm spatial resolution**

---

J. Meijer, S. Pezzagna, T. Vogel, B. Burchard, H. H. Bukow, I. W. Rangelow, Y. Sarov,  
H. Wiggers, I. Plümel, F. Jelezko, J. Wrachtrup, F. Schmidt-Kaler, W. Schnitzler and  
K. Singer

Published on 1st May 2008 in the scientific journal:

**Applied Physics A**

(Volume: 91 / Page: 567 / Year: 2008)

J. MEIJER<sup>1,✉</sup>  
 S. PEZZAGNA<sup>1</sup>  
 T. VOGEL<sup>1</sup>  
 B. BURCHARD<sup>1</sup>  
 H.H. BUKOW<sup>1</sup>  
 I.W. RANGELOW<sup>2</sup>  
 Y. SAROV<sup>2</sup>  
 H. WIGGERS<sup>3</sup>  
 I. PLÜMEL<sup>3</sup>  
 F. JELEZKO<sup>4</sup>  
 J. WRACHTRUP<sup>4</sup>  
 F. SCHMIDT-KALER<sup>5</sup>  
 W. SCHNITZLER<sup>5</sup>  
 K. SINGER<sup>5</sup>

## Towards the implanting of ions and positioning of nanoparticles with nm spatial resolution

<sup>1</sup> RUBION, Ruhr-Universität Bochum, 44780 Bochum, Germany

<sup>2</sup> Department of Micro- and Nanoelectrical Systems, Institute of Micro- and Nanoelectronics, Technical University of Ilmenau, PF 10 05 65, 98684 Ilmenau, Germany

<sup>3</sup> Institut für Verbrennung und Gasdynamik, Universität Duisburg-Essen, 47057 Duisburg, Germany

<sup>4</sup> 3. Physikalisches Institut, University Stuttgart, Pfaffenwaldring 57, 70550 Stuttgart, Germany

<sup>5</sup> Institut für Quanteninformationsverarbeitung, University Ulm, Albert-Einstein-Allee, 89069 Ulm, Germany

Received: 22 February 2008 / Accepted: 18 March 2008  
 Published online: 1 May 2008 • © Springer-Verlag 2008

**ABSTRACT** Decreasing structure sizes in both conventional and quantum solid state devices require novel fabrication methods: we present a technology which allows to implant ions through a small hole in the tip of an atomic force microscope. This technique offers a maskless addressing of small structures using different projectiles at kinetic energies between 0.5 and 5.0 keV. Our method aims to implant single atomic ions, molecular ions or charged nanoparticles with nm resolution. We test the method by implanting N<sup>+</sup> ions into diamond and generating nitrogen-vacancy color centers. The system is operated with a conventional ion gun. However, in future we will employ an ion trap as a deterministic source of cold single ions.

PACS 03.67.-a; 29.25.Ni; 61.72.Ji; 81.16.Rf; 85.40.Ry

### 1 Introduction

Currently, structure sizes in modern nano-electronics reach a few tens of nm and we will certainly see a further miniaturization in the near future. Examples of conventional devices are nanotransistors where structure sizes of less than 30 nm are state of the art. Quantum solid state devices aiming for a future quantum computer also require novel fabrication methods. Examples of these quantum devices such as quantum dots, magnetic impurities, single embedded impurity ions or color centers in solid-state matrices are employed to store and process quantum information. So far, only rudimentary and non-scalable few-qubit processors based on phosphorus dopants have been investigated [1, 2]. Recently, qubit operation at room temperature has been demonstrated using nitrogen-vacancy (NV) centers in diamond crystals [3, 4], which are generated by nitrogen implantation.

The development of such structures is impeded by the lack of suitable nano-implantation methods. Required is a very high spatial resolution with low beam energy to avoid ion straggling in the substrate. Major challenges are the focusing and the precise alignment of the ion beam into the substrate. A mask technology might be a solution but the application below 5 nm is challenging. Only few groups worldwide are able to meet the technical requirements. A maskless technique such as focused ion beams (FIBs) has the advantage to be very flexible and to allow a quick modification of doping structures. FIBs with a spatial resolution of 3 nm are state of the art and commercially available. The advantage of the FIB as a maskless implanter is based on a liquid metal ion source (LMIS) with high brightness. Different LMISs have been developed and a variety of ions were successfully tested. However, the disadvantage of the LMIS is a large energy spread and the requirement of mass separation. Additionally, the energy spread leads to a chromatic aberration at low beam energies, which in turn spoils a narrow focusing with ion optical elements.

We introduce a new setup based on the combination of an atomic force microscope (AFM) with a collimator and a low-energy ion gun as a method to implant ions with high spatial resolution [5]. The advantage of an AFM collimator is that the implantation becomes independent of the ion-beam focus. The AFM tip easily allows an exact placement of the tip or collimator with an accuracy of better than 1 nm. This combination enables the separation of the ion beam positioning and addressing systems. Additionally, the method is easy to handle and allows using topological markers. Please note that it might be important to implant doping ions precisely with respect to e.g. an electrical control gate [6]. The ion gun can be equipped with a standard source thus allowing the production of a wide range of ion species, especially nitrogen or oxygen. The advantage of the present setup is that it can be combined with different types of sources. The paper gives some experimental details of the method, shows results with maskless

✉ Fax: +40-234-32-14215, E-mail: jan.meijer@rub.de

implanted  $N^+$  ions in diamond and discusses the limits of this method. We sketch future improvements and extensions of the method.

## 2 Experimental setup

The use of a pierced AFM tip as a collimator for ion-beam implantation has been developed in a cooperation between Berkeley, Bochum and Ilmenau [7]. The method is based on a beam of low-energy ions or particles focused on the cantilever tip of an AFM system (Fig. 1). In the Bochum system an ion source (SPECS, model IQE12/38) can deliver different kinds of ions in an energy range between 0.5 and 5 keV. The source is equipped with a mass separator and an electrostatic lens to focus the ion beam. The beam is guided through a pierced mirror at  $45^\circ$  on which an optical microscope is pointed to achieve an in situ optical inspection. The microscope uses a long working distance objective and is connected to a high resolution and high sensitivity CCD camera outside the vacuum chamber. The resolution of the microscope is about  $1 \mu\text{m}$  and the image covers about  $700 \mu\text{m} \times 700 \mu\text{m}$ . Focalization is obtained by moving the objective in a high-precision guide inside the vacuum chamber. The microscope allows an easy and precise alignment between the AFM tip and the beam. To reduce the beam spot size, we use an aperture-lens system close to the AFM cantilever. The ion lens demagnifies the image of an aperture with a diameter between 1 and  $20 \mu\text{m}$  to the surface of the AFM tip. The AFM system (Alpha contact) is based on a piezoresistive cantilever with a hollow tip. On the apex of the tip a hole of some nm diameter is drilled<sup>1</sup> in order to act as a collimator. It is of great importance to drill the hole close to the apex and not into the cantilever in order to minimize the vertical distance between hole and target. A vertical distance of only  $5 \mu\text{m}$  will broaden the beam by a factor of 5 or more depending on the divergence of the beam and scattering effects. Especially for small holes, scattering becomes quite dominant. The AFM enables the alignment of the hole within some nm. The AFM stage itself is positioned using a three-axis PI table (Physik Instrumente (PI) GmbH) with a resolution of 200 nm. Polymethylmethacrylate (PMMA) on silicon is used for the alignment procedure. Due to the incident beam the irradiated PMMA changes its color and the AFM stage can thus be moved to the indicated position. The piezoresistive positioning sensor system [8] allows a very compact AFM system with a resolution of about 1 nm. A single ion detector with a detection efficiency of more than 90% is used to measure the ion current through the AFM tip. The detector is covered by a  $1\text{-}\mu\text{m}$  aperture in front of it to ensure that only ions having crossed the tip will be measured. The system is mounted in the piezo-driven table and allows routinely inspecting the hole in the AFM tip. The substrate is placed on a piezotranslation stage with a resolution of 0.1 nm and a moving range of  $150 \mu\text{m}$  in horizontal and  $20 \mu\text{m}$  in vertical directions. To extend the moving range, the setup is mounted on a second step motor driven translation stage with a resolution of  $1 \mu\text{m}$  and a moving range of 11 cm in the horizontal

<sup>1</sup> Drilling has been performed by the FIB installation of Institut für Angewandte Festkörperphysik, Ruhr-Universität Bochum (Prof. A. Wieck). We want to thank Dr. Melnikow for his assistance.

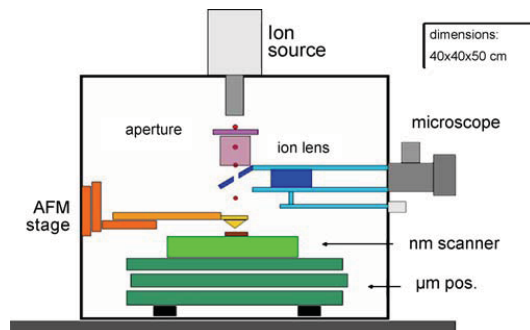


**FIGURE 1** From top to bottom: the ion gun providing different kinds of ions, a micro ion lens with apertures, an optical microscope with a pierced mirror and a table with sub-nm resolution. The pierced AFM tip can be moved precisely in all directions using micromotors. The target is based on a PI piezo table with 0.1-nm resolution and a stepping motor driven table for  $\mu\text{m}$  alignment

direction. Figure 2 gives a view of the setup inside the vacuum chamber.

### 2.1 AFM-tip-based nanocollimator

AFM devices based on Wheatstone-bridge piezoresistive cantilevers allow for many applications. The integration of the piezoresistive readout provides the best solution to realize a very compact high-resolution AFM, attractive as compared to the conventional optical beam deflection technique especially in those cases where laser detection may not fit the overall system. Piezoresistive cantilevers are irreplaceable in such areas as high vacuum, AFM arrays of cantilevers and high-frequency small cantilevers and in applications such as microbalances, infrared radiation detection or cryogenic conditions. The extreme sensitivity and short response times of micromechanical cantilevers used for nanoscale AFMs have been extended beyond those of a surface-imaging tool. In previous publications [9, 10], we have demonstrated that the minimum detectable deflection for piezoresistive cantilevers can be as low as 0.01 nm for a 1-kHz bandwidth, confirming that this detection scheme is adequate for AFM operation. Piezoresistive cantilevers with integrated and glued hollow tips were microfabricated using standard CMOS processing and double-sided micromachining techniques. The glued hollow tips are based on SiN and are produced by standard moulding techniques. The thickness of the hollow tips is about 150 nm. The hollow AFM tips with a drilled hole are fabricated by FIB milling with Ga ions at 30 keV. Figure 3 shows a drilled hollow tip glued onto a cantilever. A Faraday cup behind the AFM tip is used to turn off the beam just at the moment when the transmission current indicates that a hole was drilled. The entrance of a typical hole is about 140 nm, the exit in the range of 30 nm or below [5]. The AFM operation with resistive cantilevers allows imaging the surface in contact mode with a resolution in  $z$  better than 1 nm. A similar result is achieved for a tip pierced at the apex.

We studied the lifetime of the AFM tips with drilled holes and realized that the holes tend to become closed with increas-

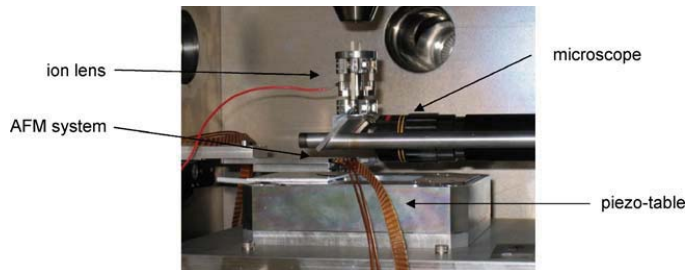


**FIGURE 2** A view inside the nano-addressing chamber

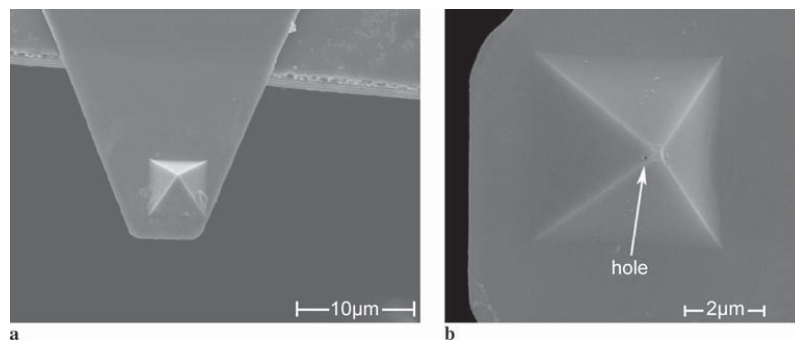


**FIGURE 3** (a) Glued hollow AFM tip with piezoresistive cantilevers. (b) Hole drilled into AFM tip using a focused ion beam (FIB)

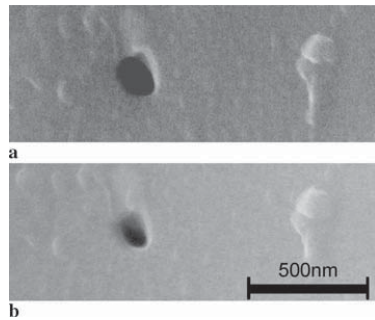


**FIGURE 4** (a) Hole in the AFM tip, before ion-implantation procedure; (b) after ion-implantation procedure of Ar and N with a dose of  $4 \times 10^{16}$  ions/cm<sup>2</sup>

ing ion exposure (see Fig. 4). Under typical working conditions the drilled tip can be used for several hours. Whether this effect depends on the cone of the FIB drilled hole (i.e. from which side the hole is drilled into the tip) is currently being investigated. First results also show a strong dependence of this effect on the impact angle of the ion beam. The hole-size reduction under ion-beam exposure could be exploited for manufacturing holes smaller than the limit of state of the art FIB milling devices.

### 3 Application: production of NV centers

Our goal is the production of quantum devices by implantation of single nitrogen ions. The long coherence time of nitrogen-vacancy (NV) centers of  $\sim 0.6$  ms for the electron

spin even at room temperature allows studying quantum effects [11, 12]. We showed the fabrication of single NV centers using implantation of  $N^+$  [3]. A mutual dipole-dipole coupling of nearby NV centers has also been shown [4]. Color centers find applications as single-photon sources [13, 14] (and for cavity quantum electrodynamic experiments with micro-optical resonators [15]) or as ultra-sensitive magnetometers.

Conditions to build devices of this sort are challenging: implanting within a lateral accuracy of a few nm may be possible when the diameter of the hole inside the AFM tip is reduced to this size. It remains to be shown that the hole does not become clogged, and that proximity effects do not spoil the spatial resolution. The second question is the yield of implanted  $N^+$  ions into NV centers, which should be as high as possible. Experiments with ion implantation at high energy (2 MeV) showed a yield of 20 to 100%, which is reduced for low-energy implantation to below 2.5% [16]. Figure 5a shows a picture of the fluorescence from a single NV center fabricated by  $^{15}N^+$  implantation at high energy using a microprobe system [17] and low kinetic energy using our nano-addressing tool through an AFM tip (Fig. 5b). The implantation is performed with  $^{15}N^+$  to distinguish the implanted ions from natural  $^{14}N$ -isotope content of diamond samples. The depth of the vacancy production plays an important role in the NV center production process, when the sample is annealed at a temperature of 800 K. We speculate that  $N^+$  ions near the surface may not easily combine with a vacancy as they are trapped at the surface during annealing. Thus, they are no longer available to produce NV centers.

However, work on novel techniques to enlarge the efficiency by co-implantation and electron and photon irradiation is under way. Also, the use of other color centers or nickel-

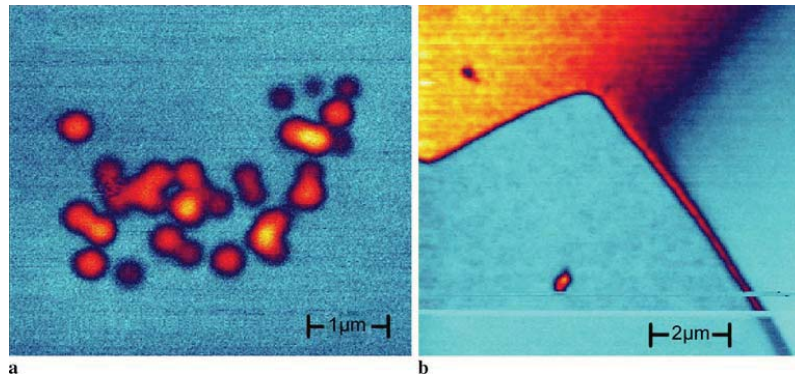


**FIGURE 5** (a) A group of NV centers produced by MeV implantation using a nanoprobe implantation system. (b) A NV center produced by the nano-addressing system with an ion gun having an ion kinetic energy of 2 keV

nitrogen complexes [18] seems to be a possible way since they do not need an additional vacancy.

#### 4 Future developments: deterministic ion implantation and nanoparticle addressing

Typically, solid-state devices are doped in order to tailor their electrical properties. Once the devices reach dimensions such that the Poissonian number fluctuations of dopants become too high, their operation will be largely affected. For example, with a typical doping concentration of  $10^{15}/\text{cm}^3$ , the gate region of a nano-FET contains only 30 doping atoms such that the relative number fluctuation reaches 20%. For quantum devices, e.g. single embedded ions carrying a nuclear spin to encode quantum bits, it is essential to reach the absolute control of the number of dopants.

One may detect the event of the single-ion impact: the detection of secondary electrons works in an efficient way only for energies above 30 keV. At low energies, highly charged ions can be used as the impact generates an electron shower [19], but these ions may cause severe damage to the surface [20]. In some cases, it is possible to measure electron-hole pairs from a single ion impact in semiconductors, if prepared as a Si-diode structure [21]. However, the method is restricted to dedicated structures and materials. Our method for a single-ion source observes the dopant ion prior to the implantation by laser light fluorescence in a Paul trap. A single ion can be identified and manipulated such that its temperature is reduced to a fraction of a mK, corresponding to  $10^{-7}$  eV. In turn, chromatic aberration is expected to be largely reduced [3]. The method is universal, and should work for almost all types of atomic ions.

The advantage of the presented system is that almost all types of sources can be used. Beside ions, nanoparticles as well as molecules can be collimated.

Especially, a singly charged nanoparticle could be produced inside a plasma reactor combined with a velocity measurement and size-selecting system [22]. This source is now available and its combination with highly resolved deposition is in preparation. The aim of the project 'Cluster jet' is the development of a technique that allows for the addressing of countable nanoparticles with a spatial resolution of 10 nm or less to a pre-structured surface.

The nanoparticle beam will be transferred to the AFM chamber using a tube and ion lenses. This horizontal beam will be connected to the focusing unit using a  $90^\circ$  bending system. The bending system will be installed between the ion source and the ion optical elements (scanning units, lenses, quadruplet systems, etc.). We expect that the pre-alignment procedure of the optical components will simplify the adjustment of the nanoparticle beam. For a particle beam a degeneration of the tip hole due to sputtering effects is not expected. Nevertheless, the holes may also become clogged by the nanoparticles themselves. If this happens, an additional  $\mu$ -lens will be necessary. However, a ray-tracing calculation shows that a focusing of nanoparticles below 50 nm is possible at the given conditions.

#### 5 Summary

We presented a new technique that allows maskless implantation of single ions at low kinetic energy with nm resolution. The method is based on a pierced AFM tip that acts as a collimator system in the nm range. The spatial resolution is given by the size of the hole. Holes with 30-nm diameter can be fabricated routinely. As a result of our first experiments, the size of the holes became smaller during the irradiation with 2- to 5-keV ions. This effect may be useful to deliberately reduce the diameter. The system allows the implantation of ions with a kinetic energy of 500 eV produced by a conventional ion source. The combination of an AFM table and a positioning table using stepper motors enables an easy handling for different applications and an addressing within 1-nm distance to the target. One application is the implantation of  $\text{N}^+$  ions to produce NV centers in diamond. Experiments showed that the efficiency of NV production needs to be optimized. To implant a pre-determined number of ions, the method is currently improved by using an ion trap as cold source. In addition, the system can be equipped with a nanoparticle source for implanting nanoparticles with high spatial resolution.

**ACKNOWLEDGEMENTS** We acknowledge financial support in Bochum, Ilmenau and Duisburg by the Volkswagen Foundation. FJ and JW have been supported by the SFB/TR-21 of the DFG. WS, KS, FSK, FJ and JW acknowledge financial support by the Landestiftung Baden-Württemberg within the program 'Atomics'.

## REFERENCES

- 1 A.R. Stegner, C. Boehme, H. Huebl, M. Stutzmann, K. Lips, M.S. Brandt, *Nature Phys.* **2**, 835 (2006)
- 2 S.R. Schofield, N.J. Curson, M.Y. Simmons, F.J. Rue, T. Hallam, L. Oberbeck, R.G. Clark, *Phys. Rev. Lett.* **91**, 136 104 (2003)
- 3 J. Meijer, B. Burchard, M. Domhan, C. Wittmann, T. Gaebel, I. Popa, F. Jelezko, J. Wrachtrup, *Appl. Phys. Lett.* **87**, 261 909 (2005)
- 4 T. Gaebel, M. Domhan, I. Popa, C. Wittmann, P. Neumann, F. Jelezko, J.R. Rabeau, N. Stavrias, A.D. Greentree, S. Prawer, J. Meijer, J. Twamley, P.R. Hemmer, J. Wrachtrup, *Nature Phys.* **2**, 408 (2006)
- 5 J. Meijer, T. Vogel, B. Burchard, I.V. Rangelow, L. Bischoff, J. Wrachtrup, M. Domhan, F. Jelezko, W. Schnitzler, S.A. Schulz, K. Singer, F. Schmidt-Kaler, *Appl. Phys.* **83**, 321 (2006)
- 6 P. Tamarat, T. Gaebel, J.R. Rabeau, M. Khan, A.D. Greentree, H. Wilson, L.C.L. Hollenberg, S. Prawer, P.R. Hemmer, F. Jelezko, J. Wrachtrup, *Phys. Rev. Lett.* **97**, 083 002 (2006)
- 7 U.S. and German Patents DE 10,347,969: *Device and Method of Positional Accurate Implantation of Individual Particles in a Substrate Surface*, inventors: J. Meijer, I.W. Rangelow, T. Schenkel, assignees: U.C. Berkeley, Universität Gh Kassel, German and U.S. Patents submitted Oct. 2003, assignation 2006
- 8 A. Persaud, K. Ivanova, Y. Sarov, T. Ivanov, B.E. Volland, I.W. Rangelow, N. Nikolov, T. Schenkel, V. Djakov, D.W.K. Jenkins, T. Vogel, J. Meijer, *J. Vac. Sci. Technol. B* **24**(6) (2006)
- 9 I.W. Rangelow, P. Grabiec, T. Gotszalk, K. Edingeret, *Surf. Interface Anal.* **33**, 59 (2002)
- 10 I.W. Rangelow, *Microelectron. Eng.* **83**, 1449 (2006)
- 11 F. Jelezko, T. Gaebel, I. Popa, A. Gruber, J. Wrachtrup, *Phys. Rev. Lett.* **92**, 076 401 (2004)
- 12 F. Jelezko, T. Gaebel, I. Popa, M. Domhan, A. Gruber, J. Wrachtrup, *Phys. Rev. Lett.* **93**, 130 501 (2004)
- 13 E. Wu, J.R. Rabeau, G. Roger, F. Treussart, H. Zeng, P. Grangier, S. Prawer, J.-F. Roch, *New J. Phys.* **9**, 434 (2007)
- 14 C. Wang, C. Kurtsiefer, H. Weinfurter, B. Burchard, *J. Phys. B* **39**, 37 (2005)
- 15 C. Kreuzer, J. Riedrich-Möller, E. Neu, C. Becher, *Opt. Express* **16**, 1632 (2008)
- 16 F. Jelezko, J. Wrachtrup, *Phys. Stat. Solidi A* **203**, 3207 (2006)
- 17 J. Meijer, A. Stephan, J. Adamczewski, H. Röcken, U. Weidenmüller, H.H. Bukow, C. Rolfs, *Nucl. Instrum. Methods B* **158**, 39 (1999)
- 18 T. Gaebel, I. Popa, A. Gruber, M. Domhan, F. Jelezko, J. Wrachtrup, *New J. Phys.* **6**, 98 (2004)
- 19 T. Schenkel, A. Persaud, S.J. Park, J. Meijer, J.R. Kingsley, J.W. McDonald, J.P. Holder, J. Bokor, D.H. Schneider, *J. Vac. Sci. Technol. B* **20**, 2819 (2002)
- 20 T. Schenkel, A.V. Hamza, A.V. Barnes, D.H. Schneider, J.C. Banks, B.L. Doyle, *Phys. Rev. Lett.* **81**, 2590 (1998)
- 21 D.N. Jamieson, C. Yang, T. Hopf, S.M. Hearne, C.I. Pakes, S. Prawer, M. Mitic, E. Gauja, S.E. Andresen, F.E. Hudson, A.S. Dzurak, R.G. Clark, *Appl. Phys. Lett.* **86**, 202 101 (2005)
- 22 K. Hitzbleck, H. Wiggers, P. Roth, *Appl. Phys. Lett.* **87**, 093 105 (2005)

**Concept of deterministic single ion doping with sub-nm spatial resolution**

---

J. Meijer, T. Vogel, B. Burchard, I. W. Rangelow, L. Bischoff, J. Wrachtrup, M. Domhan, F. Jelezko, W. Schnitzler, S. A. Schulz, K. Singer and F. Schmidt-Kaler

Published on 16th February 2006 in the scientific journal:

**Applied Physics A**

(Volume: 83 / Page: 321 / Year: 2006)

Appl. Phys. A 83, 321–327 (2006)  
 DOI: 10.1007/s00339-006-3497-0

**Applied Physics A**  
 Materials Science & Processing

J. MEIJER<sup>1</sup>  
 T. VOGEL<sup>1</sup>  
 B. BURCHARD<sup>2</sup>  
 I.W. RANGELOW<sup>3</sup>  
 L. BISCHOFF<sup>4</sup>  
 J. WRACHTRUP<sup>5</sup>  
 M. DOMHAN<sup>5</sup>  
 F. JELEZKO<sup>5</sup>  
 W. SCHNITZLER<sup>6</sup>  
 S.A. SCHULZ<sup>6</sup>  
 K. SINGER<sup>6,✉</sup>  
 F. SCHMIDT-KALER<sup>6</sup>

## Concept of deterministic single ion doping with sub-nm spatial resolution

<sup>1</sup> RUBION, Ruhr-Universität Bochum, 44780 Bochum, Germany

<sup>2</sup> Institut für Physik mit Ionenstrahlen, Ruhr-Universität Bochum, 44780 Bochum, Germany

<sup>3</sup> Institut für Nanostrukturtechnologie und Analytik (INA), Universität Kassel, Heinrich-Plett Strasse 40, 34132 Kassel, Germany

<sup>4</sup> Institute of Ion Beam Physics and Materials Research, Forschungszentrum Rossendorf e.V., P.O. Box 51 01 19, 01314 Dresden, Germany

<sup>5</sup> Physikalisches Institut, Universität Stuttgart, Pfaffenwaldring 57, 70550 Stuttgart, Germany

<sup>6</sup> Abteilung Quanten-Informationsverarbeitung, Universität Ulm, Albert-Einstein-Allee 11, 89069 Ulm, Germany

Received: 2 September 2005/Accepted: 12 January 2006  
 Published online: 16 February 2006 • © Springer-Verlag 2006

**ABSTRACT** We propose a method for deterministic implantation of single atoms into solids which relies on a linear ion trap as an ion source. Our approach allows a deterministic control of the number of implanted atoms and a spatial resolution of less than 1 nm. Furthermore, the method is expected to work for almost all chemical elements. The deterministic implantation of single phosphor or nitrogen atoms is interesting for the fabrication of scalable solid state quantum computers, in particular for silicon and diamond based schemes. A wide range of further applications is expected for the fabrication of nano and sub-nano electronic devices.

PACS 03.67.-a; 29.25.Ni; 61.72.Ji; 81.16.Rf; 85.40.Ry

### 1 Introduction

A future solid state quantum computer (QC) may be based on implanted single ions, each of them carrying a single unit of quantum information (qubit). Logic gate operations rely on the well controlled coherent interaction between individual qubits. Any coupling to the solid state bulk material would destroy the – in general – entangled global quantum state of the device. This reasoning has led to the concept of qubits logic states which are encoded into hyperfine states of single atomic phosphorous ions <sup>31</sup>P, embedded in a pure Si mono crystal[1]. More recently, experiments with single nitrogen-vacancy (NV) centers in diamond crystals have demonstrated single qubit operations [2] and two-qubit quantum logic gate operations mediated by hyperfine coupling [3], and a long coherence time [4] as necessary for a QC according to the DiVincenzo criteria [5].

However, the positioning accuracy of NV-defects was so far limited to 50 nm using a damage-implantation technique [6, 7]. The future quest is to fabricate an array of NV-centers with nm-precision for a scalable solid state QC. So far, no scheme for deterministic singly-charged single ion implantation has been yet reported for this spatial resolution.

The paper is organized as follows: after a short discussion of current approaches of ion implantation, we describe a novel method for single ion implantation with sub-nm spatial resolution. This includes a Paul trap as an ion source and a micro Einzel lens as an ion optical element for focusing through a pierced atomic force microscope (AFM)-tip. Finally, we sketch the basic concepts of a solid state QC based upon NV color centers. Though this implantation method may be applied for a large variety of atomic species we will focus here on the specific case of N<sup>+</sup> ions being implanted into diamond for the deterministic generation of NV color centers.

### 2 Ion implantation

The nitrogen-vacancy center in diamond is an atomic point-defect with a structure that consists of a nitrogen atom and a vacancy in the next lattice position (Fig. 1a). It was demonstrated that NV defects can be created in nitrogen-rich (type Ib) diamond by the creation of vacancies and a subsequent annealing step [6]. During this annealing process, vacancies migrate towards nitrogen atoms forming NV defects. The major drawback of this approach is its poor positioning accuracy of defects due to the diffusion of vacancies (50 nm). Alternatively, NV defects can be created using nitrogen implantation into nitrogen-free diamond (type IIa) [8, 9].

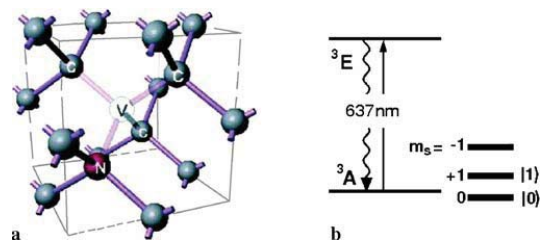


**FIGURE 1** (a) Atomic structure of the nitrogen-vacancy center in diamond consisting of a nitrogen atom (N) and a vacancy (V) in the next lattice position. (b) Scheme of the electronic and spin energy levels. Excitation and fluorescence is in the visible at 637 nm. Ground state levels may serve to store quantum information

✉ Fax: +49-731-5022839, E-mail: kilian.singer@uni-ulm.de

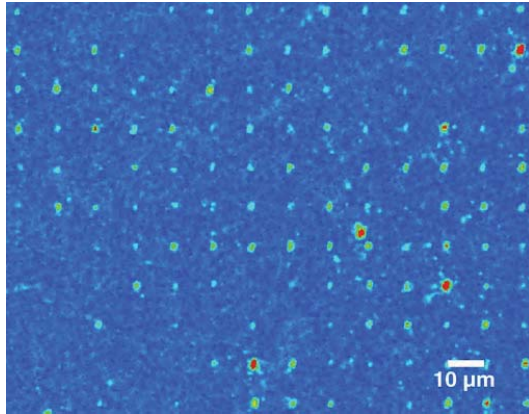


**FIGURE 2** Confocal fluorescence image of implanted NV centers generated from  $N^+$  ions implanted into type IIa diamond. Color centers are excited with light near 637 nm and the emitted fluorescence is detected by using a confocal microscope (intensity encoded in color scale)

Ion beam implantation has the advantage that the preselected position of the N-atom now defines the place of the NV center. Only the vacancies migrate during annealing ( $T \sim 850^\circ\text{C}$ ) as they become mobile above  $650^\circ\text{C}$ . The diffusion of substitutional nitrogen starts only above  $1500^\circ\text{C}$ . The creation of a single NV center relies on the migration of a vacancy to the nitrogen atom during the annealing process. The efficiency depends on the energy of the implanted ion and increases with higher energy as an increasing amount of vacancies is generated by the implantation process itself.

As an illustration of the latter method we show an array of NV centers generated using focused  $N^+$  ions (2 MeV) implanted into type IIa diamond (see Fig. 2). The efficiency of NV center creation at this energy is about 50% [9]. The spot size is about 300 nm on the target surface. Due to the stochastic nature of the ion beam some spots contain more than one NV center, while others contain none. Additionally, because of the high kinetic energies of the ions the observed spot size is mostly limited by ion straggling in the diamond matrix.

However, for single ion implantation with an aspired resolution of less than 2 nm it is necessary to reduce the ion energy down to 1 keV in order to avoid lateral displacement caused by straggling<sup>1</sup>. Recent results indicate that at these low implantation energies the efficiency of the creation of a NV defect during the annealing process is decreased to less than 10% [10]. Subsequent implantation of carbon ions could be used to increase the local density of vacancies near the nitrogen atom. Also other elements could be used which immediately generate color centers without the need of an additional vacancy like boron in diamond or chromium in sapphire. Regardless of the used ion species, the alignment of the ion beam is realized by a pierced AFM-tip acting as a stencil nano mask. The use of a pierced AFM-tip as a collimator is already successfully established [11, 12]. However, this technique has two disadvantages: firstly, a pinhole

<sup>1</sup> SRIM-2003: <http://www.srim.org/>

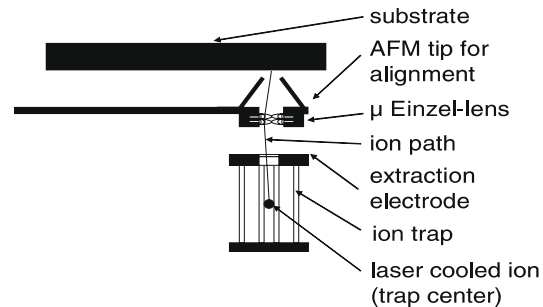


**FIGURE 3** Schematic of the setup used for deterministic implantation of single ions. The ions are trapped and subsequently laser cooled inside a Paul trap. A voltage change at the extraction electrode accelerates the ion towards the substrate. The ions are focused onto the surface with an Einzel-lens mounted together with an AFM-tip used for alignment

size of 5 nm and below will produce proximity effects, affecting the spatial resolution. Secondly, this technique needs highly charged ions for the detection of the impact of one single ion. But highly charged ions may cause severe damage to the surface [13], possibly destroying the solid state QC coherence.

A more suitable method presented in this paper is the use of an ion trap as a single ion point source.

This technique avoids any proximity effects and does not require any additional detection system. A pierced AFM tip acts as an alignment tool for the ion lens with respect to the target.

The basic ideas of the proposed system are shown in Fig. 3. A linear Paul trap is used as a source of single ions with supreme performance from an ion-optical point of view. Single ions are trapped, cooled and extracted with a spatial- and momentum-uncertainty near to the fundamental limit given solely by quantum physics. Additionally, the resonance fluorescence of those ions can be routinely excited by laser radiation and observed with a camera system. Thus, the number of trapped ions is well known and a deterministic implantation of a given number of atoms is possible. The ions are extracted and focused down to the surface of the substrate with sub-nm resolution using a micro Einzel lens. Advantageously, it is combined with a pierced AFM tip for the exact placement and accurate positioning of the system. In order to realize this design the following questions have to be addressed:

- Is it possible to extract one ion from a Paul trap without losing the position information?
- What kind of ion optics is adequate to focus ions down to nm resolution?
- How to manage the adjustment procedure for single ion implantation?
- What is the expected final spatial resolution of the entire system?

### 3 A linear Paul trap as a deterministic single ion source

Paul traps are widely used for single ion experiments [14–16]. In the specific case of a linear Paul trap, the radio-frequency (rf) voltage is applied to a set of radial elec-

trodes and generates a pseudo potential of several eV depth. The axial confinement is provided by additional dc electrodes. Various forms and sizes of linear Paul traps are known. Typically, the rf-electrodes are in the shape of four rods [17] or four blades [18]. The applied voltages result in a harmonic trapping potential for all spatial directions. Trap sizes range from a few mm to a few 100  $\mu\text{m}$  in the case of small linear traps [19]. Correspondingly, the vibrational trap frequencies vary from several MHz down to 100 kHz. Due to laser Doppler cooling, the kinetic energy of the trapped ions can be reduced down to a few mK (corresponding to  $10^{-7}$  eV). The typical wave packet extension is 20 nm for an  $^{14}\text{N}^+$  ion in the ground state at a trap frequency of  $\omega_{\text{trap}}/2\pi = 2$  MHz. Routinely, the ground state of vibration is reached by more sophisticated laser cooling techniques such as resolved side band cooling on quadrupole transitions [20] or ground state cooling exploiting electromagnetically induced transparency (EIT) [21]. As a result, the position-momentum uncertainty of the ion wave function is limited only by the Heisenberg uncertainty principle.

However, ion species which might be interesting for doping applications can usually not be laser cooled. This is due to the fact that the corresponding transition wavelengths are extremely hard to achieve by laser sources or the level scheme does not feature an adequate two-level system suitable for an optical cycling transition. Unfortunately, this is the case for  $^{31}\text{P}^+$  and for any isotope of nitrogen. This difficulty may be circumvented by sympathetic laser cooling [22–25]. We propose to sympathetically cool either phosphorous or nitrogen doping ions inside a string of  $^{40}\text{Ca}^+$  ions which are laser cooled. The linear crystal of  $^{40}\text{Ca}^+$  ions will be observed

with a CCD-camera whereas the doping ions show up as dark sites [23, 26] (Fig. 4). After Doppler cooling, a second cooling step via EIT will allow reaching almost to the vibrational ground state of all common modes of vibration [27].

Next, a single dark doping ion is separated together with a single  $^{40}\text{Ca}^+$  ion from the entire crystal in order to determine the mass of the doping ion by measuring the vibrational frequency of the mixed crystal [22]. The observation of dark sites in the fluorescence, the ground state cooling, and the deterministic separation of the doping ion are the key-elements of our method.

Finally, the ion is extracted for implantation, being delivered with an ideal brightness at the physical limit.

#### 4 Point source ion optics

The ion trap for single ions defines a completely new starting point for ion beam optics offering an ideal point source perfectly suitable for deterministic ion ray tracing. The theoretical accuracy limit of the point source is given by the uncertainty of the initial velocity distribution after optical cooling. Beam broadening by stochastic space charge effects is completely avoided.

For numerical simulation of the ion's trajectory we first model the quasi-electrostatic potential of the Paul trap and then simulate the trajectories by ray tracing. In order to cross-check the results, two fully independent software packages have been developed.

Method A relies on the calculation of the potential distribution of the trap and extractor lens using a finite-differential method (FDM) combined with a multi-grid technique to find starting values for a simultaneous over-relaxation (SOR) method [28]. The calculation of the trap potential is performed on a  $64 \times 64 \times 256$  grid. The grid distance is chosen to be 100  $\mu\text{m}$ . A ray tracing procedure uses the resulting field distribution to calculate the electric force acting on the ion using a 5th order Runge–Kutta formalism with adaptive step size control [28]. A Monte-Carlo technique simulates the influence of starting parameters. The temperature is set as the starting parameter for the random choice of the initial ion velocity. Method B applies the commercial program Femlab<sup>2</sup> for calculating the 3D trap potentials in an adaptive non-uniform grid. The trajectories are simulated in C++ in an 8th order Runge–Kutta Prince–Dormand method<sup>3</sup>.

In both simulations, the type and size of the linear quadrupole ion trap is adapted from [17, 26]. The trap consists of four parallel rods with 2 mm spacing and a length of 10 mm. Diagonally opposed rods are connected to a rf source with  $\omega_0/2\pi$  of 18 MHz and  $V_{\text{pp}} = 1$  kV, generating a quadrupole rf field. The axial confinement is provided by two disc shaped end caps at a distance of 10 mm (outer diameter 6 mm) with a centered extraction hole of 1 mm diameter. The dc voltage at the end caps is set to 500 V. The parameters for the end caps are slightly modified to [17].

To use the trap as an ion source all potentials are biased by +500 V and the temperature of the ions is assumed to be around 0.1 mK. The extraction of the ion is initiated by

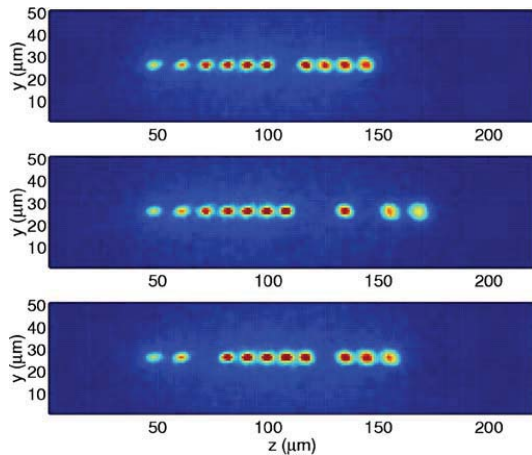


**FIGURE 4** String of  $10^{40}\text{Ca}^+$  ions plus 3 impurity ions excited and cooled by laser radiation near 397 nm and 866 nm. The ion crystal's fluorescence near 397 nm is imaged onto a CCD system. In the top image one impurity ion is in the center, the other two are at the far right. The average inter-ion spacing is 10  $\mu\text{m}$  (axial oscillation frequency  $\omega_z/2\pi = 108$  kHz, radial frequency  $\omega_{\text{rad}}/2\pi = 1.4$  MHz). Exposure time is 1 s. Between the upper, middle and lower image, the ion crystal was melted by tuning the laser radiation near 397 nm to the blue side of the atomic resonance. The positions of the impurity ions are changed after cooling the ion crystal again. The figure is taken from [26] with kind permission of the author

<sup>2</sup> Femlab: <http://www.comsol.com/>

<sup>3</sup> GSL: <http://www.gnu.org/software/gsl/>

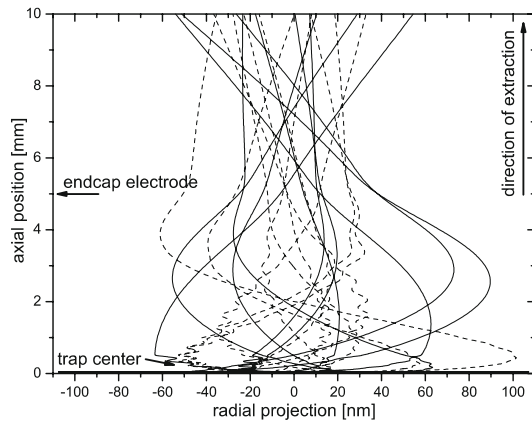


**FIGURE 5** Trajectories of 10 ions during extraction with rf field switched on (dashed curve) and switched off 6 periods after start of extraction (solid curve). The ion trajectory starts in the center of the trap and is directed to the upper part of the figure. The end cap electrode of the Paul trap is located at 5 mm axial position. Note that the radial axis is scaled in nm whereas the axis in the extraction direction is scaled in mm

switching one of the end caps from 1000 V to 0 V. Both simulation methods show that sub-nm resolution ( $< 1$  nm) can be achieved with laser cooled ions. In the following we will focus only on the results of method B. The rays of the ions inside the trap after extraction are shown in Fig. 5. One of the important questions for the optimization is the handling of the rf-field during the extraction procedure. Our first guess was to continuously apply the rf-field during extraction in order to maintain the radial confinement (Fig. 5, dashed). The lateral spread of the ion trajectories at a distance of 10 mm from the trap center in the extraction direction is about  $\pm 50$  nm. In order to focus the trajectories down to one spot at the target we simulate a small electrostatic Einzel lens between trap

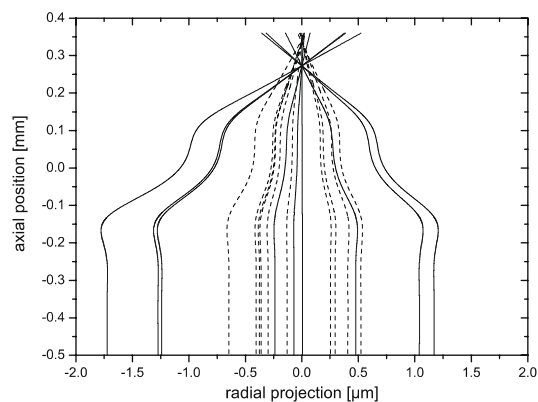


**FIGURE 6** Trajectories of 10 ions at a distance of 90 mm from the trap center (dashed and solid curves as in Fig. 5). Axial position zero denotes the place of the center electrode of the Einzel lens. The ions follow linear trajectories from the trap and are directed to the upper part of the figure where the focus is located at  $\sim 300 \mu\text{m}$  axial position

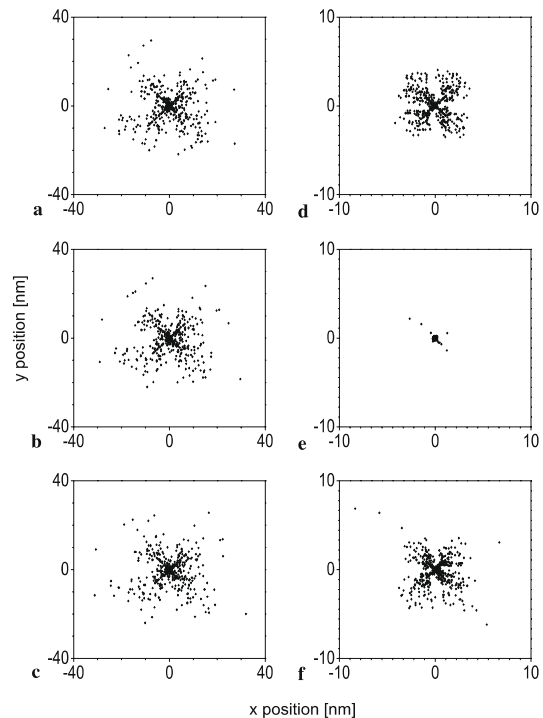


**FIGURE 7** Spot diagram of 500 ray traced ions at the target plane. Initial temperature of the single ion inside the trap is 0.1 mK. The ion is focused with an Einzel lens (located at  $z \sim 90$  mm) down to a spot size of 20 nm (rms) if the rf field is constantly applied and 0.4 nm (rms) if switched off 6 periods after the start of extraction, respectively: (a) rf on, 0.5  $\mu\text{m}$  before focal plane, (b) rf on, at focal plane, (c) rf on, 0.5  $\mu\text{m}$  after focal plane, (d) rf off, 0.5  $\mu\text{m}$  before focal plane, (e) rf off, at focal plane, (f) rf off, 0.5  $\mu\text{m}$  after focal plane

and target, located at a distance of 90 mm from the trap center. The symmetric Einzel lens consists of a stack of three equidistant conducting layers separated by about  $150 \mu\text{m}$ . The middle layer is biased to +1000 V whereas the other layers are grounded. The resulting focal length for 500 eV ions is about  $300 \mu\text{m}$  (Fig. 6, dashed). The spread of the impact positions of the ions at the target plane (Fig. 7b) is about 20 nm which would be still one order of magnitude too high. If the position of the target plane is changed within  $1 \mu\text{m}$  the spot size hardly changes (Fig. 7a–c). This situation cannot be improved by further lowering the initial temperature of the ions in the trap. The spread is caused by axial velocity kicks caused by the rf field near the extraction electrode, which lead to different focal lengths of the Einzel lens (chromatic aberration). Therefore in a future setup the ion lens will be designed to minimize chromatic aberration. If in our simulation the rf field is switched off before the ion has reached the end caps, e.g. six periods after start of the extraction, we observe a slightly larger spatial spread of the ions after the trap (Fig. 5, solid) and before the ion lens (Fig. 6, solid). However, the velocity spread in the axial direction is strongly reduced from  $\Delta v/v = 5 \times 10^{-3}$  to  $\Delta v/v = 6 \times 10^{-6}$  resulting in a spot size of around 1 nm at the target plane (Fig. 7e). In order to guarantee the latter

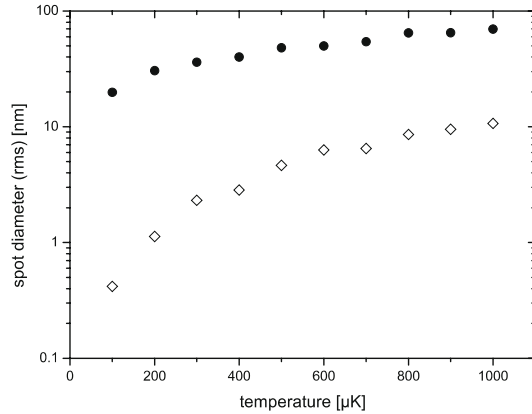


**FIGURE 8** Calculated rms spot size at the sample as a function of ion temperature, rf drive kept on (●) and switched off 6 periods after start of extraction (◊), respectively. Each data point is based on 500 simulation runs

velocity spread the power supplies have to be stabilized to a level of about 0.5 mV.<sup>4</sup> If the position of the target plane is now changed within 1  $\mu\text{m}$  the spot size changes drastically (Fig. 7d–f). Beside this focussing effect, the lens has an additional advantage: the ions always move towards the lens axis. A small displacement and misalignment of the ion trap will not affect the impact position at the target and makes the system insensitive against expected mechanical vibrations and thermal drifts.

The simulated variation of lateral positions of the ion at the target's location as a function of the ion temperature is shown in Fig. 8. A displacement below 1 nm can be expected for an ion with a temperature below 0.2 mK if spherical aberration at the ion lens can be avoided. This is routinely achieved with laser cooling techniques. The simulations also show that a preadjustment between the trap and the lens within a few  $\mu\text{m}$  is necessary to achieve a spot size in the order of a few nm. The focal depth of the lens is about 1  $\mu\text{m}$  and requires a preadjustment of the lens voltage. This can be done offline using a low energy ion gun combined with a detection system, see Sect. 5.

For ion beam optics at very low kinetic ion energies ac stray magnetic fields as produced by electric engines or radio waves are very serious concerns. Fortunately, the ion inside the trap is shielded due to the rf trap field. Simulations show that ac stray magnetic fields have to be reduced below 0.5  $\mu\text{T}$  in order to reach nm resolution.

##### 5 AFM set-up with integrated hollow tip

With the focal depth of the Einzel lens of about 1  $\mu\text{m}$  the distance to the target needs accurate preadjustment. Additionally, lateral positioning of the doping sites with respect to surface structures, e.g. markers or electric gate assemblies are required. The alignment accuracy of a few nm is desirable for functional device realization. The only known systems that allow addressing with sub-nm resolution are atomic-force microscopes (AFM) or scanning-tunneling microscopes (STM).

<sup>4</sup> This is quite challenging especially as the voltage has to be switched.

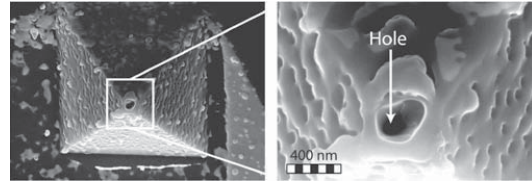


**FIGURE 9** Pierced AFM-tip consisting of SiN. The hole in the hollow pyramid is fabricated by focused ion beam (FIB) milling. The crater shaped pit on top of the pyramid ends in a 30 nm hole

We take advantage of a recent breakthrough in AFM technology. The cantilever probe consists of a SiN-tip with a hollow nitride pyramid with a drilled hole ( $\leq 30$  nm diameter) fabricated by focused ion beam (FIB) milling (Fig. 9) [29]. For this process the Rossendorf IMSA-Orsay Physics FIB was applied at an energy of 25 keV and a spot size of about 25 nm. A Faraday cup under the tip was installed as an end point detector to stop the milling just in time, as well as to image the hole by the transmission current signal. The diameter of the entrance of the milled hole was about 140 nm and the exit was in the range of 30 nm. The AFM operation with piezo resistive cantilevers [30, 31] allows imaging of the surfaces topography in conventional contact mode, with a resolution in  $z$  of better than 1 nm, and also in non-contact mode employing integrated thermal bimorph actuators [32]. The Einzel lens is combined with the AFM cantilever mount (Fig. 3) to achieve a high correlation and stability between the AFM tip and the focus position of the lens. In contrast to [4] the AFM tip has no direct ion optical function any more and will not be hit by the beam. To avoid any kind of contamination during the loading of the ion trap, an aperture size in the range of 30–50 nm is useful.

##### 6 Application of single ion implantation for quantum computing

For the realization of a solid state quantum computer several technical issues have to be solved. The major requirement is the existence of well defined qubits which can be reliably fabricated and controlled. In particular for solid-state systems, proper choice of the qubit is a challenging task because of decoherence caused by strong interactions within the bulk material. The most important issue at the moment is to proof the scalability of those qubit systems. There are several possible approaches like qubits based on quantum dots, superconducting nanostructures and nuclear spins in semiconductors [1, 33, 34]. The latter were envisaged as promising candidates because of very long coherence times (up to seconds) [35]. However, the readout with conventional NMR technology gives only access to ensemble spin states and thus causes severe scalability problems [36]. Recently, it was shown that the single electron spin of a NV center in diamond can be read out optically. As sketched in Fig. 1b, the electronic level scheme exhibits a strong dipole-allowed  $E \leftrightarrow A$  optical transition with a zero-phonon line at 1.945 eV. A second essential feature of the NV-defect is a paramagnetic ground electronic state which originates from two unpaired electron spins [37–39]. The dipolar interaction between these electronic spins leads to a zero-field splitting between  $m_s = 0$

and  $m_s = 1$  ground state spin sublevels. The readout of the electron spin is based on the fact that under excitation of the optical dipole transition (Fig. 1b) the amount of scattered photons is sensitive to the internal spin state [40].

A two qubit quantum gate was demonstrated using the hyperfine coupling between nuclear and electron spins associated with a single defect [3]. Scaling up to a multitude of defects is impeded because of the local nature of the hyperfine interaction [41]. Hence long range dipolar coupling between spins is more appropriate for scalable QC. Note that only neighboring qubits will be coupled substantially due to the  $1/r^3$  dependence of the coupling. Single qubits may be encoded in electron spin states of single NV defects and fast quantum gate operations will be performed using electron spin dipole–dipole coupling between closely spaced defects.<sup>5</sup> As opposed to the hyperfine coupling, distances of 1 nm are now sufficient for achieving a resolvable coupling of  $\Omega_{\text{Rabi}}/2\pi = 50$  MHz. Such interqubit spacings are technically feasible by the above described method. CNOT and other quantum gate operations between adjacent electron spins may be implemented using ESR analogues of well developed NMR pulse sequences [42, 43]. As an example, refocusing techniques using broad pulses resonant to all spins may be used for switching off all interactions between any spins. In order to selectively enable the interaction between specific adjacent spins an additional spectrally narrow pulse sequence has to be inserted between the refocusing pulses. The coherence time of spins associated with defects in diamond is amazingly long with a few tens of microseconds at room temperature [4].<sup>6</sup> The two qubit gate operation timescale is limited by the coupling strength in the range of tens of MHz. This will allow reaching of the quantum error correction threshold of  $T_{\text{gate}}/T_2 = 10^{-4}$ .

## 7 Conclusions

We have presented a novel method for deterministically implanting single ions with sub-nm resolution. Key elements of our method are a linear Paul trap serving as an ion source in combination with sophisticated laser cooling techniques such as EIT cooling to the vibrational ground state. This atom optical element constitutes an ideal deterministic point source of ions with the ultimate brightness only limited by the Heisenberg uncertainty principle. Our simulations predict a lateral positioning accuracy of the ions of less than 1 nm for an ion-temperature of 0.2 mK reached by laser cooling techniques.

In the future we will optimize the design of the ion trap. The ion optical system has to be designed in such a way that chromatic aberration is minimized. Experiments will be performed with various doping ions in order to explore a broad spectrum of applications. The application of our technique can also be extended to molecular or cluster particles.

<sup>5</sup> Alternatively, the dipole–dipole interaction between electronic (optical) transitions could also be explored for coupling between qubits. Thus, the coupling strength would be controlled via a selective optical excitation of the defect centers.

<sup>6</sup> Decoherence due to coupling to imperfections on the surface is not expected, since the surface of diamond can be prepared in a well controlled way using acid or H-plasma treatment.

**ACKNOWLEDGEMENTS** We acknowledge financial support in Bochum by the Volkswagen foundation. The work in Stuttgart has been supported by the DFG via SFB/TR 21. Financial support in Stuttgart and Ulm is granted by the Landestiftung BW via the program “Atomoptik”.

## REFERENCES

- 1 B.E. Kane, *Nature* **393**, 133 (1998)
- 2 F. Jelezko, T. Gaebel, I. Popa, A. Gruber, J. Wrachtrup, *Phys. Rev. Lett.* **92**, 076401 (2004)
- 3 F. Jelezko, T. Gaebel, I. Popa, M. Domhan, A. Gruber, J. Wrachtrup, *Phys. Rev. Lett.* **93**, 130501 (2004)
- 4 T.A. Kennedy, J.S. Colton, J.E. Butler, R.C. Linares, P.J. Doering, *Appl. Phys. Lett.* **83**, 4190 (2003)
- 5 A Quantum Information Science and Technology Roadmapping Project by the Advanced Research and Development Activity (ARDA), <http://qist.lanl.gov/> and European Pilot project <http://qist.ect.it/>
- 6 J. Martin, R. Wannemacher, J. Teichert, L. Bischoff, B. Köhler, *Appl. Phys. Lett.* **75**, 3096 (1999)
- 7 J. Martin, L. Bischoff, R. Wannemacher, *Opt. Commun.* **188**, 119 (2001)
- 8 R. Kalish, C. UzanSaguy, B. Philosoph, V. Richter, J.P. Lagrange, E. Gheeraert, A. Deneuille, A.T. Collins, *Diam. Relat. Mater.* **6**, 516 (1997)
- 9 J. Meijer, B. Burchard, M. Domhan, C. Wittmann, T. Gaebel, I. Popa, F. Jelezko, J. Wrachtrup, *Appl. Phys. Lett.* **87**, 261909 (2005)
- 10 J.R. Rabeau, P. Reichert, G. Tamanyan, D.N. Jamieson, S. Prawer, F. Jelezko, T. Gaebel, I. Popa, M. Domhan, J. Wrachtrup, *Appl. Phys. Lett.* **88**, 023113 (2006)
- 11 T. Schenkel, A. Persaud, *J. Appl. Phys.* **94**, 7017 (2003)
- 12 I. Rangelow, J. Meijer, T. Schenkel, German Patent Appl., DE10347969A1, 2003 (patent pending)
- 13 T. Schenkel, A.V. Hamza, A.V. Barnes, D.H. Schneider, J.C. Banks, B.L. Doyle, *Phys. Rev. Lett.* **81**, 2590 (1998)
- 14 S.A. Diddams, T. Udem, K.R. Volgel, C.W. Oates, E.A. Curtis, W.D. Lee, W.M. Itano, R.E. Drullinger, J.C. Bergquist, L. Hollberg, *Science* **293**, 825 (2001)
- 15 M. Riebe, H. Häffner, C.F. Roos, W. Hänsel, J. Benhelm, G.P.T. Lancaster, T.W. Körber, C. Becher, F. Schmidt-Kaler, D.F.V. James, R. Blatt, *Nature* **429**, 734 (2004)
- 16 M.D. Barrett, J. Chiaverini, T. Schaetz, J. Britton, W.M. Itano, J.D. Jost, E. Knill, C. Langer, D. Leibfried, R. Ozeri, D.J. Wineland, *Nature* **429**, 737 (2004)
- 17 H.C. Nägerl, C. Roos, D. Leibfried, H. Rohde, G. Thalhammer, J. Eschner, F. Schmidt-Kaler, R. Blatt, *Phys. Rev. A* **61**, 023405 (2000)
- 18 F. Schmidt-Kaler, H. Häffner, S. Gulde, M. Riebe, G.P.T. Lancaster, T. Deuschle, C. Becher, W. Hänsel, J. Eschner, C.F. Roos, R. Blatt, *Appl. Phys. B* **77**, 789 (2003)
- 19 D. Leibfried, T. Schätz, *Phys. J.* **3**, 23 (2004)
- 20 C.F. Roos, Th. Zeiger, H. Rohde, H.C. Nägerl, J. Eschner, D. Leibfried, F. Schmidt-Kaler, R. Blatt, *Phys. Rev. Lett.* **83**, 4713 (1999)
- 21 C.F. Roos, D. Leibfried, A. Mundt, F. Schmidt-Kaler, J. Eschner, R. Blatt, *Phys. Rev. Lett.* **85**, 5547 (2000)
- 22 M. Drewsen, A. Mortensen, R. Martinussen, P. Staunum, J. L. Sørensen, *Phys. Rev. Lett.* **93**, 243201 (2004)
- 23 L. Hornekaer, N. Kjærgaard, A.M. Thomsen, M. Drewsen, *Phys. Rev. Lett.* **86**, 1994 (2001)
- 24 H. Rohde, S.T. Gulde, C.F. Roos, P.A. Barton, D. Leibfried, J. Eschner, F. Schmidt-Kaler, R. Blatt, *J. Opt. B* **3**, 34 (2001)
- 25 M. Barrett, B.L. DeMarco, T. Schätz, V. Meyer, D. Leibfried, J. Britton, J. Chiaverini, W.M. Itano, B.M. Jelenkovic, J.D. Jost, C. Langer, T. Rosenband, D.J. Wineland, *Phys. Rev. A* **68**, 042302 (2003)
- 26 H.C. Nägerl, *Ion Strings for Quantum Computing*, Dissertation, Innsbruck (1998), unpublished
- 27 F. Schmidt-Kaler, J. Eschner, G. Morigi, C.F. Roos, D. Leibfried, A. Mundt, R. Blatt, *Appl. Phys. B* **73**, 807 (2001)
- 28 W.H. Press, S.A. Teukolsky, W.T. Vetterling, B.P. Flannery, *Numerical Recipes in C* (University Press, Cambridge, 1992)
- 29 I.W. Rangelow, F. Shi, P. Hudek, T. Gotszalk, P.B. Grabiec, P. Dumania, *Proc. SPIE* **2879**, 56 (1996)
- 30 I.W. Rangelow, P. Grabiec, T. Gotszalk, K. Edinger, *Surf. Interface Anal.* **33**, 59 (2002)
- 31 I.W. Rangelow, *Tech. Mess.* **72**, 103 (2005)
- 32 R. Pedrak, T. Ivanov, K. Ivanova, T. Gotszalk, N. Abedinov, I.W. Rangelow, K. Edinger, E. Tomerov, T. Schenkel, P. Hudek, *J. Vac. Sci. Technol. B* **21**, 3102 (2003)

- 33 X.Q. Li, Y.W. Wu, D. Steel, D. Gammon, T.H. Stievater, D.S. Katzer, D. Park, C. Piermarocchi, L.J. Sham, *Science* **301**, 809 (2003)
- 34 T. Yamamoto, Y.A. Pashkin, O. Astafiev, Y. Nakamura, J.S. Tsai, *Nature* **425**, 941 (2003)
- 35 T.D. Ladd, J.R. Goldman, F. Yamaguchi, Y. Yamamoto, E. Abe, K.M. Itoh, *Phys. Rev. Lett.* **89**, 017901 (2002)
- 36 W.S. Warren, *Science* **277**, 1688 (1997)
- 37 E. van Oort, P. Stroomeer, M. Glasbeek, *Phys. Rev. B* **42**, 8605 (1990)
- 38 N.R.S. Reddy, N.B. Manson, E.R. Krausz, *J. Luminesc.* **38**, 46 (1987)
- 39 D. Redman, S. Brown, S.C. Rand, *J. Opt. Soc. Am B* **9**, 768 (1992)
- 40 F. Jelezko, J. Wrachtrup, *J. Phys.: Condens. Matter* **16**, R1089 (2004)
- 41 J. Wrachtrup, S. Kilin, A.P. Nizovtsev, *Opt. Spectrosc.* **91**, 429 (2001)
- 42 J. Twamley, *Phys. Rev. A* **67**, 052318 (2003)
- 43 L.M.K. Vandersypen, I.L. Chuang, *Rev. Mod. Phys.* **76**, 1037 (2004)

## B.4 New Journal of Physics

### **Focusing a deterministic single-ion beam**

---

W. Schnitzler, G. Jacob, R. Fickler, F. Schmidt-Kaler and K. Singer

Published on 28th June 2010 in the scientific journal:

**New Journal of Physics**

(Volume: 12 / Page: 065023 / Year: 2010)

# New Journal of Physics

The open-access journal for physics

## Focusing a deterministic single-ion beam

Wolfgang Schnitzler<sup>1,3</sup>, Georg Jacob<sup>1</sup>, Robert Fickler<sup>2</sup>,  
Ferdinand Schmidt-Kaler<sup>1</sup> and Kilian Singer<sup>1</sup>

<sup>1</sup> Institut für Quanteninformationsverarbeitung, Universität Ulm,  
Albert-Einstein-Allee 11, D-89069 Ulm, Germany

<sup>2</sup> Institut für Quantenoptik, Quantennanophysik und Quanteninformation,  
Universität Wien, Boltzmannngasse 5, A-1090 Wien, Austria

E-mail: [wolfgang.schnitzler@uni-ulm.de](mailto:wolfgang.schnitzler@uni-ulm.de)

*New Journal of Physics* **12** (2010) 065023 (14pp)

Received 30 November 2009

Published 28 June 2010

Online at <http://www.njp.org/>

doi:10.1088/1367-2630/12/6/065023

**Abstract.** We focus down an ion beam consisting of single  $^{40}\text{Ca}^+$  ions to a spot size of a few micrometers using an einzel lens. Starting from a segmented linear Paul trap, we have implemented a procedure that allows us to deterministically load a predetermined number of ions by using the potential shaping capabilities of our segmented ion trap. For single-ion loading, an efficiency of 96.7(7)% has been achieved. These ions are then deterministically extracted out of the trap and focused down to a  $1\sigma$ -spot radius of  $(4.6 \pm 1.3) \mu\text{m}$  at a distance of 257 mm from the trap center. Compared to previous measurements without ion optics, the einzel lens is focusing down the single-ion beam by a factor of 12. Due to the small beam divergence and narrow velocity distribution of our ion source, chromatic and spherical aberration at the einzel lens is vastly reduced, presenting a promising starting point for focusing single ions on their way to a substrate.

<sup>3</sup> Author to whom any correspondence should be addressed.

2

IOP Institute of Physics  $\Phi$  DEUTSCHE PHYSIKALISCHE GESELLSCHAFT**Contents**

<b>1. Motivation</b>	<b>2</b>
<b>2. Experimental set-up</b>	<b>3</b>
2.1. UHV set-up . . . . .	3
2.2. Segmented linear rail trap . . . . .	3
2.3. Optical set-up . . . . .	5
2.4. Extraction mechanism and set-up . . . . .	6
2.5. Ion optics . . . . .	7
<b>3. Experimental results</b>	<b>9</b>
3.1. Deterministic single-ion loading . . . . .	9
3.2. Experimental determination of the spot size . . . . .	10
<b>4. Conclusion and outlook</b>	<b>12</b>
<b>Acknowledgments</b>	<b>13</b>
<b>References</b>	<b>13</b>

**1. Motivation**

In the age of electronic data processing, the demand for more powerful and faster computers is paramount. As already stated by Gordon E Moore in 1965, the number of transistors that can be placed inexpensively on an integrated circuit has increased exponentially, doubling approximately every two years. The miniaturization of semiconductor devices has reached length scales of a few tens of nanometers, where statistical Poissonian fluctuations in the number of doping atoms in a single transistor significantly affect the characteristic properties of the device, e.g. gate voltage or current amplification. Especially when thinking about future solid state quantum processors, statistical fluctuations of the dopant concentration are fatal for systems that are based on single implanted qubit carriers, like color centers in diamond or phosphorus dopants in silicon [1]–[4]. Until recently, most implantation techniques resorted to thermal sources, where control of the number of doping atoms is possible only via a postdetection of the implantation event. However, although a wide range of postdetection schemes (e.g. the observation of Auger electrons, the generation of electron–hole pairs or changes in the conductance of field effect transistors) are available [5]–[9], most of these techniques require either highly charged ions or high implantation energies, which, as a down side, generate unintentional defects in the host material. Another fabrication method revolves around the structuring of chemically treated Si surfaces. Using a hydrogen-terminated Si surface as the starting point, the tip of a tunneling microscope allows for the removal of single hydrogen atoms, which are then replaced by doping atoms such as phosphorus due to a chemical reactive surface binding [10]–[14]. Although this technique is capable of placing single dopants with sub-nm resolution, the applicability is mainly restricted to specific substrates. In order to circumvent the necessity of any postdetection schemes and to expand the applicability to a wider range of elements, deterministic single-ion sources on the basis of optical lattices [15], magneto-optical [16]–[18] and segmented linear Paul traps [19] have been developed.

Here, we present the experimental set-up to focus down on an ion beam consisting of single  $^{40}\text{Ca}^+$  ions to a spot size of a few  $\mu\text{m}$  by utilizing an einzel lens. The single-ion beam is generated by a segmented linear Paul trap that allows us to deterministically extract single ions

on demand [19]–[21]. Due to the small beam divergence and narrow velocity distribution of our single-ion source, chromatic and spherical aberration at the einzel lens is strongly reduced, presenting a promising starting point for focusing single ions on a prospective substrate.

The paper is organized as follows. We first describe in section 2 the experimental setup used for the trapping, imaging and manipulation of  $^{40}\text{Ca}^+$  and this includes a detailed description of the ultrahigh vacuum (UHV) setup, the specially designed segmented linear ion trap, the optical setup as well as the extraction mechanism and the utilized ion optics. In section 3, we present the experimental results, namely the deterministic loading of single  $^{40}\text{Ca}^+$  ions and the focusing of the single-ion beam to a  $5\ \mu\text{m}$  spot. Finally, in section 4, we give a short conclusion and sketch possible future applications.

## 2. Experimental set-up

### 2.1. UHV set-up

The core piece of the UHV set-up is a Magdeburg hemisphere from Kimball Physics<sup>4</sup> with an inner diameter of 91.5 mm and a total length of 106 mm. It features a total of seven different access ports with flange sizes ranging from DN16CF to DN63CF. A specifically designed segmented linear ion trap (see section 2.2) is mounted inside the hemisphere with the trap axis being located 165 mm above the optical table.

All access ports are equipped with fused silica ( $\text{SiO}_2$ ) windows, allowing for optical access with laser beams and for imaging the ions. A 20-pin vacuum feedthrough for the dc electrodes and the ovens is connected via a T-piece to the hemisphere, whereas the power supply for the rf electrodes is managed using a separate 4-pin vacuum feedthrough, which is mounted on a four-way cross, see also figure 1. Using an all-metal gate valve from VAT<sup>5</sup>, the main vacuum chamber is connected to a separate detector chamber, which is attached to a specifically designed translation stage. In combination with a membrane below, the translation stage allows for rotating the detector chamber in the horizontal and vertical directions with respect to the trapping position of the ion, compensating for any misalignment between the trap axis and the optical axis of the utilized ion optics. The complete set-up measures 850 mm in length with a depth of 480 mm and a total height of about 380 mm. The pressure is held by a 20 litre  $\text{s}^{-1}$  VacIon Plus StarCell ion getter pump and a titanium sublimation pump<sup>6</sup>. In addition, both the main vacuum and the detector chamber are connected via all-metal angle valves to a turbo-molecular pump from Oerlikon<sup>7</sup>. The base pressure of the UHV set-up equals  $5 \times 10^{-10}$  mbar, which is measured using a Varian UHV-24p Bayard-Alpert-type ionization gauge tube.

### 2.2. Segmented linear rail trap

The trap consists of four copper-plated polyimide blades, which were manufactured using printed circuit board (PCB) technology and are arranged in an X-shaped manner [22]. It features a total of 15 independent dc electrodes, which can be assigned to three different trap sections: a wide loading zone (electrodes 1–4) is connected via a taper (electrode 5) to a narrow

<sup>4</sup> Kimball Physics Inc., USA.

<sup>5</sup> VAT Deutschland GmbH, Germany.

<sup>6</sup> Varian Inc., USA.

<sup>7</sup> Oerlikon Leybold Vacuum GmbH, Germany.

4

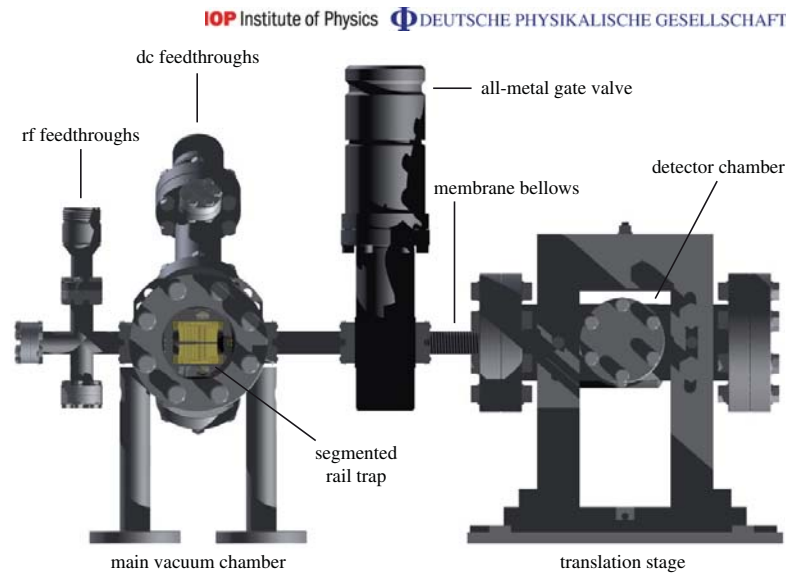


**Figure 1.** Schematic drawing of the UHV set-up. The set-up consists of a main vacuum chamber and a detector chamber, which are connected via an all-metal gate valve. A membrane below in combination with a specifically designed translation stage allows for rotating the detector chamber in the horizontal and vertical directions with respect to the trapping position of the ion.

experimental zone (electrodes 6–14). A deflection electrode (electrode 15) is used to alter the trajectories of ions that are extracted out of the trap. In order to generate the radial confinement, an additional electrode runs along the inner front face of each blade, which will be referred to as a rail in the following. The blade itself has a total length of 65 mm and a thickness of 410  $\mu\text{m}$  with 18  $\mu\text{m}$  copper plating on both sides. Electrodes 2–5 as well as electrode 14 have a width of 2.8 mm, and electrodes 6–13 have a width of 0.7 mm. In order to efficiently deflect ions by targeted application of low voltages, the deflection electrode has been elongated in the extraction direction, featuring a total length of 20.6 mm. The distance between the rf rail and the dc electrodes as well as between adjacent dc electrodes equals 0.1 mm (see also figure 2 for a technical drawing of one of the four trap blades).

The distance between the inner front faces of opposing blades equals 4 mm in the loading zone and 2 mm in the experimental zone. In the case of a standard Paul trap, the rf voltage is supplied to two of the four blades. The other two blades are used for the axial confinement and are therefore divided into several electrodes. However, in the case of our rail trap, all four blades are identical. Apart from the deflection electrodes, the corresponding electrodes on all four blades (i.e. electrode 1 of each of the blades) are electrically connected together, resulting in a stronger and more symmetrical axial confinement than in the standard case. The rf voltage is only applied to the rails of two opposing blades; the front faces of both of the other blades are grounded, generating the quadrupole potential for the radial confinement. As these rails run along the whole trap axis and continue around the corner at the end of each blade, the

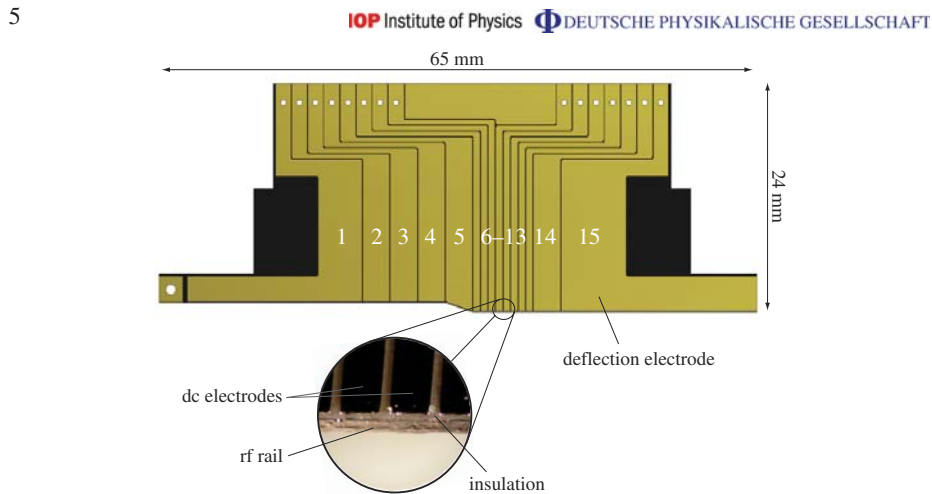


**Figure 2.** Technical drawing of one of the four trap blades featuring a total of 15 independent dc electrodes. A wide loading zone (electrodes 1–4) is connected via a taper (electrode 5) to a narrow experimental zone (electrodes 6–14). A deflection electrode (electrode 15) is used to alter the trajectories of the extracted ions. The rf rail has a thickness of about  $22 \mu\text{m}$  and covers the whole front of the blade. Isolated parts are colored black. The close-up view shows a microscope image of the front part of the blade.

radial confinement is sustained during the whole extraction process and targeted shooting is accomplished.

Under typical operating conditions, we apply a voltage of  $400 V_{\text{pp}}$  at a frequency of  $\Omega/2\pi = 12.155 \text{ MHz}$  to the rf electrodes, leading to a radial secular frequency  $\omega_{\text{rad}}/2\pi = 430 \text{ kHz}$  for a  $^{40}\text{Ca}^+$  ion. The dc-electrode trap segments 7 and 13 are supplied with  $35 \text{ V}$  and the remaining electrodes with  $0 \text{ V}$ , resulting in an axial trapping potential with  $\omega_{\text{ax}}/2\pi = 280 \text{ kHz}$ . The location of trapped ions is above electrode 10.

### 2.3. Optical set-up

The generation of the necessary laser beams is mainly done by using commercial grating stabilized diode laser systems from TOPTICA<sup>8</sup>. The ions are illuminated by resonant laser light near  $397$  and  $866 \text{ nm}$  for Doppler cooling. Scattered photons are collected by an  $f/1.76$  lens on an EMCCD camera<sup>9</sup> to image individual  $^{40}\text{Ca}^+$  ions. From the width of the laser excitation spectrum on the  $S_{1/2}-P_{1/2}$  laser cooling transition, we deduce a temperature of about  $2 \text{ mK}$ , slightly above the Doppler cooling limit. Calcium and dopant ions are generated in a multi-photon ionization process by a pulsed frequency tripled Nd-YAG laser at  $355 \text{ nm}$  with a pulse power of  $7 \text{ mJ}$ . Dopant ions are sympathetically cooled and identified from the voids in the

<sup>8</sup> TOPTICA Photonics AG, Germany.

<sup>9</sup> Andor Technology, model DV885KCS-VP.

fluorescence image compared to that of a regular linear  $^{40}\text{Ca}^+$  crystal. The species of dark ions can be identified by exciting collective vibrational modes with an ac voltage applied to electrode 9 and observing a blurring of the  $^{40}\text{Ca}^+$  fluorescence image at the resonance frequency  $\omega_{\text{ax}}$ . [23]. Alternatively, amplitude-modulated resonant laser light is used [24] to determine the charge-to-mass ratio of trapped particles at a precision of better than 0.2%. In order to suppress vibrations of the building and to reduce thermal elongations to a minimum, the complete set-up is located on an air-suspended optical table that is situated in a temperature-stabilized laboratory.

#### 2.4. Extraction mechanism and set-up

Initially, the ion is trapped at the center of electrode 10 by supplying a voltage of 35 V to electrodes 7 and 13 (see also figure 5(a) for a simulation of the trapping potential in the axial direction). However, due to the distance from the electrodes to the trap center, the generated axial trapping potential only features a depth of about 4 eV, not representing a large barrier during the extraction process. The extraction process is then initiated by increasing the dc voltages on electrodes 9 and 10 to 500 V within a few tens of nanoseconds. The extraction voltage generates a repulsive potential at the position of the ion, effectively canceling the axial confinement. However, as the ion already gets accelerated by the developing potential during the switching process, the ion does not sense the full potential strength and the effective energy transfer is lessened. In addition, due to the asymmetric voltage configuration, the peak voltage is not at the position of the ion and it is only accelerated by the shoulder of the generated potential, reducing the kinetic energy even further. From a time-of-flight analysis, one can deduce a final kinetic energy of about 80 eV for the extracted  $^{40}\text{Ca}^+$  ions [20].

Figure 3 shows a schematic drawing of the extraction set-up. After a specified number of ions has been loaded into the trap (in this case, a linear ion crystal consisting of four  $^{40}\text{Ca}^+$  ions), the extraction process is triggered via a computer-controlled TTL signal that is fed in a phase synchronization circuit (phase delay trigger). The phase synchronization circuit delays the TTL signal such that a constant delay to the next zero crossing of the trap drive frequency  $\Omega$  is ensured as the synchronization is crucial in order to minimize shot-to-shot fluctuations of the velocity and position of the extracted ions. The measured delay time shows a  $1\sigma$ -spread of 0.34 ns. The switching of the extraction voltage<sup>10</sup> is experimentally realized by two high voltage switches<sup>11</sup>, which can switch voltages of up to 4 kV within a time span of 20 ns. However, as the extraction voltage leads to a temporary charging of the trap, the TTL trigger signal is supplied for only a few milliseconds to the high-voltage switches, reducing the unintentional charging to a minimum.

The detection of the extracted ions is then performed via an electron multiplier tube (EMT)<sup>12</sup> with 20 dynodes and a main entrance aperture of 20 mm that can detect positively charged ions with a specified quantum efficiency of about 80% and a specified gain of  $5 \times 10^5$ . Under typical operating conditions, the detector is supplied with a voltage of  $-2.5$  kV, leading to detection signals with a width of 10–15 ns and an amplitude of about 100 mV, which are recorded via an oscilloscope<sup>13</sup>. As already stated in section 2.1, the detector is housed in a separate vacuum chamber with a distance of 287 mm from the trap center.

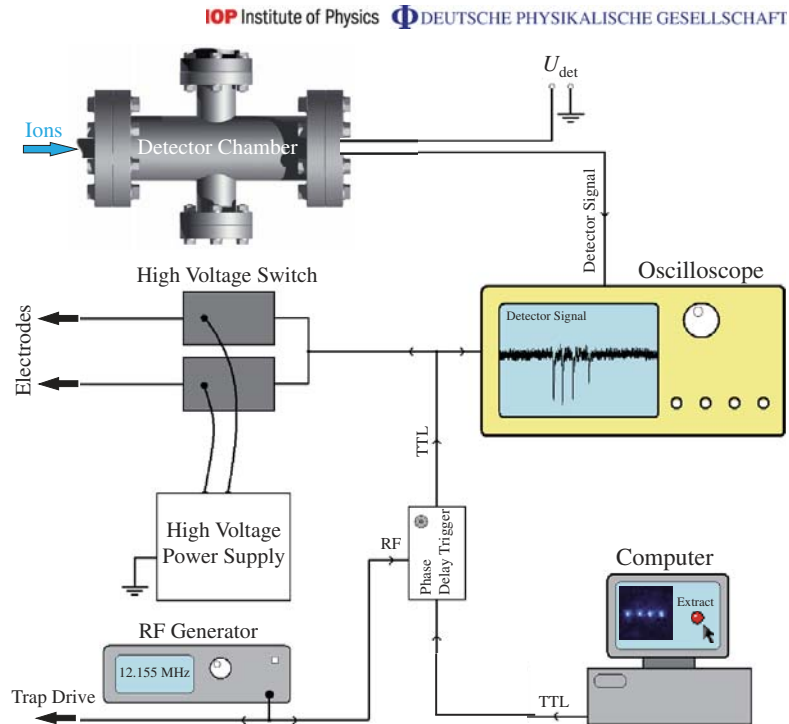
<sup>10</sup> ISEC Inc., model EHQ-8010p.

<sup>11</sup> Behlke Inc., model HTS 41-06-GSM.

<sup>12</sup> ETP Inc., model AF553.

<sup>13</sup> Agilent Infiniium 54832D MSO.

7

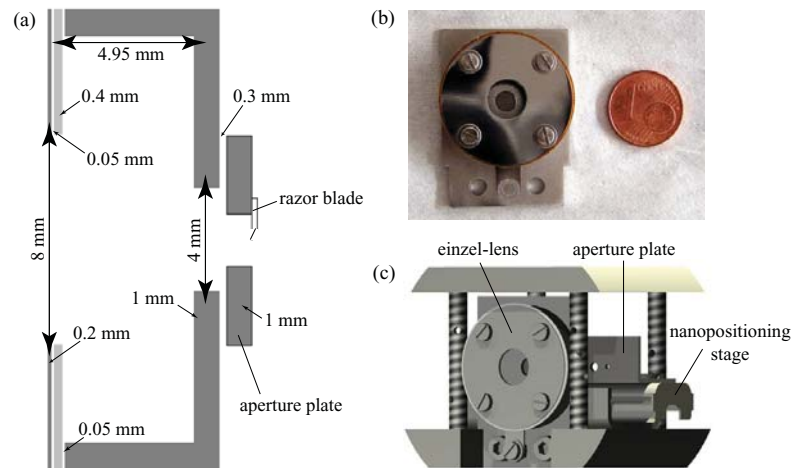


**Figure 3.** Schematic drawing of the extraction set-up. After a certain number of ions have been loaded into the trap, the extraction process is triggered via a TTL signal that is synchronized to the trap drive frequency  $\Omega$  using a phase synchronization circuit (phase delay trigger). Two high-voltage switches then increase the dc voltages on electrodes 9 and 10 to 500 V within a few tens of nanoseconds, leading to the extraction of the trapped ions. Upon entering the detector chamber, the extracted ions are detected using an electron multiplier tube, leading to signal dips on an oscilloscope.

### 2.5. Ion optics

The utilized einzel lens consists of three stainless steel electrodes that feature an outer diameter of 27 mm. The first electrode has a thickness of 0.2 mm with an inner diameter of 8 mm, and the second electrode has a thickness of 0.4 mm and an inner diameter of 8 mm. The third electrode consists of two parts: the first part is a cylindrical-shaped spacer with an inner diameter of 16 mm and a thickness of 4.95 mm, whereas the second part consists of a stainless steel plate with a thickness of 1 mm featuring a 4 mm aperture that is also used as a mounting for all the other electrodes. The first and third electrodes are conductively interconnected, whereas the second electrode is electrically insulated by using Kapton sheets with a thickness of 0.05 mm (see also figure 4(a) for a schematic drawing of the einzel lens). The calculation of the electrostatic

8

IOP Institute of Physics  $\Phi$  DEUTSCHE PHYSIKALISCHE GESELLSCHAFT

**Figure 4.** (a) Schematic drawing of the einzel lens with the dc electrode depicted in light grey and grounded electrodes colored dark grey. The razor blade (depicted in white), which is mounted behind the 2 mm aperture of the movable aperture plate, is also included. (b) Picture of the assembled einzel lens, with a one-cent coin for size comparison. Under typical operating conditions, the dc electrode is supplied with a voltage of 150 V. (c) Schematic drawing of the einzel lens and the nanositioning stage, which are located at the beginning of the detector chamber directly in front of the EMT.

potentials of the einzel lens and the ion ray tracing simulations are performed by a high-accuracy boundary-element solver package [25]. A detailed description of the imaging characteristics for different types of lens configurations can be found in [26].

All parts are electropolished in order to remove ridges that were formed during the manufacturing process and to reduce the overall surface roughness. For electropolishing, we use a solution of phosphoric acid ( $\text{H}_3\text{PO}_4$ ), methanesulfonic acid ( $\text{CH}_3\text{SO}_3\text{H}$ ) and triethanolamine ( $\text{C}_6\text{H}_{15}\text{NO}_3$ ).<sup>14</sup> The parts are polished for a timespan of 15 min at a temperature of 65 °C using an anodic current density of 5 A dm<sup>-2</sup>. Figure 4(b) shows a picture of the assembled einzel lens, with a one-cent coin for size comparison. Under typical operating conditions, the second electrode of the einzel lens is supplied with a voltage of 150 V, whereas the other two electrodes are grounded.

In order to determine the diameter of the single-ion beam, a movable aperture plate is installed between the einzel lens and the detector, featuring hole diameters ranging from 5 mm down to 300  $\mu\text{m}$ . In addition, a razor blade is attached behind the 2 mm aperture, effectively creating a well-defined tearing edge (see also figure 4(a) and section 3.2). The plate is mounted on a nanositioning stage<sup>15</sup>, which allows the aperture plate to be moved with an accuracy of

<sup>14</sup> Patent specification DE102006050317B3.

<sup>15</sup> SmarAct, model SL-2040.

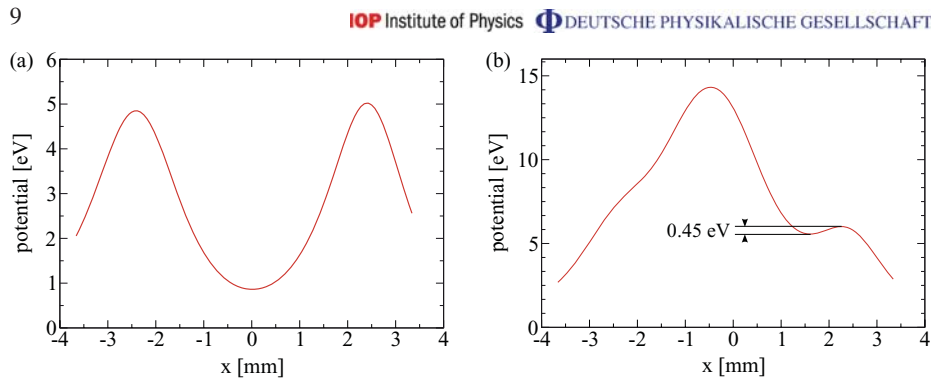


**Figure 5.** (a) Simulated trapping potential in the axial direction. The potential is generated by supplying dc electrodes 7 and 13 with a voltage of 35 V and all the remaining electrodes with 0 V, resulting in an axial trapping frequency  $\omega_{\text{ax.}} = 2\pi \times 280$  kHz and a trap depth of about 4 eV. The center of electrode 10 is used as the point of reference for the axial position. (b) The same potential as in (a) but with a voltage of 54.8 V applied to electrodes 9 and 10, reducing the axial trap depth to about 0.45 eV in order to get rid of the surplus ions.

a few tens of nanometers. An internal sensor module guarantees that the absolute position of the stage is kept constant. Figure 4(c) shows a schematic drawing of the einzel lens and the nanopositioning stage, which are located at the beginning of the detector chamber directly in front of the EMT.

### 3. Experimental results

#### 3.1. Deterministic single-ion loading

In order to reduce the divergence of the ion beam to a minimum, it is necessary to ensure that only one ion is extracted out of the trap with each shot. In the case of a Paul trap, there are, in principle, two options to achieve this goal. The first option is to avoid the loading of more than one ion at a time. Since this is not feasible due to the fact that the number of loaded ions follows a Poissonian distribution for equal loading times, one needs to implement a feedback control in order to stop the ionization after one ion has been loaded into the trap. As it turned out, it was not possible to implement this method in our set-up as the time that elapses between the ionization and crystallization of a one-ion crystal has to be much shorter than the average time between ionization incidents of two different ions. Therefore, we have chosen the second possibility, namely to get rid of the redundant ions after the crystallization process. For this task, we have come up with a very simple and robust procedure that is described next.

To drop the surplus ions, we exploit the potential shaping capabilities offered by our segmented linear rail trap (see also section 2.2). At the beginning, the ions are trapped above electrode 10 by supplying a voltage of 35 V to electrodes 7 and 13, leading to an axial trapping potential with a trap depth of about 4 eV (see also figure 5(a)). By using the offset input of our high-voltage switches (see also section 2.4), the voltage supplied to electrodes 9 and 10 is

linearly ramped up from 0 to 54.8 V within a timespan of about 50 ms before it is again linearly reduced to 0 V after a waiting time of 200 ms. As a consequence, the depth of the axial trapping potential is reduced to about 0.45 eV, thus becoming shallow enough that only one ion will remain inside the trap (see also figure 5(b)). In order to determine the reproducibility of our method, we repeated the procedure described above with ion crystals of various sizes, yielding a total efficiency of 96.7(7)% for reducing the amount of ions to exactly one. By means of this approach, it is also possible to reduce the number of ions in the chain to an arbitrary predefined quantity, e.g. from 5 to 4 ions, but since this is not used for the experiments below, we do not discuss it any further.

### 3.2. Experimental determination of the spot size

In former measurements, we determined the size of our ion beam by shooting single ions through the 300  $\mu\text{m}$  aperture, yielding a spot radius of  $83^{(+8)}_{(-3)} \mu\text{m}$  and a full-angle beam divergence of 600  $\mu\text{rad}$  at a distance of 257 mm from the trap center [20]. Here, 68.3% of all detected ions were located inside the stated spot radius. However, in order to compare these values with our current measurements, we converted them according to equation (1), resulting in a  $1\sigma$ -spot radius of  $55^{(+5)}_{(-2)} \mu\text{m}$ . To further improve the resolution of our single-ion beam, we installed an einzel lens between the trap and the detector (see also section 2.5). In order to obtain an optimal alignment with respect to the optical axis of the einzel lens, the radial adjustment of the ion beam is performed by utilizing the deflection electrodes of our segmented rail trap. Using the 1 mm aperture behind the einzel lens, the optimal deflection voltages are retrieved by gradually changing them, maximizing the hit rate on the detector. As it turns out, the hit rate is very sensitive to changes of the deflection and compensation voltages, i.e. a minor change in the range of a few millivolts is already sufficient to miss the 1 mm aperture, effectively reducing the measured hit rate to zero. Hence, to keep adjacent measurements consistent with each other, all the measurements presented were conducted with a fixed set of deflection and compensation voltages.

In order to determine the spot size of the ion beam in the focal plane of the installed ion optics, we utilize the aforementioned razor blade that is mounted behind the 2 mm aperture (see also section 2.5). By moving the razor blade stepwise into the path of the generated single-ion beam, a gradual cut-off of the ion trajectories is achieved, leading to a reduction in the overall hit rate on the detector. To derive the  $1\sigma$ -spot radius, these points are then fitted with an error function, which itself is obtained by integrating a Gaussian distribution that will be assumed for the radial cross-section of the single-ion beam:

$$f(x) = \int_{-\infty}^x \frac{c}{\sigma \sqrt{2\pi}} \exp\left[-\frac{1}{2} \left(\frac{y-a}{\sigma}\right)^2\right] dy = \frac{c}{2} \left(1 + \operatorname{erf}\left(\frac{x-a}{\sigma \sqrt{2}}\right)\right). \quad (1)$$

Here,  $\sigma$  denotes the radius of the ion beam with  $a$  being the offset in the  $x$ -direction. The parameter  $c$  is used as a scaling factor in order to account for the detector efficiency, which has been experimentally measured to be 0.87 [20]. As the timespan needed for doing a single measurement is considerably long ( $\approx 3$  incidents per minute), we had to reduce the number of measurements taken for each blade position to a total of ten individual shots. This was done in order to avoid changes in the deflection and compensation voltages, which would have been necessary to counteract long-term drifts caused by a thermal expansion of the trap.

11

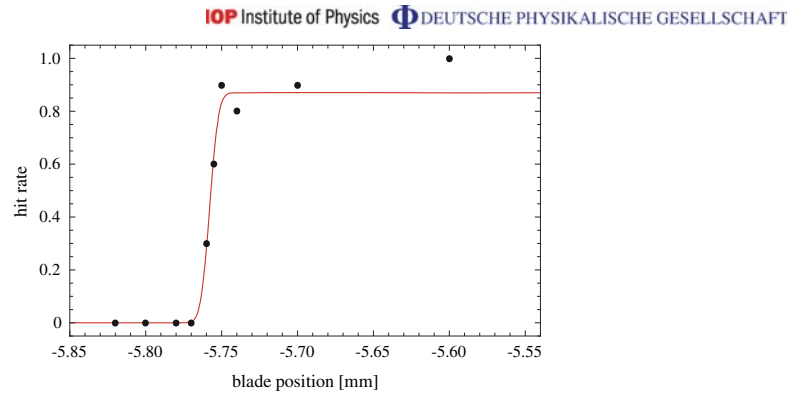


**Figure 6.** Experimental determination of the spot size. The graph shows the hit rate for single ions as a function of the blade position for a lens voltage of 150 V, resulting in a  $1\sigma$ -spot radius of  $(4.6 \pm 1.3) \mu\text{m}$ .

Because the exact focal distance of our einzel lens is unknown, one would normally have to repeat the measurement described above for different spacings between the einzel lens and the razor blade. However, as our nanopositioning stage is only capable of moving perpendicular to the ion beam, the location of the focal plane of the einzel lens has to be adjusted by changing the lens voltage. Measuring the spot radius for different lens voltages in the plane of the razor blade, therefore, should allow for obtaining the minimal spot radius. In the experiment, we have measured a  $1\sigma$ -spot radius of  $(4.6 \pm 1.3) \mu\text{m}$  for a lens voltage of 150 V (see also figure 6). Compared to the original beam diameter, our einzel lens is thus capable of focusing the single-ion beam by a factor of 12.

Numerical simulations predict that an even higher resolution should be feasible. In the case of ground-state cooled ions with a temperature of  $100 \mu\text{K}$ , simulations predict a  $1\sigma$ -spot radius of 1 nm, which is enlarged to 45 nm for a temperature of 2 mK. However, in the experiment, additional deflection voltages are needed in order to align the ion beam with respect to the optical axis of the utilized einzel lens. Including these deflection voltages in the numerical simulations leads to a further decline in resolution, resulting in a  $1\sigma$ -spot radius of about 270 nm. Only taking into account a spatial displacement of the incident ion beam in the principal plane of the lens, numerical simulations predict that a mismatch of  $520 \mu\text{m}$  with respect to the optical axis is already sufficient in order to obtain a spot size of  $4.6 \mu\text{m}$  in the focal plane of the lens (see also figure 7). In the case of our experiment, this displacement is caused by a mechanical misalignment of the center of the aperture with respect to the optical axis of the einzel lens, as well as a displacement of the ion beam itself within the 1 mm aperture. The former can be ascribed to manufacturing imperfections, which are estimated to be about  $200 \mu\text{m}$ . The latter is caused by the initial adjustment of the ion beam using the 1 mm aperture. By taking into account the original beam diameter, a displacement of less than  $400 \mu\text{m}$  can be assumed. Hence, both errors result in a maximum total deviation of  $600 \mu\text{m}$ , explaining the numerically predicted mismatch. A more compact experimental set-up as compared with the total length of about 260 mm (see figure 1) is envisioned for the future.

12

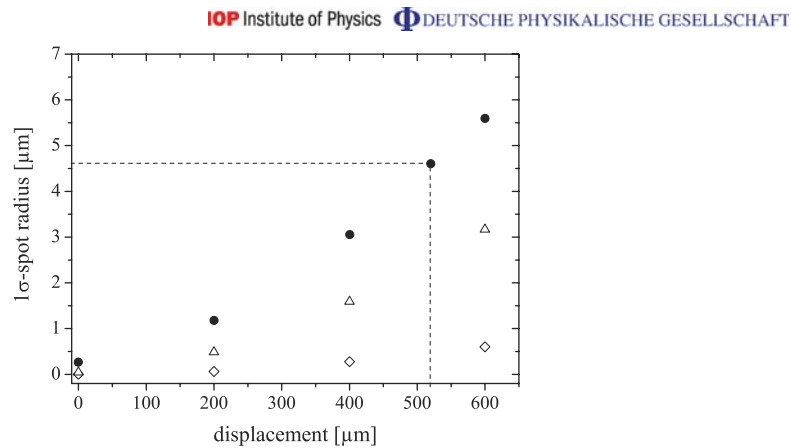


**Figure 7.** Simulated  $1\sigma$ -spot radii as a function of the spatial displacement of the ion beam in the principal plane of the lens. The radii were calculated for an initial ion temperature of 2 mK with (●) and without (△) deflection voltages as well as for an initial ion temperature of 100  $\mu\text{K}$  without deflection voltages (◇). In order to explain the experimentally measured  $1\sigma$ -spot radius of 4.6  $\mu\text{m}$  for 2 mK laser-cooled ions, a displacement of half a millimeter is already sufficient (dashed lines). Note that the initial ion temperature and deflection voltages for the simulated dataset (●) match the experimental conditions, whereas the spatial displacement was not determined experimentally.

#### 4. Conclusion and outlook

Using a segmented linear Paul trap as a deterministic point source for laser-cooled ions, we have demonstrated the focusing of an ion beam consisting of single  $^{40}\text{Ca}^+$  ions to a spot size of a few micrometers. By utilizing the potential shaping capabilities of our ion trap, we were able to deterministically load a predetermined number of ions, which will allow for further automatization of the loading and extraction procedure, resulting in orders of magnitude increased repetition rates. In future experiments, efforts will be made to avoid the usage of the deflection electrodes by aligning the beam mechanically and to implement more sophisticated cooling techniques like side band or EIT cooling in order to reduce the divergence of the ion beam. Moreover, the utilized nanopositioning stage will be exchanged for a modular set-up consisting of three independent stages in order to move apertures and substrates in all three spatial directions. The additional degrees of freedom will not only allow for a more precise alignment with respect to the optical axis of the einzel lens but also allow us to determine the optimal focal length and spot size more accurately. Using two perpendicular edges of the substrate in the same way as the razor blade will then allow for approaching a specific location on the substrate relative to the corner formed by the two edges. Alternatively, one could think of mounting the einzel lens on the tip of an AFM, thus allowing for determining the implantation position with respect to potential surface structures [21]. A new lens design, which is currently in development, will facilitate better focusing of the single-ion beam and additionally allow for

post-accelerating the extracted ions in order to reach higher implantation energies of a few keV, i.e. improving the conversion efficiency for the generation of color centers in diamond [27]. Due to the high spatial and temporal resolution of the focused single-ion beam, one might also consider shooting ions from one ion trap into another. This would allow us to transport quantum information stored in the internal, electronic states of the ions much more quickly and over larger distances than currently possible when performing standard ion transport in multi-segmented micro ion traps.

### Acknowledgments

We acknowledge the financial support of the Landesstiftung Baden–Württemberg in the framework of ‘Atomics’ (contract no. PN 63.14) and the excellence program.

### References

- [1] Gurudev Dutt M V, Childress L, Jiang L, Togan E, Maze J, Jelezko F, Hemmer P R, Zibrov A S and Lukin M D 2007 Quantum register based on individual electronic and nuclear spin qubits in diamond *Science* **316** 1312
- [2] Neumann P, Mizuochi N, Rempp F, Hemmer P, Watanabe H, Yamasaki S, Jacques V, Gaebel T, Jelezko F and Wrachtrup J 2008 Multipartite entanglement among single spins in diamond *Science* **320** 1326
- [3] Kane B E 1998 A silicon-based nuclear spin quantum computer *Nature* **393** 133
- [4] Greentree A D, Fairchild B A, Hossain F M and Prawer S 2008 Diamond integrated quantum photonics *Mater. Today* **11** 22
- [5] Shinada T, Koyama H, Hinshita C, Imamura K and Ohdomari I 2002 Improvement of focused ion-beam optics in single-ion implantation for higher aiming precision of one-by-one doping of impurity atoms into nano-scale semiconductor devices *Japan. J. Appl. Phys.* **41** L287
- [6] Persaud A, Park S J, Liddle J A, Rangelow I W, Bokor J, Keller R, Allen F I, Schneider D H and Schenkel T 2004 Quantum computer development with single ion implantation *Quantum Inf. Process.* **3** 233
- [7] Mitic M *et al* 2005 Single atom Si nanoelectronics using controlled single-ion implantation *Microelectron. Eng.* **78–79** 279
- [8] Batra A, Weis C D, Reijonen J, Persaud A, Schenkel T, Cabrini S, Lo C C and Bokor J 2007 Detection of low energy single ion impacts in micron scale transistors at room temperature *Appl. Phys. Lett.* **91** 193502
- [9] Shinada T, Kurosawa T, Nakayama H, Zhu Y, Hori M and Ohdomari I 2008 A reliable method for the counting and control of single ions for single-dopant controlled devices *Nanotechnology* **19** 345202
- [10] O’Brien J L, Schofield S R, Simmons M Y, Clark R G, Dzurak A S, N J, Curson Kane B E, McAlpine N S, Hawley M E and Brown G W 2001 Towards the fabrication of phosphorus qubits for a silicon quantum computer *Phys. Rev. B* **64** 161401
- [11] Schofield S R, Curson N J, Simmons M Y, Ruess F J, Hallam T, Oberbeck L and Clark R G 2003 Atomically precise placement of single dopants in Si *Phys. Rev. Lett.* **91** 136104
- [12] Ruess F J, Oberbeck L, Simmons M Y, Goh K E J, Hamilton A R, Hallam T, Schofield S R, Curson N J and Clark R G 2004 Toward atomic-scale device fabrication in silicon using scanning probe microscopy *Nano. Lett.* **4** 1969
- [13] Pok W, Reusch T C G, Scappucci G, Rueb F J, Hamilton A R and Simmons M Y 2007 Electrical characterization of ordered Si:P dopant arrays *Trans. IEEE. Nanotechnol.* **6** 213
- [14] Ruess F J, Pok W, Reusch T C G, Butcher M J, Goh K E J, Scappucci G, Hamilton A R and Simmons M Y 2007 Realization of atomically controlled dopant devices in silicon *Small* **3** 563
- [15] Greiner A, Sebastian J, Rehme P, Aghajani-Talesh A, Griesmaier A and Pfau T 2007 Loading chromium atoms in a magnetic guide *J. Phys. B: At. Mol. Phys.* **40** F77

14

IOP Institute of Physics  $\Phi$  DEUTSCHE PHYSIKALISCHE GESELLSCHAFT

- [16] Hill S B and McClelland J J 2003 Performance of a feedback-controlled, deterministic source of single chromium atoms *J. Opt. Soc. Am. B* **21** 473
- [17] Hanssen J L, McClelland J J, Dakin E A and Jacka M 2006 Laser-cooled atoms as a focused ion-beam source *Phys. Rev. A* **74** 063416
- [18] Hanssen J L, Hill S B, Orloff J and McClelland J J 2008 Magneto-optical-trap-based, high brightness ion source for use as a nanoscale probe *Nano Lett.* **8** 2844
- [19] Meijer J *et al* 2006 Concept of deterministic single ion doping with sub-nm spatial resolution *Appl. Phys. A* **83** 321
- [20] Schnitzler W, Linke N M, Fickler R, Meijer J, Schmidt-Kaler F and Singer K 2009 Deterministic ultracold ion source targeting the Heisenberg limit *Phys. Rev. Lett.* **102** 070501
- [21] Meijer J *et al* 2008 Towards the implanting of ions and positioning of nanoparticles with nm spatial resolution *Appl. Phys. A* **91** 567
- [22] Huber G, Deuschle T, Schnitzler W, Reichle R, Singer K and Schmidt-Kaler F 2008 Transport of ions in a segmented linear Paul trap in printed-circuit-board technology *New J. Phys.* **10** 013004
- [23] Naegerl H, Blatt R, Eschner J, Schmidt-Kaler F and Leibfried D 1998 Coherent excitation of normal modes in a string of  $\text{Ca}^+$  ions *Opt. Express* **3** 89
- [24] Drewsen M, Mortensen A, Martinussen R, Staunum P and Sørensen J L 2004 Nondestructive identification of cold and extremely localized single molecular ions *Phys. Rev. Lett.* **93** 243201
- [25] Singer K, Poschinger U, Murphy M, Ivanov P, Ziesel F, Calarco T and Schmidt-Kaler F 2009 Colloquium: experiments with atomic quantum bits—essential numerical tools [arXiv:0912.0196](https://arxiv.org/abs/0912.0196)
- [26] Fickler R, Schnitzler W, Linke N M, Schmidt-Kaler F and Singer K 2009 Optimized focusing ion optics for an ultracold deterministic single ion source targeting nm resolution *J. Mod. Opt.* **56** 2061
- [27] Jelezko F and Wrachtrup J 2006 Single defect centres in diamond: a review *Phys. Status Solidi a* **203** 3207



**Transport of ions in a segmented linear Paul trap in printed-circuit-board  
technology**

---

G. Huber, T. Deuschle, W. Schnitzler, R. Reichle, K. Singer and F. Schmidt-Kaler

Published on 14th January 2008 in the scientific journal:

**New Journal of Physics**

(Volume: 10 / Page: 013004 / Year: 2008)

# New Journal of Physics

The open-access journal for physics

## Transport of ions in a segmented linear Paul trap in printed-circuit-board technology

G Huber<sup>1</sup>, T Deuschle, W Schnitzler, R Reichle, K Singer  
and F Schmidt-Kaler

Institut für Quanteninformationsverarbeitung, Universität Ulm,  
Albert-Einstein-Allee 11, D-89069 Ulm, Germany  
E-mail: [gerhard.huber@uni-ulm.de](mailto:gerhard.huber@uni-ulm.de)

*New Journal of Physics* **10** (2008) 013004 (15pp)

Received 5 October 2007

Published 14 January 2008

Online at <http://www.njp.org/>

doi:10.1088/1367-2630/10/1/013004

**Abstract.** We describe the construction and operation of a segmented linear Paul trap, fabricated in printed-circuit-board technology with an electrode segment width of  $500\ \mu\text{m}$ . We prove the applicability of this technology to reliable ion trapping and report the observation of Doppler-cooled ion crystals of  $^{40}\text{Ca}^+$  with this kind of trap. Measured trap frequencies agree with numerical simulations at the level of a few percent from which we infer a high fabrication accuracy of the segmented trap. To demonstrate its usefulness and versatility for trapped ion experiments we study the fast transport of a single ion. Our experimental results show a success rate of 99.0(1)% for a transport distance of  $2 \times 2\ \text{mm}$  in a round-trip time of  $T = 20\ \mu\text{s}$ , which corresponds to 4 axial oscillations only. We theoretically and experimentally investigate the excitation of oscillations caused by fast ion transports with error-function voltage ramps: for a slightly slower transport (a round-trip shuttle within  $T = 30\ \mu\text{s}$ ) we observe non-adiabatic motional excitation of 0.89(15) meV.

<sup>1</sup> Author to whom any correspondence should be addressed.

2

IOP Institute of Physics  $\Phi$  DEUTSCHE PHYSIKALISCHE GESELLSCHAFT**Contents**

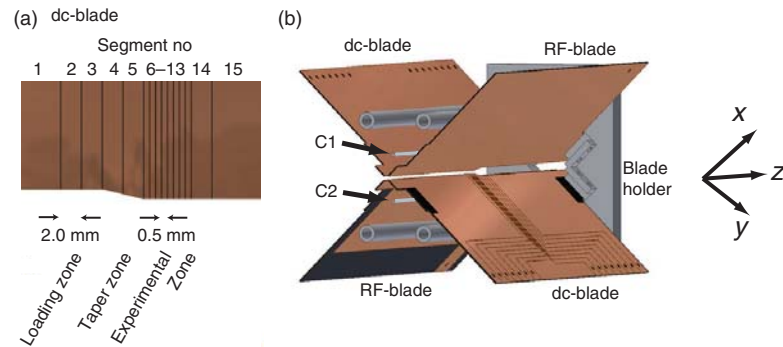
<b>1. Introduction</b>	<b>2</b>
<b>2. Experimental set-up</b>	<b>3</b>
2.1. Design, fabrication and operation of PCB-traps . . . . .	3
2.2. Laser excitation and fluorescence detection . . . . .	4
<b>3. Numerical simulations</b>	<b>5</b>
3.1. Radial confinement . . . . .	5
3.2. Axial confinement . . . . .	6
<b>4. Cold ion crystals</b>	<b>6</b>
4.1. Observation of linear crystals and measurement of trap frequencies . . . . .	6
4.2. Compensation of micromotion . . . . .	7
<b>5. Transport of single ions and ion crystals</b>	<b>9</b>
5.1. Transport probabilities . . . . .	12
5.2. Coherent excitation during transport . . . . .	13
<b>6. Conclusion and outlook</b>	<b>14</b>
<b>Acknowledgments</b>	<b>15</b>
<b>References</b>	<b>15</b>

**1. Introduction**

Three-dimensional (3D) linear Paul traps are currently used for ion-based quantum computing [1]–[4] and high-precision spectroscopy [5]–[7]. An axial segmentation of the dc electrodes in these traps enables the combination of individual traps to a whole array of micro-traps. Structure sizes down to the range of a few tens of micrometres [8, 9] are nowadays in use and mainly limited by fabrication technology. However, most of these fabrication methods require advanced and non-standard techniques of micro-fabrication as is known from micro-electro-mechanical system (MEMS) processing or advanced laser machining. Long turn-around times and high costs are complicating the progress in ion trap development. In this paper, we present a segmented 3D ion trap which is fabricated in UHV-compatible printed-circuit-board (PCB) technology. While with this technology, spatial dimensions of electrodes are typically limited to more than  $100\ \mu\text{m}$ , the production of sub-millimetre sized segments is simplified by the commonly used etching process. The advantages of PCB-traps are therefore a fast and reliable fabrication and consequently a quick turn-around time, combined with low fabrication costs. The feasibility of the PCB-technique for trapping ion clouds in a surface-electrode trap has already been shown in [10]. In future, we anticipate enormous impact of the PCB-technology by including standard multi-layer techniques in the trap design. On a longer timescale on-board electronics may be directly included in the layout of the PCB-boards, e.g. digital-to-analog (DA) converters may generate axial trap control voltages or digital radio frequency (RF)-synthesizers could be used for dynamical ion confinement.

In this paper, we first describe the fabrication of our PCB-trap and the overall experimental set-up in section 2. The following section 3 is dedicated to a comparison of measured trap frequencies with numerical simulations for a characterization of radial and axial trapping. Special attention is paid in section 4 to the compensation of electrical charging effects of the

3

IOP Institute of Physics  $\Phi$  DEUTSCHE PHYSIKALISCHE GESELLSCHAFT

**Figure 1.** Electrode design. (a) Close-up view of the blade design: the dc-blade segment width is 2 mm in the loading and taper zone, and 0.5 mm in the experimental zone. The trap consists of a 4 mm wide loading zone, a tapered intermediate zone, and a 2 mm wide experimental zone. (b) Sketch of the assembled X-trap consisting of four blades, drawn with missing front blade holder for sake of clarity. Compensation electrodes C1 and C2 are parallel to the trap axis.

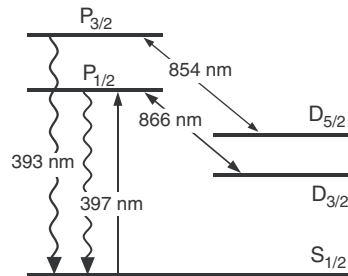
trap electrodes since PCB-technology requires insulating grooves between the electrodes that may limit the performance of the trap. We adjust the compensation voltages to cancel the effect of stray charges and investigate the stability of these compensation voltages over a period of months. Our measurements show that PCB-traps are easy to handle, similar to standard linear traps comprising solely metallic electrodes. In section 5, the segmentation of the dc-electrodes is exploited to demonstrate the transport of a single ion, or a small crystal of ions, along twice the distance of 2 mm in a round-trip shuttle over three axial trap segments. Special attention is given to fast transports within total transport times of  $T = 20\text{--}100\ \mu\text{s}$ , corresponding to only 4–20 times the oscillation period of the ion in the potential. We checked the consistency of the measured data with a simple transport model.

## 2. Experimental set-up

### 2.1. Design, fabrication and operation of PCB-traps

The trap consists of four blades, two of them are connected to a RF supply and the two remaining, segmented blades are supplied with static (dc) voltages, see figure 1. The dc- and RF-blades are assembled normal to each other (the cross-section is X-shaped). In a loading zone, the two opposing blades are at a distance of 4 mm. A tapered zone is included in order to flatten the potential during a transport between the wider loading and the narrower experimental zone. In the latter zone, the distance between the blades is reduced to 2 mm. The material of the blades is a standard polyimide material coated by  $\sim 18\ \mu\text{m}$  of copper on all sides of the substrate. Etched insulation grooves of  $120\ \mu\text{m}$  in the copper define dc-electrodes. The RF-drive frequency near  $\Omega/2\pi = 11.81\ \text{MHz}$  is amplified and its amplitude is further increased

4

IOP Institute of Physics  $\Phi$  DEUTSCHE PHYSIKALISCHE GESELLSCHAFT

**Figure 2.** Energy levels and relevant optical transitions of  $^{40}\text{Ca}^+$ .

by a helical resonator before it is applied to the RF blades. At typical operating conditions, we measure a peak-to-peak voltage of about  $V = 400 V_{pp}$  by using a home-built capacitive divider with a small input capacitance to avoid artificial distortion of the signal by the measurement. The dc-control voltages from a computer card are connected to the trap segments via low-pass RC-filters with corner frequency at 1 MHz. The trap is housed in a stainless steel vacuum chamber with enhanced optical access held by an ion getter and a titanium sublimation pump at a pressure of  $3 \times 10^{-10}$  mbar. This value was reached without bakeout, indicating the UHV-compatibility of the PCB-materials<sup>2</sup>.

## 2.2. Laser excitation and fluorescence detection

The relevant energy levels of  $^{40}\text{Ca}^+$  ions are shown in figure 2. All transitions can be either driven directly by grating stabilized diode lasers, or by frequency doubled diode lasers<sup>3</sup>. The lasers are locked according to the Pound–Drever–Hall scheme to Zerodur Fabry–Perot cavities for long-term frequency stability. Each laser can quickly be switched on and off by acousto-optical modulators. Optical cooling and detection of resonance fluorescence is achieved by simultaneous application of laser light at 397 and 866 nm. Radiation near 854 nm depopulates the  $D_{5/2}$  metastable state (1.2 s lifetime).

Two laser sources at 423 ( $\leq 5$  mW) and 375 nm ( $\leq 1$  mW) are used for photoionization loading of ions [11, 12]. The high loading efficiency allows for a significant reduction of the Ca flux from the resistively heated oven and minimizes the contamination of the trap electrodes. By avoiding the use of electron impact ionization the occurrence of stray charges is greatly suppressed.

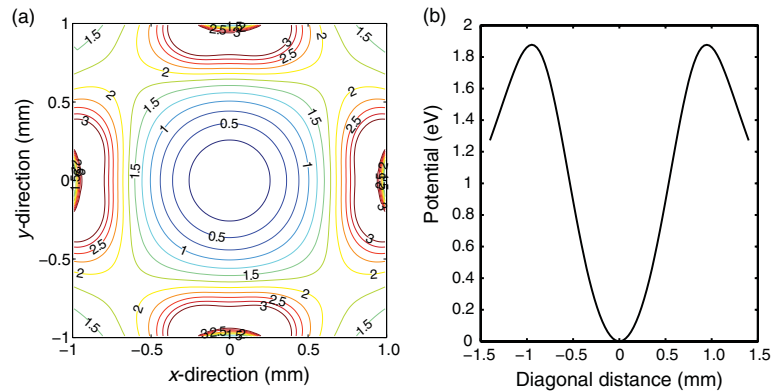
In this experiment, laser beams near 397, 866 and 854 nm are superimposed and focused into the trap along two directions: one of these directions (D1) is aligned vertically under  $5^\circ$  with respect to the top–bottom axis and the other beam (D2) enters horizontally and intersects the trap axis under an angle of  $45^\circ$ . A high-NA lens is placed 60 mm from the trap center behind an inverted viewport to monitor the fluorescence of trapped ions at an angle perpendicular to the trap axis direction. The fluorescence light near 397 nm is imaged on to the chip of an EMCCD camera<sup>4</sup> in order to achieve a photon detection efficiency of about 40%.

<sup>2</sup> Material P97 by Isola, PCB manufacturer (<http://www.micro-pcb.ch>).

<sup>3</sup> Topica DL100, DL-SHG110 and TA100.

<sup>4</sup> Electron multiplying CCD camera, Andor iXon DV860-BI.

5

IOP Institute of Physics  $\Phi$  DEUTSCHE PHYSIKALISCHE GESELLSCHAFT

**Figure 3.** (a) Simulation of the pseudo-potential in the  $(x-y)$ -plane in the experimental zone for  $V = 408 V_{pp}$ . (b) Cross-section through the potential shown in (a) along the  $x = y$ -direction yielding a radial trap frequency of  $\omega_{rad}/2\pi = 663$  kHz and a trapping depth of approx. 1.9 eV.

### 3. Numerical simulations

#### 3.1. Radial confinement

The complex layout of the multi-segmented trap requires elaborate numerical techniques to simulate the electrical potentials accurately in order to avoid artificial effects. Instead of using widespread commercial FEM routines that mesh the whole volume between the electrodes, boundary-element methods (BEM) are more suited but also more complex in their implementation. The effort in such methods is reduced for large-space computations since they only need to mesh surfaces of nearby electrodes and multipole approximations are done to include far distant segments in order to speed up computations. We have written a framework for the solution of multipole-accelerated Laplace problems<sup>5</sup>. This method is not limited in the number of meshed areas and thus allows for accurate calculations with a fine mesh. In the simulations presented here, we typically subdivide the surfaces of the trap electrodes into approx. 29 000 plane areas to determine the charge distributions and the free-space potential within the trap volume numerically. Figure 3(a) shows the calculated pseudo-potential in the  $(x-y)$ -plane of the experimental zone for a RF of  $\Omega/2\pi = 11.81$  MHz and a RF peak-to-peak voltage  $V = 408 V_{pp}$ . By symmetry the diagonal directions along  $x = \pm y$  contain the nearest local maximum and thus determine the relevant trap depth of approx. 1.9 eV for the applied experimental parameters. A cross-section through the pseudo-potential along this direction is shown in figure 3(b) at the same axial position as in figure 3(a). From these simulations, we are able to extract a radial trap frequency of  $\omega_{rad}/2\pi = 663$  kHz in the absence of applied dc potentials.

<sup>5</sup> The solver was developed by the MIT Computational Prototyping Group (<http://www.rle.mit.edu/cpg>).

6

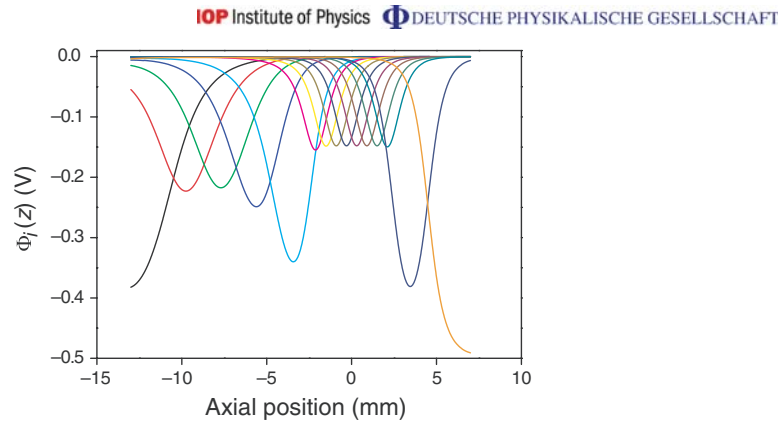


**Figure 4.** Individual axial electrode pair potentials  $\phi_i(z)$ . For detailed description see text in section 3.2. Narrow electrodes show a lower maximum potential due to the smaller amount of surface charges. An arbitrary axial potential is formed by superposing individual contributions.

### 3.2. Axial confinement

For axial confinement opposing dc electrodes are set to the same voltage  $U_i$ ,  $i = 1, \dots, 15$  labeling the electrode number as depicted in figure 1. These voltages are supplied by DA converters covering a voltage range of  $\pm 10$  V with a maximum update rate of 1 MHz. Figure 4 illustrates the potentials  $\phi_i(z)$  obtained when only  $U_i$  is set to  $-1$  V and all other voltages are set to zero. For arbitrary voltage configurations, the axial potential  $\phi(z) = \sum_i U_i \phi_i(z)$  is a linear superposition of the single electrode potentials. Tailored axial potentials for the generation of single or multiple axial wells with given secular frequency, depth and position of the potential minimum are obtained by solving the linear equation given above for the voltages  $U_i$ . Time-dependent voltages are used to move the potential minimum guiding the trapped ion along the trap axis.

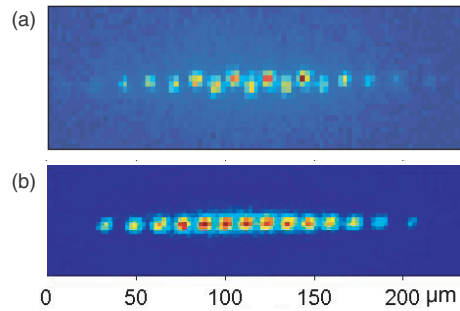
## 4. Cold ion crystals

### 4.1. Observation of linear crystals and measurement of trap frequencies

The trap is operated in the loading configuration with dc voltages of  $U_{\text{load}} = \{\dots, U_7, \dots, U_{13}, \dots\}_{i=0} = \{\dots, 6 \text{ V}, \dots, 8 \text{ V}, \dots\}$  while non-specified segment voltages are held at ground potential. From simulations we estimate that the axial trap frequency is  $\omega_z/2\pi = 199$  kHz at the potential minimum close to the center of electrode 10. Linear strings and single ions crystallize under continuous Doppler cooling with beams D1 and D2, consisting of superimposed beams at 397 (0.3 mW with  $60 \mu\text{m}$  beam waist), 866 and 854 nm (both 3 mW with  $100 \mu\text{m}$  beam waist), cf figure 5.

Applying a sinusoidal waveform with 1 mV amplitude to electrode segment 10 allows for a parametrical excitation near resonance. Observation of the ion excitation through decreasing fluorescence on the EMCCD image signifies a resonance condition. This way,

7

IOP Institute of Physics  $\Phi$  DEUTSCHE PHYSIKALISCHE GESELLSCHAFT

**Figure 5.** (a) Fluorescence of an ion crystal with 14 ions in a zig-zag configuration as observed with the EMCCD camera. Exposure time was set to 100 ms (optical magnification is 10.4). (b) Linear crystal with 14 ions and a slightly more relaxed axial trap frequency than in (a). This induces a phase transition into a purely linear configuration of ion positions.

we experimentally find a radial frequency of  $\omega_{\text{rad}}/2\pi = 700(2)$  kHz and an axial frequency of  $\omega_z/2\pi = 191(2)$  kHz. We attribute the 5% deviations to residual electric fields arising mainly from charging of the etched insulation groove cuts as well as to the limited accuracy of the RF-voltage amplitude measurement. Stable trapping at a  $q$ -value of about 0.16 is achieved. Measuring the mutual distances in a linear two- or three-ion crystal easily allows for calibrating the optical magnification of the imaging optics to be 10.4, with a CCD-pixel size of  $24 \mu\text{m}$ . For determining the resonant frequency of the cycling transition used for Doppler cooling the fluorescence is detected on a photomultiplier tube (PMT) while scanning the laser frequency at 397 and/or 866 nm. This yields an asymmetric line profile of about 30–50 MHz FWHM, exhibiting the features of a dark resonance with a maximum count rate of 20 kHz. For all following measurements we keep the detuning of the 397 nm laser at  $\Gamma/2$  (half of the linewidth) fixed and adjust the frequency of the 866 nm laser to obtain a maximum fluorescence rate.

#### 4.2. Compensation of micromotion

Ions in small traps are likely to be affected by stray charges that shift the ions out of the RF null since those charges can often not be neglected in most ion traps. Therefore, the dynamics of ions in general exhibits a driven micromotion oscillation at a frequency of  $\Omega/2\pi$  leading to a broadening of the Doppler cooling transition and higher motional excitation [13]. A second disadvantage of micromotion is a reduced photon scattering rate at the ideal laser detuning of  $\Gamma/2$ . To correct for potentials induced by stray charges and maybe geometric imperfections we can apply compensation voltages to the electrodes labeled C1 and C2, as sketched in figure 1(b).

For detecting the micromotion we trigger a counter with a photon event measured by the PMT in the experimental zone and stop the counter by a TTL phase locked to half the trap drive frequency  $\Omega/2\pi$ . If the ion undergoes driven motion, the fluorescence rate is modulated as a cause of a modulated Doppler line shape, see figure 6(a). Here, we detect the ion motion

8

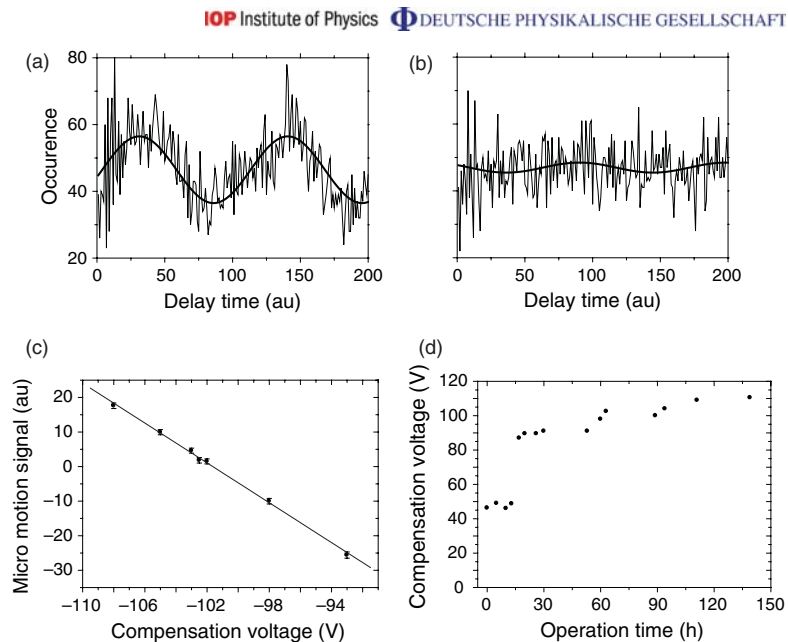


**Figure 6.** Histogram of photon count events for different values of micromotion compensation voltages: (a) Trace far from compensation with  $U_{C1} = 98$  V fitted to a sine function. (b) Near to optimum compensation with  $U_{C1} = 102.5$  V. (c) The amplitude of a sinusoidal fit for different compensation voltages shows a linear dependence between the amplitude and applied compensation. Negative amplitudes correspond to a  $180^\circ$  phase flip; this happens when the ion passes the RF null. A linear fit reveals the optimal value at  $U_{C1} = 101.6$  V. With this data an optimal compensation is determined within an uncertainty of less than 0.3 V. The overall data collection time is less than 5 min. (d) Optimum compensation voltage plotted versus the operation time of the oven. We attribute the long-term drift of this voltage to an increasing calcium contamination on the trap electrodes in the experimental zone.

in the direction of the laser beam. If a flat histogram is measured the ion does not possess a correlated motion with the RF driving voltage. Then, it resides close to the RF null where the modulation vanishes, cf figure 6(b). From taking a series of histograms for different values of the compensation voltage a linear relation between observed modulation and applied compensation is obtained. The optimal compensation voltage can then be read from the abscissa for zero correlation amplitude, figure 6(c).

Our long-term observation of the optimum compensation voltage indicates a weak increase over three months. Since we did not bakeout the vacuum chamber, storage times of ions are several minutes so that we needed to reload ions from time to time. During all experimental sessions, we kept the temperature of the oven fixed so that the flux of neutral Ca atoms was

sustained. This is not necessary in a better vacuum environment. An oven current of 7 A leads to a flux such that we reach a high loading rate of 0.1–0.4 ions per second. Thus, by operating the oven continuously we could accumulate a long operation time of over 150 h. The 20% step in figure 6(d) was caused by a power failure.

By comparing our measurements to the long-term recording of [14] for a 2 mm linear trap [15] with stainless steel electrodes we find similar drifts in compensation voltages. Thus, it seems that PCB-traps can be corrected equally well for micromotion so that the larger insulation grooves do not harm the performance.

In all of the experiments presented here the beam of neutral calcium is directed into the narrow experimental zone where micromotion is compensated as described above. In future, however, we plan to use the loading zone where a higher loading rate through the larger involved phase space during trapping is expected. Then, ions can be shuttled into the cleaner experimental zone 8 mm apart. Calcium contamination will then be completely avoided and much lower compensation voltages and drifts are expected. The segmented PCB-trap operated this way may even show an improved micromotion compensation stability as compared to traditional linear and 3D traps having less insulation exposed to the ions.

### 5. Transport of single ions and ion crystals

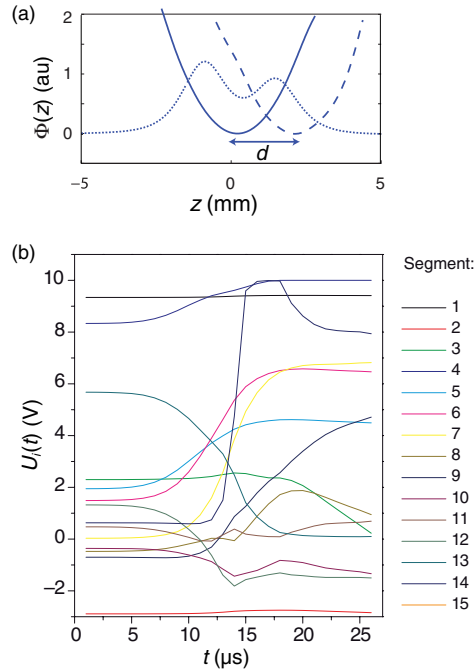
As recently suggested [16], ions in a future quantum computer based on a segmented linear Paul trap might be even shuttled through stationary laser beams to enable gate interactions. In a different approach, one might shuttle ions between the quantum logic operations [17]. This would alleviate more complex algorithms and reduce the enormous technological requirements extensively. According to theoretical investigations [18], transport could occupy up to 95% of operation time in realistic algorithms. Given the limited coherence time for qubits, shuttling times need therefore to be minimized. Our work as described below may be seen in the context of the theoretical and experimental works found in [19]–[21]. With our multi-segmented Paul trap, we have made first investigations of these speed limits in order to enter the non-adiabatic regime and studied the corresponding energy transfer. Preferred transport ramps are theoretically well understood [22]. The current challenge arises from experimental issues, i.e. how accurate potentials can be supplied, how drifts in potentials can be avoided and whether sophisticated shuttling protocols can be used [23]. First transport studies have been made some years ago by the Boulder group using an extremely sparse electrode array [24]. Non-adiabatic transports of cold neutral atom clouds in a dipole trap have been demonstrated in [25] and show very similar qualitative behavior, even though on a completely different timescale (axial frequency of approx.  $2\pi \times 8$  Hz).

The PCB-trap described here contains 15 pairs of dc-segments. Using a suitable time sequence of control voltages  $U_i(t)$ ,  $i = 1, \dots, 15$ , the axial potential can be shaped time-dependently in a way to transport ions along the trap axis. In the following, we present the results of various transport functions for a distance of  $2d = 4$  mm.

For these measurements, we follow a six-step sequence:

- 1) Initially, we confine an ion in an axial trapping potential in the loading configuration  $U_{\text{load}}$ , figure 7(a). The single ion is laser cooled by radiation near 397 and 866 nm. Compensation voltages have previously been optimized for this trap configuration such that the width of the excitation resonance near 397 nm is minimal. Then, the laser beams are switched off.

10

IOP Institute of Physics  $\Phi$  DEUTSCHE PHYSIKALISCHE GESELLSCHAFT

**Figure 7.** (a) Axial potentials for loading and observing ions (dotted line)  $U_{\text{load}}$ , at the beginning (solid line) of the transport with  $U_{\text{trans}}(t=0) = \{-8.77, 9.34, -2.89, 2.30, 8.33, 1.95, 1.49, 0.03, -0.48, -0.70, -0.36, 0.47, 1.32, 5.68, 0.63\}$  V and at its turning point (dashed line). (b) Trap control voltages  $U_1$  to  $U_{15}$  for transporting the ion by an error function ramp. Discontinuities in the curves result from the time discretization in steps of  $1 \mu\text{s}$ .

- 2) Before starting the transport,  $U_{\text{load}}$  is linearly changed into the initial transport potential  $U_{\text{trans}}(t=0)$  in 10 steps each taking  $1 \mu\text{s}$ . Note that the transport potential should be adapted in shape and depth, and is not necessarily identical to the optimum potential for laser excitation, for fluorescence observation, and for quantum logic gate operations. In our case, the axial trap frequency for  $U_{\text{trans}}(t=0)$  is adjusted for  $\omega_z/2\pi = 200 \text{ kHz}$ , and the minimum positions of  $U_{\text{load}}$  and  $U_{\text{trans}}$  both coincide with the center of segment 10. The voltages for the transport potential are chosen according to the regularization of [22].
- 3) By changing the control voltages such that the potential minimum of  $U_{\text{trans}}$  moves according to an error function, the ion is accelerated and moved to a turning point 2 mm away, centered roughly above segment 13.
- 4) The ion is accelerated back to the starting point again using the same time-inverted waveforms. By our calculations, we aim to determine the control voltages such that the ion always remains within a harmonic potential well of constant frequency  $\omega_z$  throughout the whole transport procedure.

11

IOP Institute of Physics  $\Phi$  DEUTSCHE PHYSIKALISCHE GESELLSCHAFT

- 5) Finally, the transport potential  $U_{\text{trans}}$  is ramped back linearly in  $10 \mu\text{s}$  into the initial potential  $U_{\text{load}}$ .
- 6) The laser radiation is switched on again to investigate either the success probability of the transport or the motional excitation of the ion.

The sequence is repeated about  $10^3$ – $10^5$  times, then the parameters of the transport ramp in step (3) and (4) are changed and the scheme is repeated.

Ideally, we would create an axial potential that closely approximates  $\phi(z, t) = m\omega_z^2(z - z_0(t))^2/2q$  with an explicit time-dependent position of the potential minimum  $z_0(t)$ . However, all presented simulations and motional excitation energies were deduced from the numerical axial potentials instead. Moving the potential minimum from its starting point  $z_0(0) = 0$  to the turning point  $z_0(T/2) = 2 \text{ mm}$  and back again to  $z_0(T) = 0$  leads to a drag on the trapped ion. For sake of convenience, we express the total time for a round-trip  $T$  in units of the trap period  $\tau \equiv T\omega_z/2\pi$ . The dimensionless parameter  $\tau$  then denotes the number of oscillations the ion undergoes in the harmonic well during the transport time. The functional form of the time-dependent position of the potential minimum  $z_0(t)$  is crucial for the transport success and the motional excitation. We have chosen a truncated error-function according to

$$f_\sigma(t) = \frac{d}{2} \left( 1 + \frac{\text{Erf}[(4t/T - 1)\sigma]}{\text{Erf}[\sigma]} \right), \quad z_0(t) = \begin{cases} f_\sigma(t), & 0 \leq t \leq T/2, \\ d - f_\sigma(T - t), & T/2 < t \leq T, \end{cases} \quad (1)$$

as input to find the waveforms of all contributing electrode pairs, figure 7(b).

Small first and second derivatives at the corner points assure that the ion experiences only smoothly varying accelerations at these times. The parameter  $\sigma$  determines the maximum slope of the function. The smoother the shuttling begins the higher average and maximum velocities are needed for a fast transport. A high maximum velocity  $\dot{z}_0$  results in far excursions of the ion from the potential minimum so that it may experience higher derivatives not fulfilling the harmonic potential approximation anymore. A compromise can be found between slowly varying corner point conditions and ion excitation due to fast, non-adiabatic potential movements. Experimentally, we found the lowest energy accumulated for  $\sigma = 2.3$ . In our experiment, the update time of the supply hardware for the electrode voltages is limited to  $1 \mu\text{s}$ . To account for this effect in our simulations we also discretize  $z_0(t)$  in time steps. These discontinuities are evident in figure 7(b) already indicating that a higher sampling rate of the DA channels would be desirable. Furthermore, for short shuttles the amplitude discretization through the DA converters makes an exact reproduction of  $z_0(t)$  impossible. This gives rise to discrete dragging forces transferring motional excess energy to the ion. We verified by numerical simulations that even for the fastest transports with durations of only  $T \approx 10$ – $12 \mu\text{s}$ , deviations from the non-discretized time evolution were negligible. Since in our case, the typical involved motional energies are much larger than  $\hbar\omega$ , a simple classical and one-dimensional model of the ion transport is justified with the equation of motion

$$\ddot{z}(t) = -\frac{q}{m} \frac{d\phi(z, t)}{dz} = -\omega^2(z - z_0(t))^2. \quad (2)$$

We solve this equation numerically for functions  $z_0(t)$  with varying  $\sigma$ . The resulting phase space trajectories  $\{z(t), \dot{z}(t)\}$  are plotted in figure 8 for  $T = 20 \mu\text{s}$  ( $\tau = 4$ ) and  $T = 16 \mu\text{s}$  ( $\tau = 3.2$ ). In the first case, the phase space trajectory starts and ends close to  $\{0,0\}$ , i.e. both the potential and the kinetic energy are modest after the transport. In the second case, the particle reaches

12

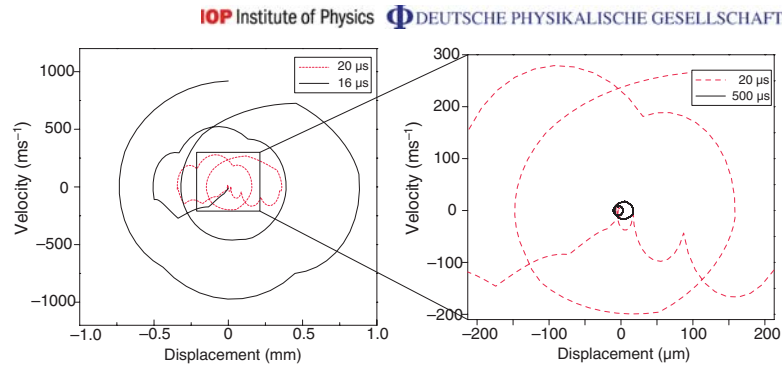


**Figure 8.** Phase space trajectories of an ion for two different transport durations. The closed loop (dotted line,  $\tau = 4$ ) indicates a transport with low final motional energy. For  $\tau = 3.2$  (dashed line) the ion does not reach zero velocity at  $t = T$  and a final energy of 171 meV. Discontinuities in the trajectories result from the time discretization in steps of  $1 \mu\text{s}$ .

its starting point  $z_0(T) = z(0)$  again, but resides with a high oscillating velocity  $\dot{z}(T)$  but small displacement.

### 5.1. Transport probabilities

This section addresses the question of how fast the transport of an ion in the manner described above can eventually be performed before it gets lost. In the following, we discuss transports in the adiabatic regime  $\tau \gg 1$  and far off this regime. For the measurements, an experimental sequence with transport duration  $\tau$  is interleaved by Doppler cooling cycles of 1 s duration to ensure to start always from the same initial energy close to the Doppler limit. After  $n_i$  successful transports with  $i = 1, \dots, N$ , the ion may finally be lost. After 100–1000 repetitions, we bin the data into a histogram of  $n_i$  approximating the success probability  $P_\tau(n)$  that allows for deduction of the fraction of ions having performed at least  $n$  successful transports.  $P_\tau(n)$  is fitted to an exponential decay introducing the single transport success probability  $\tilde{p}_\tau$ ,  $P_\tau(n) = (\tilde{p}_\tau)^n$ . The probability for  $n$  successful transports equals  $(\tilde{p}_\tau)^n$  as the processes are independent with a sufficiently long Doppler cooling period. To account for other sources of ion loss, e.g. from background gas collisions, a loss rate without transport in sequence steps (3) and (4) was subtracted. These losses can be modeled by introducing a second decay channel in  $P_\tau(n)$  to finally yield net transport probabilities  $p_\tau$ .

Figure 9 depicts values  $p_\tau$  for different transport durations  $\tau$  performed with a transport function  $z_0(t)$  according to equation (1) with  $\sigma = 2$ . In the adiabatic regime, we obtain a success probability of 99.8% for  $\tau = 100$ . The ion stays deep within the potential well guaranteeing low losses. This is in good agreement with theoretical predictions. The very high success probability stays almost constant within the adiabatic regime down to  $\tau = 4$  ( $p_4 = 99.0\%$ ). According to our model, the ion experiences a relative displacement of over  $300 \mu\text{m}$  gaining a potential energy of more than 30 meV. Even faster transports lead to higher transport losses resulting in probabilities around 85%. When the energy of the ion exceeds about 30% of the depth of the potential, we observe a strongly increased loss probability.

13

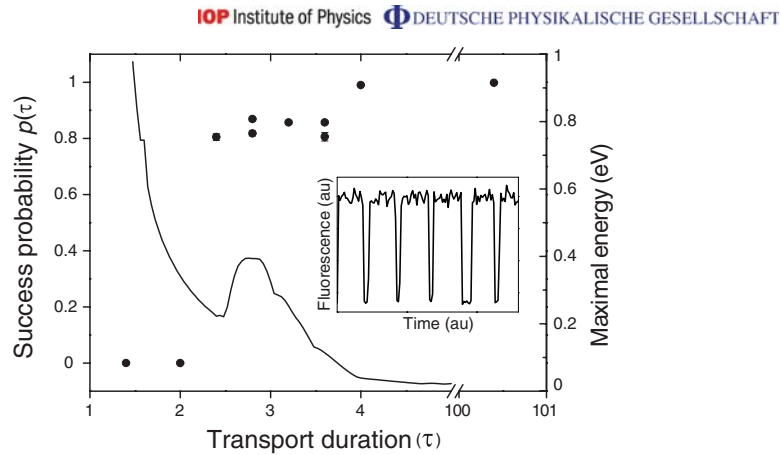


**Figure 9.** Transport success probability as a function of transport time (dots), y-scale on left. Slow transports with large  $\tau$  show a success probability close to unity. In the intermediate range  $2.5 \leq \tau \leq 4$ , the probability reduces to approx. 85%. From the model we deduce the ion's maximum energy during the transport (solid), y-scale on right side. Inset: fluorescence level as observed by the CCD camera showing the dark periods during the transport while the bright periods indicate a successful transport.

### 5.2. Coherent excitation during transport

If the ions are to be laser-cooled after a fast shuttle, it is important to keep the excitation of vibrational degrees of freedom minimal. Therefore, we quantitatively investigate the ion's kinetic energy after the transport for ramps in the non-adiabatic regime with  $4 < \tau \leq 20$ . We generalize a method which was recently employed [26, 27] to measure motional heating rates in a micro-ion trap.

After a transport, in step (6) of the experimental sequence, the oscillating ion is Doppler-cooled by laser light, and scatters an increasing amount of photons as it cools down. We observe the scattered photons by a PMT as a function of time. The scattering rate in our model depends on the laser power quantified by a saturation parameter  $s$ , the laser detuning  $\Delta$ , and the motional energy of the ion. In contrary to [26] we do not average over a thermal state. For large excitations, the oscillation amplitude exceeds the waist of the cooling laser resulting in a low scattering rate. A uniform laser intensity is therefore not appropriate for describing our experiments. We take this effect into account by including a Gaussian beam waist of  $w_0 = 60 \mu\text{m}$  in our simulations. The efficiency of the laser cooling sets in with a sharp rise of PMT counts shortly after  $t_{\text{recover}}$ . Only then, the scattering rate reaches its steady state value at the Doppler-cooling limit, see figure 10(a). Adapting the theoretical treatment for a thermal motional state in [26] to the case of a coherent motional oscillation [27] and including a spatial laser beam profile, the recovery time of fluorescence is quantitatively identified with the energy after the transport. The results are shown in figure 10(b) and compared to the theoretical simulations of our simple classical model. As expected, the motional excitation

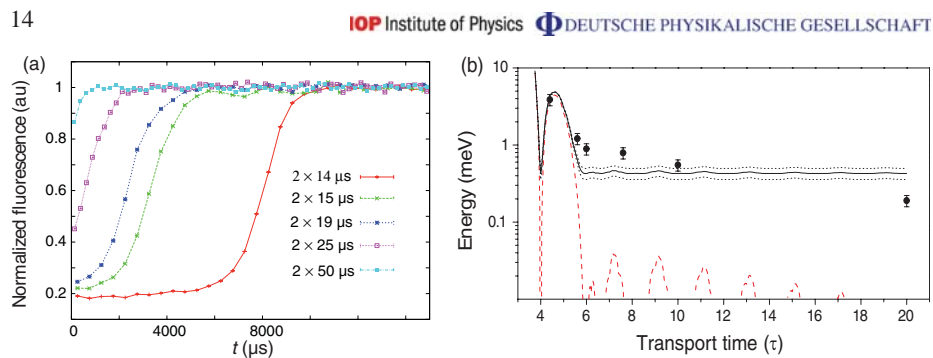


**Figure 10.** (a) Fluorescence rate after the transport and during application of Doppler cooling. Fast transport results in large excitation and a late recovery of the fluorescence level from vibrational excitation. (b) Measured excitation energy after an error function transport with  $\tau = 4$ –20. Error bars of the data points account for the uncertainty of the excitation energy from the photon scattering rate, taking into account uncertainties in the laser beam waist  $60(10) \mu\text{m}$ , laser saturation uncertainty of 15%, and laser detuning uncertainty of 30 MHz. The overall uncertainty results in 15% errors for the excitation energy. The theoretical prediction of the simple model (dashed line) for solely the error function transport does not agree with the data. However, we found a motional excitation of  $0.427(73) \text{ meV}$  due to the morphing steps of the potential before and after the transport by replacing steps (3) and (4) in the measurement cycle by a waiting time of equal length. The solid line shows this modified prediction together with its standard deviation (dotted).

increases for short transport times  $\tau$ . For slow transports, i.e.  $\tau \gg 1$ , the excitation does not drop below a certain threshold. We found that this excess excitation is due to the morphing steps (2) and (5) and might be caused by a non-ideal matching of the respective potential minima. Even a few micrometres difference leads to a large kick during the linear morphing ramp. We measured this effect independently by replacing steps (3) and (4) by equal waiting times without voltage ramps. Corrected for this excess heating, the model agrees well with the measured data.

The motional heating rate omitting any transport or morphing steps has been measured independently for our trap by replacing steps (2)–(4) by waiting times of 500 and 2000 ms. We deduce an energy gain of  $3(1) \text{ meV s}^{-1}$ . During our transport cycles this increase in energy only amounts to about  $1.5 \mu\text{eV}$ . This minor energy gain does not affect our measurement results and conclusions on the transport-induced excitation.

## 6. Conclusion and outlook

Employing a novel segmented linear Paul trap, we demonstrated stable trapping of single ions and cold ion crystals. For the first time we have shown fast, non-adiabatic transports over  $2 \times 2 \text{ mm}$  travels within a few microseconds by error function ramps. The main achievement

15

IOP Institute of Physics  $\Phi$  DEUTSCHE PHYSIKALISCHE GESELLSCHAFT

is the characterization of the ion's motional excitation. The method is based on the measured modification of the ion's scattering rate during Doppler cooling. In the future, however, sideband cooling and spectroscopic sideband analysis will be applied yielding a much more sensitive tool to investigate motional energy transfers. This will lead to a largely improved determination of ion excess motion. Then subtle changes of the parameters and the application of optimal control theory for the voltage ramps may be applied to yield lower motional excitation. Furthermore, we will establish a dedicated loading zone and optimize the transport of single ions and linear crystals through the tapered zone.

For micro-structured segmented ion traps with axial trap frequencies of several megahertz, the application of the demonstrated techniques will lead to transport times of a few microseconds only. This way, future quantum algorithms may no longer be limited by the ion transport but only by the time required for logic gate operations.

#### Acknowledgments

We acknowledge financial support by the Landesstiftung Baden-Württemberg, the Deutsche Forschungsgemeinschaft within the SFB-TR21, the European Commission and the European Union under the contract no. MRTN-CT-2006-035369 (EMALI).

#### References

- [1] Wineland D J *et al* 2005 *Proc. 17th Int. Conf. on Laser Spectroscopy* (Singapore: World Scientific) p 393
- [2] Becher C *et al* 2005 *Proc. 17th Int. Conf. on Laser Spectroscopy* (Singapore: World Scientific) p 381
- [3] Barrett M D *et al* 2004 *Nature* **429** 737
- [4] Riebe M *et al* 2004 *Nature* **429** 734
- [5] Schmidt P O *et al* 2005 *Science* **309** 749
- [6] Rosenband T *et al* 2007 *Phys. Rev. Lett.* **98** 220801
- [7] Roos C F *et al* 2006 *Nature* **443** 316
- [8] Stick D *et al* 2006 *Nat. Phys.* **2** 36
- [9] Seidelin S *et al* 2006 *Phys. Rev. Lett.* **96** 253003
- [10] Brown K R *et al* 2007 *Phys. Rev. A* **75** 015401
- [11] Gulde S *et al* 2001 *Appl. Phys. B* **73** 861
- [12] Kjaergaard N *et al* 2000 *Appl. Phys. B* **71** 207
- [13] Berkeland D J *et al* 1998 *J. Appl. Phys.* **83** 5025
- [14] Rotter D 2003 *Diploma Thesis* Universität Innsbruck
- [15] Schmidt-Kaler F *et al* 2003 *Appl. Phys. B* **77** 789
- [16] Leibfried D, Knill E, Ospelkaus C and Wineland D J 2007 *Phys. Rev. A* **76** 032324
- [17] Kielpinski D, Monroe C and Wineland D J 2002 *Nature* **417** 709
- [18] Chuang I 2006 private communication
- [19] Home J P *et al* 2006 *Quantum Inf. Comput.* **6** 289
- [20] Hucul D *et al* 2007 *Preprint quant-ph/0702175v2*
- [21] Hensinger W K *et al* 2006 *Appl. Phys. Lett.* **88** 034101
- [22] Reichle R *et al* 2006 *Fortschr. Phys.* **54** 666
- [23] Schulz S, Poschinger U, Singer K and Schmidt-Kaler F 2006 *Fortschr. Phys.* **54** 648
- [24] Rowe M A *et al* 2002 *Quantum Inf. Comput.* **2** 257
- [25] Couvert A *et al* 2007 *Preprint 0708.4197v1*
- [26] Wesenberg J H *et al* 2007 *Preprint 0707.1314*
- [27] Reichle R *et al* in preparation

*New Journal of Physics* **10** (2008) 013004 (<http://www.njp.org/>)

# Bibliography

- [Abr72] M. Abramowitz and I. A. Stegun, *Handbook of Mathematical Functions*, NBS Applied Mathematics Series No. 55, New York: Dover, 1972.
- [Ash96] R. C. Ashoori, *Electrons in artificial atoms*, Nature **379**, 413 (1996).
- [Bat07] A. Batra, C. D. Weis, J. Reijonen, A. Persaud, T. Schenkel, S. Cabrini, C. C. Lo, and J. Bokor, *Detection of low energy single ion impacts in micron scale transistors at room temperature*, Applied Physics Letters **91**, 193502 (2007).
- [Bec92] A. A. Becker, *The boundary element method in engineering: a complete course*, New York: McGraw-Hill Book Company, 1992.
- [Ber98] D. J. Berkeland, J. D. Miller, J. C. Bergquist, W. M. Itano, and D. J. Wineland, *Minimization of ion micromotion in a Paul trap*, Journal of Applied Physics **83**, 5025 (1998).
- [Bla09] R. B. Blakestad, C. Ospelkaus, A. P. VanDevender, J. M. Amini, J. Britton, D. Leibfried, and D. J. Wineland, *High-Fidelity Transport of Trapped-Ion Qubits through an X-Junction Trap Array*, Physical Review Letters **102**, 153002 (2009).
- [Boy68] G. D. Boyd and D. A. Kleinman, *Parametric Interaction of Focused Gaussian Light Beams*, Journal of Applied Physics **39**, 3597 (1968).
- [Bre92] C. A. Brebbia and J. Dominguez, *Boundary Elements - An Introductory Course*, 2nd edition, Boston: WIT Press, 1992.
- [Chi06] L. Childress, M. V. G. Dutt, J. M. Taylor, A. S. Zibrov, F. Jelezko, J. Wrachtrup, P. R. Hemmer, and M. D. Lukin, *Coherent Dynamics of Coupled Electron and Nuclear Spin Qubits in Diamond*, Science **314**, 281 (2006).

- [Cre02] P. Cren, C. F. Roos, A. Aclan, J. Dalibard, and D. Guéry-Odelina, *Loading of a cold atomic beam into a magnetic guide*, European Physical Journal D **20**, 107 (2002).
- [Cro93] M. F. Crommie, C. P. Lutz, and D. M. Eigler, *Confinement of Electrons to Quantum Corrals on a Metal Surface*, Science **262**, 218 (1993).
- [Deh67] H. G. Dehmelt, *Radiofrequency Spectroscopy of Stored Ions, Part I*, Adv. At. Mol. Phys. **3**, 53 (1967).
- [Deu07] T. W. Deuschle, *Kalte Ionenkristalle in einer segmentierten Paul-Falle*, Dissertation, Universität Ulm (2007).
- [Dev07] S. J. Devitt, A. D. Greentree, R. Ionicioiu, J. L. O'Brien, W. J. Munro, and L. C. L. Hollenberg, *Photonic module: An on-demand resource for photonic entanglement*, Physical Review A **76**, 052312 (2007).
- [Die87] F. Diedrich and H. Walther, *Nonclassical Radiation of a Single Stored Ion*, Physical Review Letters **58**, 203 (1987).
- [Die89] F. Diedrich, J. C. Bergquist, W. M. Itano, and D. J. Wineland, *Laser Cooling to the Zero-Point Energy of Motion*, Physical Review Letters **62**, 403 (1989).
- [Don06] G. Donnert, J. Keller, R. Medda, M. A. Andrei, S. O. Rizzoli, R. Lührmann, R. Jahn, C. Eggeling, and S. W. Hell, *Macromolecular-scale resolution in biological fluorescence microscopy*, Proceedings of the National Academy of Sciences **103**, 11440 (2006).
- [Dre83] R. W. P. Drever, J. L. Hall, F. V. Kowalski, J. Hough, G. M. Ford, A. J. Munley, and H. Ward, *Laser Phase and Frequency Stabilization Using an Optical Resonator*, Applied Physics B **31**, 97 (1983).
- [Dre04] M. Drewsen, A. Mortensen, R. Martinussen, P. Staantum, and J. L. Sørensen, *Nondestructive Identification of Cold and Extremely Localized Single Molecular Ions*, Physical Review Letters **93**, 243201 (2004).
- [Ebe04] P. Ebert, N. D. Jäger, K. Urban, and E. R. Weber, *Nanoscale fluctuations in the distribution of dopant atoms: Dopant-induced dots and roughness of electronic interfaces*, Journal of Vacuum Science and Technology B **22**, 2018 (2004).
- [Ebl06] J. F. Eble, *Stabilisierung von Lasern zum Erzeugen und Kühlen von Ionen in einer Paul-Falle*, Diplomarbeit, Universität Ulm (2006).

- [Eblxx] J. F. Eble, *Dissertation (in Vorbereitung)*, Universität Ulm (20xx).
- [Enz00] D. G. Enzer, M. M. Schauer, J. J. Gomez, M. S. Gulley, M. H. Holzscheiter, P. G. Kwiat, S. K. Lamoreaux, C. G. Peterson, V. D. Sandberg, D. Tupa, A. G. White, R. J. Hughes, and D. F. V. James, *Observation of Power-Law Scaling for Phase Transitions in Linear Trapped Ion Crystals*, *Physical Review Letters* **85**, 2466 (2000).
- [Esc03] J. Eschner, G. Morigi, F. Schmidt-Kaler, and R. Blatt, *Laser cooling of trapped ions*, *Journal of the Optical Society of America B: Optical Physics* **20**, 1003 (2003).
- [Fic09a] R. Fickler, *Kalte einzelne Ionen für die Implantation in Festkörper mit nm Auflösung*, Diplomarbeit, Universität Ulm (2009).
- [Fic09b] R. Fickler, W. Schnitzler, N. M. Linke, F. Schmidt-Kaler, and K. Singer, *Optimized focusing ion optics for an ultracold deterministic single ion source targeting nm resolution*, *Journal of Modern Optics* **56**, 2061 (2009).
- [Gae06] T. Gaebel, M. Domhan, I. Popa, C. Wittmann, P. Neumann, F. Jelezko, J. R. Rabeau, N. Stavrias, A. D. Greentree, S. Praver, J. Meijer, J. Twamley, P. R. Hemmer, and J. Wrachtrup, *Room-temperature coherent coupling of single spins in diamond*, *Nature Physics* **2**, 408 (2006).
- [Gho95] P. K. Ghosh, *Ion Traps*, Oxford: Clarendon Press, 1995.
- [Gre96] L. Greengard and V. Rohklin, *A New Version of the Fast Multipole Method for the Laplace Equation in Three Dimensions*, Research Report YALEU/DCS **RR-1115** (1996).
- [Gre07] A. Greiner, J. Sebastian, P. Rehme, A. Aghajani-Talesh, A. Griesmaier, and T. Pfau, *Loading chromium atoms in a magnetic guide*, *Journal of Physics B* **40**, F77 (2007).
- [Gre08a] A. D. Greentree, B. A. Fairchild, F. M. Hossain, and S. Praver, *Diamond integrated quantum photonics*, *Materials Today* **11**, 22 (2008).
- [Gre08b] A. Greiner, *Erzeugung eines lasergekühlten Atomstrahls in einem Magnetleiter - Eine intensive Quelle für die Atomlithographie*, Dissertation, Universität Stuttgart (2008).

- [Gri05] A. Griesmaier, J. Werner, S. Hensler, J. Stuhler, and T. Pfau, *Bose-Einstein Condensation of Chromium*, Physical Review Letters **94**, 160401 (2005).
- [Gul03] S. T. Gulde, *Experimental Realization of Quantum Gates and the Deutsch-Jozsa Algorithm with Trapped  $^{40}\text{Ca}^+$  Ions*, Dissertation, Universität Innsbruck (2003).
- [Gur07] M. V. Gurudev Dutt, L. Childress, L. Jiang, E. Togan, J. Maze, F. Jelezko, A. S. Zibrov, P. R. Hemmer, and M. D. Lukin, *Quantum Register Based on Individual Electronic and Nuclear Spin Qubits in Diamond*, Science **316**, 1312 (2007).
- [Han06a] R. Hanson, F. M. Mendoza, R. J. Epstein, and D. D. Awschalom, *Polarization and Readout of Coupled Single Spins in Diamond*, Physical Review Letters **97**, 087601 (2006).
- [Han06b] J. L. Hanssen, J. J. McClelland, E. A. Dakin, and M. Jacka, *Laser-cooled atoms as a focused ion-beam source*, Physical Review A **74**, 063416 (2006).
- [Han08] J. L. Hanssen, S. B. Hill, J. Orloff, and J. J. McClelland, *Magneto-Optical-Trap-Based, High Brightness Ion Source for Use as a Nanoscale Probe*, Nano Letters **8**, 2844 (2008).
- [Haw89] P. W. Hawkes and E. Kasper, *Principles of Electron Optics*, Academic Press: London, 1989.
- [Hed00] D. W. O. Heddle, *Electrostatic Lens Systems*, 2nd edition, Institute of Physics Publishing Bristol and Philadelphia, 2000.
- [Hei90] D. J. Heinzen and D. J. Wineland, *Quantum-limited cooling and detection of radio-frequency oscillations by laser-cooled ions*, Physical Review A **42**, 2977 (1990).
- [Hei09] A. J. Heinrich, *Looking Below the Surface*, Science **323**, 1178 (2009).
- [Höf97] J. T. Höffges, H. W. Baldauf, T. Eichler, S. R. Helmfrid, and H. Walther, *Heterodyne measurement of the fluorescent radiation of a single trapped ion*, Optical Communications **133**, 170 (1997).
- [Häf05] H. Häffner, W. Hänsel, C. F. Roos, J. Benhelm, D. Chek-al-kar, M. Chwalla, T. Körber, U. D. Rapol, M. Riebe, P. O. Schmidt, C. Becher, O. Gühne, W. Dür, and R. Blatt, *Scalable multiparticle entanglement of trapped ions*, Nature **438**, 643 (2005).

- [Hil03a] S. B. Hill and J. J. McClelland, *Atoms on demand: Fast, deterministic production of single Cr atoms*, Applied Physics Letters **82**, 3128 (2003).
- [Hil03b] S. B. Hill and J. J. McClelland, *Performance of a feedback-controlled, deterministic source of single chromium atoms*, Journal of the Optical Society of America B: Optical Physics **21**, 473 (2003).
- [Hän75] T. Hänsch and A. Schawlow, *Cooling of gases by laser radiation*, Optical Communications **13**, 68 (1975).
- [Hol03] L. C. L. Hollenberg, A. S. Dzurak, C. Wellard, A. R. Hamilton, D. J. Reilly, G. J. Milburn, and R. G. Clark, *Charge-based quantum computing using single donors in semiconductors*, Physical Review B **69**, 113301 (2003).
- [Hop08] T. Hopf, C. Yang, S. M. Hearne, D. N. Jamieson, E. Gauja, S. E. Andresen, and A. S. Dzurak, *Low-Noise Detection System for the Counted Implantation of Single Ions in Silicon*, IEEE Transactions on Nuclear Science **55**, 812 (2008).
- [Hub08] G. Huber, T. Deuschle, W. Schnitzler, R. Reichle, K. Singer, and F. Schmidt-Kaler, *Transport of ions in a segmented linear Paul trap in printed-circuit-board technology*, New Journal of Physics **10**, 013004 (2008).
- [Jam98] D. F. V. James, *Quantum dynamics of cold trapped ions with application to quantum computation*, Applied Physics B **66**, 181 (1998).
- [Jam05] D. N. Jamieson, C. Yang, T. Hopf, S. M. Hearne, C. I. Pakes, S. Prawer, M. Mitic, E. Gauja, S. E. Andresen, F. E. Hudson, A. S. Dzurak, and R. G. Clark, *Controlled shallow single-ion implantation in silicon using an active substrate for sub-20-keV ions*, Applied Physics Letters **86**, 202101 (2005).
- [Jel04a] F. Jelezko, T. Gaebel, I. Popa, A. Gruber, and J. Wrachtrup, *Observation of Coherent Oscillations in a Single Electron Spin*, Physical Review Letters **92**, 076401 (2004).
- [Jel04b] F. Jelezko, T. Gaebel, I. Popa, M. Domhan, A. Gruber, and J. Wrachtrup, *Observation of Coherent Oscillation of a Single Nuclear Spin and Realization of a Two-Qubit Conditional Quantum Gate*, Physical Review Letters **93**, 130501 (2004).
- [Kan98] B. E. Kane, *A silicon-based nuclear spin quantum computer*, Nature **393**, 133 (1998).

- [Kie00] D. Kielpinski, B. E. King, C. J. Myatt, C. A. Sackett, Q. A. Turchette, W. M. Itano, C. Monroe, D. J. Wineland, and W. H. Zurek, *Sympathetic cooling of trapped ions for quantum logic*, Physical Review A **61**, 032310 (2000).
- [Kja00] N. Kjaergaard, L. Hornekaer, A. M. Thommesen, Z. Videsen, and M. Drewsen, *Isotope selective loading of an ion trap using resonance-enhanced two-photon ionization*, Applied Physics B **71**, 207 (2000).
- [Lar86] D. J. Larson, J. C. Bergquist, J. J. Bollinger, W. M. Itano, and D. J. Wineland, *Sympathetic Cooling of Trapped Ions: A Laser-Cooled Two-Species Nonneutral Ion Plasma*, Physical Review Letters **57**, 70 (1986).
- [Lei03] D. Leibfried, R. Blatt, C. Monroe, and D. J. Wineland, *Quantum dynamics of single trapped ions*, Reviews of Modern Physics **75**, 281 (2003).
- [Lei05] D. Leibfried, E. Knill, S. Seidelin, J. Britton, R. B. Blakestad, J. Chiaverini, D. B. Hume, W. M. Itano, J. D. Jost, C. Langer, R. Ozeri, R. Reichle, and D. J. Wineland, *Creation of a six-atom Schrödinger cat state*, Nature **438**, 639 (2005).
- [Lie08] H. Liebl, *Applied Charged Particle Optics*, Springer Verlag: Berlin, 2008.
- [Lin07] N. M. Linke, *Kalte Ionenkristalle in einer segmentierten Paul-Falle als deterministische Einzelionenquelle*, Diplomarbeit, Universität Ulm (2007).
- [Los98] D. Loss and D. P. DiVincenzo, *Quantum computation with quantum dots*, Physical Review A **57**, 120 (1998).
- [Lou92] B. Lounis and C. Cohen-Tannoudji, *Coherent population trapping and Fano profiles*, Journal de Physique II **2**, 579 (1992).
- [Luc00] Lucent Technologies, *60nm pMOS nano-transistor*, <http://www.bell-labs.com/org/physicalsciences/projects/60nm/60nm2.html>, Bell Laboratories Physical Science Research (2000).
- [Mac59] W. W. Macalpine and R. O. Schildknecht, *Coaxial Resonators with Helical Inner Conductor*, Proc. of the IEEE **47**, 2099 (1959).
- [Mai06] R. Maiwald, *Abbildungs- und Steuerungssystem für ein Experiment mit einzelnen Ionen*, Diplomarbeit, Universität Ulm (2006).
- [Mar94] I. Marzoli, J. I. Cirac, R. Blatt, and P. Zoller, *Laser cooling of trapped three-level ions: Designing two-level systems for sideband cooling*, Physical Review A **49**, 2771 (1994).

- [Maz08] J. R. Maze, P. L. Stanwix, J. S. Hodges, S. Hong, J. M. Taylor, P. Cappellaro, L. Jiang, M. V. Gurudev Dutt, E. Togan, A. S. Zibrov, A. Yacoby, R. L. Walsworth, and M. D. Lukin, *Nanoscale magnetic sensing with an individual electronic spin in diamond*, *Nature* **455**, 644 (2008).
- [Mei05] J. Meijer, B. Burchard, M. Domhan, C. Wittmann, T. Gaebel, I. Popa, F. Jelezko, and J. Wrachtrup, *Generation of single color centers by focused nitrogen implantation*, *Applied Physics Letters* **87**, 261909 (2005).
- [Mei06] J. Meijer, T. Vogel, B. Burchard, I. W. Rangelow, L. Bischoff, J. Wrachtrup, M. Domhan, F. Jelezko, W. Schnitzler, S. A. Schulz, K. Singer, and F. Schmidt-Kaler, *Concept of deterministic single ion doping with sub-nm spatial resolution*, *Applied Physics A* **83**, 321 (2006).
- [Mei08a] F. Meier, , L. Zhou, J. Wiebe, and R. Wiesendanger, *Revealing Magnetic Interactions from Single-Atom Magnetization Curves*, *Science* **320**, 82 (2008).
- [Mei08b] J. Meijer, S. Pezzagna, T. Vogel, B. Burchard, H. H. Bukow, I. W. Rangelow, Y. Sarov, H. Wiggers, I. Plümel, F. Jelezko, J. Wrachtrup, F. Schmidt-Kaler, W. Schnitzler, and K. Singer, *Towards the implanting of ions and positioning of nanoparticles with nm spatial resolution*, *Applied Physics A* **91**, 567 (2008).
- [Mit05] M. Mitic, S. E. Andresen, C. Yang, T. Hopf, V. Chan, E. Gauja, F. E. Hudson, T. M. Buehler, R. Brenner, A. J. Ferguson, C. I. Pakes, S. M. Hearne, G. Tamanyan, D. J. Reilly, A. R. Hamilton, D. N. Jamieson, A. S. Dzurak, and R. G. Clark, *Single atom Si nanoelectronics using controlled single-ion implantation*, *Microelectronic Engineering* **78-79**, 279 (2005).
- [Moe05] D. L. Moehring, M. Acton, B. B. Blinov, K.-A. Brickman, L. Deslauriers, P. C. Haljan, W. K. Hensinger, D. Hucul, R. N. Kohn, P. J. Lee, M. J. Madsen, P. Maunz, S. Olmschenk, D. Stick, M. Yeo, and C. Monroe, *Ion Trap Networking: Cold, Fast, and Small*, *Proceedings of the XVII International Conference on Laser Spectroscopy*, 421–428 (2005).
- [Moo65] G. Moore, *Cramming more components onto integrated circuits*, *Electronics* **38**, 8 (1965).
- [Moo08] C. R. Moon, L. S. Mattos, B. K. Foster, G. Zeltzer, W. Ko, and H. C. Manoharan, *Quantum Phase Extraction in Isospectral Electronic Nanostructures*, *Science* **319**, 782 (2008).

- [Mor00a] G. Morigi, J. Eschner, and C. H. Keitel, *Ground state laser cooling using electromagnetically induced transparency*, Physical Review Letters **85**, 4458 (2000).
- [Mor00b] G. Morigi and H. Walther, *Low temperature dynamics and laser-cooling of two-species Coulomb chains for quantum logic*, arXiv:0005082v3 [quant-ph] (2000).
- [Nae98] H. Naegerl, R. Blatt, J. Eschner, F. Schmidt-Kaler, and D. Leibfried, *Coherent excitation of normal modes in a string of  $Ca^+$  ions*, Optics Express **3**, 89 (1998).
- [Nat06] National Institute of Standards and Technology, *NIST Atomic Spectra Database*, <http://physics.nist.gov/PhysRefData/ASD/index.html> (2006).
- [Nat08] S. Natarajan, *A 32 nm Logic Technology Featuring 2<sup>nd</sup>-Generation High-k + Metal-Gate Transistors, Enhanced Channel Strain and 0.171  $\mu m^2$  SRAM Cell Size in a 291 Mb Array*, Electron Devices Meeting 2008 IEEE, **IEDM 2008** (2008).
- [Neu78] W. Neuhauser, M. Hohenstatt, P. Toschek, and H. Dehmelt, *Optical-Sideband Cooling of Visible Atom Cloud Confined in Parabolic Well*, Physical Review Letters **41**, 233 (1978).
- [Neu08] P. Neumann, N. Mizuochi, F. Rempp, P. Hemmer, H. Watanabe, S. Yamasaki, V. Jacques, T. Gaebel, F. Jelezko, and J. Wrachtrup, *Multipartite Entanglement Among Single Spins in Diamond*, Science **320**, 1326 (2008).
- [Neu09] P. Neumann, R. Kolesov, V. Jacques, J. Beck, J. Tisler, A. Batalov, L. Rogers, N. B. Manson, G. Balasubramanian, F. Jelezko, and J. Wrachtrup, *Excited-state spectroscopy of single NV defects in diamond using optically detected magnetic resonance*, New Journal of Physics **11**, 013017 (2009).
- [O'B01] J. L. O'Brien, S. R. Schofield, M. Y. Simmons, R. G. Clark, A. S. Dzurak, N. J. Curson, B. E. Kane, N. S. McAlpine, M. E. Hawley, and G. W. Brown, *Towards the fabrication of phosphorus qubits for a silicon quantum computer*, Physical Review B **64**, 161401(R) (2001).
- [Of01] G. Of, *Die Multipolmethode für Randintegralgleichungen*, Diplomarbeit, Universität Stuttgart (2001).
- [Paq98] P. M. Paquet, J.-F. Gravel, P. Nobert, and D. Boudreau, *Speciation of chromium by ion chromatography and laser-enhanced ionization: optimization of the excitation-ionization scheme*, Spectrochimica Acta Part B **53**, 1907 (1998).

- [Pau53] W. Paul and H. Steinwedel, *Quadrupole mass filter*, *Zeitschrift für Naturforschung* **A8**, 448 (1953).
- [Pau58] W. Paul, O. Osberghaus, and E. Fischer, *Ein Ionenkäfig*, *Forschungsberichte des Wirtschafts- und Verkehrsministeriums Nordrhein-Westfalen* **415** (1958).
- [Pei99] E. Peik, J. Abel, T. Becker, J. von Zanthier, and H. Walther, *Sideband cooling of ions in radio-frequency traps*, *Physical Review A* **60**, 439 (1999).
- [Per04a] A. Persaud, F. I. Allen, F. Gicquel, S. J. Park, J. A. Liddle, T. Schenkel, T. Ivanov, K. Ivanova, I. W. Rangelow, and J. Bokor, *Single ion implantation with scanning probe alignment*, *Vacuum Science and Technology B* **22**, 2992 (2004).
- [Per04b] A. Persaud, S. J. Park, J. A. Liddle, I. W. Rangelow, J. Bokor, R. Keller, F. I. Allen, D. H. Schneider, and T. Schenkel, *Quantum Computer Development with Single Ion Implantation*, *Quantum Information Processing* **3**, 233 (2004).
- [Pez10] S. Pezzagna, B. Naydenov, F. Jelezko, J. Wrachtrup, and J. Meijer, *Creation efficiency of nitrogen-vacancy centres in diamond*, *New Journal of Physics* **12**, 065017 (2010).
- [Pic32] J. Picht, *Beiträge zur Theorie der geometrischen Elektronenoptik*, *Annalen der Physik* **15**, 926 (1932).
- [Pok07] W. Pok, T. C. G. Reusch, G. Scappucci, F. J. Rueb, A. R. Hamilton, and M. Y. Simmons, *Electrical Characterization of Ordered Si:P Dopant Arrays*, *IEEE Transactions on Nanotechnology* **6(2)**, 213 (2007).
- [Pos09] U. G. Poschinger, G. Huber, F. Ziesel, M. Deiss, M. Hettrich, S. A. Schulz, G. Poulsen, M. Drewsen, R. J. Hendricks, K. Singer, and F. Schmidt-Kaler, *Coherent Manipulation of a  $^{40}\text{Ca}^+$  Spin Qubit in a Micro Ion Trap*, *Journal of Physics B* **42**, 154013 (2009).
- [Pra08] S. Praver and A. D. Greentree, *Diamond for Quantum Computing*, *Science* **320**, 1601 (2008).
- [Rab06] J. R. Rabeau, P. Reichart, G. Tamanyan, D. N. Jamieson, S. Praver, F. Jelezko, T. Gaebel, I. Popa, M. Domhan, and J. Wrachtrup, *Implantation of labeled single nitrogen vacancy centers in diamond using  $^{15}\text{N}$* , *Applied Physics Letters* **88**, 023113 (2006).

- [Rai92] M. G. Raizen, J. M. Gilligan, J. C. Bergquist, W. M. Itano, and D. J. Wineland, *Ionic crystals in a linear Paul trap*, Physical Review A **45**, 6493 (1992).
- [Rid78] G. H. N. Riddle, *Electrostatic einzel lenses with reduced spherical aberration for use in field-emission guns*, Journal of Vacuum Science and Technology **15**, 857 (1978).
- [Rit09] E. Rittweger, K. Y. Han, S. E. Irvine, C. Eggeling, and S. W. Hell, *STED microscopy reveals crystal colour centres with nanometric resolution*, Nature Photonics **3**, 144 (2009).
- [Roo00a] C. F. Roos, *Controlling the quantum state of trapped ions*, Dissertation, Universität Innsbruck (2000).
- [Roo00b] C. F. Roos, D. Leibfried, A. Mundt, F. Schmidt-Kaler, J. Eschner, and R. Blatt, *Experimental Demonstration of Ground State Laser Cooling with Electromagnetically Induced Transparency*, Physical Review Letters **85**, 5547 (2000).
- [Rot03] D. Rotter, *Photoionisation von Kalzium*, Diplomarbeit, Universität Innsbruck (2003).
- [Row02] M. A. Rowe, A. Ben-Kish, B. DeMarco, D. Leibfried, V. Meyer, J. Beall, J. Britton, J. Hughes, W. M. Itano, B. Jelenkovic, C. Langer, T. Rosenband, and D. J. Wineland, *Transport of Quantum States and Separation of Ions in a Dual RF Ion Trap*, Quantum Information & Computation **2**, 257 (2002).
- [Rue04] F. J. Ruess, L. Oberbeck, M. Y. Simmons, K. E. J. Goh, A. R. Hamilton, T. Hallam, S. R. Schofield, N. J. Curson, and R. G. Clark, *Toward Atomic-Scale Device Fabrication in Silicon Using Scanning Probe Microscopy*, Nano Letters **4**(10), 1969 (2004).
- [Rue07] F. J. Ruess, W. Pok, T. C. G. Reusch, M. J. Butcher, K. E. J. Goh, G. Scappucci, A. R. Hamilton, and M. Y. Simmons, *Realization of Atomically Controlled Dopant Devices in Silicon*, Small **3**(4), 563 (2007).
- [San01] N. Sano and M. Tomizawa, *Random dopant model for three-dimensional drift-diffusion simulations in metal-oxide-semiconductor field-effect-transistors*, Applied Physics Letters **79**, 2267 (2001).
- [Sch36] O. Scherzer, *Über einige Fehler von Elektronenlinsen*, Zeitschrift für Physik A Hadrons and Nuclei **101**, 593 (1936).

- [Sch93] J. P. Schiffer, *Phase transitions in anisotropically confined ionic crystals*, Physical Review Letters **70**, 818 (1993).
- [Sch02] G. Schönhense and H. Spiecker, *Correction of chromatic and spherical aberration in electron microscopy utilizing the time structure of pulsed excitation sources*, Journal of Vacuum Science and Technology B **20**, 2526 (2002).
- [Sch03] S. R. Schofield, N. J. Curson, M. Y. Simmons, F. J. Ruess, T. Hallam, L. Oberbeck, and R. G. Clark, *Atomically Precise Placement of Single Dopants in Si*, Physical Review Letters **91**, 136104 (2003).
- [Sch08] S. A. Schulz, U. G. Poschinger, F. Ziesel, and F. Schmidt-Kaler, *Sideband cooling and coherent dynamics in a microchip multi-segmented ion trap*, New Journal of Physics **10**, 045007 (2008).
- [Sch09a] W. Schnitzler, N. M. Linke, R. Fickler, J. Meijer, F. Schmidt-Kaler, and K. Singer, *Deterministic Ultracold Ion Source Targeting the Heisenberg Limit*, Physical Review Letters **102**, 070501 (2009).
- [Sch09b] S. A. Schulz, *Scalable Microchip Ion Traps for Quantum Computation*, Dissertation, Universität Ulm (2009).
- [Sch10] W. Schnitzler, G. Jacob, R. Fickler, F. Schmidt-Kaler, and K. Singer, *Focusing a deterministic single-ion beam*, New Journal of Physics **12**, 065023 (2010).
- [Sem07] Semiconductor Industry Association, *The International Technology Roadmap for Semiconductors* (2007).
- [Sep60] A. Septier, *Aberration spherique de quelques lentilles electrostatiques a symetrie de revolution pour des faisceaux de grande ouverture*, CERN Report **60-39** (1960).
- [She07] L. Shen and Y. J. Liu, *An adaptive fast multipole boundary element method for three-dimensional potential problems*, Computational Mechanics **39**, 681 (2007).
- [Shi83] K. Shimizu, *Determination of the Optimum Electrode Shape of Electrostatic Einzel Lenses*, Japanese Journal of Applied Physics **22**, 1623 (1983).
- [Shi98] T. Shinada, Y. Kumura, J. Okabe, T. Matsukawa, and I. Ohdomari, *Current status of single ion implantation*, Journal of Vacuum Science and Technology B **16**, 2489 (1998).

- [Shi99] T. Shinada, A. Ishikawa, M. Fujita, K. Yamashita, and I. Ohdomari, *Influence of Secondary Electron Detection Efficiency on Controllability of Dopant Ion Number in Single Ion Implantation*, Japanese Journal of Applied Physics **38**, 3419 (1999).
- [Shi02] T. Shinada, H. Koyama, C. Hinshita, K. Imamura, and I. Ohdomari, *Improvement of Focused Ion-Beam Optics in Single-Ion Implantation for Higher Aiming Precision of One-by-One Doping of Impurity Atoms into Nano-Scale Semiconductor Devices*, Japanese Journal of Applied Physics **41**, L287 (2002).
- [Shi05] T. Shinada, S. Okamoto, T. Kobayashi, and I. Ohdomari, *Enhancing semiconductor device performance using ordered dopant arrays*, Nature **437**, 1128 (2005).
- [Shi08] T. Shinada, T. Kurosawa, H. Nakayama, Y. Zhu, M. Hori, and I. Ohdomari, *A reliable method for the counting and control of single ions for single-dopant controlled devices*, Nanotechnology **19**, 345202 (2008).
- [Sin02] K. Singer, S. Jochim, M. Mudrich, A. Mosk, and M. Weidemüller, *Low-cost mechanical shutter for light beams*, Review of Scientific Instruments **73**, 4402 (2002).
- [Sin10] K. Singer, U. Poschinger, M. Murphy, P. Ivanov, F. Ziesel, T. Calarco, and F. Schmidt-Kaler, *Colloquium: Experiments with atomic quantum bits: Essential numerical tools*, accepted for publication in Reviews of Modern Physics, arXiv:0912.0196v3 (2010).
- [Ste86] S. Stenholm, *The semiclassical theory of laser cooling*, Review of Modern Physics **58**, 699 (1986).
- [Ste92] A. M. Steane, M. Chowdhury, and C. J. Foot, *Radiation force in the magneto-optical trap*, Journal of the Optical Society of America B **9**, 2142 (1992).
- [Ste97] A. Steane, *The ion trap quantum information processor*, Applied Physics B **64**, 632 (1997).
- [Su08] C.-H. Su, A. D. Greentree, and L. J. L. Hollenberg, *Towards a picosecond transform-limited nitrogen-vacancy based single photon source*, Optics Express **16**, 6240 (2008).
- [Sze88] J. Szepe and M. Szilagy, *A novel approach to the synthesis of electrostatic lenses with minimized aberrations*, IEEE Transactions on Electronic Devices **35**, 1181 (1988).

- [Tay08] J. M. Taylor, P. Cappellaro, L. Childress, L. Jiang, D. Budker, P. R. Hemmer, A. Yacoby, R. Walsworth, and M. D. Lukin, *High-sensitivity diamond magnetometer with nanoscale resolution*, *Nature Physics* **4**, 810 (2008).
- [Tha99] G. Thalhammer, *Frequenzstabilisierung von Diodenlasern bei 850, 854 und 866 nm mit Linienbreiten im Kilohertz-Bereich*, Diplomarbeit, Leopold-Franzens-Universität Innsbruck (1999).
- [Ver67] L. Verlet, *Computer experiments on classical fluids. I. Thermodynamical properties of Lennard-Jones molecules*, *Physical Review* **159**, 98 (1967).
- [Wei01] C. Weißbäcker and H. Rose, *Electrostatic correction of the chromatic and of the spherical aberration of charged-particle lenses*, *Journal of Electron Microscopy* **50**, 383 (2001).
- [Wei02] C. Weißbäcker and H. Rose, *Electrostatic correction of the chromatic and of the spherical aberration of charged-particle lenses (Part II)*, *Journal of Electron Microscopy* **51**, 45 (2002).
- [Wei09] A. Weismann, M. Wenderoth, S. Lounis, P. Zahn, N. Quaas, R. G. Ulbrich, P. H. Dederichs, and S. Blügel, *Seeing the Fermi Surface in Real Space by Nanoscale Electron Focusing*, *Science* **323**, 1190 (2009).
- [Wes08] V. Westphal, S. O. Rizzoli, M. A. Lauterbach, D. Kamin, R. Jahn, and S. W. Hell, *Video-rate far-field optical nanoscopy dissects synaptic vesicle movement*, *Science* **320**, 246 (2008).
- [Win73] D. Wineland, P. Ekstrom, and H. G. Dehmelt, *Monoelectron Oscillator*, *Physical Review Letters* **31**, 1279 (1973).
- [Win75] D. J. Wineland and H. G. Dehmelt, *Proposed  $10^{14} \Delta\nu < \nu$  Laser Fluorescence Spectroscopy on  $Tl^+$  Mono-Ion Oscillator III*, *Bulletin of the American Physical Society* **20**, 637 (1975).
- [Win78] D. J. Wineland, R. E. Drullinger, and F. L. Walls, *Radiation-pressure cooling of bound resonant absorbers*, *Physical Review Letters* **40**, 1639 (1978).
- [Zai01] A. M. Zaitsev, *Optical Properties of Diamond: A Data Handbook*, Springer Verlag Berlin, 2001.
- [Zie08] F. Ziesel, *Spektroskopie und Transport von Ionen in einer Mikrofalle*, Diplomarbeit, Universität Ulm (2008).

- [Zve61] A. I. Zverev and H. J. Blinchikoff, *Realization of a Filter with Helical Components*, IRE Transactions on Component Parts **8**, 99 (1961).

Hiermit erkläre ich, Wolfgang Schnitzler, dass ich die vorliegende Dissertation selbstständig angefertigt und keine anderen als die angegebenen Quellen und Hilfsmittel verwendet sowie die wörtlich und inhaltlich übernommenen Stellen als solche kenntlich gemacht und die Satzung der Universität Ulm zur Sicherung guter wissenschaftlicher Praxis beachtet habe.

Ulm, 5. Juli 2010

Wolfgang Schnitzler

